ANALYSIS OF TIME-LAPSE 3-D VSP DATA FOR SEISMIC MONITORING OF CO_2 FLOOD IN WEYBURN FIELD, SASKATCHEWAN

A Thesis Submitted to the College of

Graduate Studies and Research

In Partial Fulfillment of the Requirements

For the Degree of Doctor of Philosophy

In the Department of Geological Sciences

University of Saskatchewan

Saskatoon

By

AMIN BAHARVAND AHMADI

Permission to Use

In presenting this thesis in partial fulfilment of the requirements for a Postgraduate degree from the University of Saskatchewan, I agree that the Libraries of this University may make it freely available for inspection. I further agree that permission for copying of this thesis in any manner, in whole or in part, for scholarly purposes may be granted by the professor or professors who supervised my thesis work or, in their absence, by the Head of the Department or the Dean of the College in which my thesis work was done. It is understood that any copying or publication or use of this thesis or parts thereof for financial gain shall not be allowed without my written permission. It is also understood that due recognition shall be given to me and to the University of Saskatchewan in any scholarly use which may be made of any material in my thesis.

Requests for permission to copy or to make other use of material in this thesis in whole or part should be addressed to:

Head of the Department of Geological Sciences

University of Saskatchewan

Saskatoon, Saskatchewan (S7N 5E2)

ABSTRACT

This study explores the potential of VSP data in reservoir studies and particularly in separating the effects of CO_2 pore pressure and saturation after fluid injection into the reservoir. It helps establishing robust and reliable links between physical properties of hydrocarbon reservoirs and seismic data. It also reduces the uncertainties of the AVA analysis through constructing a detailed model of first-arrival amplitude decay combining geometric spreading, scattering, and inelastic dissipation. The inversion of seismic data reveals anisotropic variations of geometric attenuation (wavefront curvatures and scattering, denoted γ) and the effective attenuation parameter (κ) with depth. Statistical analysis of model uncertainties quantitatively measures the significance of these results. This model correctly predicts the observed frequency-dependent first-arrival amplitudes at all frequencies and can be used for reflected waves.

Scattering and geometric spreading (focusing and defocusing of wave fronts) significantly affect seismic amplitudes at lower frequencies and shallower depths. Using of complete well logs, a model of P- and S-wave scattering is derived from direct-wave attenuation observations by numerical and analytical methods. Both approaches reveal fluctuations in the transmitted-energy flux within different depth intervals, and particularly at frequencies above 60 Hz. A randomization of well logs suggests that the upper envelope of the transmitted energy flux (corresponding to strongest transmission) is a reasonable estimate for random scattering. The lower envelope corresponding to the strongest reflectivity appears to be a useful characteristic of the fluctuations in the scattered wavefields. Once these ‘random’ and ‘fluctuation’ attenuations are modeled, they can be isolated from the intrinsic and geometric effects.

Finally, three amplitude-based methods are used to separate the effects of CO_2 pressure and saturation in the Weyburn reservoir. Based on these results, an area close to an injection well within the southern part of the study area is interpreted as having the highest pressure, and the area between the northern and eastern wells show the highest CO_2 saturation. Near the center of the study area, the effects of CO_2 saturation and pressure appear to be the weakest.

ACKNOWLEDGMENTS

I would first like to thank my advisor, Professor Igor Morozov, for supporting me over the duration of this project. I am grateful for his guidance and the opportunities he has afforded me. He is incredibly organized and a great problem solver, both of these qualities were immensely helpful in moving my project forward. Under his mentorship, I have learned the particulars of problem solving, which is an invaluable tool to have as my career moves forward.

I am thankful to Drs. Samuel Butler, Jim Merriam, Kevin Ansdell, and Larry Lines for serving on my committee. I also thank all colleagues with whom I had many useful conversations.

I gratefully acknowledge the support from IEA GHG Weyburn CO_2 Storage and Monitoring Project and NSERC Discovery Grant RGPIN261610-03. Software donated by Landmark Graphics (ProMAX), CGG Hampson-Russell (AVO, GLI3D, and STRATA), GEDCO/Schlumberger (Vista Seismic Processing) and IGeoS was used for seismic data analysis. Matlab (by Mathworks) and Octave software (http://www.gnu.org/software/octave/) were used for modeling and inversion. Generic Mapping Tools (GMT, http://www.soest.hawaii.edu/gmt/) were used for spatial interpolation, making maps, and plotting some of the illustrations.

Dedication

To my lovely wife Razieh and my parents

TABLE OF CONTENTS

LIST OF TABLES

Table page

LIST OF FIGURES

LIST OF NOTATION

This list gives the most common abbreviations and mathematical symbols used in multiple parts of this Dissertation.

Abbreviation	Description
3-C	three-component
3-D	three-dimensional
AVA	(seismic reflection) amplitude variation with angle
AVO	(seismic reflection) amplitude variation with offset
CDP	common depth point (older name for CMP)
CMP	common midpoint
CO_2	carbon dioxide
$E(\omega)$, $R(\omega)$	power spectrum of a reflection-coefficient series
EOR	enhanced oil recovery
f-k	frequency-wavenumber (domain)
G	AVA gradient
I	AVA intercept
IEA GHG	International Energy Agency greenhouse gas (program)
IGeoS	Integrated GeoScience Data Analysis (software)
MMSCFD	Million of standard cubic feet per day
Q	quality factor
P, S, SV	seismic phases (compressional, shear, vertically-polarized shear)
$R(\omega)$	power spectrum of a one-dimensional reflection-coefficient series
RMS, r.m.s.	root-mean square
t^*	parameter describing cumulative frequency dependence of amplitude
VSP	vertical seismic profile
W1	baseline Weyburn VSP survey

Abbreviation	Description
W2	monitor Weyburn VSP survey
χ	temporal attenuation coefficient
χ^*	cumulative exponent for attenuation
δ	Thomsen's parameter of anisotropy
γ	zero-frequency limit of attenuation coefficient (χ)
κ	frequency dependence component of attenuation coefficient (χ)

CHAPTER 1: INTRODUCTION

Hydrocarbon reservoirs often occur in challenging geological setting with variable lithologies, thicknesses, and heterogeneous physical properties. Knowledge of this heterogeneity and properties of the *in situ* reservoir rock and fluids is essential for predicting future production, planning further oil-field development, and evaluating alternative reservoir management scenarios.

Conventional seismic interpretation mostly focuses on interpolation of seismic reflectors for mapping geologic structures, and assessing the stratigraphy and reservoir architecture. The ultimate goal of this structural analysis is to detect hydrocarbon accumulations, delineate their extents, and calculate their volumes (Avseth et al, 2005). However, traditional seismic methods still put little emphasis on physical understanding of seismic amplitudes.

In recent decades, seismic methods have become increasingly used for the characterization and assessment of petrophysical properties of reservoirs. Seismic data analysis is able to establish a link between petrophysical rock properties and elastic and inelastic properties of the rock. Seismic reservoir characterization can provide understanding of the reservoir's internal architecture and physical properties. Quantitative techniques for seismic interpretation are used to validate hydrocarbon anomalies and give additional information during prospect evaluation and reservoir characterization (Avseth et al, 2005). The most important groups of such techniques include post-stack amplitude analysis (bright-spot and dim-spot analysis), amplitude variations with angle and offset (AVA and AVO analysis), acoustic and elastic impedance inversion, forward seismic modeling (Avseth et al., 2005), and time-lapse reflection

seismic data analysis. Studies of seismic attenuation such as inversion and modeling of the quality factor (Q) and its compensation are also important for recovering the true petrophysical properties. Several of these advanced methods, such as vertical seismic profile (VSP) imaging, AVO, and new approaches to seismic attenuation were investigated in this Dissertation in application to time-lapse seismic datasets acquired during CO_2 flooding of Weyburn oil reservoir in southern Saskatchewan.

1.1 Motivation and Objectives

The motivation of this Dissertation is in measuring the physical properties of hydrocarbon reservoirs effectively and precisely. This includes establishing a robust and reliable link between these properties and seismic data in the study area. This can be very crucial for monitoring producing reservoirs and specifically the reservoirs undergoing fluid injection. My general objective in this Dissertation consists in developing improved seismic methods that can help measuring the more subtle physical properties of reservoir rock, such as its seismic attenuation and scattering, and the relations of these properties to fluid content. Knowledge of such properties is important for understanding production history, performing monitoring and making reservoir development plans.

The specific objectives of this study are as follows:

1) Improve time-lapse seismic monitoring with a focus on the physical parameters of the reservoir. This task requires accurate processing of the time-lapse, three component (3-C) three-dimensional (3-D) VSP datasets of this project. This VSP processing also requires extracting the reflected P and SV waves from the VSP data, which can provide valuable information about fluid-content variations within the subsurface.

2) Calibration of the time-lapse VSP datasets to ensure comparable information in the two years of acquisition. After such calibration, any differences between the time-lapse datasets can be attributed to changes in reservoir conditions occurring between the times of the surveys.
3) In order to extract accurate seismic amplitudes, it is necessary to accurately model and invert for the geometrical spreading, scattering and attenuation of seismic waves. A realistic model for seismic attenuation reaching beyond the usual *Q*-factor allows me to improve the true-amplitude recovery, which is further used in AVO analysis. This objective is reached through constructing a detailed and anisotropic model combining the geometric spreading, scattering and intrinsic attenuation.
4) The ultimate practical objective is in utilizing the above seismic techniques to improve the understanding of the flows of enhanced oil recovery (EOR) fluids, such as the CO_2 injected into Weyburn reservoir. The improved seismic methods also reveal the detailed structure of the reservoir and also help estimating the accuracy of pre-stack, time-lapse seismic VSP measurements.

1.2 Enhanced Oil Recovery at Weyburn Reservoir

Enhanced oil recovery (EOR) is a general term for multiple oilfield engineering techniques aiming to increase the production of an oilfield. In recent years, injection of CO_2 has become broadly used for EOR purposes worldwide. In addition to the beneficial effects of increasing reservoir pressure, reducing the viscosity of oil, and increasing the life of the reservoir, CO_2 injection helps in a net reduction of CO_2 in atmospheric greenhouse gases. At the time of its start in 1999, the International Energy Agency Greenhouse Gas (IEAGHG) Weyburn-

Midale CO_2 Monitoring and Storage Project was among the largest CO_2 injection projects in the world.

1.2.1 Geology of Weyburn Reservoir

The Weyburn field is located in the northern part of the Williston Basin in south-eastern Saskatchewan, Canada (Figure 1.1). The Williston Basin contains sediments of shallow marine origin and Cambrian to Tertiary age. In the Weyburn reservoir, crude oil is produced from the Midale beds of the Mississippian Charles formation. The Midale reservoir beds were deposited in a shallow carbonate shelf environment and are sub-divided into three main units. These units are, starting from the stratigraphically lowest to highest: the Frobisher Evaporite, the Midale Vuggy, and the Midale Marly (Pendrigh, 2004). The Midale Marly is overlain by the Midale Evaporite, which forms the basal unit of the Ratcliffe Beds (Figure 1.2). These units make a carbonate sequence deposited in progressively shallower water. The sequence of deposition from bottom to top is: sub tidal shoal and inter shoal, intertidal inner shelf deposits, and supratidal evaporitic deposits on top (Churcher and Edmunds, 1994).

Reservoir beds range from 16 to 28 m in thickness and contain two litho-stratigraphic units: the lower Vuggy limestone (8~22 m thick) and the upper Marly dolostone (2~12 m). The porosity of the Marly zone is high (29%); however, its permeability is low, with an average of about 10 mD. Within the Vuggy zone, the porosity is near 10%, and the average permeability is higher (~50 mD) (Brown, 2002; White et al., 2004).

Figure 1.1: Location of the Williston basin (brown) in central North America. The small red rectangle indicates the Weyburn oilfield.

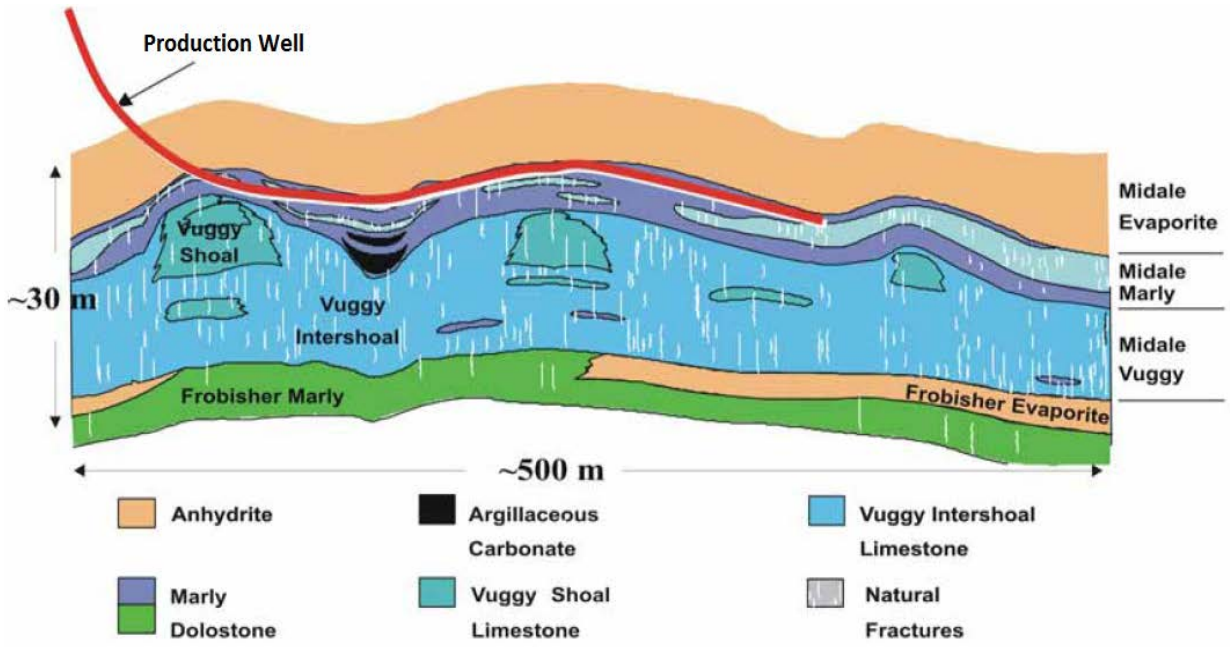

Figure 1.2: Schematic reservoir geology of Weyburn oilfield (modified after White et al., 2004).

1.2.2 CO_2 injection

The Weyburn oilfield was discovered in 1954. Water-flooding process was initiated in 1964 in order to increase production. After waterflooding, the production peaked at about 46,000 barrels/day and has been decreasing since then. In 1991, drilling of horizontal wells was initiated to increase production, targeting in particular the less permeable Marly layer. It is estimated that prior to CO_2 injection, 25% of the original oil in place had been recovered (Verdon, 2012). In October 2000, EOR using CO_2 started with initial injection rate of 5000 tonnes/day (equivalent to 95 MMSCFD[1]) by Apache Canada, and continued by EnCana (presently Cenovus Energy). CO_2 flooding was performed concurrently with the IEAGHG Weyburn-Midale CO_2 Monitoring and Storage Project. The CO_2 is sourced from a coal gasification plant in North Dakota, and is transported through a pipeline to the field. CO_2 is injected through horizontal wells, while water continues to be injected through vertical wells.

More than 15 million tonnes of CO_2 have been stored at Weyburn since 2000 to 2011, with total field injection rates (new and recycled CO_2) of 13,000 tonnes per day (White et al, 2011). By the end of the production life of the Weyburn and Midale oil fields, approximately 40 million tonnes of CO_2 will have been stored in the two reservoirs (The Petroleum Technology Research Centre website, 2015).

1.3 Seismic methods

A variety of techniques are used to monitor the injected CO_2 flood in Weyburn reservoir: geochemical analyses, geophysical methods, well-head pressure tests and soil gas sampling

[1] Million standard cubic feet per day, a unit of measurement for gases commonly used in the United States.

(White et al., 2004). Among these techniques, seismic methods provide by far the greatest continuity of subsurface sampling. These methods are applicable in a variety of geological settings and sensitive to changes in the reservoir pressure and CO_2 saturation. Seismic techniques have demonstrated the ability to detect anomalies in the reservoir induced by CO_2 invasion at Weyburn and other similar projects (White, 2004).

The injection of CO_2 into the reservoir affects its seismic properties through a number of mechanisms. In saturated porous rock, seismic characteristics are largely controlled by the stiffness, density, and porosity of the rock matrix, the nature of the fluid occupying the pore space, and the confining and pore pressures. Apart from chemical alteration of the rock matrix, the physical effects of CO_2 injection consist in modification of the pore fluid and changing pore pressure within the rock.

1.3.1 Time Lapse 3-D VSP

This Dissertation is mostly based on the analysis and modeling of vertical seismic profile (VSP) data. VSPs are intermediate-scale geophysical surveys providing information between the large lateral scales of surface seismic datasets (kilometers) and the much smaller vertical scales of well logs (meters to centimeters). Compared with surface seismic surveys, the principal advantage of a VSP is in recording with receivers traversing the target zone, which allows close correlation of the results with geological information and geophysical logging. Because of recording below the surface, VSP records have generally broader frequency bandwidths and higher resolution and overall quality, which helps calibrating and interpreting surface seismic results. Taken together, surface seismic and VSP surveys provide the best combination of lateral coverage of the study area, high resolution in depth near the observation wells, and close connections to well-log measurements. Therefore, in the dataset of this study, VSP data analysis

helps measuring the relatively weak effects of CO_2 injection and also for understanding the larger-scale surface 3-C 3-D measurements.

Prior to most of the analysis of this Dissertation and also in order to achieve best results, VSP data need to be subjected to extensive processing. This processing is described in Chapter 2. The procedure is relatively standard for VSP data processing but contains several steps critical for retaining the relative amplitudes required for AVA time-lapse analysis and also for taking advantage of the 3-C recording. The two time-lapse datasets were processed through a common processing sequence and with common parameters. The data were further calibrated by correlating the reflections with key geologic horizons at known depths, isolating the up-going P-wave and SV reflections from the total wavefields.

1.3.2 Variation of Reflection Amplitudes with Angle and Offset

Seismic techniques called Amplitude Variation with Angle (AVA) and Offset (AVO) measure reflected seismic amplitude variations from the target layer. AVA analysis has the potential of discriminating between pore-fluid and pressure effects in time-lapse seismic monitoring (Tura and Lumley, 1999; Landro, 2001; Ma and Morozov, 2010). AVA time-lapse monitoring should be more sensitive to changes in reservoir fluid than the traditional reflection monitoring due to the fact that it incorporates the shear-wave effects (Castagna et al., 1985). For Weyburn time-lapse datasets, the AVA technique was selected as the principal method for detecting the shear-wave effects, discriminating the presence of CO_2 within the reservoir and separating the CO_2 saturation and pressure effects (Baharvand Ahmadi et al, 2011).

1.3.3 Attenuation

The Weyburn VSP dataset reveals a very important observation from its pre-stack amplitudes. Figure 1.3 shows the raw amplitudes picked from the vertical components of the first

arrivals from the dataset W1 (1999), from a near-offset FFID #276. Because of the shot being located near the borehole, the depth-amplitude dependence is close to a power law, which can be observed from this log-log plot. However, the exponent of this power law appears to be quite high for geometric spreading: $A \propto Z^{-1.9}$ (Figure 1.3). For near-spherical wavefronts, a dependence close to $A \propto Z^{-1}$ should be expected, and considering rays slightly bending upward, the actual exponent should be somewhat below 1.0.

A detailed investigation of this observation shows that the fast amplitude decay is caused by back-scattering and attenuation of downgoing seismic waves (Chapter 3). As shown in Chapter 3, the conventional quality factor (Q) model of attenuation fails to represent the accurate model of attenuation and therefore, the Q-factor may have a limited physical meaning. In my approach, the attenuation of seismic waves is measured together with geometric spreading and scattering, and reveals a new view on these important phenomena.

1.3.4 Geometrical Spreading and Scattering

Accurate models for geometric spreading and scattering of body waves are important for many seismic methods relying on accurate amplitudes, such as true-amplitude reflection imaging, inversion, attenuation measurements, Q-compensation, or AVA/AVO analysis. The geometric spreading is particularly strong in the VSP case, in which the receivers are located at progressively increasing distances from the source. The geometric spreading has the dominant effect on the VSP AVA, and this effect needs to be corrected before interpreting the dependencies of reflection amplitudes on incidence angles. Due to the variations within the subsurface, the geometric spreading and scattering can also be highly variable and anisotropic (Chapter 3). These effects cannot be assumed from theoretical considerations and need to be measured from the data.

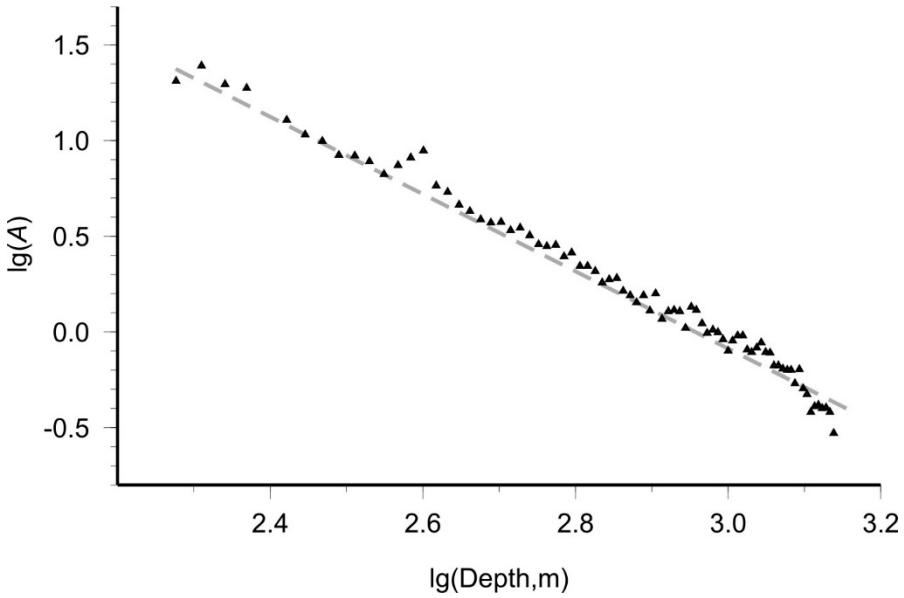

Figure 1.3. Amplitudes of the vertical components of first arrivals in the raw dataset W1 (triangles). The dashed grey line shows an empirical trend of $A \propto z^{-1.9}$.

In this Dissertation, I propose two empirical approaches to the measurement of geometric spreading. Both of these approaches use the amplitudes of direct waves to create anisotropic models of amplitude decay within the subsurface. The first model is the traditional, empirical model for geometric spreading using the straight-ray approximation. This model optimizes a simple parametric form for the geometric spreading based on the angle of reflection and the total travel distance between the source and receiver. In the second method, a layered model of the subsurface combining the geometric spreading, scattering, and inelastic dissipation is inverted from the VSP dataset. In contrast to the traditional approaches, this frequency-dependent model is formulated in terms of path integrals over the rays without reliance on a *Q*-factor.

1.4 Contributions

The key contributions of this Dissertation can be summarized as follows:

1) I develop a combined model of geometric spreading, scattering and intrinsic attenuation. This approach is related to the conventional relations based on the *Q* factor but also represents a major innovation offering two important advantages. First, this model recognizes that geometric spreading and scattering occurs locally and is therefore variable and measureable concurrently with the *Q*. Second, in contrast to most conventional models, it is not assumed that the geometric spreading can be modeled accurately and/or that the scattering is absent. Without being restricted to some specific (inevitably limited) models for the geometric spreading, internal friction, or scattering, I directly model the variations of the frequency spectrum of the signal as it travels through the medium. This model accurately predicts the amplitudes and attenuation properties of direct waves traveling at any angles, and therefore it is useful for true-amplitude studies such as AVA analysis.
2) The most challenging part of the attenuation problem is in the separation of the geometric, scattering, and intrinsic attenuation, and also the *Q* resulting from fluctuations of the background structure (Morozov and Baharvand Ahmadi, 2015). To analyse these effects in VSP data, I develop a numerical model of scattered seismic wavefields in realistic short-scale layering observed in Weyburn area. This modeling approach can be related to the conventional methods used for reservoir characterization using seismic attenuation. The modeling yields a more complete characterization of the observable macroscopic attenuation parameters associated with the subsurface structure. For example, the internal friction is related to the presence of mobile pore fluids, moving

dislocations, or grain-boundary sliding should lead to effects similar to solid and fluid viscosity (Biot, 1956; Landau and Lifshitz, 1986). Such parameters should be very useful for petrophysical characterization of the reservoir.

3) I process and calibrate the time-lapse 3-C 3-D VSP data in a way that preserves the amplitude information and allows comparisons of the two years of acquisition. I also separate reflected P and SV waves and calibrate VSP data to 3-D surface seismic data. The resulting VSP records show an improved resolution, especially around the relatively thin reservoir.
4) Accurate amplitude-spreading and scattering models allow a more accurate time-lapse AVA analysis of Weyburn VSP data. AVA attributes are derived and used for separating the pressure and saturation effects caused by CO_2 injection in the reservoir. Time-lapse AVA analysis reveals distinct trends around the CO_2 injection wells in VSP area. I argue that these trends may be due to CO_2 movement within the reservoir.

In summary, in this study, I develop two key approaches for analyzing the propagation properties of the wavefield, apply them to time-lapse and derive modified AVA attributes suitable for petrophysical analysis of the reservoir. These subjects have not been addressed in other studies before. The key results of this Dissertation are given in Baharvand Ahmadi et al. (2011), Baharvand Ahmadi and Morozov (2013 and 2014), and also Morozov and Baharvand Ahmadi (2015).

1.5 Organization of this Dissertation

This Dissertation is organized as follows. Chapter 2 introduces the time-lapse, 3-D 3-C VSP and other types of data used in this study. It also describes the processing and calibration of

VSP data and the procedures for extracting the upgoing P and SV waves, deconvolution and VSP to CMP transformation.

Chapter 3 presents an amplitude-decay model for direct waves and reflections observed in VSP data. This problem is addressed by two different methods using the same frequency-dependent direct-wave VSP arrivals. The first model follows a conventional, frequency-independent approach. In the second method, a more sophisticated frequency-dependent model is considered, in which the entire amplitude-decay problem is treated together, and inverting for both the variations of geometric spreading and Q.

Chapter 4 further develops the combined (second) model of Chapter 3 by separating the contributions of geometric spreading, intrinsic Q, scattering, and spectral fluctuations. This analysis is performed by numerical modeling of "random" and "non-random" scattering effects, so that the geometric spreading, scattering, and attenuation effects are separated.

In Chapter 5, I perform an AVA analysis and apply it to fluid-substitution and AVO models of pressure-saturation effects in Weyburn CO_2 earlier proposed by Morozov and Ma (2010). I correct spreading effects for the reflected amplitude from the reservoir by employing proposed frequency dependent spreading model and perform AVA analysis for the time-lapse VSP data. Several sets of seismic attributes sensitive to the presence of CO_2 are measured, and using AVA cross plot, general trends related to CO_2 injection in the area are detected.

Finally, Chapter 6 presents the conclusions and makes some recommendation for future studies. Appendices A and B illustrate Matlab codes used during key steps of data analysis in Chapters 4 and 5.

CHAPTER 2: WEYBURN 3-D 3-C VSP DATA AND PROCESSING

In this Chapter, I describe the seismic and well-log datasets used in this study and summarize the data processing and calibration applied to them in order to minimize the acquisition differences and to reveal the variations of reflectivity (potentially) related to the flow of CO_2 within the reservoir.

The presentation in this Chapter is based on the following paper and a section from University of Saskatchewan Weyburn report by the University of Saskatchewan:

> ***Baharvand Ahmadi, A.**, and I. Morozov, 2011a, Time-lapse VSP data analysis from Weyburn CO2 project: 2011 CSPG/CSEG/CWLS Convention, p. 1-4, http://cseg.ca/assets/files/resources/abstracts/2011/096-Time-Lapse_VSP_Data_Analysis_from_Weyburn_CO2_Project.pdf, last accessed Oct 22, 2016.*

 Parts of these results were also published in Baharvand Ahmadi and Morozov (2011b).

> ***Baharvand Ahmadi, A.**, L. Gao, J. Ma and I. Morozov, 2011, CO_2 Saturation vs. Pressure Effects from time-lapse 3-D P-S surface and VSP seismic data: Final report as part of IEA GHG Weyburn-Midale CO_2 Monitoring and Storage Project, http://seisweb.usask.ca/Reports/Weyburn_USask_Report_Apr2011.pdf, last accessed October 22, 2016*

This is a multi-year final report for a major project conducted at the University of Saskatchewan. My placement as the first author of this report was incidental and resulted from alphabetic listing of the authors. However, the section of the report on VSP data processing and analysis is entirely my work under the supervision of Prof. I. Morozov. In this Chapter, I include parts of this report related to initial VSP data processing. The same Weyburn IEA GHG report was co-authored by Le Gao, who is another PhD student in our group at the University of Saskatchewan. It is anticipated that she will also use parts of this report in her Ph.D. thesis. We used different datasets, and there is no overlap between the work by Le Gao and my work presented in this Dissertation. The focus of Le Gao's research was on analyzing 3-D/3-C surface seismic data, and my research used the VSP datasets.

Copyright of the above report belongs to the authors, which allows using these materials for student theses. Parts of the above materials were modified and reformatted for inclusion in this Dissertation. Figures were re-plotted and modified in order to meet the requirements of the University of Saskatchewan. The contribution by my supervisor (Professor Igor Morozov) consisted in setting the problem, general guidance and advice, help with his own seismic processing software, many discussions of the results and supervision of this work.

2.1 Data

Three types of data from Phase I of Weyburn project were used in this study: 1) time-lapse 3-C 3-D VSP, 2) time-lapse 3-C 3-D surface seismic and 3) well-log data. These data were provided by Encana Corporation (currently Cenovus Energy) and completely reprocessed by myself (VSP data) and Jinfeng Ma and Le Gao (surface reflection data) at the University of

Saskatchewan for the present and other projects. In the following subsections, I describe these datasets and their contributions to the present study.

2.1.1 Vertical Seismic Profile Data

Analysis of 3-D VSP data provides important information for time-lapse reservoir imaging. Downhole recording used in VSP surveying provides higher quality and frequency content resulting in usually superior images in the vicinity of the borehole. Although the VSP covers a relatively small area, the improved detail should help constraining the injected fluids better than it would be possible by using surface recordings alone. In areas with very thin reservoir layers similar to those in Weyburn oilfield, VSP's role in providing complementary data is particularly significant.

In this study, I analyze two 80-level, 3-D 3-C VSP surveys acquired in the same well #191121200614 (Figure 2.1). The baseline dataset was acquired in 1999, prior to CO_2 injection, and it is hereafter denoted W1. The second, monitor dataset was acquired in 2001 and is denoted W2. Dynamite sources were fired at depths of 10–12 m, from all azimuths around the borehole and at surface offsets from the top of the borehole ranging from ~30 to 1500 m. Figure 2.1 shows the shot locations for both VSP datasets, and Figure 2.2 shows their relation to the surface seismic study (described later in Section 2.4).

These data were acquired by using borehole receivers placed at 15-m intervals at depths ranging from 190 m to 1390 m with no cable movement. At each depth level, two geophones were oriented horizontally perpendicular to each other and denoted X for the orientation toward the east and Y toward the north Figure 2.3). The third geophone was orientated downward

vertically and designated Z. The VSP acquisition parameters for baseline and monitoring VSP surveys are summarized in Table 2.1. Sample records from raw Z-, Y-, and X-components of the VSP data from a near-offset shot are shown in Figure 2.4.

Table 2.1: VSP acquisition parameters.

VSP Acquisition Parameters	Baseline (1999)	Monitor (2001)
Number of Components	3	3
Number of Channels per shot	240	240
Receiver Interval	15 m	15 m
Number of Source points	247	253
Offsets	31-1510.39 m	128-1503 m
Shot depths	10-12 m	10-12 m
File Numbers	6-568	37-503
Receiver Elevations (from sea level)	390.3-(-811.8) m	391.8-(-812.07) m
Depths of Receivers	189-1393 m	188-1391 m
Total number of records	59280	60720

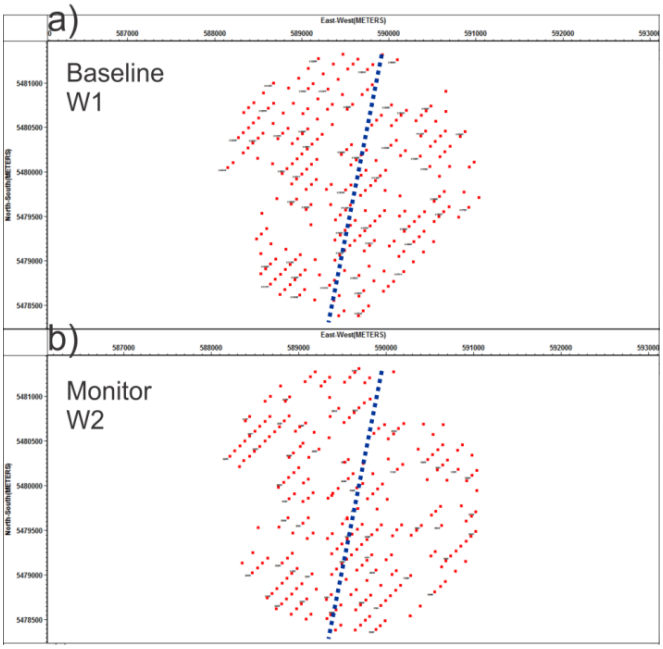

Figure 2.1: VSP shot locations in baseline (a) and monitor (b) datasets.. Blue dashed lines are the profiles of the cross-sections shown in Figure 2.18 and Figure 2.19.

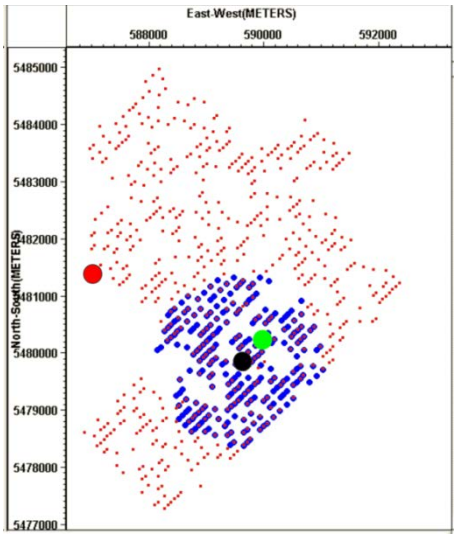

Figure 2.2. Base maps of baseline CDP and VSP surveys. Blue dots are time-lapse VSP shot positions compared to surface reflection shot points (red). VSP well (black circle), and other wells used in this study for generating VSP synthetic (green circle). The well in northwest edge of the survey used for fluid substitution and AVO model (red circle).

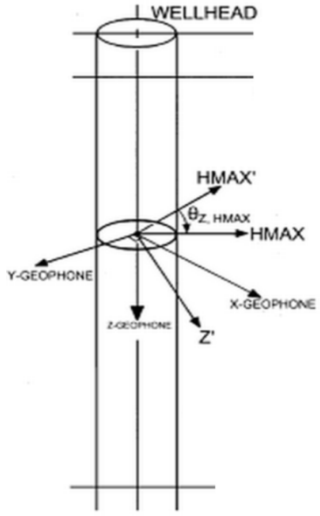

Figure 2.3: Schematic view of the VSP component rotation (modified from Hinds et al., 1996). The first rotation transforms the horizontal-component records (X and Y) into projections onto the direction of maximum horizontal-component energy within the first arrival ($H_{\max}$) and the direction orthogonal to it ($H_{\min}$). b) The second rotation maximizes the energy in the $H'_{\max}$.

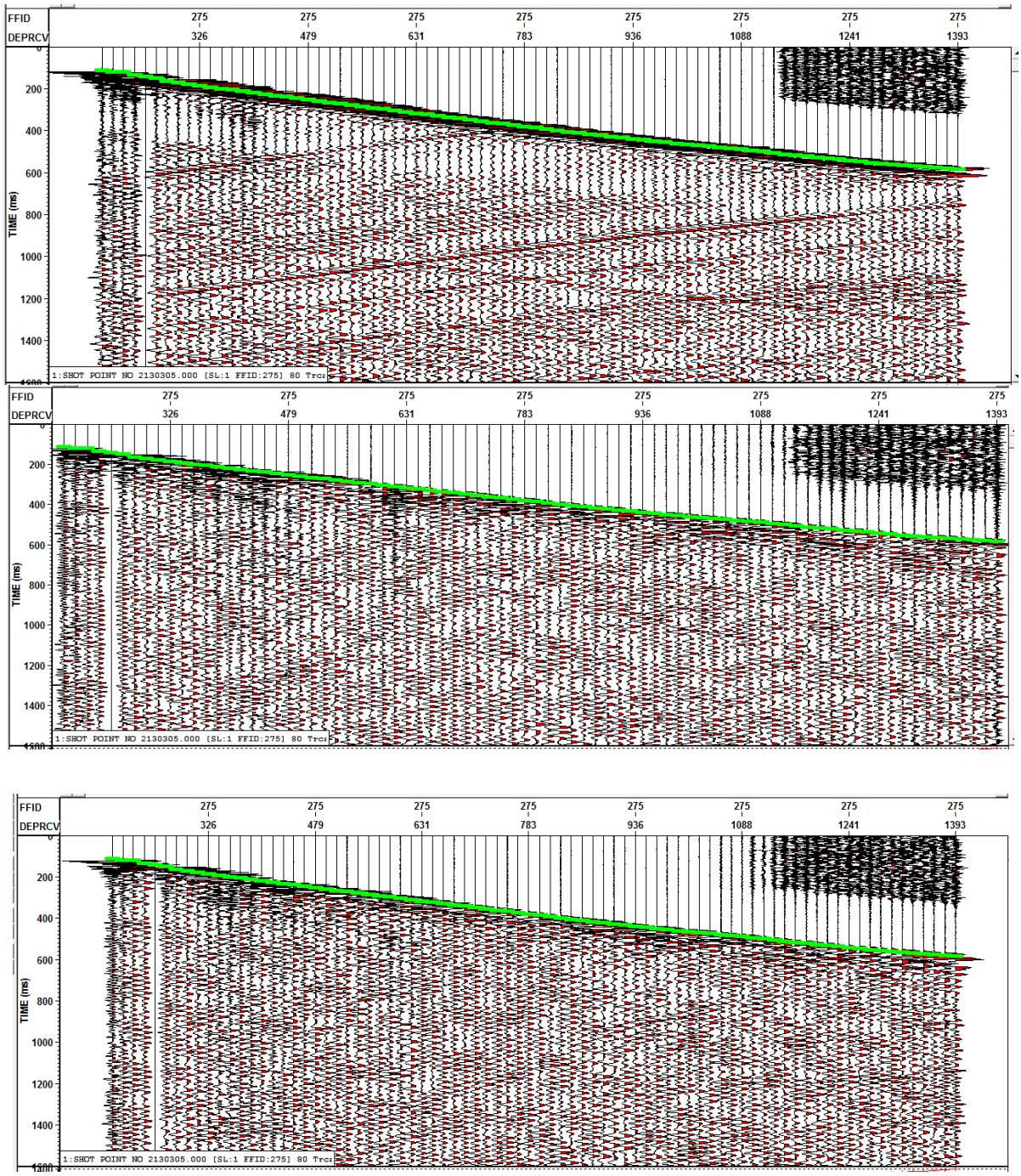

Figure 2.4: Raw records from the near-offset VSP shot (FFID 276). From top to bottom: Z- , Y-, and X components. Green lines show the first-arrival travel times. Only Automatic Gain Control (AGC) was applied to these sections. The header DEPRCV is the depth of each borehole receiver (in meters) from the surface.

2.1.2 Surface 3-C 3-D data

Starting from a baseline survey in 1999, surface 3-D datasets were acquired for CO_2 monitoring in Weyburn project almost annually. Three-component (3-C) surface datasets were also acquired in order to evaluate the ability to constrain the pressure-saturation effects by using S wave information. Three of these 3-C, 3-D datasets were included Phase I of Weyburn project and were available to the present study: the baseline 1999, and monitoring 2001 and 2002 vintages.

Basic parameters of Weyburn 3-C, 3-D data acquisition are given in Table 2.2, and the positions of shots for the baseline dataset are shown in Figure 2.1a. These data were re-processed by Jinfeng Ma and Le Gao at the University of Saskatchewan (Morozov and Gao, 2009; Gao and Morozov, 2010, 2014).

Compared to VSP, surface reflection seismic data provide broader and more spatially-uniform coverage. These properties make the time-laps surface reflection dataset the principal tool for seismic monitoring the processes of EOR and CO_2 sequestration. At the same time, VSP contributes a higher-quality coverage of the area of the well, and allows performing a detailed seismic analysis of the kind carried out in this Dissertation.

2.1.3 Well log data

Well logs provide detailed information about the physical properties of the geologic formations in depth. Well logs and cores are used to measure the depths of formation tops, their thicknesses, porosities, water saturation, temperature, lithologies, presence of oil, brine and/or

Table 2.2: Weyburn surface 3C-3D acquisition parameters.

Parameters\Year	Baseline (1999)	Monitor (2001)	Monitor (2002)
Shot number	630	882	630
Receiver station	986	986	986
Sample rate	2 ms	2 ms	1 ms
Maximum offset	2152.87 m	3445.84 m	2105.627 m
Maximum fold	77	132	78
Source type	Dynamite,1 kg, 12 m	Dynamite, 1kg, 12 m	Dynamite,1 kg, 12 m
Receiver type	Mitcham, 3C 10Hz Damping 70%	OYO, 3C 10Hz Damping 1%	I/O, VectorSeis, 3C, MEMS
Source interval	160 m	160 m	160 m
Receiver interval	160 m	160 m	160 m
Swath	19 lines × 39 stations	19 lines × 39 stations	19 lines × 39 stations

gas, estimated permeability, reservoir pressures and formation dips. Many of these types of information are useful for calibration and analysis of surface seismic and VSP data.

In this study, geophysical logs from two wells are used. The first well #102042300614 is located in the northwestern part of the Phase I Weyburn project area (red circle in Figure 2.2). This well contains the most complete logs, including the P and S-wave velocities and is used for constructing the fluid substitution and AVA models (Chapter 5). The second well #111071300614 is located within the VSP survey area (green circle in Figure 2.2). The P-wave velocity and density logs from this well are used for calibration of VSP data processing, as described in the following section.

2.2 Processing of VSP data

Corridor stacks, VSP to CDP transforms and/or migrations usually represent the final products of VSP data processing. However, in this study, I use VSP data for direct AVA/AVO analysis, which poses much more stringent requirements on the basic VSP data processing. These requirements are generally due to comparatively narrow angular apertures in VSP surveys, by the presence of both downgoing and upward-reflected waves, and by the lack of redundancy in reflection-point coverage.

The general processing of Weyburn VSP data in this Dissertation was performed by using a combination of the available seismic processing software: ProMax VSP (by Landmark Geophysical/Haliburton), VISTA (Gedco, currently Schlumberger) and our in-house package called IGeoS[2]. The more specialized analysis and inversion of the data was performed by using custom codes written in MATLAB (by MathWorks).

Similar to surface seismic data, 3-D VSP processing begins with applying the geometry (creating the geometry database and assigning trace header values), trace editing, first-break picking and component rotation. Because the first-arrival times are unique to 3-C seismograms, the first breaks were picked in the vertical-component records (as having the highest signal to noise ratios) and transferred to other components. Further, a number of additional steps are required to process the VSP data (Table 2.3). In the following subsections, I summarize these steps for the Weyburn datasets.

[2] Integrated GeoScience data analysis (Morozov, 2008).

Table 2.3: General processing steps applied to Weyburn VSP datasets.

Weyburn VSP processing steps
Data Loading
Trace Editing
Geometry Loading
First Break Picking
Hodogram Analysis
Wave field Separation
VSP Deconvolution
Velocity Picking
VSP CDP Transform
Binning to 3-D surface seismic Data
Calibration of VSP data to Surface data
3-D Stacking

2.2.1 Three-component rotation

Three-component VSP data contain the reflected P and SV wavefield, which deliver the most information about the subsurface. The P and SV waves were approximately separated by 3-C component rotations of the seismograms, implemented as a horizontal rotation followed by a rotation in the vertical plane. Both of these rotations were based on analysing the particle motion diagrams (hodograms) of the first arrivals (Figure 2.5). The first rotation transformed the horizontal-component records (*X* and *Y*) into projections onto the direction of maximum horizontal-component energy within the first arrival (denoted H_{max}) and the direction orthogonal to it (H_{min}). In the absence of horizontal anisotropy, H_{max} points toward the seismic source (Figure 2.3; Hinds et al., 1996). Figure 2.6 illustrates the results of H_{max} and H_{min} after the first rotation of horizontal components.

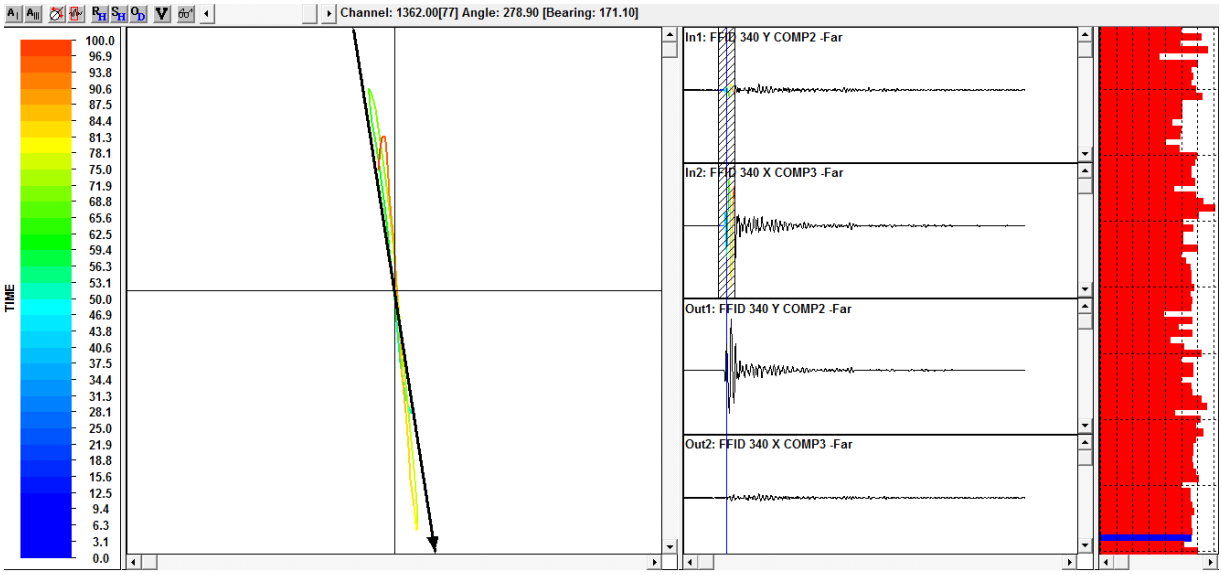

Figure 2.5: Horizontal-component polarization analysis in VISTA software for a far-offset VSP shot (FFID 340). Left panel: The bearing and rotation angles (black arrow) calculated for a 100-ms first-arrival window. Right panel, top to bottom: a) Input Y-component signal, b) Input X-component signal; c) hodogram maximum ($H_{\max}$) signal, d) hodogram minimum ($H_{\min}$) signal.

The second rotation was performed in the vertical plane containing the direction $H_{\max}$ (Figure 2.5). This procedure maximizes the energy in the primary rotated component (designated $H'_{\max}$), which is interpreted as the polarization direction of the downgoing P wave. The direction orthogonal to it (Z') contains predominately upgoing P and downgoing SV waves (Figure 2.5). Figure 2.7 illustrates the results of this second rotation, which will be used later for separating the upgoing P and SV waves (section 2.2.3).

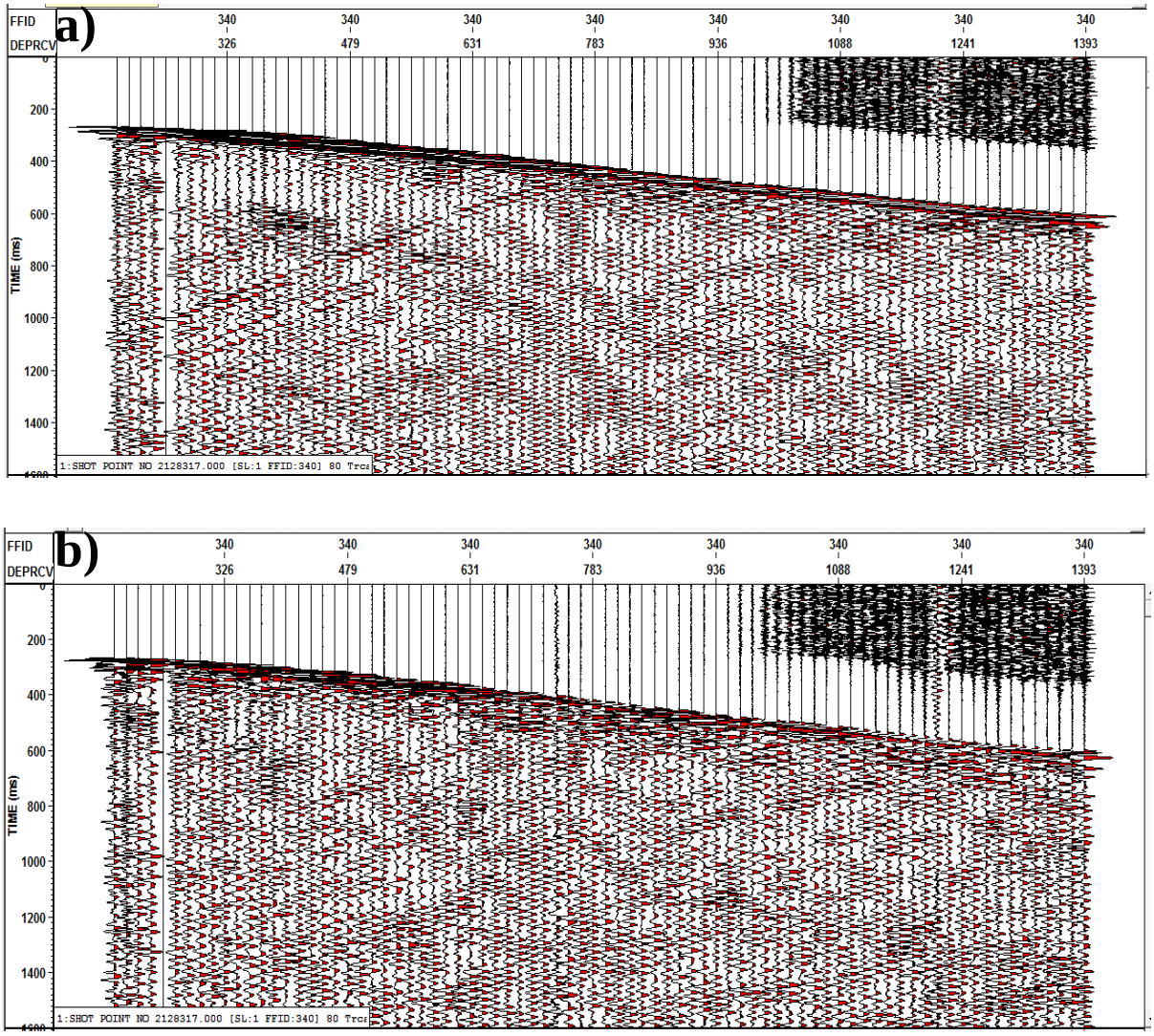

Figure 2.6: a) H_{max} and b) H_{min} sections resulted from the first rotation of horizontal components after hodogram analysis in Figure 2.5.

2.2.2 Velocity analysis

Similar to processing of surface seismic data, velocity analysis is critical for VSP data analysis. However, in addition to reflection moveouts, velocity analysis in a VSP can be conducted by using first arrivals. The geometry of vertical seismic profiling allows determining

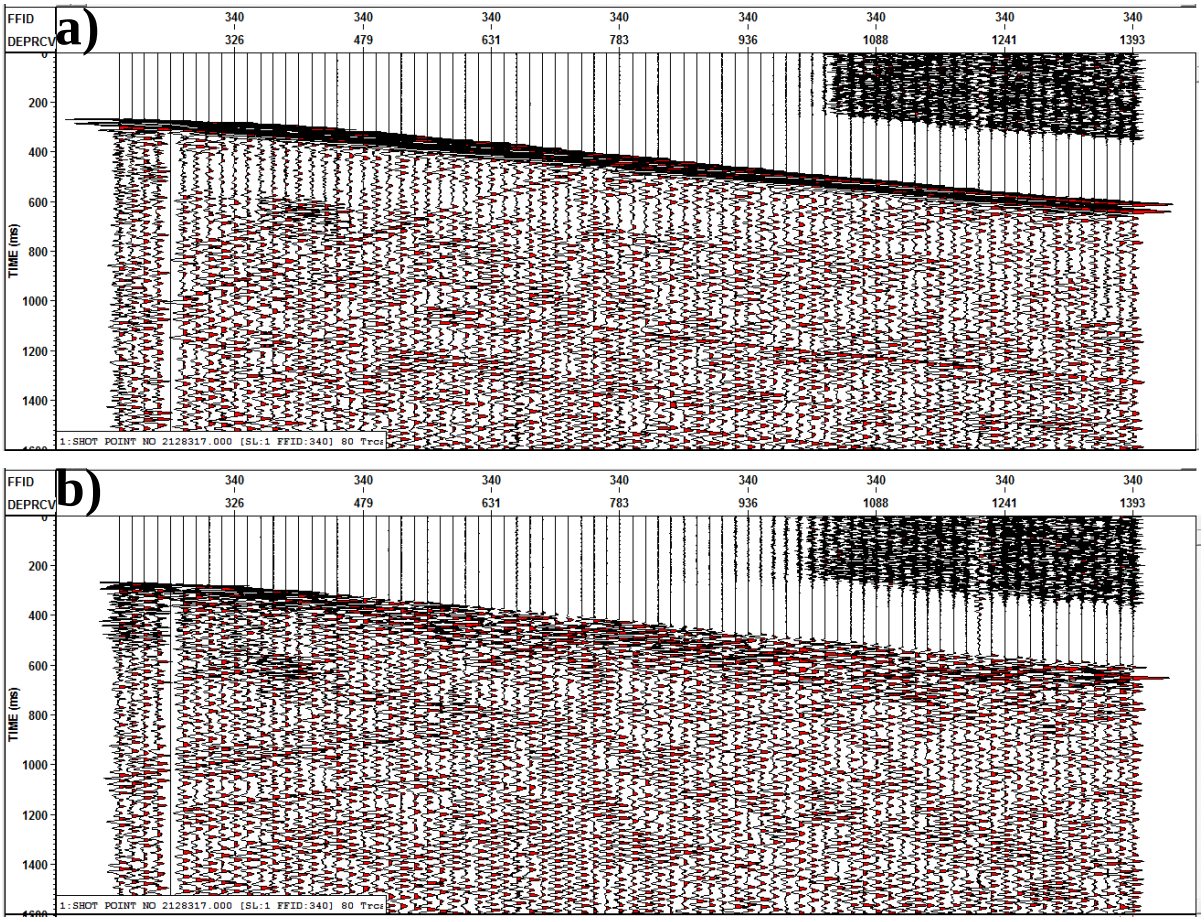

Figure 2.7: a) $H'_{\max}$ and b) Z' sections resulted from rotation of the vertical component (Z) and rotated horizontal component toward source ($H_{\max}$).

the interval velocity directly as a function of depth instead of travel time. This depth model can be useful for tying log records to seismic data, giving a precise relation between the two-way time and the corresponding depth in the area, and also in other processing and inversion applications.

The travel times picked from the first arrivals times, t_{SR}, can be viewed as a function of the geophone depth, z, or of the source-receiver distance, D_{SR}. Two important velocity measures

are derived directly from these functions: 1) the interval velocity at depth z near the well, $V_{\text{int}} \equiv dz/dt_{SR}$, and 2) the average velocity $V_{SR} \equiv D_{SR}/t_{SR}$ between the source and receiver. Some VSP processing operations, such as the spherical-divergence correction also require a root-mean square (r.m.s.) velocity function, V_{rms}. This function was also obtained as a function of depth by transforming the V_{int} and V_{SR}. The resulting $V_{\text{rms}}(z)$ approximates the stacking velocity in an equivalent surface refection survey recorded in the same area. Figure 2.8 shows a comparison of the average and interval velocities generated from a near-offset and far-offset VSP shots.

By using the inverted interval or r.m.s. velocity profiles, ray tracing generates a set of direct and reflected rays to generate arrival times and incident angles for each VSP receiver. Figure 2.9 shows an example of ray tracing of a far-offset shot in Weyburn VSP.

The r.m.s. velocity derived from the interval velocities for first arrivals may still not be

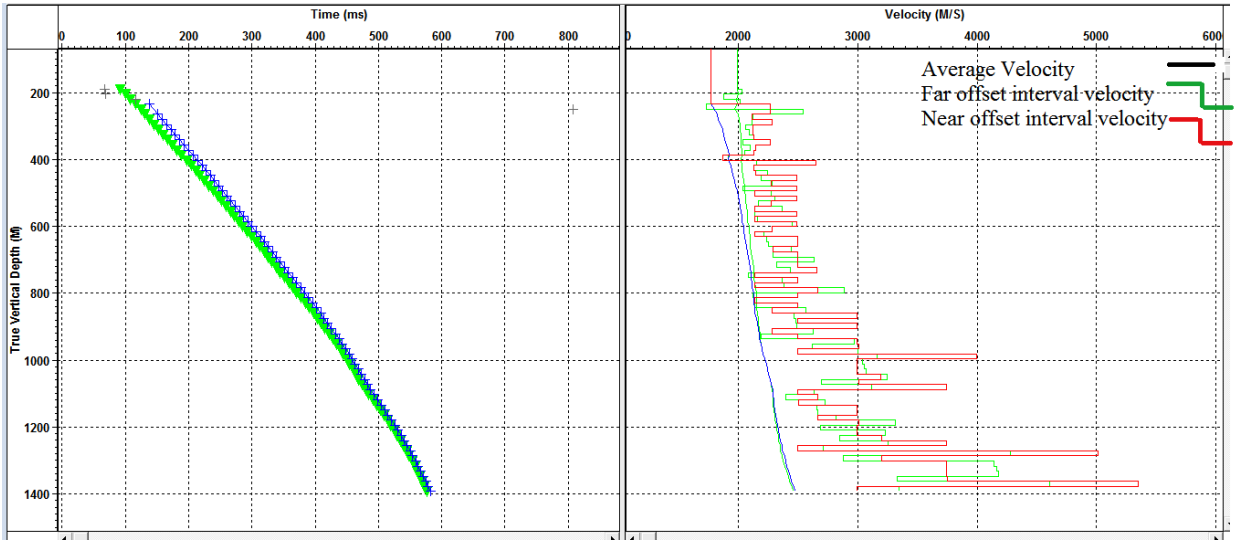

Figure 2.8: Average and interval velocities calculated from the first-arrival times of a near-offset and far-offset VSP shots. Left panel: the first breaks times picked for a near offset (blue) and far offset (green) VSP shots. Right panel: average and interval velocity in depth for near and far offset VSP.

sufficiently accurate for focusing the reflections. In this study, in addition to the inverted r.m.s. velocity, I determined another, detailed stacking velocity from the reservoir reflection times measured in shot records. This allowed achieving higher accuracy near the reservoir while mitigating the low data redundancy inherent in VSP recording. To perform this stacking velocity analysis, I:

1) Using an initial model derived from the well logs, modeled the times of reflections from the reservoir caprock level,
2) Superimposing these modeled times on the shot records, identified and picked the actual reflection from the caprock, and
3) Inverted these reflection travel times for the stacking velocity V_{stack} above the caprock by using the hyperbolic travel-time equation:
4) are predicted reservoir times using equation (2.1).
5) $$t(x) = \frac{\sqrt{x^2 + (2z_c - z)^2}}{V_{\text{stack}}}, \qquad (2.1)$$
6) where z is the depth of the geophone, z_c is the depth to the caprock known from the borehole, x is the horizontal source distance from the top of the well.

Figure 2.10 illustrates the travel-time data fit in relation (2.1) for four shots. Some systematic deviations seen in the misfits are likely due to ray bending and anisotropy, which are not included in equation (2.1).

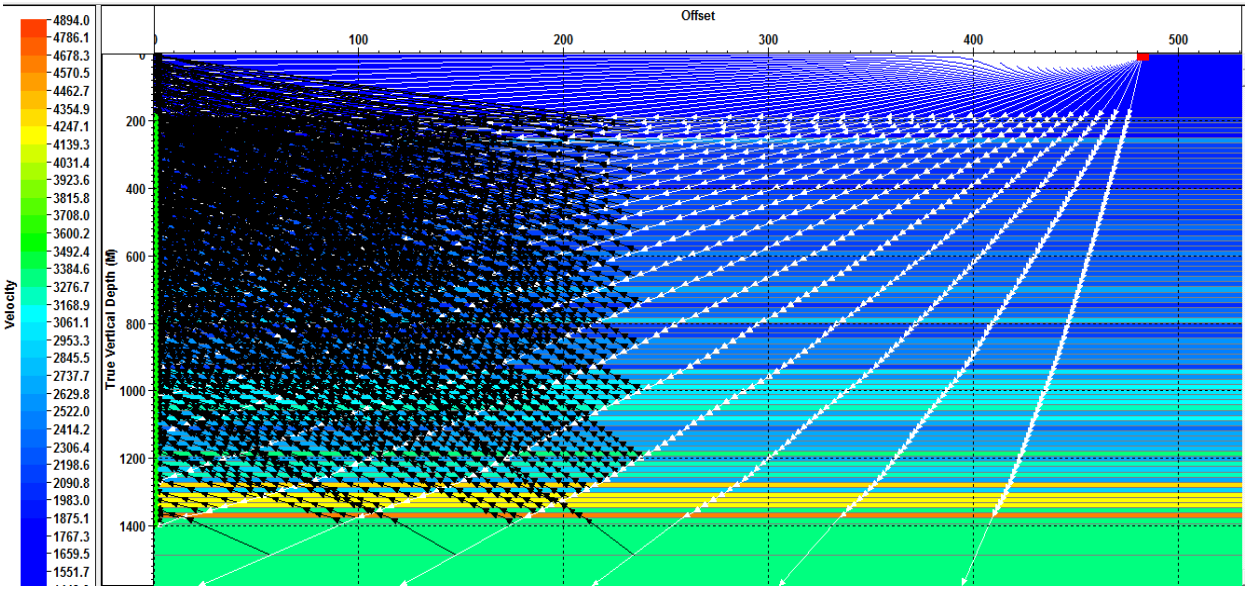

Figure 2.9: Incident (white) and reflected (black) rays from a far-offset VSP shot at a 480-m offset from the borehole. The velocities of the layers are illustrated by colors (color bar on the left). The receiver array is shown by green on the left.

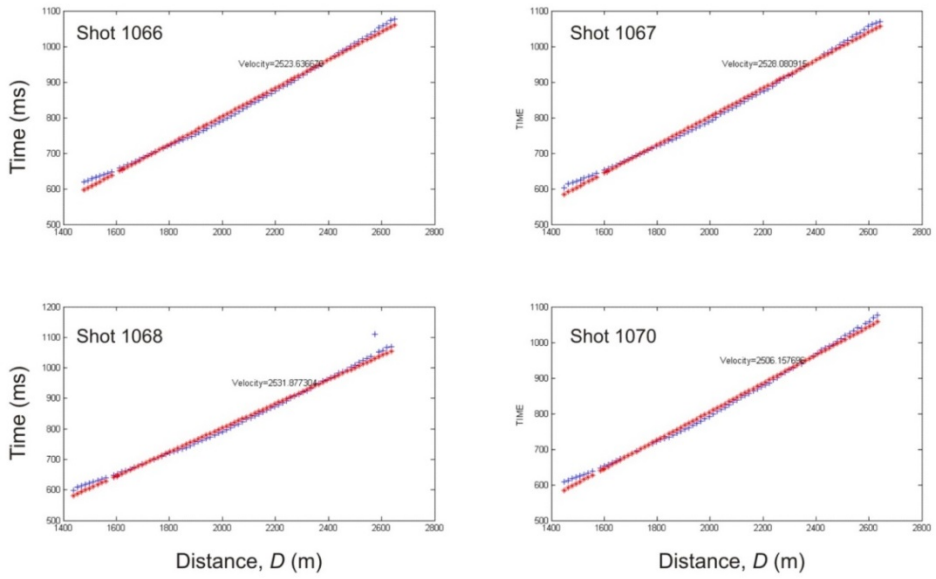

Figure 2.10: Stacking velocity at reservoir level in VSP area derived from four shots by using equation (2.1). The red dots are observed travel times from the reservoir and the blue dots

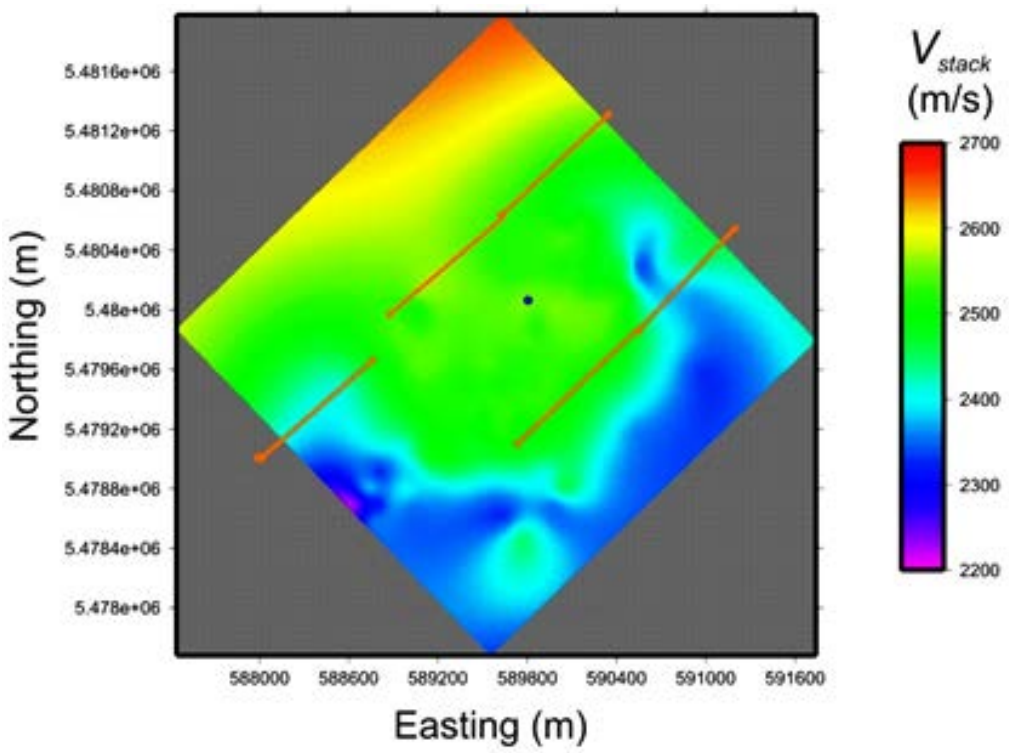

Figure 2.11: Stacking velocity variation at reservoir level in VSP area from the baseline dataset. Black dot is the VSP well location and orange lines are horizontal CO_2 injection wells.

Using equation (2.1), stacking velocities for all VSP shots were calculated and assigned to midpoints between each shot and borehole. Figure 2.11 shows the stacking velocity variation around the borehole at the reservoir level for the baseline dataset W1. This velocity complements the r.m.s. velocity inverted from the first breaks and used for producing more accurate seismic images around the well (subsection 2.2.6).

2.2.3 Wavefield separation

The VSP wavefield consists of a superposition of the downgoing and upgoing waves, which need to be separated and interpreted differently. The reflected P-wave field is useful for

constructing corridor stacks for calibration of surface seismic data, producing pseudo-CMP sections by using the VSP to CMP transform. The reflected field is also required for performing the reflection AVA analysis of this study. The downgoing wavefield is useful for analyzing the velocities, attenuation, source signatures and constructing deconvolution operators.

There exist several approaches to separating the downgoing and upgoing wavefields from a VSP wave field. All of these approaches utilize the differences in the signs of the moveouts for the downgoing and upgoing wavefields. The most common techniques use the median, *f-k* and eigenvector (Karhunen–Loève, or KLT) filters. The first of these methods was utilized in this study.

The median filter, when applied along the appropriate moveout, is very effective in estimating the flattened event amplitudes despite the interfering events with different moveouts. If the input records can be flattened and the waveforms are stable, then the median filter performs well in upward-downward wavefield separation. Typically, the amplitudes of consistent downward-directed events are estimated and then subtracted from the input, leaving the upgoing wavefield. I applied a median filter with a 13-trace window to compute the downgoing P wave field from the $H'_{\max}$ component (section 2.2.1) flattened on the first arrivals. Figure 2.12 shows the separated downgoing P wave from a far-offset VSP shot using the median filter. Figure 2.13 shows the separated Z and $H'_{\max}$ upgoing waves from the same shot. These Figures show that the median filter is very effective for separating the downgoing and upgoing waves in Weyburn VSP data. These results are used in the next subsection to separate the P and SV waves in the upgoing wavefield.

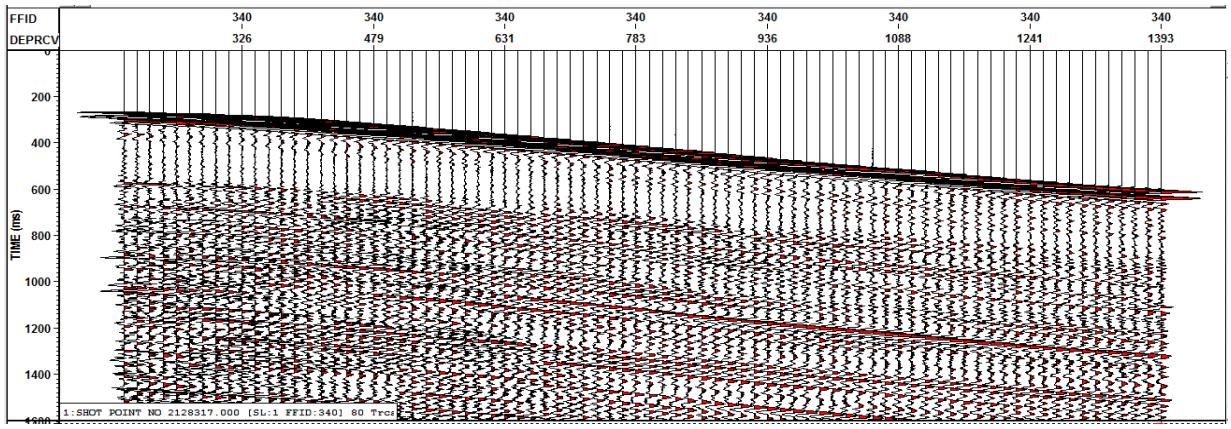

Figure 2.12: Downgoing P wave separated from a far offset VSP shot (FFID 340) using a median filter with 13 points (traces).

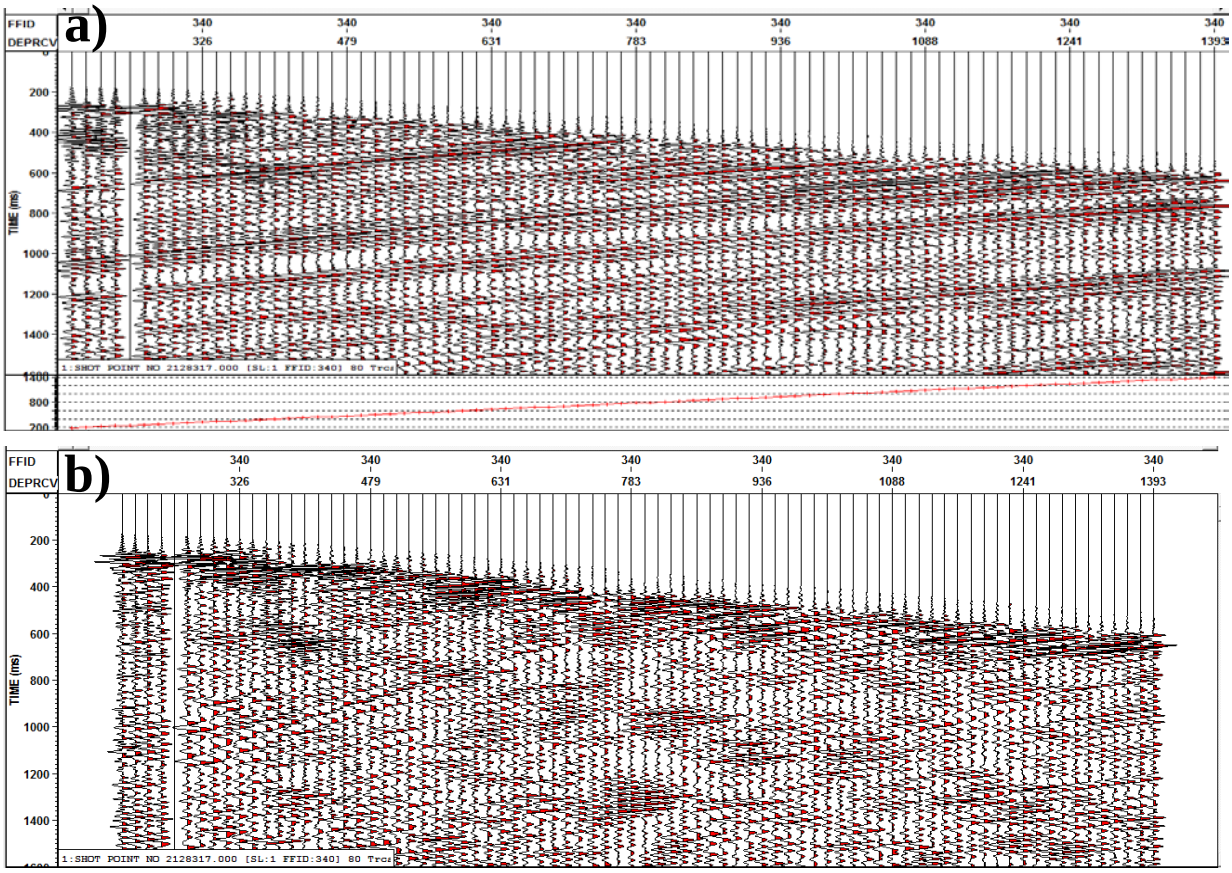

Figure 2.13: a) Upgoing waves separated from vertical component (Z) and b) from horizontal component of a VSP shot (FFID 340). Only AGC applied to above sections for display purposes.

2.2.4 Separation of upgoing P and SV waves

Separation of P and SV waves was first introduced by Dankbaar (1985) and applied to both 3-component surface (Dankbaar, 1985) and VSP data (Dankbaar, 1987). In his method, the horizontal and vertical geophone records are expressed in terms of receiver characteristics and incident P- and S-waves. To derive a P/S-mode separation filter, the data are decomposed into plane waves, i.e. transformed into the *f*-*k*-domain. The Fourier components of the incident P- and incident S-waves (P_{in} and S_{in}, respectively) can be expressed as linear combinations of the radial- (U_H) and vertical-component records (U_z):

$$P_{in}(k, f) = F_Z^P(k, f)U_Z(k, f) + F_H^P(k, f)U_H(k, f), \tag{2.2}$$

$$S_{in}(k, f) = F_V^S(k, f)U_Z(k, f) + F_H^S(k, f)U_H(k, f). \tag{2.3}$$

The coefficients $\boldsymbol{F}$ represent the plane-wave P/S-separation/filter coefficients (Dankbaar, 1985). The above method can also be used for separating reflected P and SV waves.

If the input wavefields U_V and U_H are separated into the up- and downgoing fields, then a transformation analogous to (2.2) and (2.3) can be performed in the time domain for depth-dependent velocities (Miong et al., 2008). I used the time-variant component rotation method by Miong et al. (2008) to separate P and SV wave in the upgoing Z and $H_{\max}$ datasets (section 2.2.1) by using arrival times and incident angles calculated by ray tracing from each shot. Figure 2.14 illustrates the resulting upgoing P and SV waves extracted from a far-offset VSP shot.

2.2.5 VSP corridor stack

Corridor stacks are commonly produced from VSP data processing in zero- (or near-) offset surveys. These stacks are tied to surface seismic stacked sections to help interpreting the

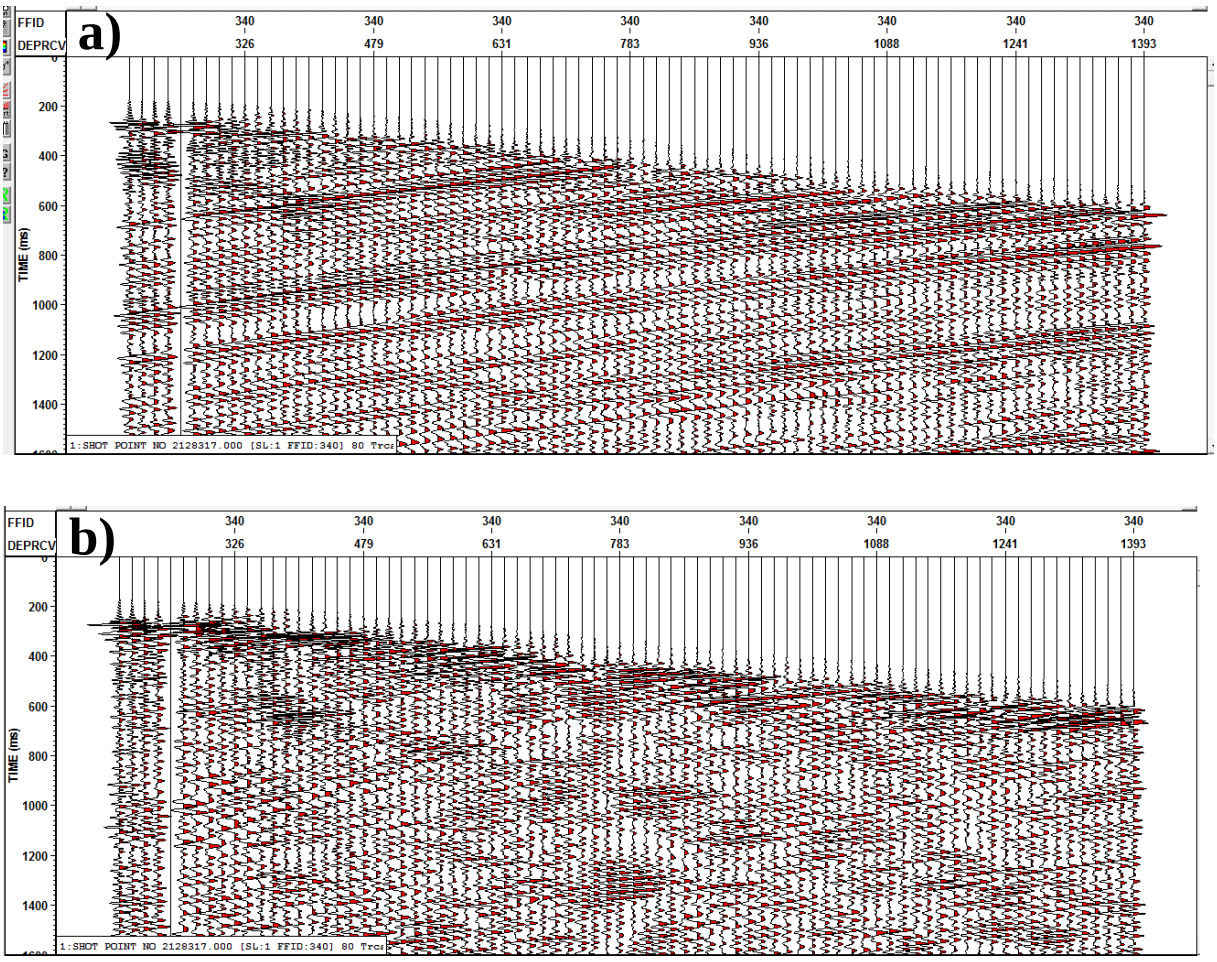

Figure 2.14: a) Upgoing P and b) SV waves separated from a VSP shot (FFID 340) using the time-variant component rotation by Miong et al., (2008).

key geologic horizons and reflections seen in seismic sections. In seismic-while-drilling monitoring, corridor stacks also can help the drillers to anticipate what is coming up deeper in the borehole (Poletto, et al, 2004).

A corridor stack for near-offset Weyburn VSP data was created by travel-time shifting the upgoing-wave field from a near-offset shot by using the times of the first arrivals. This operation is known as the “VSP static shift” and results in VSP reflections aligned horizontally.

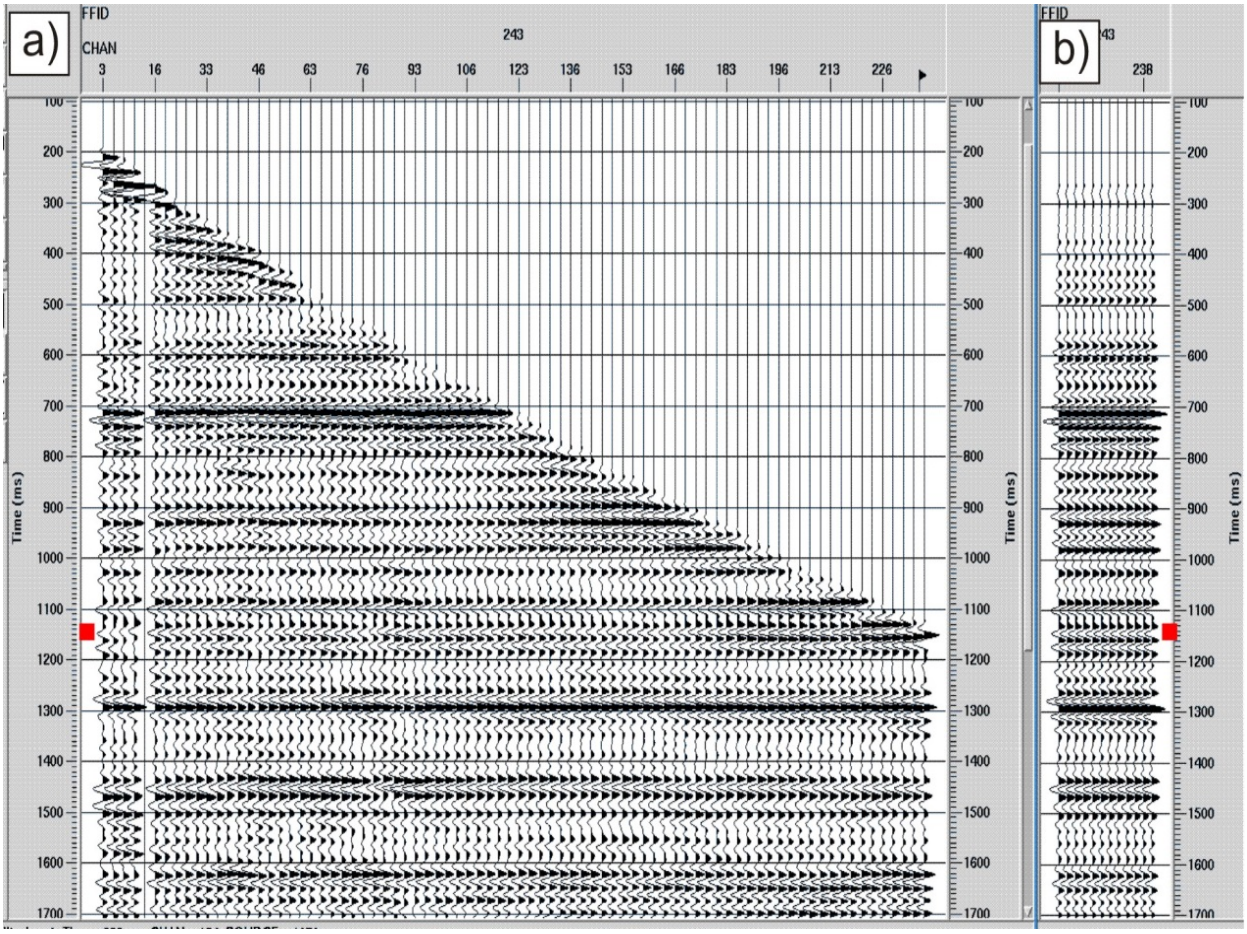

Figure 2.15: Near-offset VSP shot from dataset W1: a) upgoing wavefield after an application of "VSP statics", b) corridor stack. Red bar indicates the reservoir interval (Marly + Vuggy).

By summing these records, a corridor stack was produced, which was equivalent to a normal-incidence reflection record in the vicinity of the borehole (Figure 2.15). This stack was further compared to synthetics generated from well logs. As in usual seismic interpretation, to adjust for the uncertainties of the static time shifts and velocities, the geophysical and lithological logs were shifted and stretched vertically, so that the reflection synthetics created from such logs match the observed reflection sequence (Stewart and DiSiena, 1989) (Figure 2.16).

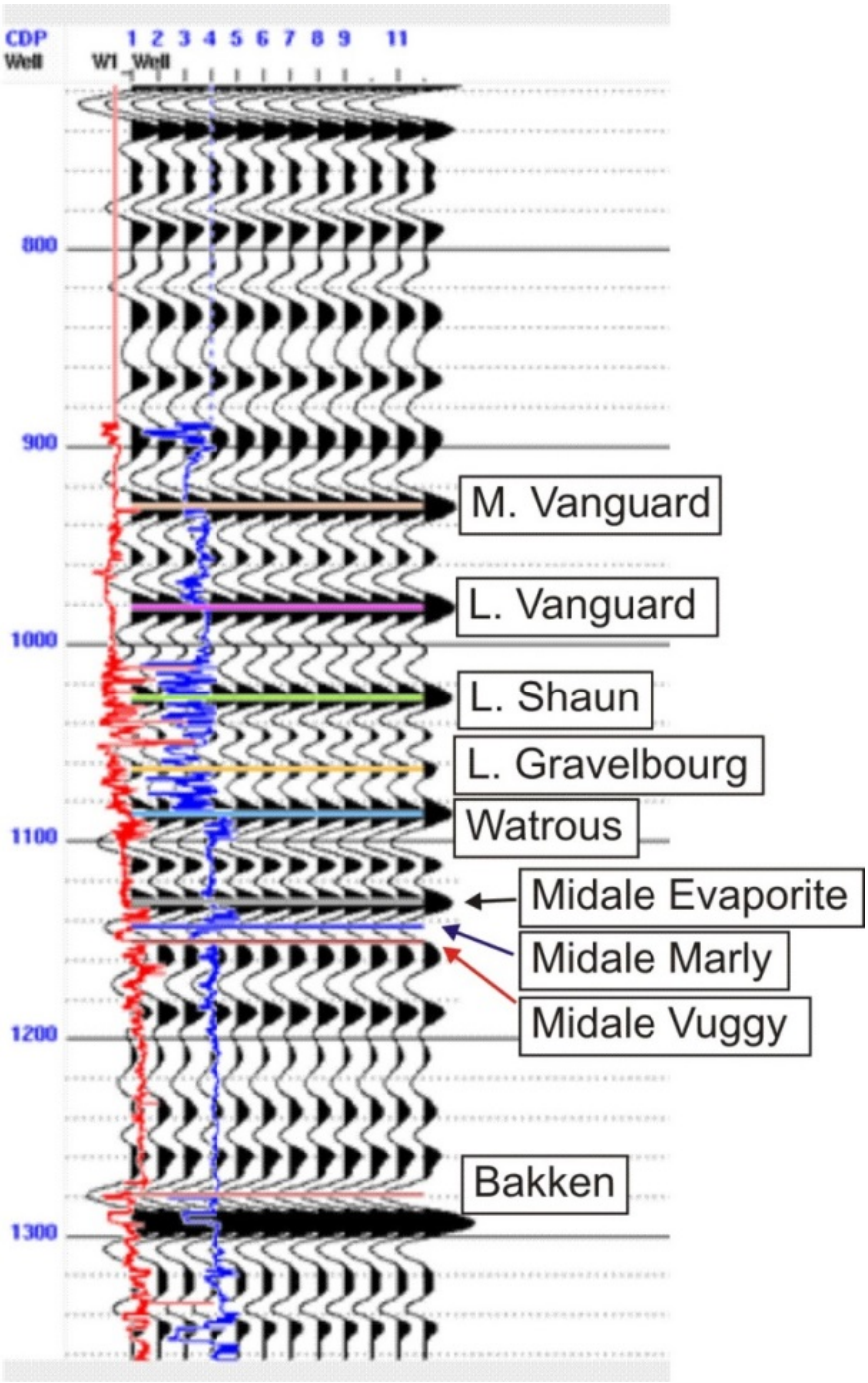

Figure 2.16: Weyburn VSP corridor stack with interpreted reflections from lithological boundaries. Red line is the P-wave velocity well log and blue line shows the density log.

2.2.6 VSP to CMP transformation

In contrast to surface reflection seismic data, VSP data are recorded in the time-depth- rather than time-distance domain. Therefore, in order to compare 3-D VSP images to reflection seismic volumes recorded from the surface, data transformation of the VSP into the form of a surface reflection image is required. One way of performing this transformation is by using the VSP-to-CMP transform (Figure 2.17; Wyatt and Wyatt, 1981). In this approach, surface and VSP reflection travel times are computed by ray tracing through the stacking velocity model, and the VSP reflection times increased by the times required for the reflections to reach the surface (dashed line in Figure 2.17). Note that for near offsets (near-vertical rays in Figure 2.17), the additional reflection time is nearly equal the direct-wave time (purple arrow labeled *D* in Figure 2.17), giving the "VSP static shift" procedure described in the preceding section. Figure 2.18-Figure 2.19 show an example of VSP-to-CMP transformed upgoing VSP field stacked along blue dashed line in Figure 2.1 for baseline and monitoring surveys.

Although the VSP-to-CMP mapping is a convenient tool for presenting VSP data in a form directly comparable to surface CMP record sections, it is only used for illustration purposes in this dissertation. A major drawback of this procedure is in inaccurate handling of amplitudes and in modifying the reflection angles. Both of these factors are not acceptable for AVA measurements. Therefore, in the AVA analysis (Chapter 5), I do not use the VSP-to-CMP transform and rely on direct measurements of the amplitudes from raw shots. Geometrical spreading combined with attenuation and effects of anisotropy will be discussed in Chapter 3 and is applied to the data prior to the AVA analysis.

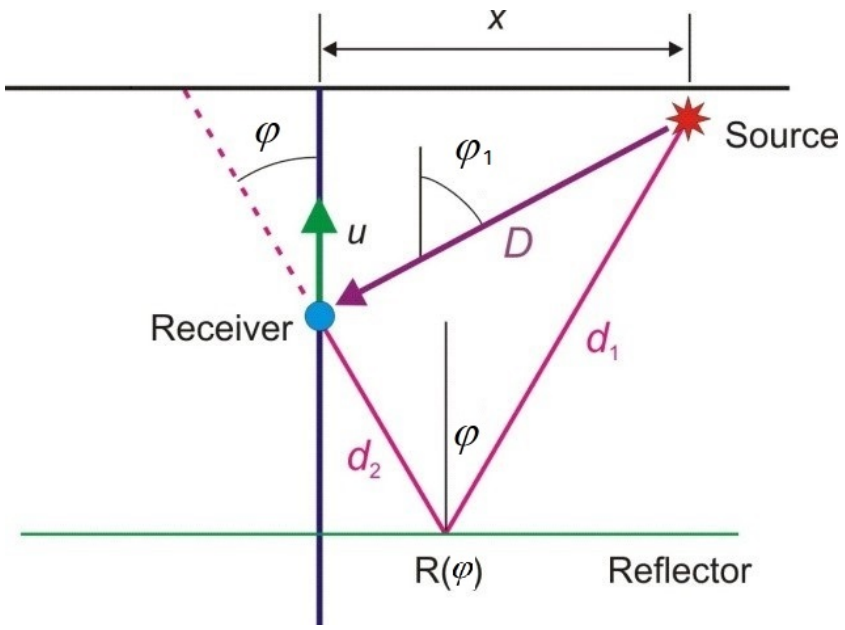

Figure 2.17: Offset-VSP geometry. The VSP-to CMP transform consists in adding to the VSP reflection time (pink ray) the time corresponding to the extension of this ray to the surface (dashed line). Labels also indicate the notation in equation (2.1). Purple ray corresponds to the first arrival, and D is the source-receiver distance. $R(\phi)$ is the angle (AVA) dependence of the reflection amplitude measured later in this Dissertation.

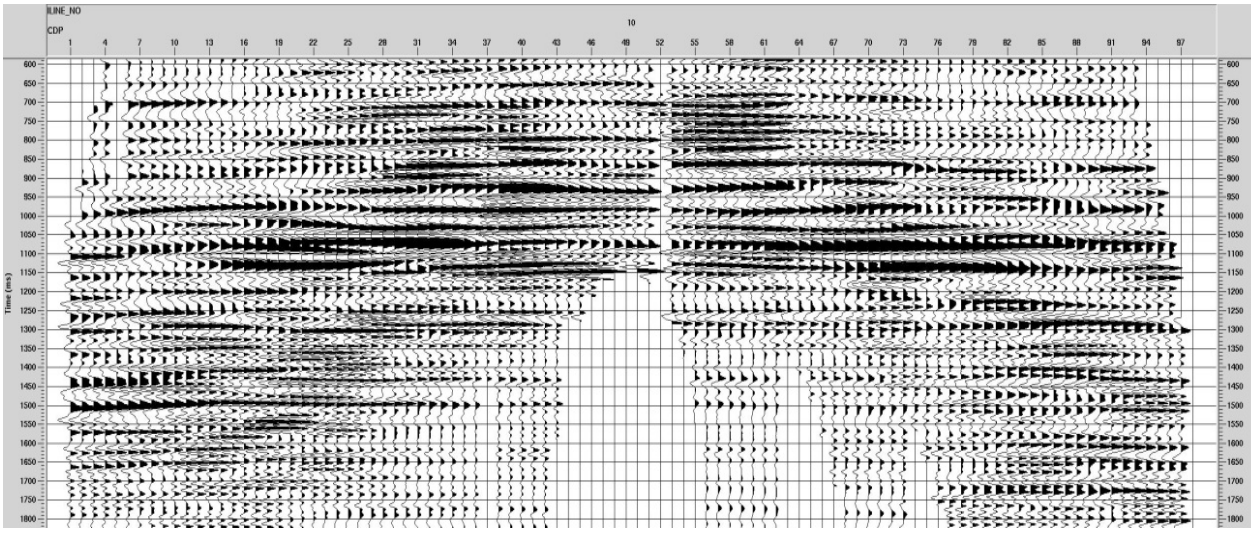

Figure 2.18: VSP-to-CMP transformed upgoing VSP field from dataset W1 stacked along the blue dashed line in Figure 2.1.

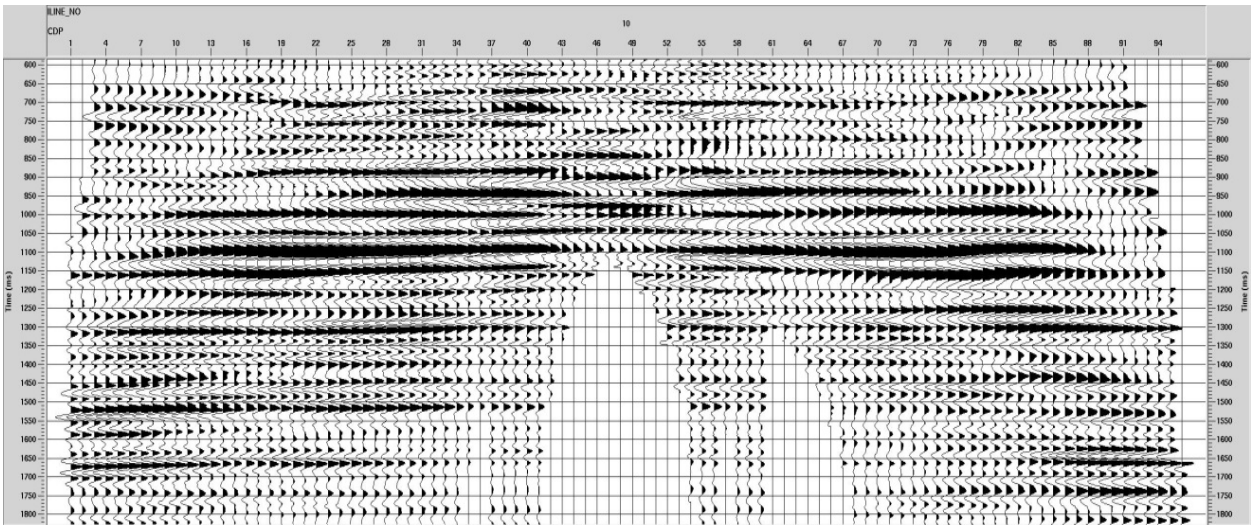

Figure 2.19: VSP-to-CMP transformed upgoing VSP field from dataset W2 stacked along the same line as in Figure 2.1.

2.3 Calibration of time-lapse VSP data

Calibration of seismic datasets is the most critical part of time-lapse seismic monitoring. In term of acquisition, calibration requires maintaining constant positions of the sources and receivers, consistent charge types and sizes, and similar recording conditions. During seismic processing, calibration also requires common binning, identical processing steps and parameters, and also consistent statics and velocity models that can be rigorously correlated between the baseline and monitor versions of the dataset.

To improve the consistency of the amplitudes in datasets W1 and W2 used in AVA analysis, I used pre-stack spectral balancing of these datasets. Fast Fourier transforms were used to compute the averaged amplitude spectra for each pair of closely-located, raw shots from the datasets W1 and W2. As shown in Figure 2.20, the amplitudes and spectra of the shots recorded in the different years of acquisition were significantly different. By smoothing these spectra and

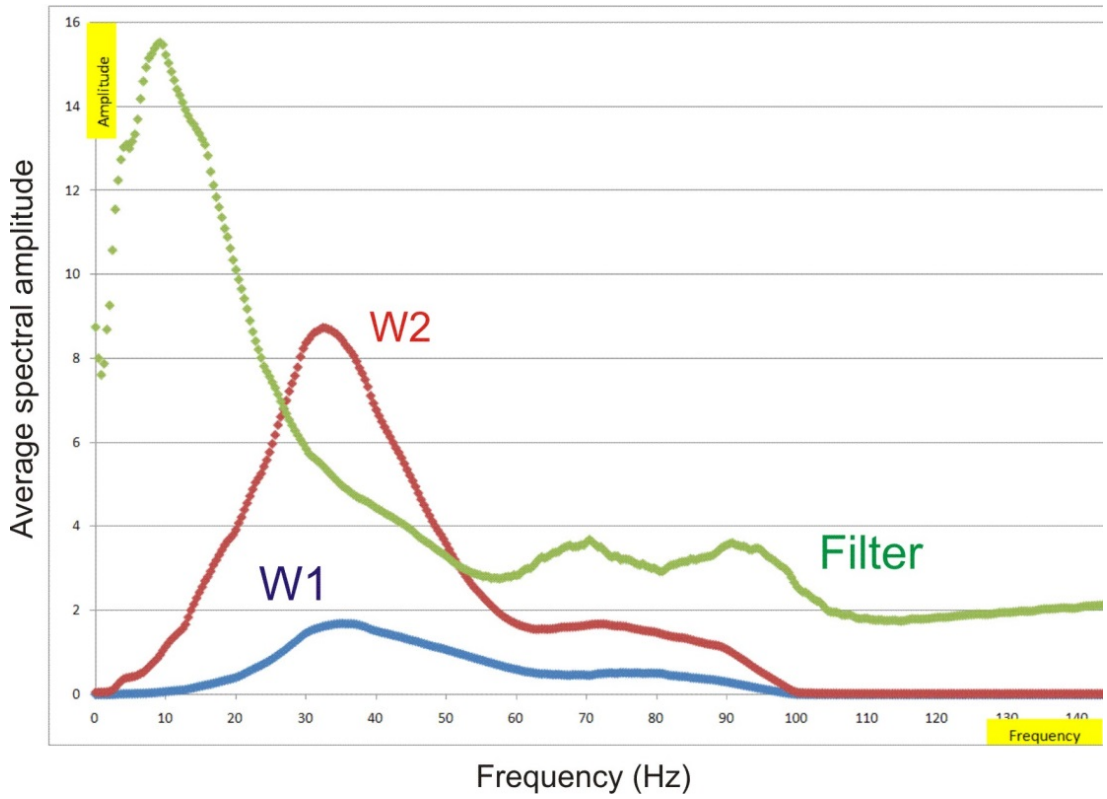

Figure 2.20: Amplitude balancing for a pair of collocated VSP shots. Blue line indicates the amplitude spectrum for FFID 17 in dataset W1, red line is the amplitude spectrum of the closely-located FFID 460 from W2. Green line shows the response of the calculated matching filter.

taking their ratios, a simple zero-phase matching filter was calculated (green line in Figure 2.20). These filters were further applied to the data from dataset W1, making their average amplitudes and spectral responses close to those in dataset W2.

2.4 Calibration of the VSP with surface seismic data

In order to correlate and calibrate the NMO-corrected VSP to the surface seismic records, the VSP to CMP transformation was conducted by using the same CMP binning as in the surface seismic study (Gao and Morozov, 2011). Further, any differences in timing and stacking velocities between the VSP and surface datasets were removed by applying depth-variant time

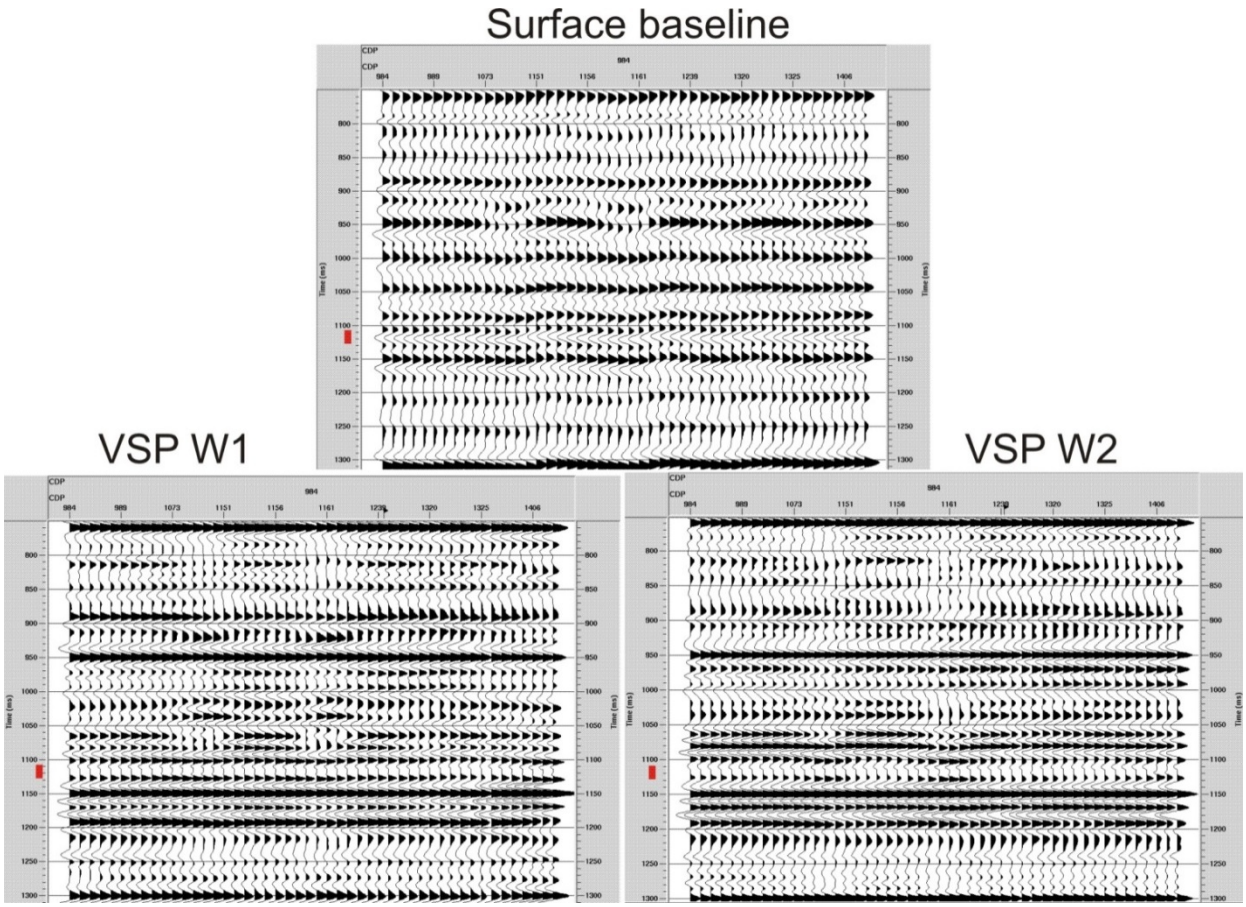

Figure 2.21: Comparison of reflection sections from the stacked surface baseline dataset and the two vintages of VSP datasets transformed into CMP form. Red bars indicate the reservoir range (Marly +Vuggy).

shifts similar to the well-log “stretching” commonly used during reflection seismic interpretation. As a result, the calibrated pre-stack VSP dataset became directly comparable to the surface one in terms of both reflection-point locations and reflection times (Figure 2.21). Note that after such calibration, VSP data show good quality and better resolution, particularly around the reservoir level (red bar in Figure 2.21).

CHAPTER 3: ANISOTROPIC FREQUENCY-DEPENDENT SPREADING OF SEISMIC WAVES

Attenuation of seismic-wave amplitudes is a complex phenomenon that is important to understand for many applications such as true-amplitude imaging, inversion, *Q*-compensation, and analysis of amplitude variations with offset (AVO). Accurate accounting for wave attenuation helps in understanding the lithology, physical state, fracturing, fluid and gas content of reservoir rock.

The process of energy dissipation in wave propagation is time- (space-) and frequency-dependent. Physically, energy dissipation is caused by a combination of three factors: (1) local variations of geometric spreading, (2) scattering (such as transmission losses and reflectivity), and (3) internal friction within the material (transformation of the mechanical energy of seismic waves into heat), usually described by its intrinsic *Q*.

In this Chapter, I derive an amplitude-spreading model from the spectra of first arrivals of a 3-D vertical seismic profile (VSP). A conceptually new model parameterization is based on combining the observable variations of geometric spreading, intrinsic attenuation, and small-scale scattering. The model is formulated in terms of two empirical physical parameters and path integrals along the rays. A model of depth-dependent and anisotropic parameters γ and κ is derived, which will be used for both direct arrivals and reflections in the study area (Chapter 6). Application of the resulting model to seismic records allows predicting the amplitudes of the first arrivals. The modeled frequency-dependent amplitudes can be used for accurate *Q*-compensation as well as for corrections for scattering and focusing/defocusing. Similarly, the model can likely be used for other waves, for example, to correct the geometric spreading and attenuation effects

for reflected and converted waves. The resulting empirical, frequency-dependent, anisotropic model of amplitudes should be useful for many true-amplitude studies, including inversion and AVA analysis. Model parameters can also be used to constrain petrophysical properties and for constructing frequency-dependent Q values suitable for synthetic modeling and inverse Q filtering.

The presentation in this Chapter is based on the following paper:

***Baharvand Ahmadi, A.**, and I. Morozov, 2013a, Anisotropic frequency-dependent spreading of seismic waves from first-arrival vertical seismic profile data analysis: Geophysics, 78, no. 6, C41–C52.*

 This paper was modified and reformatted for inclusion in this Dissertation. Figures were re-plotted and modified in order to meet the requirements of the University of Saskatchewan. The contribution by my supervisor (Professor Igor Morozov) consisted in setting the problem, general guidance and advice, help with his own seismic processing software, many discussions of the results and supervision of this work. Preliminary results of this work were also published in Baharvand Ahmadi and Morozov (2012).

3.1 Descriptions of seismic attenuation

Amplitude decay is time- (space-) and frequency-dependent, and physically, it is due to combination of three factors: 1) geometric spreading, 2) elastic scattering, and 3) internal friction within the material, usually described by its intrinsic Q. Models for seismic amplitudes often rely on separation of the geometric spreading and Q-type contributions by using empirical relations, such as:

$$P(f,\Pi) = G(\Pi)\exp(-\pi f t^*) \equiv G(\Pi)\exp(-\pi Q_a^{-1} f t), \tag{3.1}$$

where Π denotes the ray path, P is the path effect on the amplitude, G is the geometric spreading, t is the travel time, f is the frequency, t^* is a parameter responsible for the cumulative frequency dependence of the amplitude, and $Q_a \equiv t/t^*$ is the path-averaged (apparent) quality factor. For traveling waves, quantity t^* is accumulated along the ray (e.g., Der and Lees, 1985):

$$t^* = \int_{\Pi} Q^{-1} dt\,, \tag{3.2}$$

where Q is the local quality factor. This Q is believed to be related to the physical properties and microstructure (pores, fractures, fluids, heterogeneity) of the material, although the rigorous relation may be difficult to establish. In this study, I understand the Q as an empirical property attributed to a point of the medium and show how this property can be measured *in combination* with the spatially-variable geometric spreading in equation (3.1).

Many approaches to measuring the Q and t^* from body-wave arrivals were developed based on corrections for $G(\Pi)$, amplitude ratios, pulse rise time, dispersion, and instantaneous frequency (Tonn, 1991). Broadly, all of these methods are based on the difference in the functional dependence on f and t expected from the geometric spreading and Q-related factors in equation (3.1). The geometric spreading is usually considered as frequency-independent and for simplicity, often expressed as $G(\Pi) \propto R^{-\alpha}$ or $G(\Pi) \approx G(t) \propto t^{-\alpha}$, where $R = Vt$ is the source-receiver distance, V is the average velocity, and α is an empirical exponent (Frankel et al., 1990). This model is independent of ray azimuths and implies straight rays, but allows the path effect $P(f,\Pi)$ to empirically deviate from the theoretical limit (which is $\alpha = 1$ for body waves).

3.1.1 Trade-off between intrinsic attenuation, scattering, and geometric spreading

In many practical cases, amplitude decays disagree with the ray-based relation (3.1), and particularly with the simple time-dependent model $G(t)$. Empirically-determined exponent α in the approximation $G(\Pi) \propto R^{-\alpha}$ are often large and may reach or even exceed two (Hardage, 1985). Fast frequency-independent amplitude decays are likely caused by ray bending and back-scattering (reflections predominantly directed upward or downward in exploration and earthquake cases, respectively). In both of these cases, the geometric spreading is anisotropic, depth-dependent and no longer consistent with the simple power-law form of $R^{-\alpha}$. Improved, broadly used approaches to geometric spreading account for bending rays in layered structures (Newman, 1973) and for offset dependences (for example, Ursin, 1990). Most importantly, the geometric spreading is variable within the structure, and *no theoretical model* should likely predict it reliably with accuracy necessary to measure the detail in Q (i.e., with relative accuracy of $1/Q \sim 10^{-2}$; Morozov, 2010a). In addition, in structures with pronounced layering and refractions (common in exploration problems), geometric spreading can be frequency dependent (Yang et al., 2007).

The exponential frequency-dependent amplitude factor in equations (3.1) and (3.2) can be similarly limited for accurately describing the data, with errors related to anisotropy (e.g., Carcione, 1992; Zhu et al., 2007; Behura and Tsvankin, 2009) or the assumption of a frequency-independent Q. Frequency dependence of Q is broadly accepted in global seismic studies and viewed as the key property of Earth materials (for example, Aki and Richards, 2002). Frequency-dependent Q and the associated velocity dispersion were also studied in exploration (VSP) seismic records (Harris et al., 1997; Sun et al., 2009). However, frequency-dependent Q strongly trades off with the choice for $G(t)$ (e.g., Kinoshita, 1994), which increases the difficulty of

finding a suitable approximation for geometric spreading. Recently, Morozov (2008, 2010a) pointed out that in many seismic measurements, the trade-off with the geometric spreading is so large that it does not allow constraining the frequency-dependent Q reliably. For example, in earthquake coda studies, scattering Q^{-1} is often found to be nearly proportional to the frequency (Aki, 1980; Wu, 1985), which can be written as $Q^{-1} = (\gamma/\pi) f$, where γ is some constant whose meaning will be revealed in the next subsection. However, in this case, the exponential factor in equation (3.1) equals simply $\exp(-\gamma t)$, showing that this amplitude decay is only a frequency-independent variation in the geometric spreading. In several case studies, small variations in γ were shown to cause as large as 20–30-fold variations in the interpreted values of Q at 1 Hz (Morozov, 2008). Parameters α and γ can also be spatially variable, leading to spurious frequency dependences in Q. Scattering on small-scale structures, in its turn, is also conceptually difficult to separate from the empirical geometric spreading and Q. When measured from the data, scattering strongly trades off with both geometric spreading and Q, and particularly with the frequency-dependent Q (Dainty, 1981). Such uncertainties present significant difficulties for modeling and interpretation.

3.1.2 Attenuation-coefficient formulation

The solution to the rather complicated time-frequency trade-off above, as suggested by Morozov (2008, 2010a), consists in a simple generalization of the t^* method (equation (3.2)). Instead of assuming that the exponent in relation (3.1) is automatically proportional to f, I treat the entire amplitude-decay problem together and without attempting to subdivide it into a geometric spreading, "intrinsic Q," or scattering. In this way, I focus on forward modeling of the amplitudes by using minimal assumptions and postpone the separation between the geometric

spreading, scattering, and Q effects to the interpretation (see *Discussion*). Equations (3.1) and (3.2) can be generalized to describing the observed wave amplitude u by frequency-dependent attenuation coefficients accumulated along the rays:

$$u(f,\Pi) = A_R(f)\,A_S(f)\,G_0(\Pi)\exp\left[-\chi^*(f,\Pi)\right], \tag{3.3}$$

where A_S and A_R are the source and receiver factors, $G_0(\Pi)$ is some "background" geometric spreading (some theoretical approximation in a known structure), the ray end time equals t, and the perturbation amount χ^* is accumulated along the ray:

$$\chi^*(f,t) = \int_{\Pi} \chi(f,t')\,dt', \tag{3.4}$$

where χ is the differential, temporal "intrinsic attenuation coefficient" (Morozov, 2010b). This attenuation coefficient includes variations of wavefront curvatures, small-scale reflectivity and scattering, as well as differences of the real structure from the one approximated by the selected background model. Its difference from the product $\pi f Q^{-1}$ ratio used in t^*-type relations (3.1) and (3.2) is in removing the assumption of proportionality to f. The only assumption made in the spreading law (3.3) is that the total deviation of the amplitude from $G_0(\Pi)$ is accumulated along the ray path and relatively small. This is the perturbation-theory approximation for $P(f,\Pi)$ (Chernov, 1960). In geophysical literature, this approximation was also referred to as the localization theory (van der Baan, 2002).

The attenuation coefficient χ in equation (3.3) is generally frequency-dependent, which can be written as:

$$\chi(f) = \gamma + \kappa f, \tag{3.5}$$

where γ is the zero-frequency ($f \to 0$) limit of χ, and κ represents the remaining frequency dependence of χ. Note that parameters χ and γ in this equation are measured in frequency units, whereas κ is dimensionless. Parameter γ contains the cumulative effects of geometric spreading (relative to the background model G_0) and/or scattering, in which we can further recognize back-scattering (predominantly upward-directed reflectivity in a finely-layered structure) and forward scattering (transmission). For comparisons with the conventional Q-based approach, parameter κ can be transformed into an "effective" Q_e of the medium as $\kappa = \pi / Q_e$ (Morozov, 2008). Quantity κ is empirical and includes the frequency-dependent part of scattering, geometric spreading (if a background geometric spreading model is considered), and internal friction (energy dissipation into heat), which may caused by a broad variety of mechanisms. Some of these mechanisms are described in chapter 4.

In general, parameter κ in relation (3.5) can be frequency-dependent, but from many case studies, a constant-κ approximation appears sufficient (Morozov, 2008, 2010a, b). In addition to the dependence on frequency (equation (3.5)), χ should generally depend on the propagation direction in equation (3.3). Thus, similarly to Q (Červený and Pšenčík, 2008), both γ and κ should be anisotropic.

The approach in equations (3.3) and (3.5) is similar to the conventional relations (3.1) and (3.2) but offers two important advantages. First, expression (3.3) recognizes that the geometric spreading and scattering occur locally and can be measured concurrently with attenuation. Second, this model does not assume that the geometric spreading model can be modeled accurately and/or that scattering can be considered absent. Without restricting ourselves to some specific (inevitably limited) models for the geometric spreading, internal friction, or

scattering, expression (3.3) directly models the variations of the frequency spectrum of the signal as it travels through the medium. As a result, this approach is free from the uncertainties of the material-Q model.

The frequency-independent quantity κ in equation (3.5) is analogous but not equivalent to the frequency-independent Q^{-1} commonly used in exploration seismology. If spectral ratios canceling the source and receiver effects can be formed, κ can be measured from their slopes ($d\chi/df$) while bypassing the inversion for γ. For example, Reine et al. (2012) used spectral ratios to measure the Q between reflectors in pre-stack surface seismic records, and Behura and Tsvankin (2009) proposed a similar method for anisotropic media. These spectral-ratio Q's are comparable to our Q_e model below, in the sense of including the averaged effects of frequency-dependent part of scattering (reflectivity) and intrinsic attenuation but omitting the frequency-independent small-scale ("white") reflectivity represented by the intercept values in the spectral ratios. Rickett (2006) used a method similar to the one in this Chapter to measure the Q and a spatial analog of our zero-frequency attenuation coefficient γ (denoted β in that paper) from log-amplitude spectra for a vertically-propagating VSP wavelet. He also gave a notable discussion of the possibility of negative Q (i.e., $\kappa < 0$ in equation (3.5)) and an approach to inversion ensuring $\kappa > 0$. Recently, Blias (2012) used an amplitude model similar to equations (3.3) and (3.5), in which the constant term (γ) was inverted for implicitly and used to derive weights for more accurate determination of the spectral-ratio Q factors. Comparisons to the above methods show that measurement of γ is generally required for accurate measurement of $Q^{-1} \propto \kappa$. The principal contribution of the present approach consists in treating the γ and κ completely similarly, as parts of the frequency-dependent $\chi(f)$, and always interpreting these quantities together.

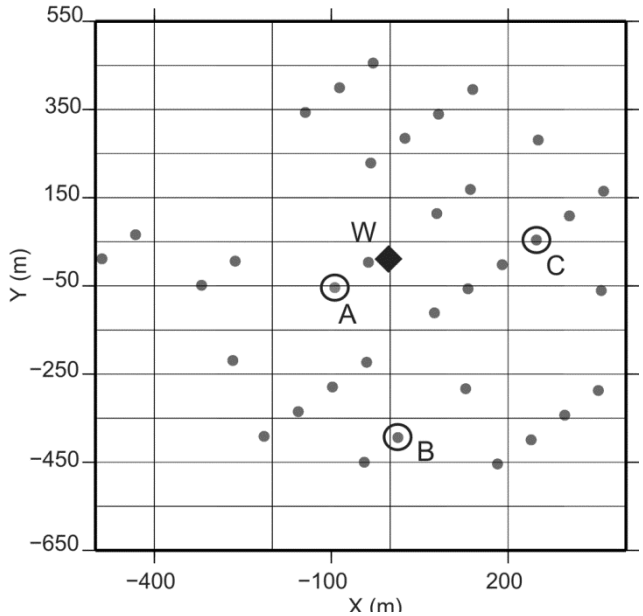

Figure 3.1: Base map showing 35 VSP shots (grey dots) used in inverting for first-arrival attenuation in this study. Black diamond is the VSP borehole position, and circles indicate shots used in further illustrations (Figure 3.5 and Figure 3.14). Shot coordinates are relative to the borehole.

3.2 Wave Spreading and Attenuation model for Weyburn VSP

3.2.1 Model

First-arrival waveforms from 35 Weyburn VSP shots with offsets 30 to 500 m and all azimuths around the borehole were used in this attenuation study (Figure 3.1). Using an interpreted well-log data in the VSP area and a geologic model of Weyburn oilfield (Whittaker, 2005), I constructed an initial interval-velocity model consisting of six horizontal layers (Figure 3.2).

In this model, rays were traced by using straight segments within each layer (Figure 3.2c), and the velocities were adjusted by fitting the observed first-arrival travel times in the sense of the L_1 norm (i.e., the mean absolute value of the travel-time residuals). Each layer is

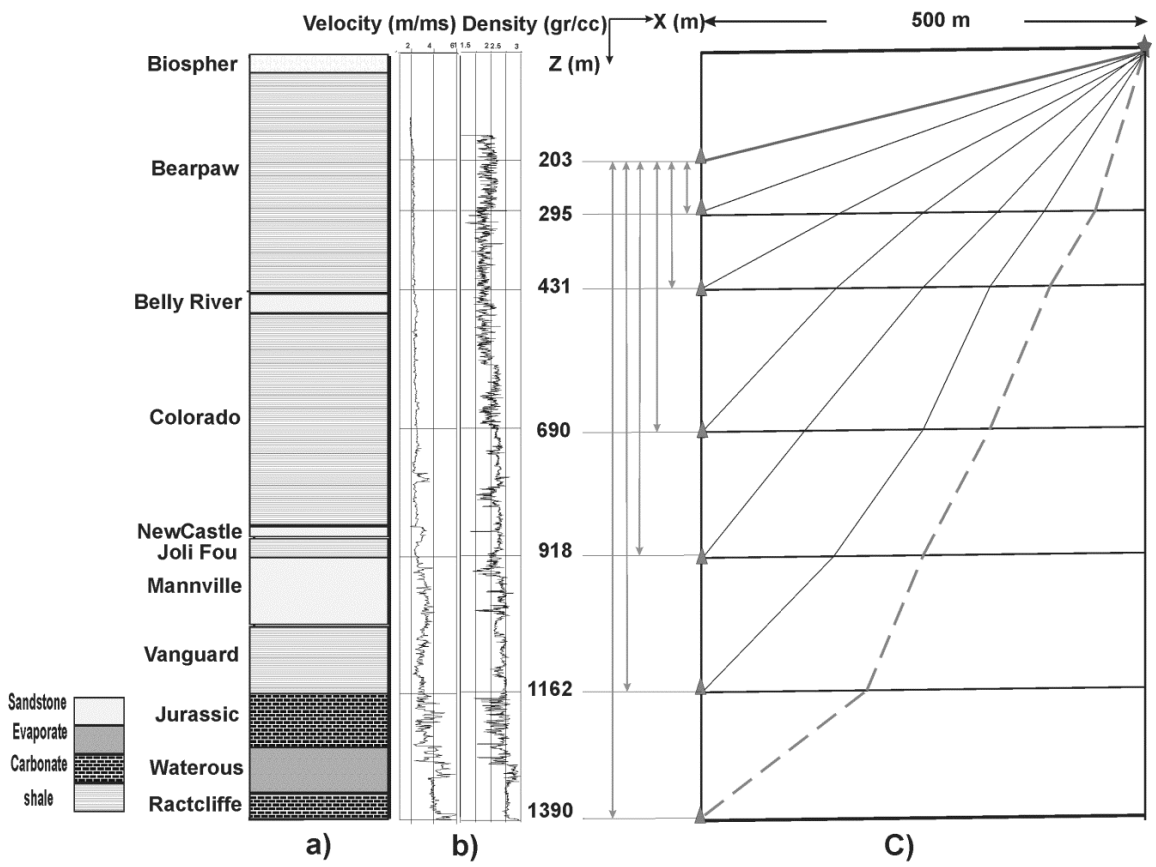

Figure 3.2: Depth model: a) geologic section, b) density and acoustic velocity well logs, c) model layers. Thick black and dashed lines show rays traced from a shot to the geophones at the smallest and largest depths. Gray arrows indicate pairs of geophones used for measuring the attenuation parameters of each layer.

further assigned a pair of anisotropic attenuation parameters γ and κ, and the forward and inverse problems formulated as described in the following sections.

3.2.2 Velocity anisotropy

Anisotropy represents a significant factor in broad-offset seismic observations in sedimentary environments. As shown below, the attenuation structure in Weyburn area shows an about 3% VTI anisotropy (transverse isotropy with a vertical axis of symmetry). Nevertheless, for simplicity, I use an isotropic background model $G_0(\Pi)$ (equation (3.3)) for deriving the

attenuation, and consequently the velocity anisotropy becomes included in the empirical geometric-spreading parameters γ (equation (3.5)). However, before proceeding with this using an isotropic background velocity model, let us estimate the velocity anisotropy in the study area from the first-arrival travel-time data.

To estimate the inaccuracy introduced by the approximation of velocity isotropy, I considered the relative deviations of the first-arrival travel times from the times predicted in the layered model (Figure 3.2) and selected for rays predominantly oriented in the northeast, southeast, southwest, and northwest directions (Figure 3.3). In all azimuthal directions, the far-offset shots show systematically smaller travel-time deviations compared to the near-offset shots, with differences increasing to ~4% at shallow receiver depths (Figure 3.3). The azimuthal travel-time variations are smaller (for example, 2% between the NW and SW directions in Figure 3.3), suggesting a weaker HTI anisotropy. Thus, the velocity anisotropy is by over an order of magnitude weaker than the resulting VTI anisotropy for attenuation (see section 3.3), and the isotropic velocity model is acceptable for making first-order observation considered here.

I also measured an anisotropic velocity model from travel-time deviations calculated above. Thomsen (1986) listed the characteristic anisotropy parameters for a number of sedimentary rocks. For the case of anisotropic rock with a vertical axis of symmetry (VTI), these data were interpreted by using five elastic moduli and recast in terms of the P and S-wave velocities in the vertical direction (denoted α_0, and β_0, respectively), and the three parameters of anisotropy ε, δ and γ. Thomsen (1986) showed that for weak anisotropy, the dependence of P-wave phase velocity V_P on the ray angle φ can be approximated as:

$$V_p(\varphi) = \alpha_0(1 + \delta \sin^2 \varphi \cos^2 \varphi + \varepsilon \sin^4 \varphi) . \qquad (3.6)$$

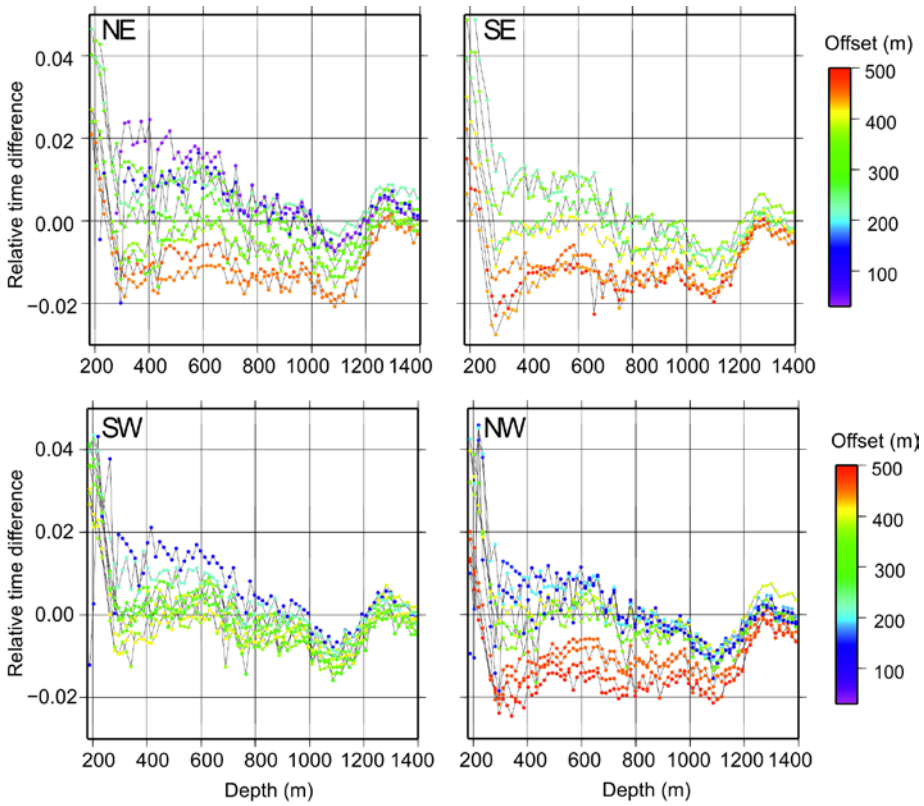

Figure 3.3: Relative deviations of the first-arrival travel times from those modeled by ray tracing (Figure 3.2) for source-receiver azimuths oriented close in the NE, SE, SW and NW directions (labels). Symbol colors indicate the source offsets from the VSP borehole (Figure 3.1).

I rewrite this equation as:

$$V_p(\varphi) = \alpha_0(1+\delta\sin^2\varphi(1-\sin^2\varphi)+\varepsilon\sin^4\varphi), \tag{3.7}$$

and express from it the relative variations of the travel-time fitting calculated above and by using:

$$-\frac{\delta t}{t} = \frac{V_P(\varphi)-V_{\text{model}}}{V_{\text{model}}} = \frac{\alpha_0-V_{\text{model}}}{V_{\text{model}}} + \frac{\alpha_0}{V_{\text{model}}}\delta\sin^2\varphi + \frac{\alpha_0}{V_{\text{model}}}(\varepsilon-\delta)\sin^4\varphi\,, \tag{3.8}$$

Table 3.1: Anisotropic parameter δ in four main azimuthal directions.

Direction	Azimuth (deg)	$V_P(\varphi)$	δ
NE	0-90	2640	0.023
SE	90-180	2672	0.01
SW	180-270	2652	0.007
NW	270-360	2633	0.03

where V_{model} as the average isotropic velocity. By ignoring the small fourth-order term $\sin^4(\varphi)$ and plotting $(-\delta t/t)$ versus $\sin^2\varphi$, the vertical-direction velocity α_0 can be found from the intercept and anisotropy δ from the slope of this dependence. Figure 3.4 shows the anisotropic velocity variation (equation (3.7)) measured in in four azimuthal bins. By setting V_{model} equal the average model velocity (2659 m/s) and interpretively fitting straight lines to these dependences, the VTI anisotropy δ calculated in the four azimuth directions and provided in Table 3.1. The anisotropic parameter δ is variable from 0.007 in SW direction to 0.03 in NW direction.

As shown in Table 3.1, the resulting anisotropic parameters δ for velocity in the area of Weyburn VSP are relatively small, as discussed above. The velocity anisotropy is much weaker than the anisotropy of attenuation parameters considered below.

3.2.3 Attenuation anisotropy

In the strongly and finely layered sedimentary sequence in the study area (Figure 3.2b) parameters γ_i and κ_i should also depend on the plunge angle of a seismic ray, similarly, for example, to the Q factor in Zhu et al. (2007). Therefore, I use a simple two-parameter VTI model similar to the first two terms in model (3.6) to describe the anisotropic character of γ and κ

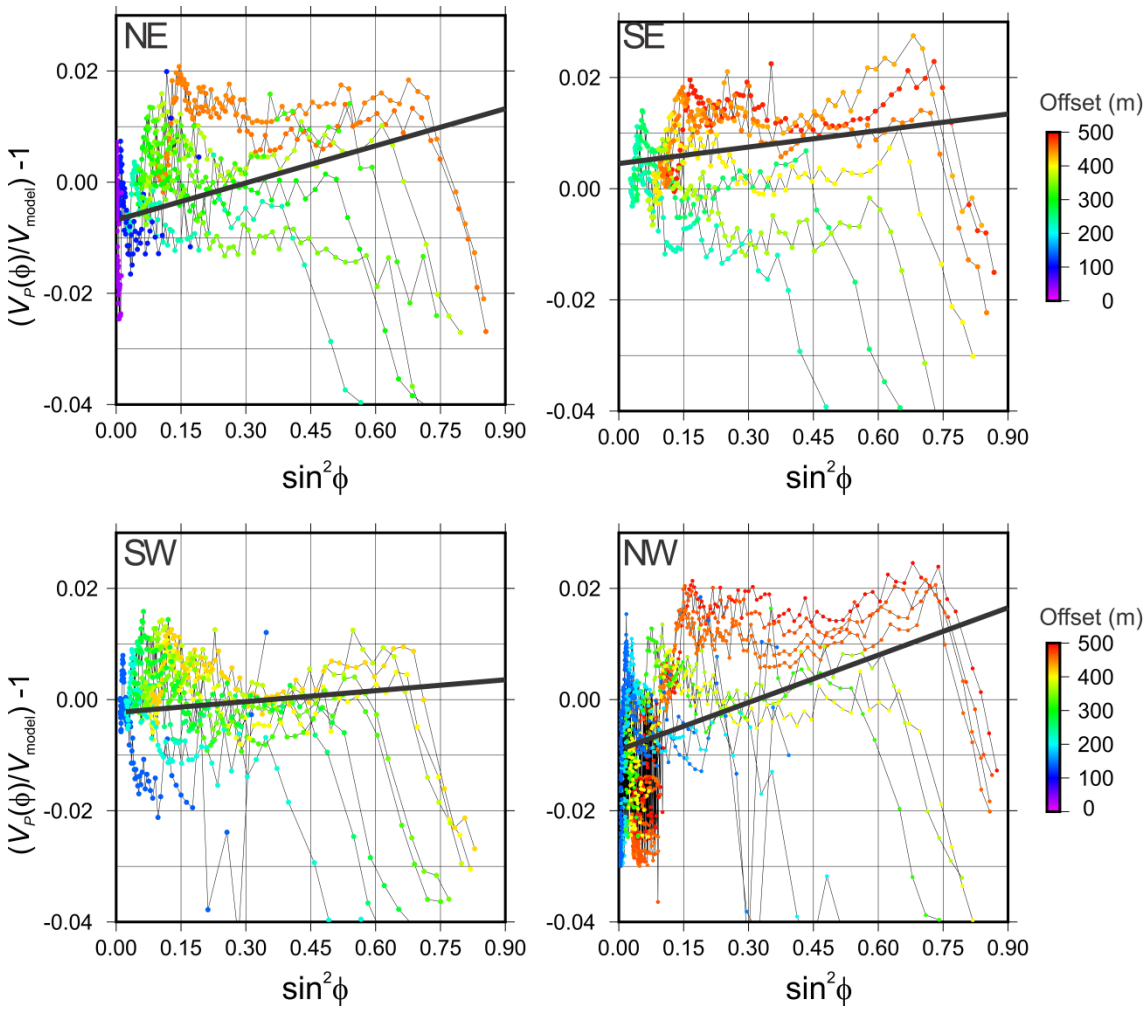

Figure 3.4: Relative anisotropic velocity errors for source-receiver azimuths plotted versus Sine-squared of incidence angle and oriented close in the NE, SE, SW and NW directions (labels). Symbol colors indicate the source offsets from the VSP borehole (Figure 3.1). Black lines indicate anisotropy parameter δ measured using eye fitting in equation (3.8) for different azimuthal directions.

$$\gamma(\varphi) = \gamma_1 + \gamma_3 \sin^2\varphi, \text{and } \kappa(\varphi) = \kappa_1 + \kappa_3 \sin^2\varphi, \tag{3.9}$$

where φ us the ray angle relative to the downward vertical direction, γ_1 and κ_1 are the attenuation parameters in the vertical direction ($\varphi = 0$), and γ_3 and κ_3 are the corresponding anisotropy parameters, selected so that for horizontal propagation (at $\varphi = 90°$), the attenuation parameters equal $\gamma_2 = \gamma_1 + \gamma_3$ and $\kappa_2 = \kappa_1 + \kappa_3$, respectively.

3.2.4 Forward problem for γ and κ

When applied to a piecewise-straight ray (source/geophone pair) number j in a stack of uniform layers, the forward model for body P-wave amplitudes (equations (3.3)–(3.5)) becomes:

$$u_j(f,t) = A_{Rj}(f)\,A_S(f)\,G_{0j}(\Pi)\exp\left(-\chi_j^*\right), \tag{3.10}$$

where:

$$\chi_j^* \equiv \int_{\text{Ray } j} \chi(f,t')\,dt' = \sum_{i=1}^{N_{layers}} \left[(\gamma_{1i} + f\kappa_{1i})\,t_i^{(j)} + (\gamma_{3i} + f\kappa_{3i})\,\overline{t}_i^{(j)} \right], \tag{3.11}$$

where $t_i^{(j)}$ is the travel time of the j^{th} ray in i^{th} layer, $\overline{t}_i^{(j)} = t_i^{(j)} \sin^2 \varphi_i^{(j)}$ is the "horizontal" travel time, and $\varphi_i^{(j)}$ is the angle of the corresponding ray segment relative to the vertical direction, and the summation is over all layers in the model, (Figure 3.2c). The geophone response is further factored as $A_{Rj}(f) = \Omega_j R_j A_G(f)$, where Ω_j is the directional factor (cosine of its orientation angle relative to the direction of wave propagation), $A_R(f)$ is the frequency response assumed to be the same for all geophones, and R_j is the scalar approximating the variation of geophone coupling within the VSP spread.

To remove the effects of $A_S(f)$ and $A_G(f)$ and emphasize those of the ray paths, I further correct the recorded amplitudes for $G_0(t)$ and Ω and form logarithms of spectral ratios for pairs of rays (j,l) within each shot:

$$\tilde{A}_{jl}(f) \equiv \ln\left[\frac{u_j / (\Omega G_0)_j}{u_l / (\Omega G_0)_l} \right] = \ln\frac{R_j}{R_l} - \sum_{i=1}^{N_{layers}} \left[(\gamma_{1i} + f\kappa_{1i})\left(t_i^{(j)} - t_i^{(l)}\right) + (\gamma_{3i} + f\kappa_{3i})\left(\overline{t}_i^{(j)} - \overline{t}_i^{(l)}\right) \right]. \tag{3.12}$$

To form these receiver pairs, I used receivers located near the bottom of each layer and a common reference receiver at the top of the downhole receiver spread (for example, the rays

shown in thick black and dashed lines in Figure 3.2c).

To evaluate the amplitude ratios $\tilde{A}_{jl}(f)$, I used the first-arrival amplitudes measured in raw records from the selected 35 shots (Figure 3.1). The wavefield was not separated into down- and upward-propagating waves, because in the first arrivals, the upgoing waves consist of back-scattering (reflectivity) which is expected to be included in the attenuation coefficient, $\chi(f)$. For measuring the P-wave amplitudes (ratios u/Ω in equation (3.1)), I tried two approaches (Figure 3.5). By rotating the 3-C records into the principal directions of particle motion, 3-C P-wave amplitudes u_P were obtained directly (and thus $\Omega = 1$; Figure 3.5c). The same amplitudes can also be inferred from the vertical-component records, as $u_P = u_z/\Omega$ with $\Omega = \cos\varphi$ (Figure 3.5a and d). To measure these amplitudes from first-arrival waveforms, I used time windows from -10 to 50 ms relative to the picked first-arrival travel times (Figure 3.5a and c) and calculated the RMS amplitudes across three peaks or troughs adjacent to the largest peak within this window. This amplitude measure is (relatively) insensitive to the selection of the time windows and also to dispersion and variations of wavelet shape during propagation. The resulting two measures of u_P were found close to each other (black and gray lines in Figure 3.5d), and the second of them was used for producing the dataset of spectral ratios $\tilde{A}_{jl}(f)$ in equations (3.1).

Figure 3.6 shows the logarithms of power spectra of several traces from a near-offset shot, which suggest that frequency bands from about 10 to 150 Hz are suitable for attenuation analysis. To produce frequency-dependent amplitudes and $\tilde{A}_{jl}(f)$, I used the time-domain RMS

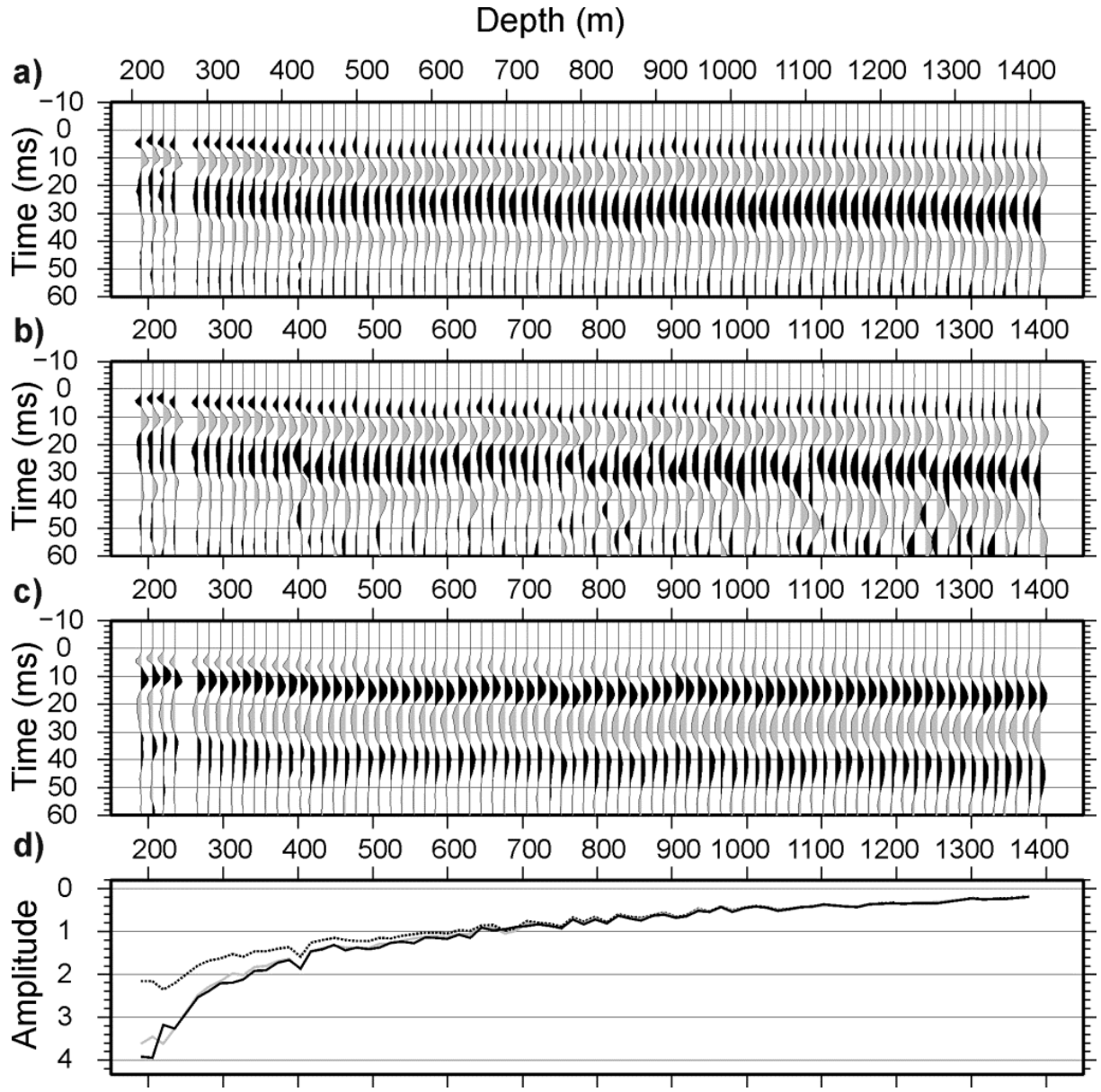

Figure 3.5: 3-C amplitudes for a shot at 258-m offset (C in Figure 3.1): a) vertical component, b) rotated radial component, c) P-wave amplitude obtained by projecting the 3-C records onto the principal direction of first-arrival motion. d) Graphs of measured first-arrival amplitudes. Solid black line is the total P-wave amplitude u_P, dashed black line is the vertical-component amplitude, u_z, and gray line is the total amplitude derived from the vertical-component by $u_P = u_z/\cos(\varphi)$.

amplitude measurement described above (Figure 3.5) and applied to waveforms filtered within overlapping frequency bands centered from 10 to 150 Hz. Band-pass frequency bands were

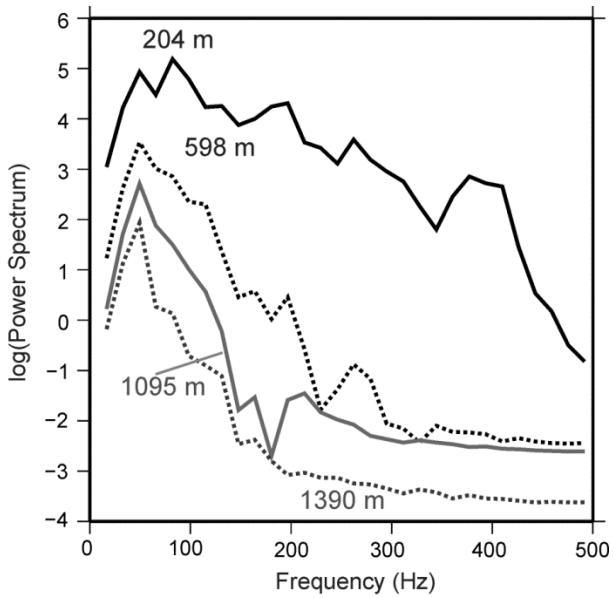

Figure 3.6: Logarithm of averaged power spectra for near-offset VSP shots. The labels in the picture representing the depth of corresponding receiver in meter.

selected of the form [$0.5f_0$/$0.8\ f_0$/$1.2f_0$/ $2f_0$], where f_0 varied from 10 to 150 Hz in 2-Hz increments. The selected broadening of the filter bands with increasing f_0 also helps reducing the ringiness of the filtered wavelets, as generally recommended in seismic processing. This broadening should also increase the signal to noise ratio at the expense of reducing the frequency resolution. Finally, the selected uniform increments in f_0 produce a redundant time-frequency sampling of amplitudes which, however, favours the statistical inversion procedure below.

To invert the resulting frequency-dependent $\tilde{A}_{jl}(f)$ for model parameters γ_1, κ_1, γ_3 and κ_3, I used a layer-stripping procedure, starting from the uppermost layer and progressively moving to the deeper layers. This method also allows a layer-by-layer, visual control of the results. In the following, I first disregard the receiver coupling variations, i.e., drop the first term in the right-hand side of equation (3.1) and then return to this term later in subsection 3.3.

3.2.5 Inversion

Relations (3.1) represent a linear inverse problem that can be solved in various ways. My approach is motivated by two principles: 1) observation that the anisotropic parameters γ_3 and κ_3 are generally constrained much poorer than the isotropic γ_1 and κ_1, and 2) the desire to perform some visual quality control and interpretation of the solution. Therefore, I use an iterative layer-stripping procedure. In the iteration for layer k, I assume the anisotropy parameters $\gamma_{3,k}$ and $\kappa_{3,k}$ in it to be fixed and all parameters of the overlaying layers $i = 1 \ldots k-1$ known. Equation (3.1) can then be written as:

$$\tilde{\tilde{A}}_{jl}(f) = \gamma_{1,k} + f\kappa_{1,k} \ , \tag{3.13}$$

where:

$$\tilde{\tilde{A}}_{jl} \equiv \frac{1}{t_i^{(l)} - t_i^{(j)}} \left\{ \tilde{A}_{jl} - \sum_{i=1}^{k-1} \left[\left(\gamma_{1i} + f\kappa_{1i}\right)\left(t_i^{(j)} - t_i^{(l)}\right) + \left(\gamma_{3i} + f\kappa_{3i}\right)\left(\bar{t}_i^{(j)} - \bar{t}_i^{(l)}\right) \right] \right\} - \left(\gamma_{3,k} + f\kappa_{3,k}\right)\sin^2\varphi \tag{3.14}$$

is the spectral ratio corrected for the cumulative effects the background geometric spreading and all attenuation parameters (γ_1,γ_3, κ_1, and κ_3) within the overlaying layers and for the travel time differences within the layers. This spectral ratio is also corrected for the effect of anisotropy within the k^{th} layer (the last term containing $\gamma_{3,k}$ and $\kappa_{3,k}$). After these corrections, equation (3.1) predicts a linear dependence of $\tilde{\tilde{A}}_{12}$ on frequency, with intercept $\gamma_{1,k}$ and slope $\kappa_{1,k}$. This dependence can be observed visually (principally for quality control and for deciding whether $\kappa_{1,k}$ may be frequency-dependent) and inverted for by various methods. Because of the outliers and oscillations in the data, I performed the inversion by using the following statistical procedure, which was a modification of the "robust" fitting method by Walden (1991).

The optimal values of anisotropy parameters γ_3, and κ_3 for each layer of the model were determined by grid search. The grid search was employed because: 1) it is the simplest procedure (albeit computationally intensive) for finding the minimum of a complex function which is nonlinear with respect to parameters $\gamma_{3,k}$ and $\kappa_{3,k}$, and 2) most importantly, it gives the most complete picture of the trade-off between the resulting parameters. For each trial combination of ($\gamma_{3,k}$, $\kappa_{3,k}$), the total misfit is measured using the L_1 norm:

$$\Phi\left(\gamma_{1,k},\kappa_{1,k}\,|\,\gamma_{3,k},\kappa_{3,k}\right)=\sum_{j=1}^{N_{\text{rays}}}\sum_{n=1}^{N_{\text{frequences}}}\left|\gamma_{1,k}+f_n\kappa_{1,k}-\tilde{\tilde{A}}_{jl}\left(f_n\right)\right| . \tag{3.15}$$

This misfit is minimized with respect to parameters $\gamma_{1,k}$ and $\kappa_{1,k}$ as described in the next paragraph. The optimum value of this misfit is further treated as the cost function, C ($\gamma_{3,k}$, $\kappa_{3,k}$), minimized by grid search (Figure 3.7). Once the optimal anisotropy parameters are found, the corresponding values of $\gamma_{1,k}$ and $\kappa_{1,k}$ become also known and can be checked visually by using relation (3.1).

In order to determine the values of $\gamma_{1,k}$ and $\kappa_{1,k}$ from equation (3.13) (for fixed trial $\gamma_{3,k}$ and $\kappa_{3,k}$), similarly to Walden (1991), I divide the frequency-amplitude data into two parts corresponding to low- and high-frequency halves of the frequency band. After this, for each candidate pair ($\gamma_{1,k}$, $\kappa_{1,k}$), I calculate the probability for a data point in the low- and high-frequency ranges to fall below the fitting line given by equation (3.13) in the $\left(f,\tilde{\tilde{A}}\right)$ plane. These sample probabilities are denoted F_L and F_H, respectively:

$$F_L=\frac{n_L}{N_L}\ \text{and}\ F_H=\frac{n_H}{N_H}\ , \tag{3.16}$$

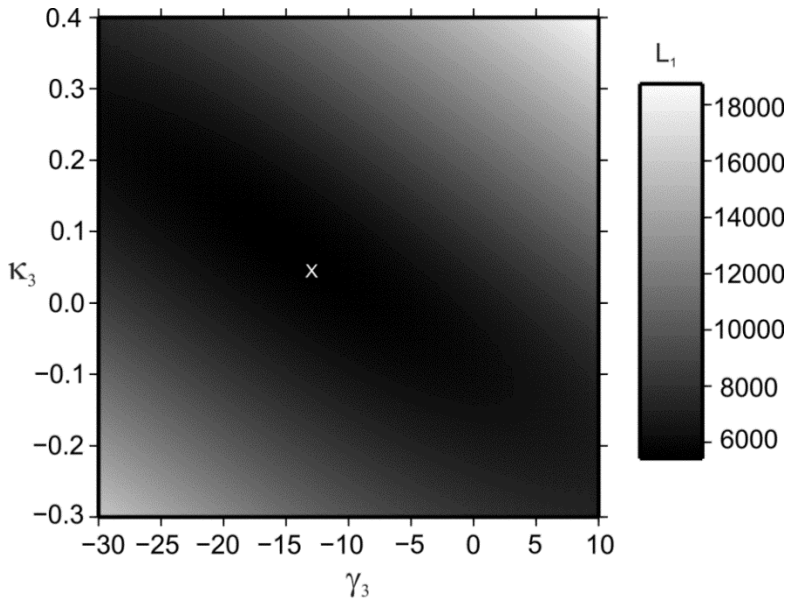

Figure 3.7: Grid search for anisotropy parameters for model layer 2. Gray shading shows L_1 error values and symbol 'X' indicates the optimal anisotropy parameters for this layer.

where n_L , n_H, are the numbers of points below the trial solution line, and N_L and N_H are the total numbers of points in the low- and high-frequency halves of the dataset. In terms of these probability functions, the "robust" solution is the one passing through the medians of both distributions, for which $F_L = F_H = 0.5$. Therefore, by contouring the values of F_L and F_H on the same plot, the optimal solution is found as the intersection of the 50% contours (black dot in Figure 3.8.

3.3 Results

Figure 3.9 illustrates the importance of anisotropic attenuation parameters in equation (3.5) for layer #2 within the model. If evaluated with no attenuation anisotropy, the corrected

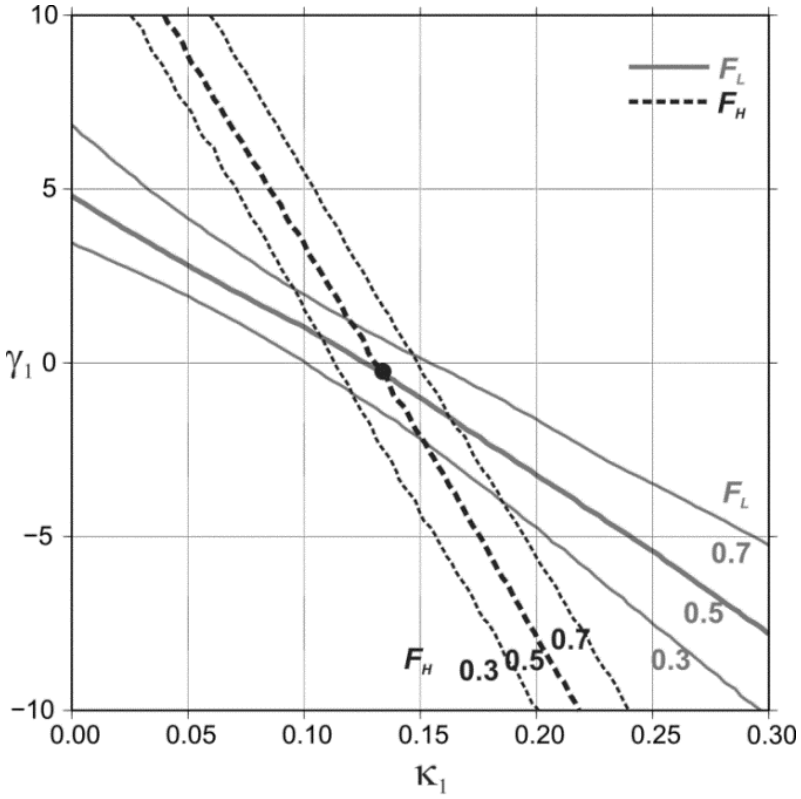

Figure 3.8: Inversion method for layer 2. Contours of low- and high-frequency probability functions (F_L and F_H) shown in gray and black. Black dot shows parameters γ_1 and κ_1 obtained by our solution using intersection of contours F_L and F_H equal 0.5.

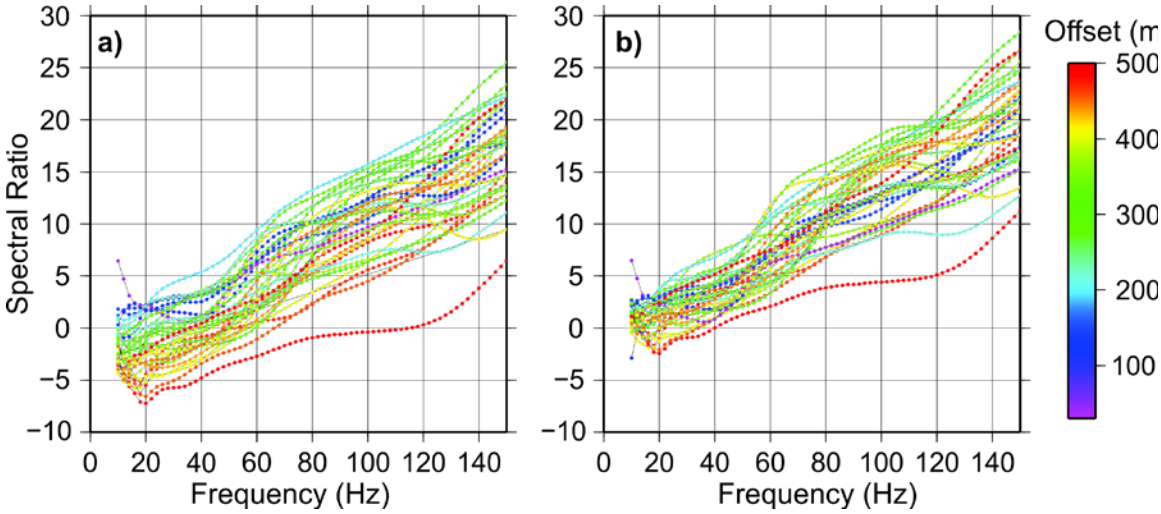

Figure 3.9: Effect of anisotropy: a) Fitting expression 3.1 for layer 2 by using $\gamma_3 = \kappa_3 = 0$, b) The same using optimal anisotropic parameters. Note the significant systematic variations of amplitudes with source-borehole offsets in plot a.

spectral ratios in this layer show systematic variations with source-borehole offsets (Figure 3.9a). In particular, the intercepts of the spectral-ratio trends tend to decrease with increasing offsets, suggesting that oblique rays encounter lower levels of γ. These variations are reduced, and the distribution of spectral ratios becomes less scattered by using non-zero values for γ_3 and κ_3 (Figure 3.9b). Data fits using the layer-stripping procedure are shown in Figure 3.10 for six layers of the model (Figure 3.2c). Note that despite some residual misfits, the values of γ_1 and κ_1 can be reliably constrained from these plots (black lines in Figure 3.10).

3.3.1 Model for γ and κ

The resulting attenuation model is shown in Figure 3.11 and Table 3.2. In addition to the anisotropic attenuation parameters in equations (3.5) and (3.9), Table 3.2 also shows the effective Q for vertical propagation within the medium, defined as $Q_e = \pi/\kappa_1$, and the "cross-over frequency" $f_c = |\gamma/\kappa_1|$ (Morozov, 2008). The meaning of f_c is the frequency below which the geometric spreading and/or scattering effects dominate the wave attenuation (*ibid*). Table 3.2 also shows the possible ranges of Q_e extracted from the error bounds on κ_1.

Table 3.2: Resulting anisotropic attenuation model.

Layer	Depth to bottom (m)	Velocity (m/s)	γ_1 (s^{-1})	κ_1	γ_3	κ_3	$Q_e=\pi/\kappa$	Q_e range	$f_c=\lvert\gamma/\kappa\rvert$ (Hz)
1	295	2185	-2	0.12	0*	0*	26	10–45	17
2	431	2230	-0.35	0.135	-13	0.05	23	17–33	3
3	690	2330	1.23	0.0473	-16	0.2	66	37–141	26
4	918	2405	-0.24	0.0163	-13	0.25	192	61–∞	15
5	1162	2970	3.92	0.0255	-34	0.5	123	45–∞	154
6	1390	3834	2.76	0.1437	-35	0.004	22	12–37	19

* Not measured for layer 1.

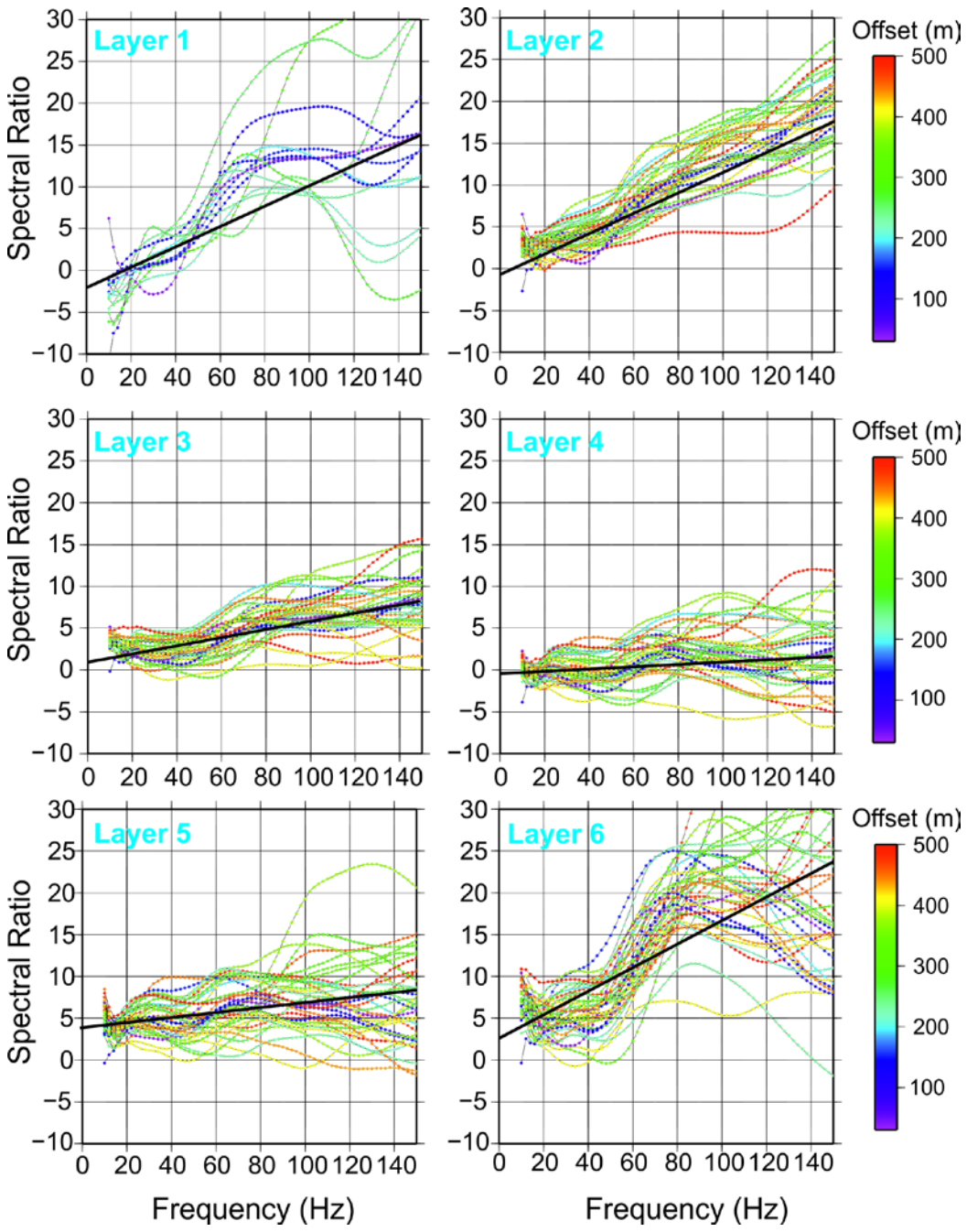

Figure 3.10: Corrected spectral ratios used to measure $\gamma_{1,k}$ and $\kappa_{1,k}$ by layer stripping. Black lines indicate the inverted model parameters $\gamma_{1,k}$ and $\kappa_{1,k}$.

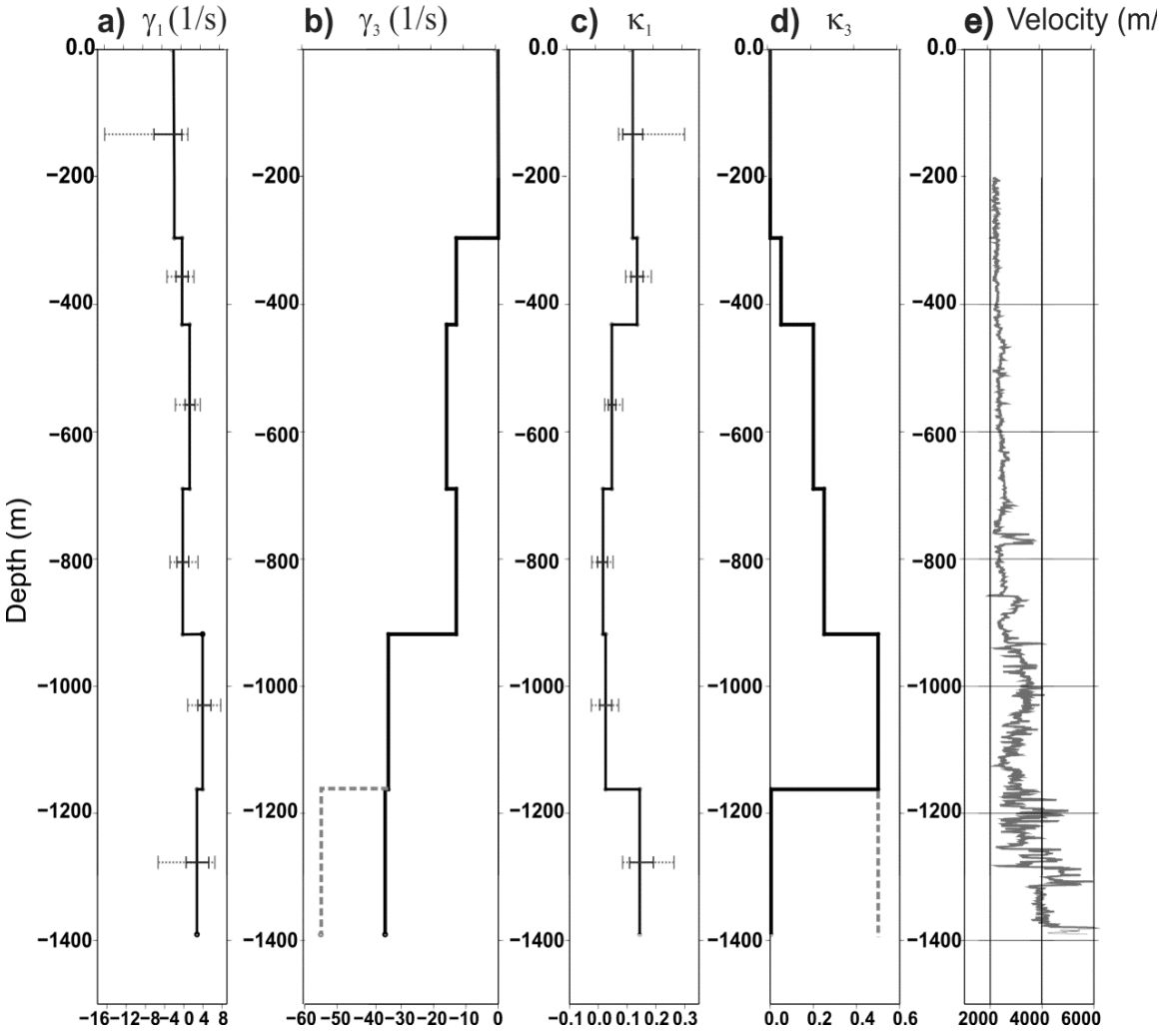

Figure 3.11: Inverted attenuation model parameters and uncertainty estimates for the resulting model (black lines): a) scattering and geometric spreading parameter γ_1; b) anisotropy parameters γ_3; c) attenuation parameter κ_1; d) anisotropy parameters κ_3, and e) velocity log. Black dots are the inverted parameters for the different layers. Dashed lines show an alternate anisotropy model for bottom layer. Black and gray dashed error bars in a) and c) are estimated as shown in Figure 3.13.

The resulting model shows negative values of γ_1 (i.e., wavefront focusing relative to the selected background geometric-spreading model G_0) down to 430-m depths which gradually increase and become positive (defocusing and backscattering) below layer 5 and to the depth of 1390 m. Overall, the frequency-dependent effect (products $f\kappa$) on seismic amplitudes is

significantly stronger than that of the "geometric attenuation" and scattering (γ). This can be seen from the values of $f_c \approx 3$–26 Hz located closer to the lower end of the frequency band and below the dominant frequency of $f \approx 40$ Hz (Table 3.2). However, in the fifth layer (918–1160 m), the geometric attenuation is stronger than effective attenuation ($f_c \approx 150$ Hz). Thus, f_c lies within the observation frequency band for most layers, and everywhere in the model, geometric attenuation is much stronger than $\gamma \approx 0.01$ s^{-1} observed for the deep crust (Morozov, 2008, 2010a, 2010b, and 2011a). Generally, the values of optimal anisotropy in γ (γ_3) decrease from –13 to –35 s^{-1} to the top of the reservoir cap rock (1390 m). These values show significant variations of anisotropy, with predominantly horizontal refraction and forward-scattering (focusing, $\gamma_2 < 0$) in the structure. Parameters of anisotropy in κ (and Q_e), κ_3, increase from 0.05 to 0.5 to 1160 m and then decrease to almost zero near 1390 m (Figure 3.11d; Table 3.2). This shows that the attenuation is somewhat stronger for near-horizontal propagation. The effective "quality factors" Q_e equal 23–26 near the surface, increase to 192 near 920-m depths, and further decrease to 22 at 1390 m (Table 3.2). A comparison of well-log data with the depth trend of κ (or Q_e^{-1}) suggest two trends:

1) the variations of the velocity and density log values generally increase with depth (Figure 3.11e), while

2) κ_1 decreases to 800 m and again increases below this depth (Figure 3.11c).

The reasons for such correlation still need to be examined by modeling. Tentatively, note that the zone of positive correlation below 800 m also corresponds to very strong layering and strong anisotropy γ_3 (Figure 3.11b and e). Consequently, the increase in κ could be caused by high reflectivity below this depth.

The bottom layer in the model (#6; Table 3.2) suggests an anomaly in the anisotropic part of κ (κ_3) dropping to near-zero below 1160-m depth (Figure 3.11d). However, parameters κ_3 and γ_3 are not very tightly constrained and exhibit significant trade-off (Figure 3.7). Therefore, I tried exploiting this trade-off by selecting a different pair of κ_3 and γ_3 for this layer (dashed lines in Figure 3.11d). This solution gives only a 2% increase in the objective function (3.15), but shows no anomalous trends in κ_3 and γ_3. Thus, it is likely that the magnitudes of both anisotropies in γ and κ continuously increase with depth, particularly below the level of 918 m, below which the reflectivity also increases (Figure 3.11b, d, and e).

3.3.2 Receiver coupling

Having inverted for propagation parameters, I consider in this subsection the variations of receiver coupling, R_l in equation (3.1). For one shot, taking the coupling of the reference geophone equal one ($R_1 = 1$), this equation gives the coupling for any other borehole geophone number l:

$$\ln R_l = -\tilde{A}_{1l} + \sum_{i=1}^{k} (\gamma_i + f\kappa_i)(t_i^{(l)} - t_i^{(1)}) + \sum_{i=1}^{k} \left(\gamma_{3,k} + f\kappa_{3,k}\right)(\bar{t}_i^{(l)} - \bar{t}_i^{(1)}) . \qquad (3.17)$$

This quantity is evaluated for all shots, and its average at each depth level gives an estimate of geophone coupling, and the standard deviation measures the residual amplitude fitting error (Figure 3.12). With several exceptions, the results show consistent and uniform coupling for borehole receivers, with values of R_l ranging from ~0.75 to 1.25. The residual frequency-dependent amplitude variations are substantially larger than coupling variations (Figure 3.12). These variations are likely caused by tuning within the layered structure, i.e. by $\chi(f)$ variations different from our simple model (equation 3.5).

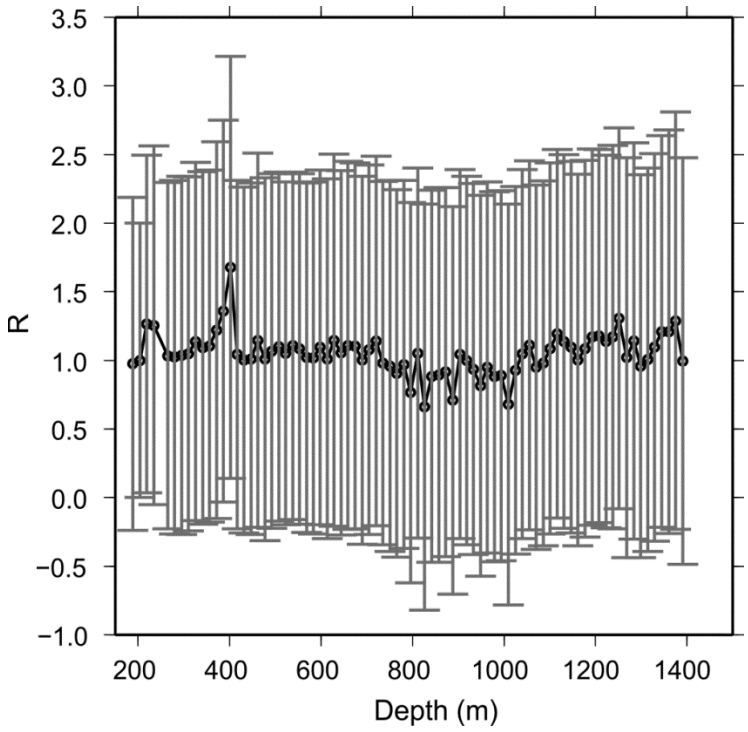

Figure 3.12: Geophone coupling values for VSP borehole geophones (black dots; equation 3.17) and their error bars.

3.3.3 Error analysis

In inversion, it is important to measure the uncertainties of the resulting model. Because of the nature of the problem and limited angular aperture of VSP data, a significant trade-off exists between parameters γ, κ and the corresponding anisotropy parameters. This trade-off can be seen in the (κ_3,γ_3) cross-plot (Figure 3.7). The estimation of parameters κ_3 and γ_3 is relatively loose, although it is supported by visual inspection (Figure 3.9 and Figure 3.10) and non-zero values are clearly required in most cases. I tried two methods for estimating the ranges of possible errors in the parameters shown in Table 3.2. The first method used the conventional χ^2 criterion, and the second directly utilized the statistical nature of our inversion method.

Considering the χ^2 criterion, note that for each layer, two ($n_p = 2$) parameters γ_1 and κ_1 were derived by using $N = 2485$ amplitude readings in equation (3.13). By assuming statistically independent data points, the number of degrees of freedom of the problem equals $n_{df} = N - n_p = 2483$. From the residual amplitude misfits, one can estimate the data variance for k-th layer as:

$$\sigma_k^2 = \frac{1}{n_{df}} \sum_{i=1}^{N} \left| \tilde{A}_{i12} - (\gamma_k + f\kappa_k) \right|^2 \quad . \tag{3.18}$$

which is evaluated for the best-fit solution (Shearer, 1999, p. 84–89). To measure the associated uncertainty of the solution, the χ^2 error criterion is then:

$$\chi_k^2 = \frac{1}{\sigma_k^2} \sum_{i=1}^{N} \left| \tilde{A}_{i12} - (\gamma_k + f\kappa_k) \right|^2 \quad . \tag{3.19}$$

To determine the confidence interval, we need to find the contour in χ_k^2 (γ_k, κ_k) corresponding to 95% percentage points of the distribution (that is, 5% probability of random error). Figure 3.13 shows such 95% and 70% contours for layer 2.

Unfortunately, the above assumption of statistically independent data made for calculating n_{df} does not hold for the first-arrival, filtered-amplitude data. For example, Figure 3.10 shows that the data points belonging to the same shot follow smooth curves with varying frequencies, and consequently they are correlated. Therefore, the true number of degrees of freedom in the data is much smaller than n_{df} above. This bias results in unrealistically small χ^2 error ellipses (dashed contours in Figure 3.13).

To produce a more consistent error estimate, I utilized the statistical distributions of data misfits in equation (3.1). By using empirical probability functions for the high- and low-

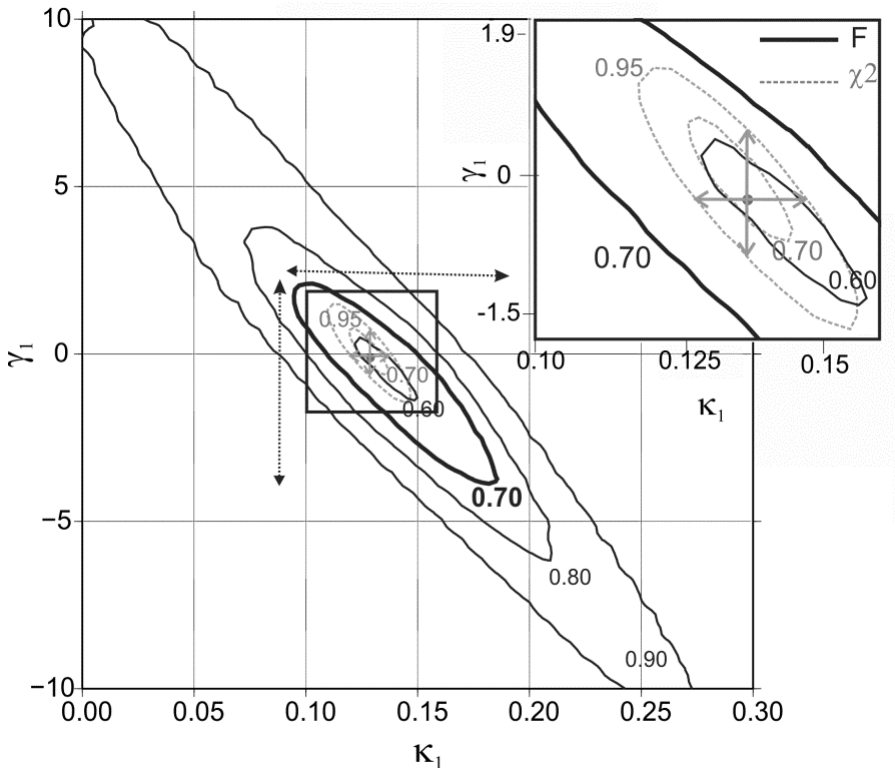

Figure 3.13: Error analysis for the result of model layer 2: dashed contours show confidence levels of 70% and 95% using the χ^2 method. Contours of function F (equation 3.2) are shown in black, labeled with the corresponding levels of F_{H} and F_{L}. Inset shows a zoom–in in the area of optimal solution. Bold contour is the selected 70% confidence level. Gray and black dashed arrows show two ways of calculating error bars in Figure 3.11.

frequency halves of the dataset, F_H and F_L defined in equation (3.16), I further defined F_1 as the probability of *at least one* of these points being located below the fitting line:

$$F_1 = 1-(1-F_L)(1-F_H) = F_L + F_H - F_L F_H \ . \tag{3.20}$$

Therefore, $1 - F_1$ is the probability that both amplitudes drawn from the low- and high-frequency parts of the distribution are above the fitting line. In another statistical test, let us draw two more random data points and define F_2 as the probability of at least one of these points being *above* the fitting line:

$$F_2 = 1-F_L F_H \ . \tag{3.21}$$

With such definition, $1 - F_2$ equals the probability for both of these points being below the fitting line. Finally, the following combination of F_1 and F_2:

$$F = F_1 + F_2 - F_1F_2 \tag{3.22}$$

will have the meaning of probability for both of these pairs of points straddling the fitting line. For the solution for model layer 2, this function is contoured in Figure 3.13.

Because the values of F_L and F_H equal 0.5 for the optimal solution (Figure 3.13; equation 3.16), the range of variation of F is from approximately 0.93 to 1.0. In order to interpret the values of F, let us choose a certainty level of 70% for both F_H and F_L, i.e., take $F_L = F_H = 0.7$. In the amplitude-frequency plots (Figure 3.10), this level corresponds to no more than 70% of the data points being located on one side of the fitting line. For such levels of F_H and F_L, the value of F is approximately 0.95. Thus, I used this level as a measure of 70% certainty for selecting the γ_1 and κ_1 values (bold line in Figure 3.13).

In order to characterize the trade-off between parameters γ_1 and κ_1 (Figure 3.11a and c), two types of error bars were obtained from the contoured function F. For one of these parameters, the first error estimate (larger; gray dashed lines in these Figures) is the maximum range of the 70% contour irrespective of the other parameter. The second estimate (smaller, shown by black lines in Figure 3.13) is the error measured for the other parameter being fixed at its optimal value.

3.3.4 Amplitude-decay model

By using equations (3.5) and (3.9), the layered velocity and attenuation model derived from the first-arrival inversion (Figure 3.11; Table 3.2) becomes able to predict the travel times and frequency-dependent amplitudes for any shot in the study area. I tested this model on several

VSP shot records by predicting the amplitudes of first arrivals at 0-, 100- and 40-Hz frequencies (Figure 3.14). Note that (somewhat counter-intuitively with respect to the ray theory), pure "geometric spreading" γ corresponds to the zero-frequency limit of $\chi(f)$.

Interestingly, the amplitudes observed from the 400-m offset shot B (Figure 3.14) support my estimation of low attenuation anisotropy for the uppermost layer, which was set equal zero because of poor resolution of these parameters (Figure 3.11; Table 3.2). The amplitudes are nearly flat at depth s above 400 m, with a suggestion of a decrease toward the surface (Figure 3.14, lower-right panel). The modeled curve (gray line) also suggests an amplitude peak near 400-m depth, due to increased negative γ_3 at this depth (Figure 3.11b). At zero frequency, this effect is stronger and extends to 400–500-m depth range (black line in Figure 3.14, lower-right).

The low- and high-frequency curves in Figure 3.14 show the range of amplitude-decay variations with frequency. As expected, the lowest attenuation is observed at zero frequency, and the amplitude decay rate increases with frequency. For the dominant frequency of the record (40 Hz), the first-arrival amplitude is predicted correctly. Within the definition of our six-layer structure, this model accurately predicts the amplitudes and attenuation properties of direct waves traveling at any angles, and therefore it should be useful for true-amplitude studies. Computationally, this model (Figure 3.14) is still relatively simple, and it offers a definite advantage of empirical accuracy and agreement with the first arrivals within the entire frequency band. In addition, it incorporates the general properties of scattering and attenuation within the structure, including their VTI anisotropy. This model can also be readily extended to 2-D and 3-D structures and other types of anisotropy.

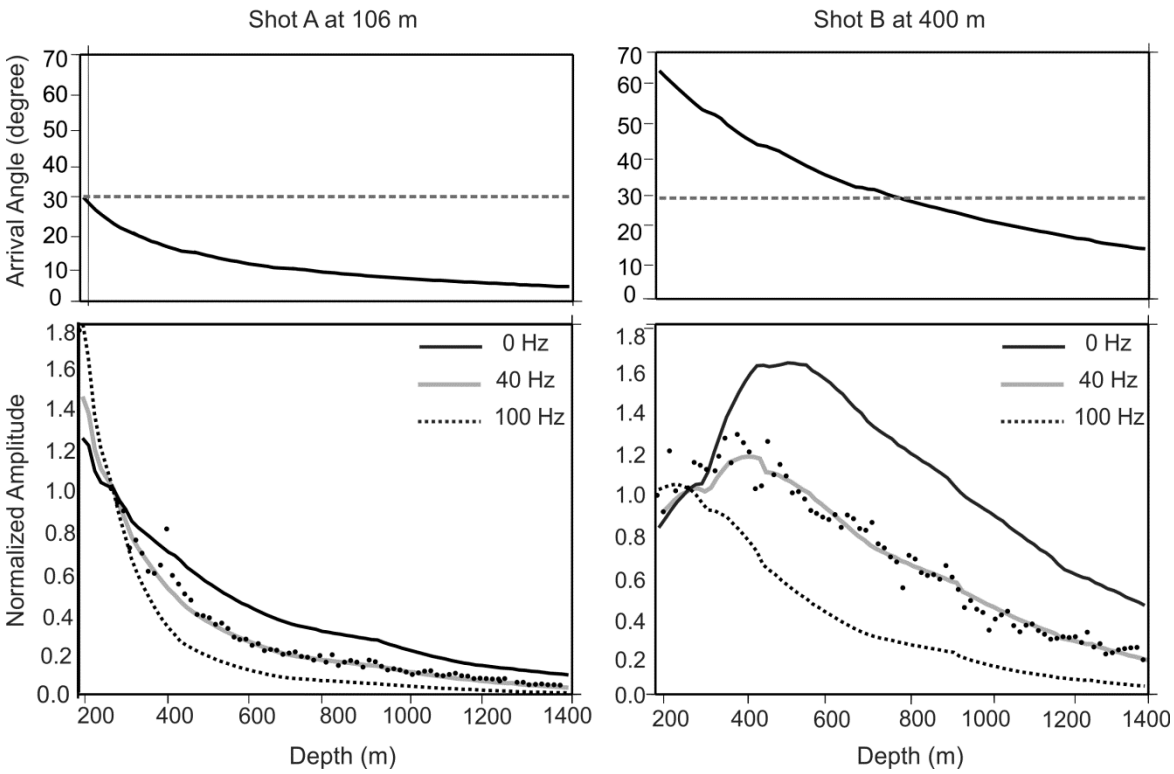

Figure 3.14: Combined geometric spreading/scattering and frequency-dependent attenuation predicted by the model (Figure 3.11 and Table 3.2) for shots A and B indicated in Figure 3.1. Upper panels show the angles of incidence on the VSP spread. For reference, dotted lines indicate the angle of 30° commonly used in AVO analysis. Lower panels show the amplitudes predicted at frequencies 0, 100 and 40 Hz (lines) and observed in the data (black dots). All amplitudes are normalized to equal one at 260-m depth. Black dots indicate the first-arrival amplitudes from a shot at 106-m offset from the borehole. Note how the change of the sign of γ near 930-m depth affects the shape of the zero-frequency amplitudes from shot A (black line). Also note the reversal of the amplitude trend at zero frequency and 40 Hz at shallow depths for shot B.

CHAPTER 4: SEPARATION OF GEOMETRIC SPREADING, SCATTERING AND INTRINSIC ATTENUATION EFFECTS IN WEYBURN VSP

In Chapter 3, I derived an amplitude-spreading model from the spectra of first arrivals of 3-D VSP data in Weyburn oilfield. This model includes combined variations of geometric spreading, intrinsic attenuation, and small-scale scattering parameters. Three key questions should be addressed in interpreting this model: 1) how to describe the contribution of spectral fluctuations in the ”scattering attenuation”, 2) how to characterize the ”random” and ”non-random” parts of scattering for a specific zone of interest, and 3) how to separate the effects of intrinsic attenuation, scattering on small-scale layering, and the variations of geometric spreading?

In this Chapter, I address the above questions by modeling the geometric spreading, scattering, statistical fluctuations, and effects of intrinsic attenuation on body seismic waves propagating through a layered reflection sequence. This numerical model is formulated to study the normal and oblique-incidence P and S waves in a finely layered medium. This model includes forward scattering (transmission), back scattering (reflectivity) and multiples, which predict the transmitted P and S energy-flux spectra. In combination with the geometric spreading, scattering and frequency-dependent attenuation parameters measured in the preceding Chapter, this model completes my geologic model of Weyburn oilfield.

This Chapter is based on the following paper:

Baharvand Ahmadi A*., and I. Morozov, 2014b, Separation of geometric spreading, scattering and intrinsic attenuation effects in a VSP: Canadian Journal of Exploration Geophysics, 38, 1, P21-29.*

 This paper was modified, expanded and reformatted for inclusion in this Dissertation. Figures were re-plotted and modified in order to meet the requirement of the University of Saskatchewan. The contribution by my supervisor (Professor Igor Morozov) consisted in setting the problem, general guidance and advice, many discussions of the results and supervise development of the work. Earlier results of this study were also published in Baharvand Ahmadi and Morozov (2012, 2013b, and 2014a).

In addition, the classification of *Q* types and the theory of fluctuation *Q* in this Chapter is based on the following paper:

Morozov, I., and ***A. Baharvand Ahmadi****, 2015, Taxonomy of Q: Geophysics, 80, no. 1, T41–T49.*

 My contribution to this paper consisted in developing the examples of scattering of transmitted waves and analysis of VSP data (sections of ‘properties and types of *Q*’, and ‘Scattering *Q*’). This part of the paper was directly related to the research of this Dissertation. I estimate my contribution to this paper as 30%.

4.1 Descriptions of seismic scattering

The process of energy dissipation within a seismic wave is time- (space-) and frequency-dependent. Physically, energy dissipation is caused by a combination of three factors: (1) local

variations of geometric spreading (focusing and defocusing of wavefronts), (2) scattering (such as transmission losses and reflectivity), and (3) internal friction within the material, usually described by its intrinsic *Q*. Separation of these three factors is important for the analysis of physical properties of the reservoir and its surroundings. Scattering represents the elastic part of attenuation, which means that it reduces the recorded amplitudes of seismic arrivals and makes the waveforms dispersive while keeping the total energy of the wavefield constant (Shearer, 1999). By isolating the effects of scattering, small-scale layering can be quantitatively characterized, which is important for stratigraphic interpretation. The geometric spreading similarly preserves the total energy, but in addition to this, the energy is associated with a continuously spreading geometrical wavefront. This effect needs to be removed when estimating the petrophysical parameters, and it also needs to be carefully corrected for during AVO analysis. Finally, the intrinsic attenuation is a most valuable indicator of the physical state of the rock.

Many studies have attempted separating the scattering and intrinsic attenuation by using different theoretical approaches, models, and types of waves. Aki (1980) measured the amplitudes of body S and coda waves within different frequency bands to test whether the attenuation of S waves was caused by the loss of energy by scattering due to small-scale heterogeneities. Using a model consisting of small and randomly distributed spheres, Dainty (1981) modeled S-waves within the lithosphere. Frankel and Wennerberg (1987) introduced an energy-flux model of seismic coda based on the balance between the energy scattered from the direct wave and the energy contained in the seismic coda. This model led to a simple formula for the amplitude and time decay of the seismic coda, which allowed differentiation between the scattering and intrinsic attenuation of the medium. Wu and Aki (1988) applied the radiative

transfer theory to determining the relative contributions of scattering and intrinsic absorption to total attenuation. Modeling of seismic-wave scattering was also used in many studies, such as seismic coda measurements by Mayeda et al. (1991), theoretical studies of seismic wave propagation in random heterogeneous media (Sato and Fehler, 1998), wavefield modeling using matrix propagator methods (Stovas and Ursin, 2007), and separation of scattering from intrinsic attenuation in the near surface (Mangriotis et al, 2013). In all of these approaches, both the intrinsic and scattering effects were represented by the corresponding intrinsic and scattering *Q*-factors of the medium. However, all of these approaches also rely in simplified models for geometric spreading (such as $1/r$ for body waves), which may be inaccurate in most practical cases (Morozov, 2008, 2010).

In Chapter 3, I utilized an extension of the *Q*-based paradigm and performed modeling of seismic amplitude decays by treating the geometric-spreading, "intrinsic *Q*," and scattering parameters jointly (Morozov, 2008, 2010a). Forward modeling of the amplitudes was performed by using minimal assumptions, and in particular, without assuming any accurately known geometrical spreading model or a frequency-independent *Q*. The observed wave amplitude *u* was written as (equation 3.3):

$$u(f,\Pi) = A_R(f)A_S(f)G_0(\Pi)\exp[-\chi^*(f,t)], \tag{4.1}$$

where A_S and A_R are the source and receiver factors, $G_0(\Pi)$ is some "background" geometric spreading (some theoretical approximation for a known structure), t is the travel time, and the logarithmic perturbation of the amplitude χ^* is accumulated along the ray:

$$\chi^*(f,t) = \int_{Ray} \chi(f,t')\,dt'. \tag{4.2}$$

In this expression, χ is the usual (temporal) differential attenuation coefficient, which is generally frequency dependent. For the frequency band typically used in seismic observations (from about 0.002 to 100 Hz), this attenuation coefficient can be written as (Morozov, 2010b):

$$\chi(f) = \gamma + \kappa f \ , \tag{4.3}$$

where γ is the limit of χ at $f \to 0$. Parameters χ and γ in this equation are measured in frequency units, whereas κ is dimensionless and can be transformed into an "effective" Q_e of the medium by: $\kappa = \pi / Q_e$ (Morozov, 2008). This quantity is empirical and includes the internal friction (energy dissipation into heat) and frequency-dependent part of scattering (as in the conventional interpretations of Q). In some cases, χ also contains the frequency-dependent part of the geometric spreading (Yang, 2007). Parameter γ contains the cumulative effects of geometric spreading (relative to the background model G_0) and/or scattering. Within the scattering part of γ, several contributions can further be recognized: 1) back-scattering (predominantly backward-directed reflectivity in a layered structure) and 2) forward scattering (transmission). As shown in Chapter 3, anisotropic values can be measured for γ and κ in a layered model by inverting the spectra of downgoing direct arrivals in a VSP survey.

An intriguing question is whether the three key contributions to wave attenuation (variations of geometric spreading, scattering, and internal friction) can be separated in the observed γ and κ. Separation of the "intrinsic" and "scattering" quality factors is often performed in earthquake coda studies (e.g., Wu, 1985), where it is based on correcting for the geometric-spreading effects predicted by modeling. In exploration environments (and in fact, in coda studies as well; see Morozov, 2010a), geometric spreading can be difficult to model and/or constrain from the data with sufficient accuracy. At the same time, scattering on fine-scale

layering can be studied effectively by using real well-log information. Such scattering contributes to both γ and κ, and consequently, models of scattering could help of the three physical attenuation effects.

Modeling of scattered wavefield conducted below suggests that two types of processes can be differentiated within the "scattering attenuation". The first type represents scattering on random, small-scale layering, which is often associated with the scattering *Q* (Aki, 1980). This small-scale heterogeneity is presumed to be randomly distributed, and therefore statistical properties of random scattered waves are related to the statistical properties of this heterogeneity (Matsushima, 2012). At larger scales, the heterogeneities cause fluctuations of the transmitted and reflected seismic waves, which I hereafter call "fluctuation attenuation" or "fluctuation *Q*". If the scales of heterogeneity are comparable to the seismic wavelengths, complicated waveforms often appear. These fluctuations manifest themselves in amplitude and travel time fluctuations of direct or reflected waves. Quantifying these fluctuations can be useful in an investigation of the localized stratigraphy of layering.

In this Chapter, I attempt to separate the effects of geometrical spreading, small-scale random scattering, fluctuations, and intrinsic attenuation in the anisotropic attenuation χ derived from direct-wave VSP records in Chapter 3. Using well logs collected in the study area, I derive models of oblique-angle P- and S- wave scattering by numerical and analytical methods. The effects of fluctuations are derived by characterizing the "random" and "non-random" parts of the scattered-wave spectra. Finally, the modeled effects of scattering and fluctuations yield constraints on the intrinsic-attenuation and geometric-spreading effects.

4.2 Data and method

In Chapter 3, first arrival waveforms from 35 80-level VSP shots acquired in 1999 as part of the Weyburn-Midale CO_2 Monitoring and Storage Project were used for inverting for the layered attenuation model. Table 4.1 shows parameters of this model including the inverted values of γ and κ in equation (4.3), which are denoted γ_1 and κ_1 for vertical propagation. These values contain contributions from scattering on small-scale layering, which are modeled by using well-log data. A set of P- and S-wave velocity and density logs acquired in a borehole in the VSP area are used for this modeling. The logs are sampled at 10-cm intervals in the range of depths from ~150 m to ~1390 m.

4.3 Numerical model of P and S-wave scattering

In order to correctly model wave scattering, one must consider the combined effects of forward scattering (transmission), back-scattering (reflectivity) and all multiples in the wavefield. This can be achieved by utilizing the propagator method, which was used by Richards

Table 4.1: Layered Attenuation model for a VSP from Chapter 3*

Layer	Depth to bottom (m)	Velocity (m/s)	γ_1 (s^{-1})	κ_1	$Q_e=\pi/\kappa$
1	295	2185	-2	0.12	26
2	431	2230	-0.35	0.135	23
3	690	2330	1.23	0.0473	66
4	918	2405	-0.24	0.0163	192
5	1162	2970	3.92	0.0255	123
6	1390	3834	2.76	0.1437	22

*) γ_1 and κ_1 are attenuation parameters in equation (4.1) for vertical rays.

and Menke (1983) and Morozov (2011) to study the scattering of a P wave at normal incidence. The propagator method is briefly summarized below, where I also extend it to oblique incidence and P- and S-wave conversions.

Consider two layers having a common horizontal welded boundary, and represent the combination of plane P- and SV-waves in each layer number l =1,2 by vector $\mathbf{v}_l \equiv \left(u_{p+}^{\ l} \quad u_{s+}^{\ l} \quad u_{p-}^{\ l} \quad u_{s-}^{\ l}\right)^T$, where u_P and u_S denote the wave amplitudes, and subscripts '+' and '-' denote the waves traveling downward and upward, respectively (Figure 4.1). For any layer l, we can express the two components of displacement and traction on the boundary as (Aki and Richards, 2002):

$$\begin{pmatrix} u_x \\ u_z \\ \sigma_{xx} \\ \sigma_{xz} \end{pmatrix} = \mathbf{N}_l \mathbf{v}_l , \tag{4.4}$$

where the matrix $\mathbf{N}_l$ is:

$$\mathbf{N}_l = \begin{pmatrix} \sin i_l & \cos j_l & \sin i_l & \cos j_l \\ \cos i_l & -\sin j_l & -\cos i_l & \sin j_l \\ 2\rho_l\beta_l^{\,2} p \cos i_l & \rho_l\beta_l(1-2\beta_l^{\,2}p^2) & -2\rho_l\beta_l^{\,2} p \cos i_l & -\rho_l\beta_l(1-2\beta_l^{\,2}p^2) \\ \rho_l\alpha_l(1-2\beta_l^{\,2}p^2) & -2\rho_l\beta_l^{\,2} p \cos j_l & \rho_l\alpha_l(1-2\beta_l^{\,2}p^2) & -2\rho_l\beta_l^{\,2} p \cos j_l \end{pmatrix}, \tag{4.5}$$

where i and j are P and S wave incidence angles measured from the vertical direction, α and β are velocities of P and S waves, ρ is density, and p is the horizontal slowness of the wave.

The continuity of displacement and traction relate the amplitudes within the two layers as:

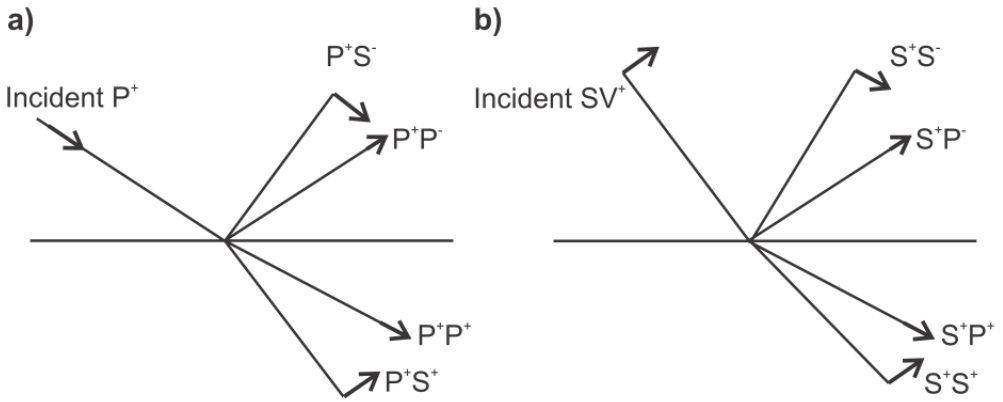

Figure 4.1: One-dimensional scattering model on a single boundary: a) Incident P wave, b) Incident SV wave. Arrows indicate the convention for positive amplitudes u_p and u_s. Subscripts '+' and '-'denote the waves traveling downward and upward, respectively.

$$\mathbf{N}_2\mathbf{v}_2 = \mathbf{N}_1\mathbf{v}_1, \tag{4.6}$$

and consequently the transmission matrix relating the amplitudes $\mathbf{v}_2$ to $\mathbf{v}_1$ equals:

$$\mathbf{T}_{2,1} = \mathbf{N}_2^{-1}\mathbf{N}_1. \tag{4.7}$$

For *n* layers (Figure 4.2), a similar relation is obtained by applying relation (4.7) recursively:

$$\mathbf{v}_n = \mathbf{T}_{n,1}\mathbf{v}_1 \ , \tag{4.8}$$

where:

$$\mathbf{T}_{n,1} = \prod_{l=2}^{n} \mathbf{T}_{l,l-1} \begin{pmatrix} e^{i\Delta\varphi_{lP}} & 0 & 0 & 0 \\ 0 & e^{i\Delta\varphi_{lS}} & 0 & 0 \\ 0 & 0 & e^{-i\Delta\varphi_{lP}} & 0 \\ 0 & 0 & 0 & e^{-i\Delta\varphi_{lS}} \end{pmatrix}, \tag{4.9}$$

and $\Delta\varphi_{l_p}$ and $\Delta\varphi_{lS}$ are the phase shifts of the downward-traveling P- and S waves across layer *l*. By recursively evaluating expressions (4.8), one can construct "well-logs" of transmission matrices **T**.

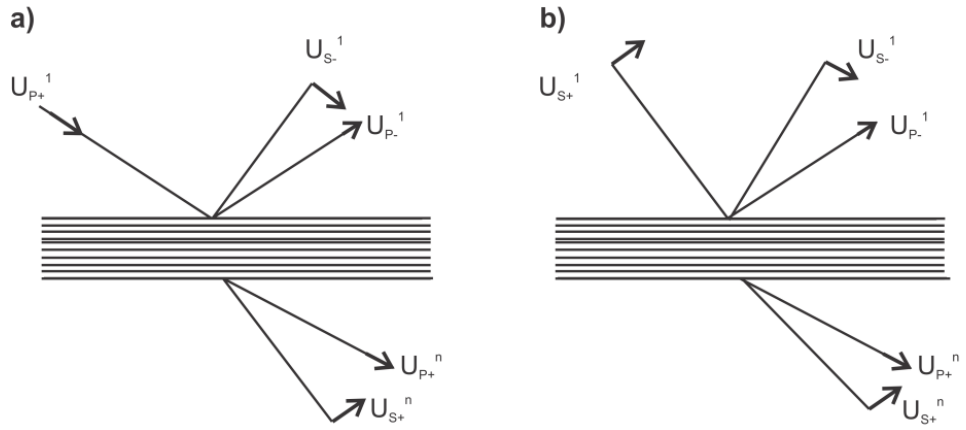

Figure 4.2: One-dimensional scattering model on a sequence of *N*-1 boundaries, a) incident P wave, b) incident SV wave.

In order to evaluate the net transmission and reflection responses for a stack of *n* layers, it is convenient to express the relation (4.8) in the form of block matrices corresponding to downward- and upward-propagating P and S waves:

$$\begin{pmatrix} \mathbf{v}_{n+} \\ \mathbf{v}_{n-} \end{pmatrix} = \begin{pmatrix} \mathbf{T}^{++} & \mathbf{T}^{+-} \\ \mathbf{T}^{-+} & \mathbf{T}^{--} \end{pmatrix} \begin{pmatrix} \mathbf{v}_{1+} \\ \mathbf{v}_{1-} \end{pmatrix}, \tag{4.10}$$

where the subscripts '^{n,1}' in $\mathbf{T}$ are dropped for brevity. The upward-propagating field below the stack of layers must equal zero (Figure 4.2): $\mathbf{v}_{n-} = 0$, and the transmitted and reflected field can be expressed through the downgoing incident field ($\mathbf{v}_{1+}$), the transmission matrix $\tilde{\mathbf{T}}$ and reflection matrix $\tilde{\mathbf{R}}$, respectively: $\mathbf{v}_{n+} = \tilde{\mathbf{T}}\mathbf{v}_{1+}$ and $\mathbf{v}_{1-} = \tilde{\mathbf{R}}\mathbf{v}_{1+}$. Consequently, from equation (4.10), the matrices describing the total P- and S- wave reflection, transmission, and all mode conversions equal:

$$\tilde{\mathbf{R}} = -\left(\mathbf{T}^{--}\right)^{-1}\mathbf{T}^{-+}, \text{ and } \tilde{\mathbf{T}} = \mathbf{T}^{++} + \mathbf{T}^{+-}\tilde{\mathbf{R}}. \tag{4.11}$$

In the following analysis, I consider a P- or S-wave of unit amplitude incident from the top of the

stack of layers, which is given by $\mathbf{v}_{1+} \equiv \begin{pmatrix} 1 & 0 \end{pmatrix}^T$ or $\mathbf{v}_{1+} \equiv \begin{pmatrix} 0 & 1 \end{pmatrix}^T$, respectively. For such an incident wave, the resulting amplitudes and phases of the transmitted P- and S-wave fields equal:

$$\begin{pmatrix} u_{p+}^n \\ u_{s+}^n \end{pmatrix} \equiv \mathbf{v}_{n+} = \tilde{\mathbf{T}}\mathbf{v}_{1+} . \tag{4.12}$$

By using these amplitudes, the upward- and downward- directed energy fluxes can be calculated at any angular frequency of the wave ω:

$$E_{\text{flux-P+}}^n = \frac{\omega}{2}\alpha_n \rho_n \left(u_{p+}^n\right)^2 \cos i_n \text{, and } E_{\text{flux-S+}}^n = \frac{\omega}{2}\beta_n \rho_n \left(u_{s+}^n\right)^2 \cos j_n \ . \tag{4.13}$$

These are the final quantities used in subsequent numerical modeling.

In modeling and data analysis, the frequency bands are selected by using the power spectra of the first arrivals in several VSP shots. For each depth interval, the highest used frequency was where the noise amplitude is half of the signal. These upper-band frequencies start from 150 Hz for the uppermost layer and decrease to 100 Hz for layer 6 (~1160–1390 m) (Table 4.1). The ray parameter, *p*, (the horizontal component of the wave slowness) varied from zero to $1.8 \cdot 10^{-4}$ s/m, which corresponded to incidence angles from zero to about 35°. The reflection coefficient across the different depth intervals (equation (4.10)) generally increases with frequency, with some fluctuations present (Figure 4.3).

The resulting energy-flux spectra computed across each of the six layer of our model are shown in Figure 4.4 (for P waves) and Figure 4.5 (S waves). Figure 4.4 shows strong fluctuations in the transmitted P-wave energy flux within different depth intervals. The weakest fluctuations are observed within layer 4 (approximately 690–918 m), whereas layer 6 (approximately1160–1390-m depths) shows the strongest fluctuations. This can be explained by the relatively

smoothly increasing reflection coefficient spectrum within layer 4 compared to highly variable variations in layer 6 (Figure 4.3). The scattering model predicts similar results for different incidence angles. Therefore, it appears that an increase in the angle of incidence from zero to about 30° causes no considerable systematic effect on the transmitted P-wave energy flux.

The transmitted S-wave energy fluxes across the different depth intervals attenuate almost four times faster than for a P wave, which means that the S-wave amplitude attenuates approximately twice faster than the P wave (Figure 4.5). Since the S-wave velocity is also about two times slower than the P-wave velocity, this observation suggests that the S-wave "scattering Q" is approximately equal that for P waves. The transmitted S-wave energy flux also shows systematic variations with the angle of incidence. It appears that S waves scatter with a similar frequency dependence for different angles, but the scattering attenuation at near-vertical incidence angle is stronger than at oblique angles (Figure 4.5).

4.4 Analysis of scattering using localization theory

O'Doherty and Anstey (1971) suggested a simple relation between the power spectrum of a one-dimensional reflection-coefficient series, R(ω), and the amplitude spectrum of the pulse transmitted through it, E(ω):

$$E(\omega) \propto e^{-R(\omega)t} \ , \tag{4.14}$$

where *t* is the two-way travel time, and multiple scattering is considered. In this study, I use my numerical experiment (equations (4.7)–(4.12)) to differentiate the multiple scattering effects of thin layers from the intrinsic attenuation. Shapiro et al. (1993, 1994) extended relation (4.14) to the angle-dependent fluctuations of plane-wave transmissivity of an acoustic (pressure) wave in a

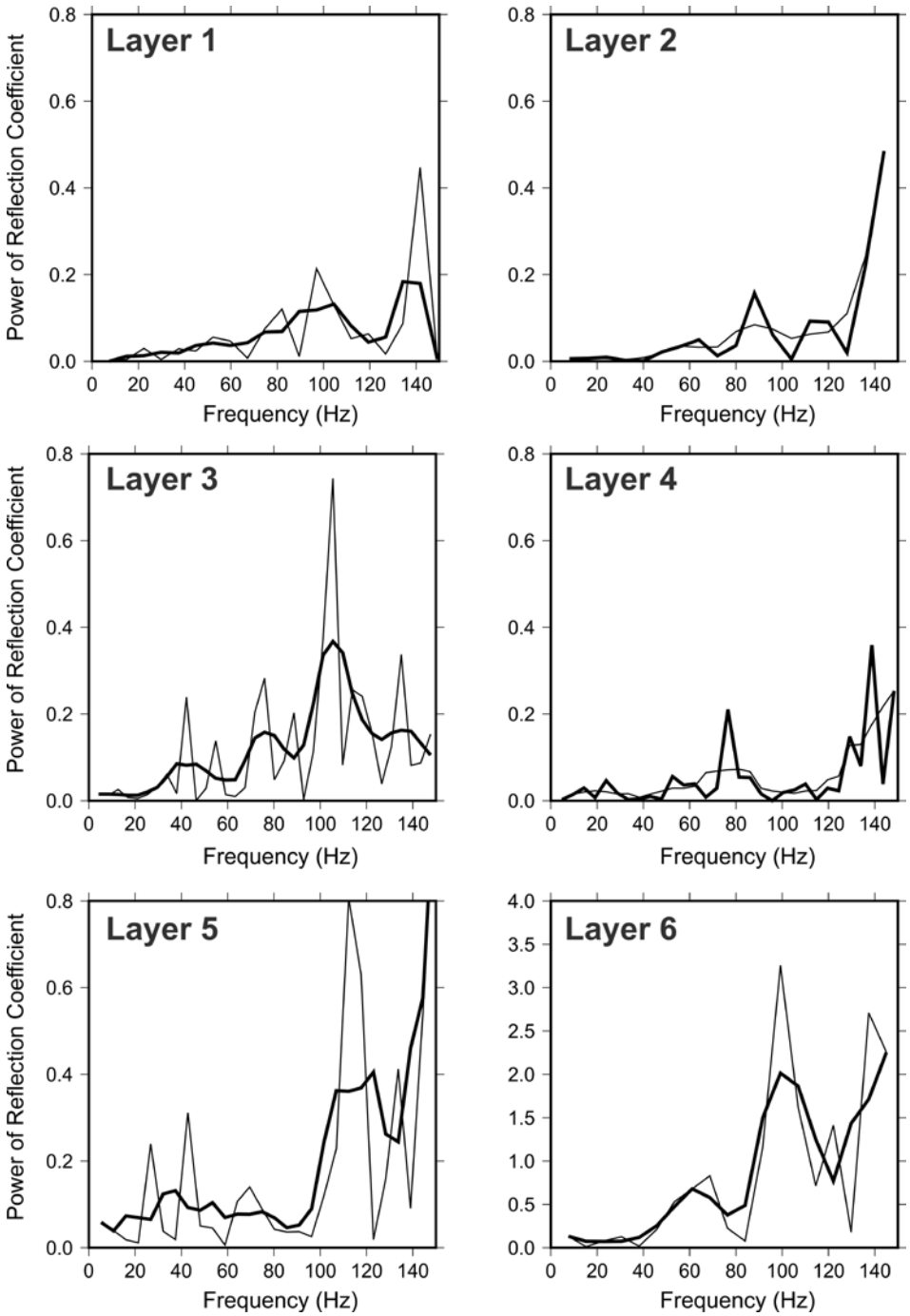

Figure 4.3: Reflection coefficient power spectra (thin lines) for different depth intervals. Thick black lines show the smoothed power spectra. Note the strong fluctuations within layer 6.

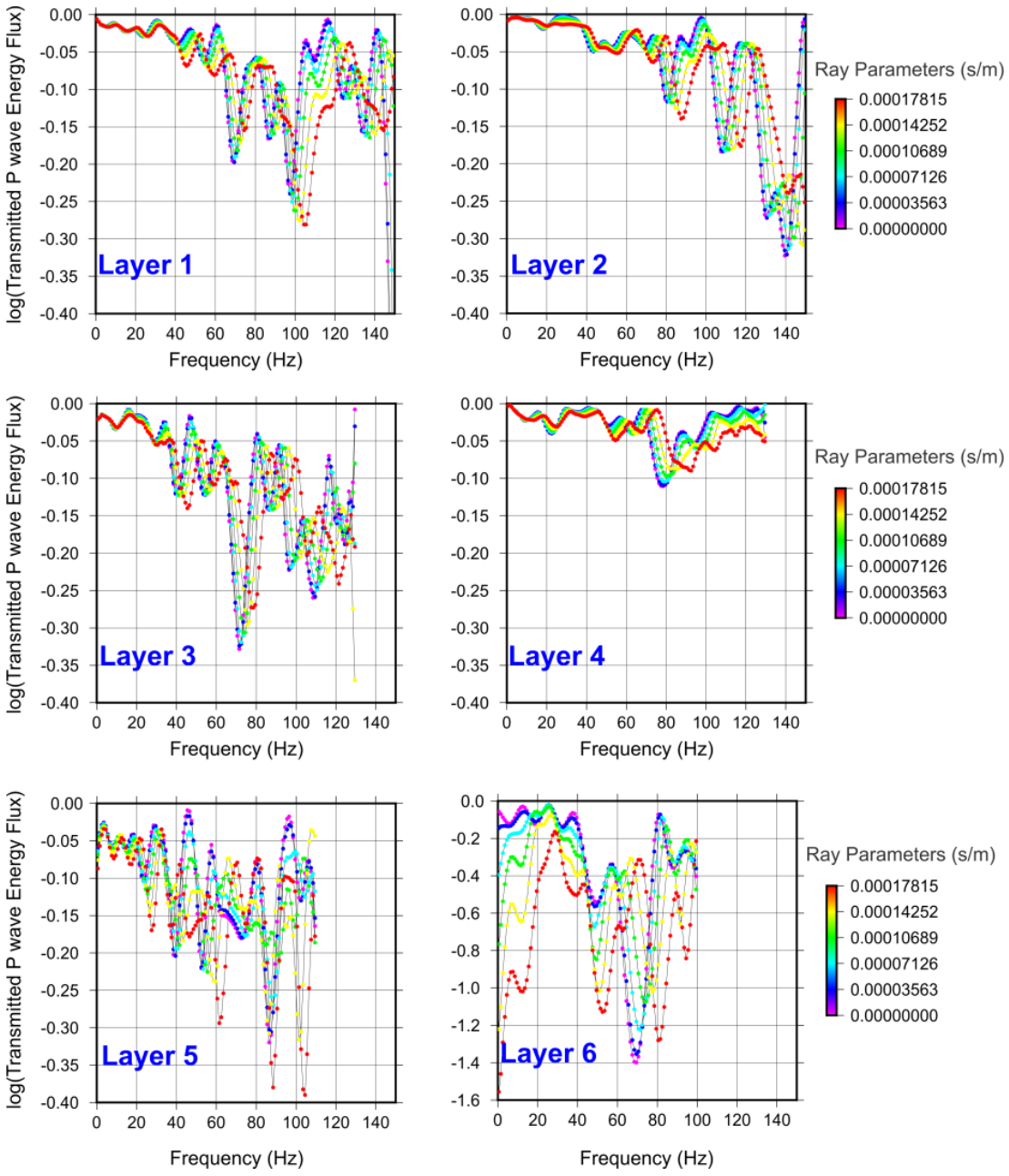

Figure 4.4: Transmitted P-wave energy flux across the different layers of the model. Colours correspond to different incidence angles relative to the vertical direction. Note that the scattering attenuation in layer 6 is almost 4 times higher than in the other layers.

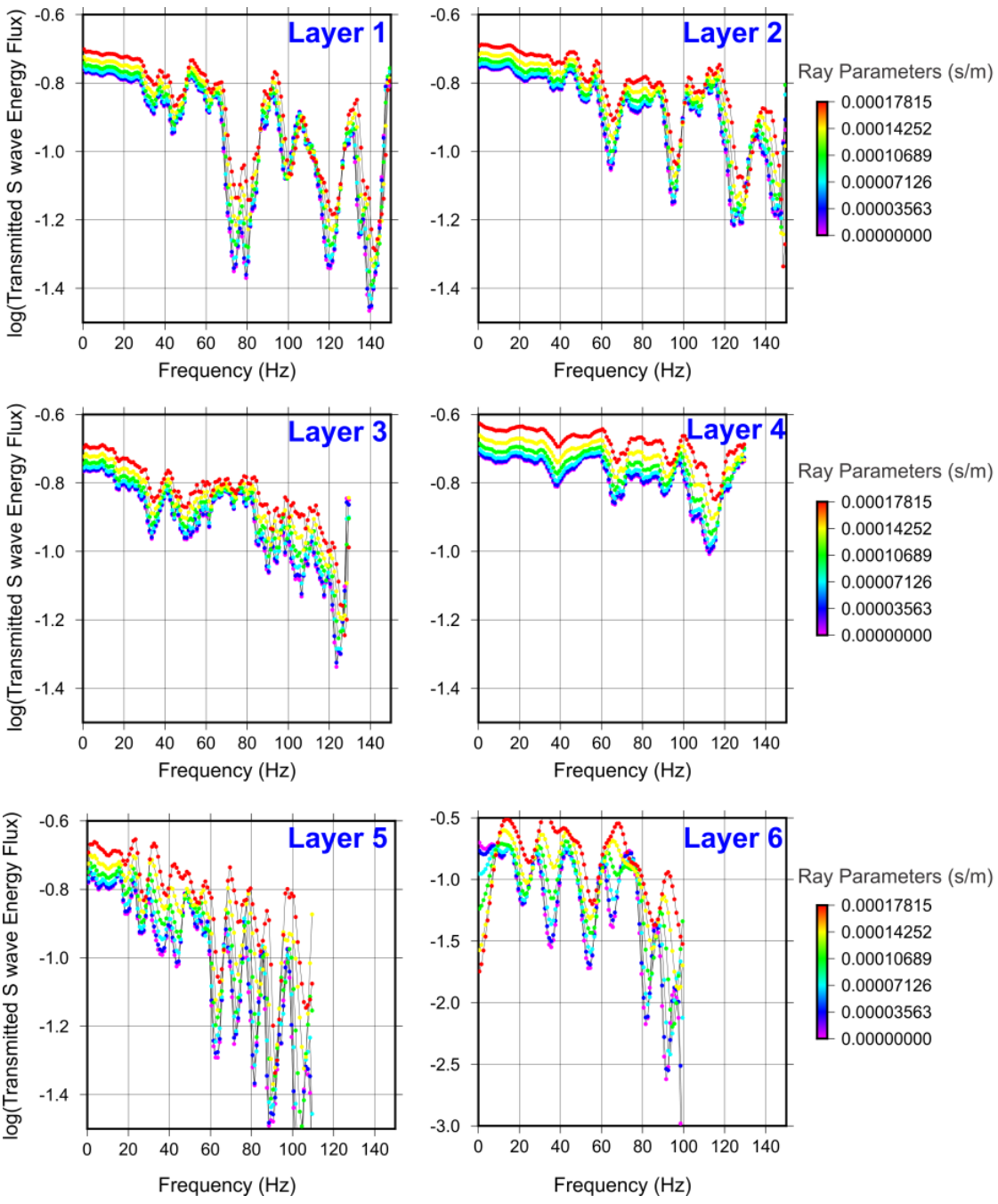

Figure 4.5: Transmitted S-wave energy flux across different layers of the model in Chapter 3. Colours show different incidence angles relative to the vertical direction.

random, finely layered, medium with variable velocity and density. Here, I refer to this approach the localization theory for fluctuations. These authors assumed that the variations of the velocity and density with depth represent realizations of a stationary random process. The fluctuations of

both velocity and density were considered as relatively small compared to their mean values, which were also taken constant within the depth interval of interest. Shapiro et al. (1993, 1994) combined the perturbation theory with the localization and self-averaging theory to obtain the amplitude decay and the variations of the phase of the time-harmonic transmissivity. They separated the density (ρ_{true}) and the square of the slowness ($1/c^2_{\text{true}}$) into the corresponding constant mean and dimensionless fluctuating contributions $\mu(z)$ and $\rho(z)$:

$$\frac{1}{c^2_{\text{true}}} = \frac{1}{c^2_0}\left[1+\mu(z)\right] , \tag{4.15}$$

$$\rho_{\text{true}} = \rho_0\left[1+\rho(z)\right]. \tag{4.16}$$

Figure 4.6 shows the velocity fluctuations calculated from equation (4.15) and its spectrum for layer 3 (~430 to 690 m). In the case of large layer thickness (L), the time-harmonic transmissivity p_{true} (ω,φ, x, L, t) of the pressure relates to the pressure $p_{\text{true}}(\omega,\varphi, x, 0, t)$ of the incident wave by:

$$p_{\text{true}}\left(w,\varphi,x,\ L,\ t\right) \ = \ p_{\text{true}}\left(w,\varphi,x,\ 0,\ t\right)\exp\left(i\,\Phi L - \alpha L\right) , \tag{4.17}$$

where φ is the angle of incidence, Φ and α are the angle- and frequency-dependent (vertical) phase increment and attenuation coefficient are given by:

$$\Phi = K + \frac{K}{2}\Sigma - \frac{K^2}{4}\int_0^\infty C(\xi)\sin(2K\xi)d\xi, \ \text{ and} \tag{4.18}$$

$$\alpha = \frac{K^2}{4}\int_0^\infty C(\xi)\cos(2K\xi)d\xi, \tag{4.19}$$

where $K = k\cos\varphi$, and k is the wavenumber: $k \equiv \omega/c_0$. The quantities C and Σ are linear

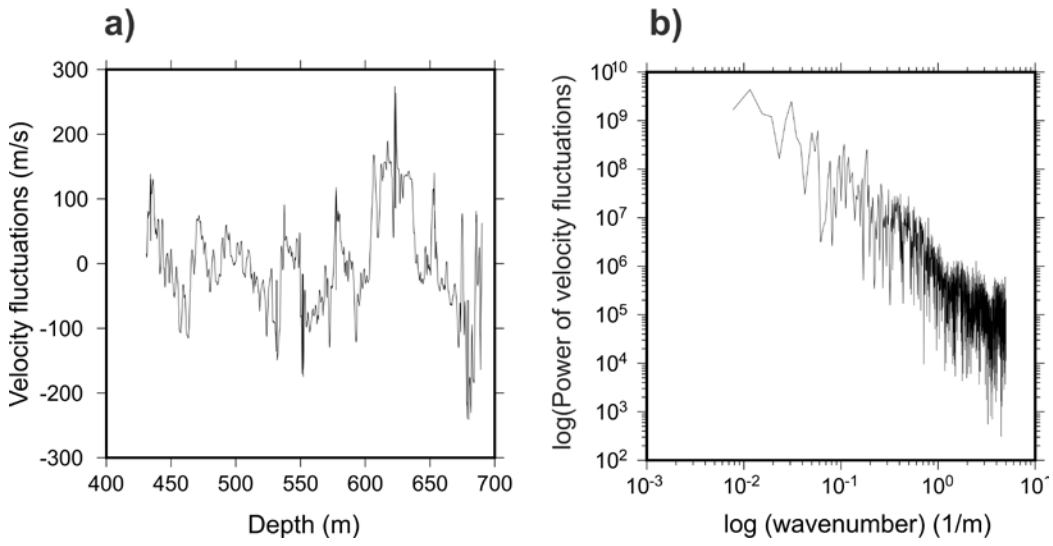

Figure 4.6: a) Relative velocity fluctuation ($\mu(z)$ in equation (4.15)) calculated for layer 3. b) Power spectrum of velocity fluctuations in layer 3 in log-log scale.

combinations of the variances of fluctuations ρ and μ:

$$C = 4C_{\rho\rho} - \frac{4C_{\rho\mu}}{\cos^2\varphi} + \frac{C_{\mu\mu}}{\cos^4\varphi}, \tag{4.20}$$

$$\Sigma = C_{\rho\rho}(0) - \frac{C_{\rho\mu}(0)}{\cos^2\varphi}, \tag{4.21}$$

where $C_{\rho\rho}(\xi) = <\rho(z)\rho(z+\xi)>$, $C_{\rho c}(\xi) = <\rho(z)c(z+\xi)>$, and $C_{cc}(\xi) = <c(z)c(z+\xi)>$ are the cross-correlation functions, and the brackets denote statistical (ensemble) averages.

Similar to the numerical method, I analyzed the transmitted energy flux at the bottom of each of the layers in my VSP depth model (Table 4.1 and Chapter 3) by using equation (4.17) for normal incidence (Figure 4.7). It can be seen that the localization-theory results are in good agreement with the exact numerical computations (Figure 4.7).

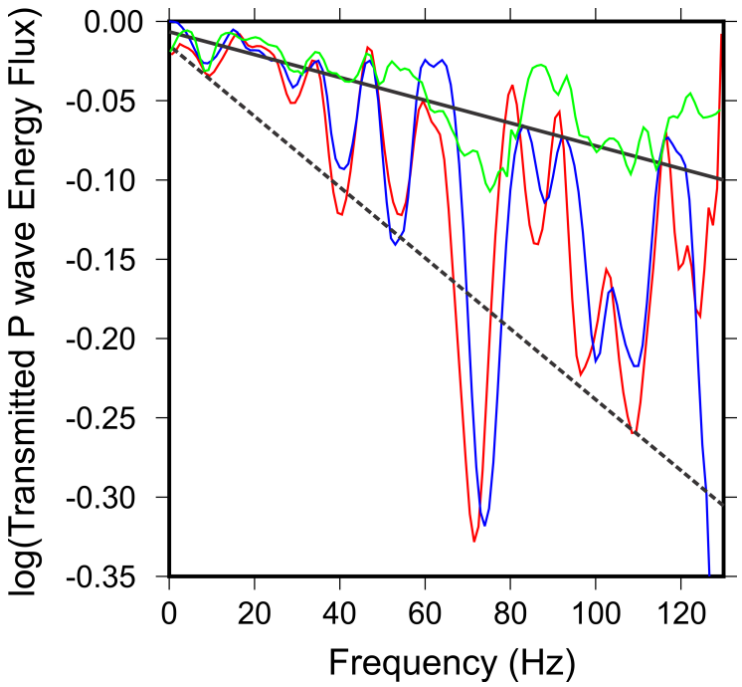

Figure 4.7: Transmitted P-wave energy flux across layer 3 estimated by the numerical method (red) and estimated by using the localization theory (blue). Note the good agreement between the two models. Green line is the average response of 100 permutations of velocity and density logs.

This shows that the observed strong fluctuations in the transmitted-energy flux, and particularly at frequencies above 60 Hz, are due to the autocorrelation of the velocity/density series, i.e. to the locally-predominant layering within the structure.

Although indicating the physical cause of scattering attenuation, the localization theory is limited to the case of thick layers, near uniform background velocities and densities, and small perturbations from this background (Shapiro et al, 1994). In practice, fluctuation variances are sometimes too large for this approximation, such as in layer 6 in our model (Figure 4.3). However, numerical modeling described in the preceding section produces accurate results for all values of parameters of the subsurface.

4.5 Randomization of the well log

Up to this point, I investigated the transmitted energy flux in a layered medium represented by the actual well log. Let us now hypothesize that the spectral amplitude decays observed within the depth ranges of interest (Figure 4.4 and Figure 4.5) contain contributions from two statistical phenomena: 1) random heterogeneity (distribution of densities and seismic velocities), and 2) fluctuations caused by spatial correlations between these random values, as discussed in the preceding section. The first of these contributions would correspond to the traditional "scattering *Q*" (Aki, 1980), whereas the second could perhaps be called "fluctuation *Q*" (Morozov and Baharvand Ahmadi, 2015).

The difference between the two statistical types of scattering defined above can be examined by performing layer permutations within different depth intervals. The permutations destroy the spatial correlations within the log and thereby isolate the "scattering *Q*". While performing the permutations, I keep the reflection-coefficient spectrum matching that of the true well log. This assures preservation of the observed reflectivity spectrum within each depth interval, and therefore the transmission and reflectivity from the randomized medium can be good estimation of the "random-scattering" properties of the medium. I performed 100 random permutations of each layer, after each of which the analysis described above was repeated, and the resulting transmitted P-wave energy flux spectra were averaged. Figure 4.8 shows the transmitted vertical and after such averaging of layer 3 (from approximately 431 to 690 m). A comparison of Figure 4.8 to Figure 4.4 shows that replacing the geologic medium with such an "equivalent" random medium causes a significantly smaller attenuation of the transmitted energy.

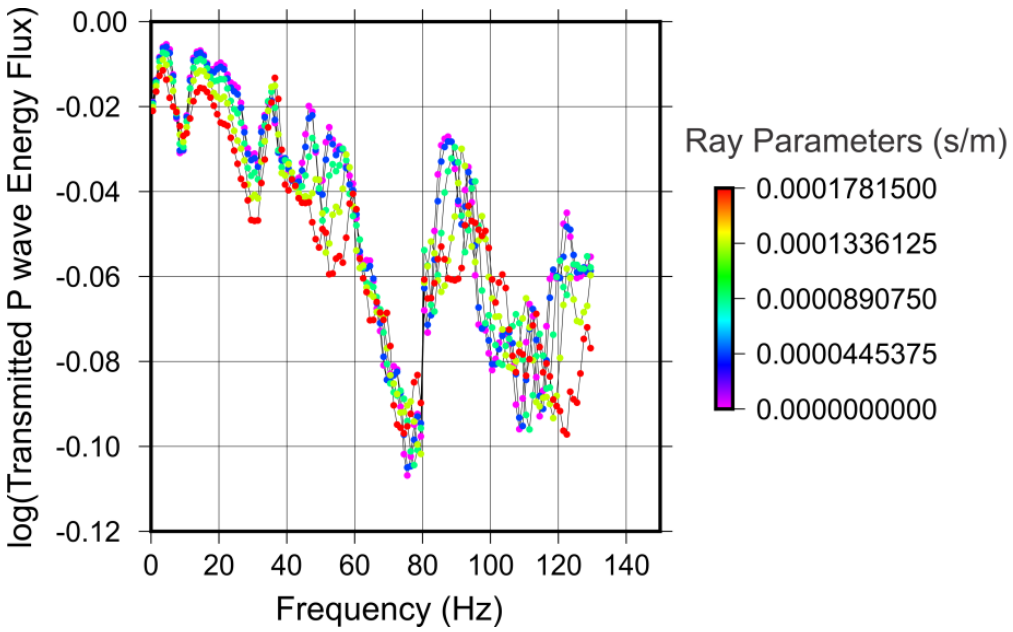

Figure 4.8: Transmitted P-wave energy flux across layer 3 after 100 permutations of velocity and density logs. Colours represent the incidence angles.

4.6 Separation of geometric spreading, scattering, fluctuations, and intrinsic attenuation

As shown in the preceding sections, the attenuation coefficient χ in equation (4.3) can be subdivided into contributions from geometrical spreading, intrinsic attenuation, and elastic scattering, of which the latter also contains statistical fluctuations. Each of these contributions to the attenuation coefficient can also be subdivided into the zero-frequency (γ) and frequency-dependent parts (κf). In cases of practical interest for seismic exploration, the geometric spreading can be taken as frequency-independent and therefore not contributing to κ (Morozov, 2008). Conversely, the intrinsic dissipation within subsurface rocks does not contribute to γ (Morozov, 2008). Scattering and fluctuations contribute to both γ and κ, and consequently by using the models of these effects in the preceding sections. Therefore, in order to separate the

scattering effects from intrinsic attenuation, I can use the above model of wave scattering in a finely layered medium.

The decrease in the transmitted energy flux caused by scattering can be treated similar to the general amplitude-decay equation (4.1). All of the above models of scattering show generally exponential decreases of the energy flux with frequency, which can be described as:

$$E(f) \propto \exp\left[-2\chi_s(f)t\right], \tag{4.22}$$

where, as above, $\chi_s(f)$ is given by:

$$\chi_s(f) = \gamma_s + \kappa_s f, \tag{4.23}$$

and γ_s and κ_s are responsible for the frequency-independent and dependent parts of scattering attenuation.

Both numerical and localization approaches reveal strong fluctuations in the transmitted-energy flux within different depth intervals, and particularly at frequencies above 60 Hz (Figure 4.4, Figure 4.5 and Figure 4.7). The key challenge is how to treat these fluctuations when measuring the average ”scattering attenuation” observed in a particular sequence of reflectors by using equation (4.22). It appears reasonable to subdivide scattering (γ_s and κ_s) into “random-scattering” ($\gamma_{s\text{-random}}$ and $\kappa_{s\text{-random}}$) and “non-random scattering”, or fluctuations ($\gamma_{s\text{-fluctuations}}$ and $\kappa_{s\text{-fluctuations}}$). Randomization of the well log (Figure 4.8) suggests that such differentiation can be achieved by taking the upper envelope of the transmitted energy flux (the envelope corresponding to the weakest scattering) as an estimate for the attenuation caused by random scattering (Figure 4.7). The lower, linear envelope (strongest reflectivity and scattering) might then be a useful characteristic of the fluctuations in the scattered wavefields (Figure 4.7; Morozov and Baharvand Ahmadi, 2015). Therefore, random-scattering attenuation ($\gamma_{s\text{-random}}$ and

$\kappa_{\text{s-random}}$) and fluctuation-attenuation ($\gamma_{\text{s-fluctuations}}$ and $\kappa_{\text{s-fluctuations}}$) can be estimated by fitting straight lines (equation (4.23)) to the upper and lower spectral-power envelopes, respectively (Figure 4.4 and Figure 4.5). Once the "random-scattering" and "fluctuation" attenuations are quantified, the intrinsic and geometric parameters can be extracted from the observed attenuation frequency-dependent coefficient, χ.

4.7 Results

Table 4.2 shows the "vertical" part of the attenuation model in Chapter 3 with geometric spreading, random-scattering, fluctuation, and internal-friction contributions. This is the case where geometric spreading, intrinsic attenuations and only "random" or "fluctuation" part of scattering contribute to the total observed decay of propagating amplitude. I also show the effective quality factors estimated for both random-scattering attenuation ($Q_{\text{s-random}} \equiv \pi/\kappa_{\text{s-random}}$) and internal friction ($Q \equiv \pi/\kappa_{\text{intrinsic}}$) and similar parameters for the fluctuation part of scattering. From Table 4.2, it appears that frequency-independent scattering ($\gamma_{\text{s-random}}$ and $\gamma_{\text{s-fluctuations}}$) is weak ($\gamma_s << 0.3\ \text{s}^{-1}$), but $\gamma_{\text{s-fluctuations}}$ is approximately 3–7 times stronger than $\gamma_{\text{s-random}}$ (Figure 4.9b). The geometric spreading has generally stronger effects than both types of scattering from the surface to the depths of ~1160m: $|\gamma_{\text{s\_random}}| << |\gamma_{\text{s\_fluctuations}}| << |\gamma_{\text{GS}}|$. However, $\gamma_{\text{s-fluctuations}}$ is stronger than the geometric spreading in layer 6 (approximately 1160–1390 m depths). This layer also has the strongest scattering fluctuations when compared to other layers (Figure 4.9a). This is in agreement with high reflection coefficient fluctuations within this depth interval (Figure 4.9e).

Figure 4.9c compares two cases of separation of the intrinsic attenuation and scattering: (1) assuming that scattering is purely random ($\kappa_{\text{intrinsic-random}}$), and (2) assuming that scattering is

entirely due to fluctuations ($\kappa_{\text{intrinsic-fluctuations}}$). In both cases, the attenuation measured in the data is predominantly intrinsic within all depth intervals: $\kappa_{\text{intrinsic}} << \kappa_s$, except within layer 6, in which the fluctuation-attenuation is about 1.3 times stronger than the intrinsic one (Figure 4.9c). In all depth intervals, scattering fluctuation dominates over random scattering, with $\kappa_{\text{s-fluctuations}} \approx (3-7)\kappa_{\text{s-random}}$ (Figure 4.9d).

In summary, the results of this Chapter show that the geometric spreading and internal friction are primarily responsible for the observed amplitude decays above about 1160 m in the area of Weyburn study. However, fluctuation-type scattering is important at depths of ~1160 to ~1390 m, where scattering effects exceed both the geometric spreading and intrinsic attenuation. This trend can also be noticed from the well-log data, in which the reflectivity generally increases with depth and reaches the highest level within this depth interval.

Table 4.2: Resulting separated geometric-spreading, random scattering, fluctuations and intrinsic-attenuation model*

Layer	$\gamma_{s\text{-random}}$	$\gamma_{s\text{-fluctuations}}$	$\kappa_{s\text{-random}}$	$\kappa_{s\text{-fluctuations}}$	$Q_{s\text{-random}}=\pi/\kappa_{s\text{-random}}$	$Q_{se}=\pi/\kappa_{s\text{-fluctuations}}$	$\gamma_{GS\text{-random}}$ (s^{-1})	$\gamma_{GS\text{-fluctuations}}$ (s^{-1})	$\kappa_{intrinsic\text{-random}}$	$\kappa_{intrinsic\text{-fluctuations}}$	$Q_{intrinsic\text{-random}}=\pi/\kappa_{v}$	$Q_{intrinsic\text{-fluctuations}}=\pi/\kappa_{v}$
1	0.06	0.07	0.002	0.013	1570	241	-2.06	-2.07	0.118	0.107	27	29
2	0.05	-0.05	0.002	0.014	1570	224	-0.4	-0.3	0.133	0.121	24	25
3	0.01	0.106	0.003	0.009	1047	349	1.22	1.12	0.0443	0.039	71	82
4	0.06	0.05	0.0003	0.002	10047	1570	-0.3	-0.29	0.016	0.014	196	224
5	0.13	0.26	0.003	0.011	1047	285	3.79	3.66	0.0225	0.014	140	224
6	0.28	1.43	0.02	0.08	157	39	2.48	1.33	0.1237	0.064	25	49

*) $\gamma_{s\text{-}random}$ and $\kappa_{s\text{-}random}$ are the corresponding parameters for random scattering, $\gamma_{GS\text{-random}}$ is the estimated geometric spreading, $\kappa_{intrinsic\text{-random}}$ is the internal friction, $Q_{s\text{-random}}$ and $Q_{intrinsic\text{-random}}$ are the effective quality factors for random scattering and internal friction in the case that *only* random-scattering component contributing to the scattering model. $\gamma_{s\text{–fluctuations}}$, $\kappa_{s\text{-fluctuations}}$, $\gamma_{GS\text{-fluctuations}}$, $\kappa_{intrinsic\text{-fluctuations}}$, $Q_{s\text{-fluctuations}}$ and $Q_{intrinsic\text{-fluctuations}}$ are the corresponding parameters for the fluctuations in the case that *only* fluctuation scattering component contributing to the scattering model.

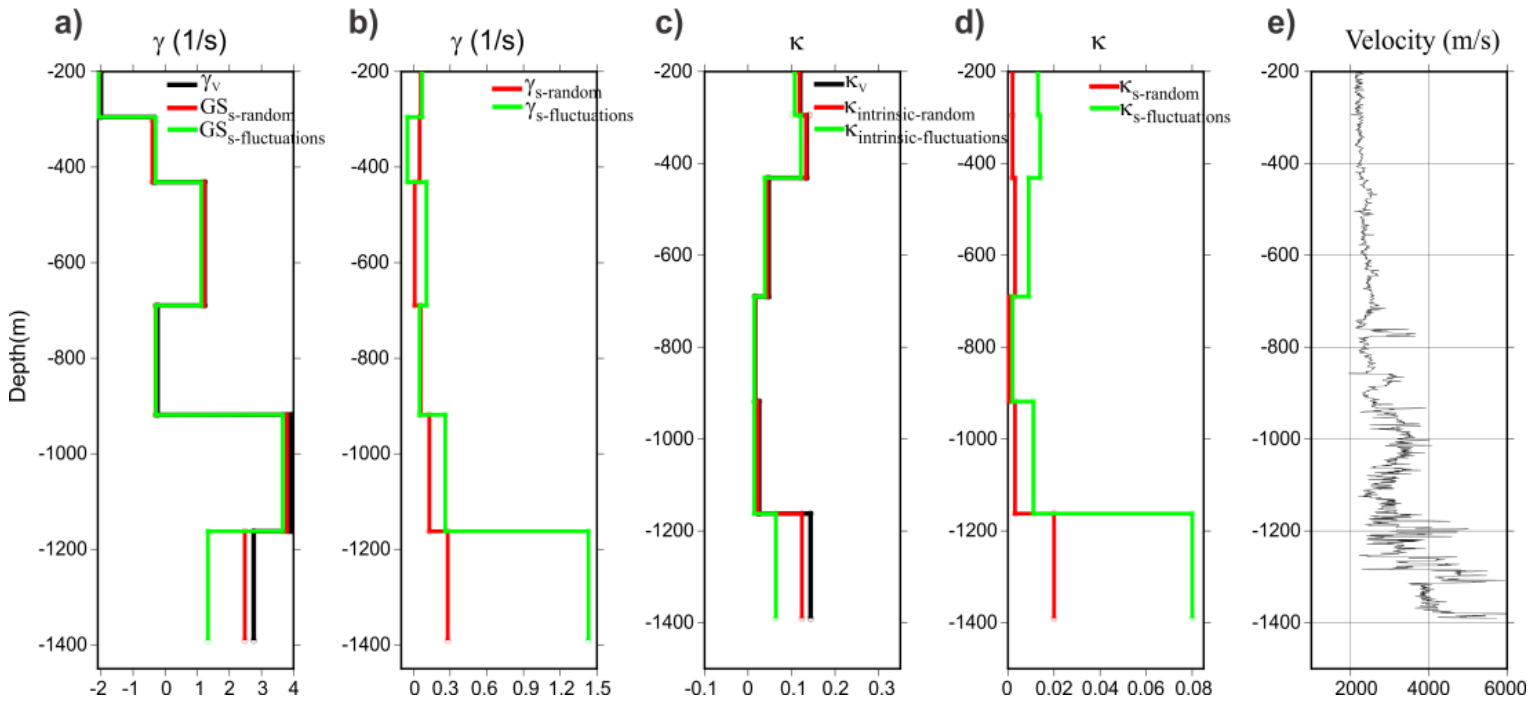

Figure 4.9: Model of geometric spreading, scattering and intrinsic attenuation: (a) Frequency-independent γ_v (black), $GS_{s\text{-}random}$ (red), and $GS_{s\text{-}fluctuations}$ (green), (b) Frequency-independent random scattering $\gamma_{s\text{-}random}$ (red), and fluctuation scattering $\gamma_{s\text{-}fluctuations}$ (green), (c) Attenuation parameter κ_v (black) $\kappa_{intrinsic\text{-}random}$ (red) and $\kappa_{intrinsic\text{-}fluctuations}$ (green), (d) Random scattering attenuation, $\kappa_{s\text{-}random}$ (red), fluctuation scattering attenuation $\kappa_{s\text{-}fluctuations}$ (green); (e) velocity log for comparison.

CHAPTER 5: MODELING OF AVO AND PRESSURE-SATURATION EFFECTS IN WEYBURN CO_2 SEQUESTRATION

The use of normal-incidence reflection-coefficient anomalies combined with some other indictors of hydrocarbon accumulations, particularly gas, has a long history in oil and gas industry. Ostrander (1982) proposed a method, which potentially distinguishes between gas-related, and non-gas related amplitude anomalies by analysing the reflection-amplitude variations with angle (AVA) or offset (AVO). He showed that the Poisson's ratio has a strong influence on the variations of the reflection coefficient as a function of angle of incidence. This pivotal work initiated the AVO methodology (Castagna, 1993). Since then, AVO and AVA analysis has become the standard tool for hydrocarbon detection in the petroleum industry (Rutherford and Williams, 1989).

This Chapter starts with a brief summary of the AVO method (section 5.1) and fluid-substitution modeling of Weyburn reservoir (sections 5.2 and 5.3), based on the approaches by Morozov and Ma (2010) and Baharvand Ahmadi et al. (2011). In sections 5.4 – 5.8, I introduce the AVA attributes that should be useful for distinguishing between pore-pressure and CO_2-saturation effects in this reservoir. In sections 5.9 to 5.11, I derive the AVA models from Weyburn VSP data, and in sections 5.12 to 5.15, I perform their qualitative and quantitative interpretation and discuss the results.

The first part of this chapter (sections 5.2 to 5.4) is a modification and expansion of the following published report:

***Baharvand Ahmadi, A.**, L. Gao, J. Ma and I. Morozov, 2011, CO_2 Saturation vs. Pressure Effects from time-lapse 3-D P-S surface and VSP seismic data: Final report*

as part of IEA GHG Weyburn-Midale CO_2 Monitoring and Storage Project, http://seisweb.usask.ca/Reports/Weyburn_USask_Report_Apr2011.pdf, last accessed October 22, 2016

My contributions to this report were explained at the beginning of Chapter 2. In this Chapter, I include parts of its sections about AVA modeling (led by Drs. Morozov and Ma in the report) which provide the general background for the AVA work. I further include sections about VSP data processing, modeling and analysis, which were done completely by myself with guidance by Professor Morozov. Copyright of this report belongs to the authors, which allows using these materials for student theses. Parts of this report were shortened and modified, and some parts were expanded and reformatted for inclusion in this Dissertation. Figures were re-plotted and modified in order to meet the requirements of the University of Saskatchewan.

Sections 5.5 through 5.16 are also based on two papers that I am currently preparing for publication:

***Baharvand Ahmadi** A., and I. Morozov, VSP AVA analysis of Weyburn reservoir in Southern Saskatchewan: in preparation for Interpretation Journal by American Association of Petroleum Geologists (AAPG)*

***Baharvand Ahmadi** A., and I. Morozov, Qualitative and quantitative interpretation of AVA attributes from a Vertical Seismic Profile: in preparation for Interpretation Journal by American Association of Petroleum Geologists (AAPG)*

These papers contain the completion of the analysis of VSP datasets after the publication of the final report for Weyburn GHG project. The contributions by my supervisor (Professor Igor Morozov) consist in general guidance and advice, discussions of the results and supervise

development of the work. These topics are directly relevant to the subject of this Dissertation and represent the main content of this Chapter.

5.1 Amplitude Variation with Offset (AVO)

Zoeppritz (1919) presented set of formulas, which described the partitioning of seismic wave energy at an interface, mainly a boundary between two geologic layers. The Zoeppritz equations are derived for an idealized welded contact of two elastic half-spaces. If we consider an incident P-wave striking the boundary between two elastic half-spaces at an angle φ, as shown in Figure 5.1, mode conversion results in reflected and transmitted P and SV-waves (Aki and Richards, 2002). As illustrated in Chapter 4, by using the continuity of stress and displacement across the boundary, the amplitudes of reflected and transmitted waves can be derived (equations (4.4)-(4.12)). These equations are the basis of the AVO analysis technique, which was initially proposed by Ostrander (1982, 1984) as a technique for detecting low velocity gas sands based on increasing reflected P wave energy with angle of incidence.

Although the original Zoeppritz equations give the plane-wave amplitudes of different waves as a function of angle, they provide little intuitive understanding of relationship between these amplitudes to various physical parameters. Several authors rearranged the Zoeppritz equations and provided approximations emphasizing the effects of relative variations of densities and Poisson's ratios. In the following section, I briefly describe some of these important approximations.

5.1.1 Approximations for P-wave reflection amplitudes

A broadly used rearrangement of Zoeppritz formulas for weak contrasts of material properties across the boundary was made by Bortfield (1961). Later, these expressions were

revisited by Richards and Frasier (1976) by Aki and Richards (2002). The Aki, Richards and Frasier approximation represents the angle-dependent P-wave reflectivity as a linear combination of (small) relative contrasts in the P-wave velocity (V_P), density (ρ) and S wave velocity (V_S):

$$R(\varphi) = \frac{1}{2}\left(\frac{\Delta V_P}{V_P} + \frac{\Delta\rho}{\rho}\right) + \left(\frac{1}{2}\frac{\Delta V_P}{V_P} - 4\frac{{V_S}^2}{{V_P}^2}\frac{\Delta V_S}{V_S} - 2\frac{{V_S}^2\Delta\rho}{{V_P}^2\rho}\right)\sin^2\varphi + \frac{1}{2}\frac{\Delta V_P}{V_P}\left(\tan^2\varphi - \sin^2\varphi\right), \quad (5.1)$$

where φ is reflection angle and Δ denotes the contrasts in the respective parameters across the reflecting boundary. This approximation is most useful when inverting for the contrasts in all three rock properties, ΔV_P, ΔV_S, and $\Delta\rho$, or further inverting them for contrasts in the elastic moduli of the medium, λ and μ,.

The most commonly used approximation for P-wave reflectivity emphasizing the effect of the Poisson's ratio (σ) was given by Shuey (1985):

$$R(\varphi) = R_0 + \left[R_0 A_0 + \frac{\Delta\sigma}{(1-\sigma)^2}\right]\sin^2\varphi + \frac{\Delta V_P}{2V_P}(\tan^2\varphi - \sin^2\varphi)\ , \quad (5.2)$$

in which the third term ("curvature") is often dropped. In this expression, $R_0 = \frac{1}{2}\left(\frac{\Delta V_P}{V_P} + \frac{\Delta\rho}{\rho}\right)$ is the normal-incidence reflection amplitude is commonly called the AVO intercept, and the factor in square brackets is called the AVO gradient. The two constants in expression (5.2) equal:

$$A_0 = B_0 - 2(1+B_0)\frac{1-2\sigma}{1-\sigma}, \quad (5.2a)$$

$$B_0 = \frac{\Delta V_P / V_P}{\Delta V_P / V_P + \Delta\rho/\rho}. \quad (5.2b)$$

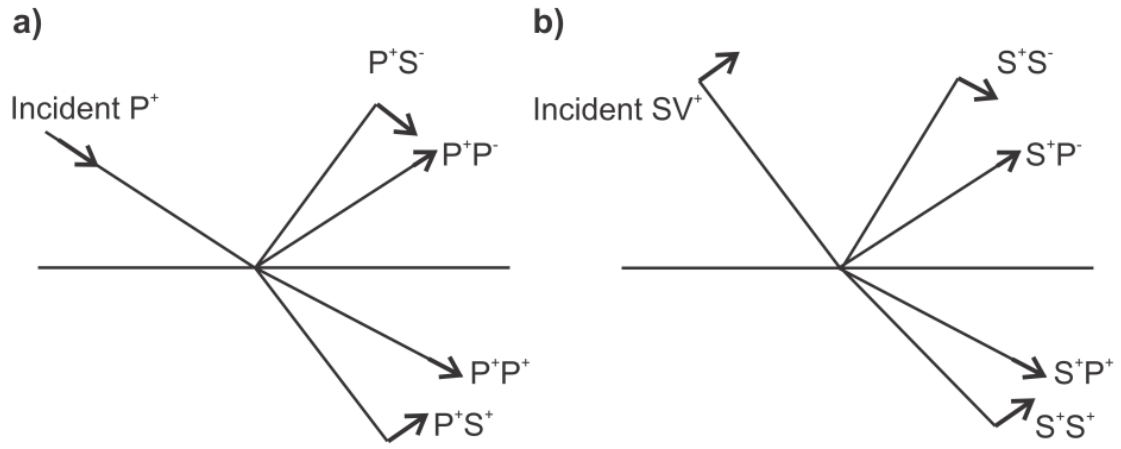

Figure 5.1: One-dimensional scattering model on a single boundary: a) Incident P wave, b) Incident SV wave. Arrows indicate the convention for positive amplitudes up and us.

Hilterman (1990) simplified Shuey's equation further by only using the first two terms and setting A_0 equal to zero. For angles of incidence below about 30°, the amplitude is approximately linear with respect to $\sin^2\varphi$, and equation (5.2) can be simplified as:

$$R(\varphi) = R_0 + \left[\frac{9}{4}\Delta\sigma - R_0\right]\sin^2\varphi, \text{ or} \tag{5.3}$$

$$R(\varphi) = I + G\sin^2\varphi \tag{5.4}$$

where I and G are the AVO intercept and gradient.

Note that the AVO intercept $R_0 = I$ gives a more accurate determination of $R_P(0)$ than the conventional P-wave stack, which represents an average of R_P over the recorded range of offsets. By combining the values of I and G, several additional useful attribute volumes can also be constructed. In particular, by approximating the "background" velocity ratio as $V_P/V_S = 2$, the S-wave reflectivity at normal incidence becomes (Rutherford and Williams, 1989):

$$R_S(0) \approx \frac{1}{2}(I - G), \tag{5.5}$$

Thus, the S-wave reflectivity can be extracted from the AVA patterns of the primary P-wave reflections.

5.1.2 AVO Classification

The AVO/AVA method is usually combined with a useful cross-plotting technique (Rutherford and Williams, 1989; Castagna et al., 1998) which helps to identify the anomalies that might be related, for example, to CO_2 flooding. The Rutherford-Williams classification subdivides the various pairs of (*I*,*G*) observations into four regions, or classes (Figure 5.2):

Class 1: High-impedance contrast with decreasing AVA (positive *I* and negative *G*);

Class 2: Near-zero impedance;

Class 2p: Same as class 2, but with reflection polarity change;

Class 3: Low impedance with increasing AVA (negative *I* and negative *G*);

Class 4: Low impedance with decreasing AVA (negative *I* and positive *G*).

The above classification is based on the notion of a linear, background "wet trend", or "mudrock line" in the (*I*, *G*) plane:

$$G(I) = -\frac{4}{5}\left[\frac{9}{(V_P/V_S)^2} - 1\right] I, \tag{5.6}$$

Deviations from this trend are usually viewed as "anomalies" and represent the primary tool of AVA interpretation.

5.2 AVA modeling of Pressure and Saturation effects

Time-lapse seismic response in Weyburn field can be considered as the result of a combination of changes in CO_2 saturation and pore pressures. Therefore, it is important to

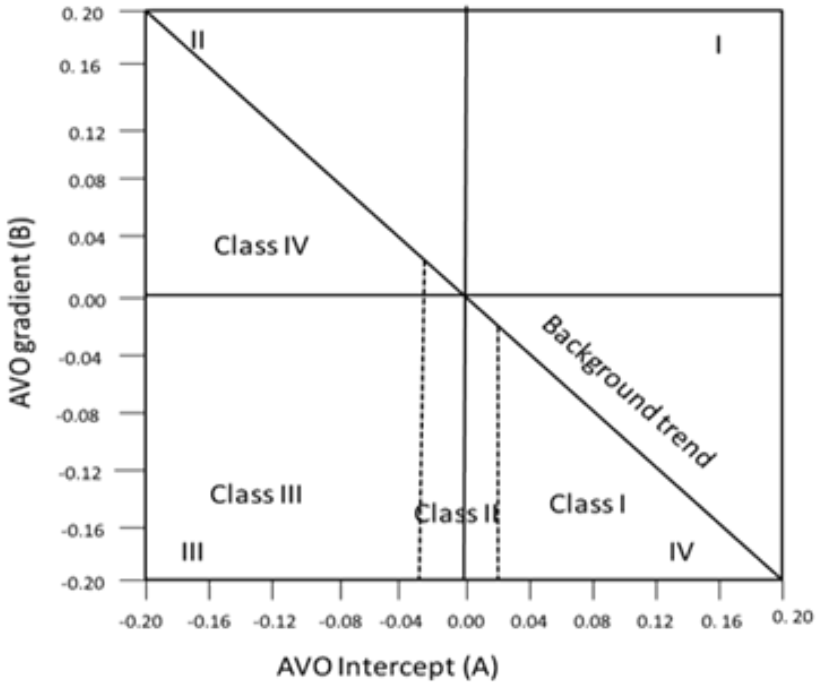

Figure 5.2. AVA (AVO) classification from Castagna et al. (1998).

understand the effects of pressure and saturation changes on rock properties to be able to separate these effects from each other.

5.3 AVA modeling of Pressure and Saturation effects

Time-lapse seismic response in Weyburn field can be considered as the result of a combination of changes in CO_2 saturation and pore pressures. Therefore, it is important to understand the effects of pressure and saturation changes on rock properties to be able to separate these effects from each other.

Conventionally, reservoir responses are interpreted based on simple two-layer models. However, such models are clearly inapplicable to Weyburn, where the AVA response represents an interference of reflections from the two units (Marly and Vuggy), and at lower frequencies

from the base of the reservoir. Thus, quantitative seismic interpretation of this reservoir should be carried out with an account for its small thickness and complex reflectivity profile.

As a basis for AVA modeling, well 102042300614 was used. This well was drilled in conjunction with the Weyburn CO_2 sequestration project, located near the southwest border of Phase 1A area and about 15 m away from a water injection well (red dot in Figure 5.3), and logged in August 2000. This well contains the most complete sets of geophysical logs available to this study, and it is suitable for AVA modeling and can be considered as representative of the reservoir. Rock-physics properties of this well were studied by Brown (2002). Pressure, oil saturation and other reservoir parameters in this well were measured prior to and during the CO_2 injection are listed in Table 5.1. Note that water saturation for the Marly and Vuggy zones in this well was recalculated by using Archie's equation and calibrated by $MnCl_2$-doping analysis. Water saturation was found to be higher than previously estimated (Table 5.1; Brown, 2002).

Brown (2002) developed a fluid-substitution model and normal-incidence synthetic seismograms for the Weyburn reservoir by using reservoir fluid parameters similar to our baseline (Table 5.1). Later, this analysis was extended to oblique incidence by Morozov and Ma (2010) and focused on the fluid-substitution effects on AVA attributes during CO_2 flooding. The main question they addressed was whether and how pressure and CO_2 saturation effects can be separated in AVA intercept-gradient measurements. In the following, by using fluid substitution model, an AVA model of Weyburn reservoir is proposed for discriminating between the CO_2 pressure and saturation effects at Weyburn. In chapter 6, this model will be used as guidance for an AVA study of time-lapse VSP data.

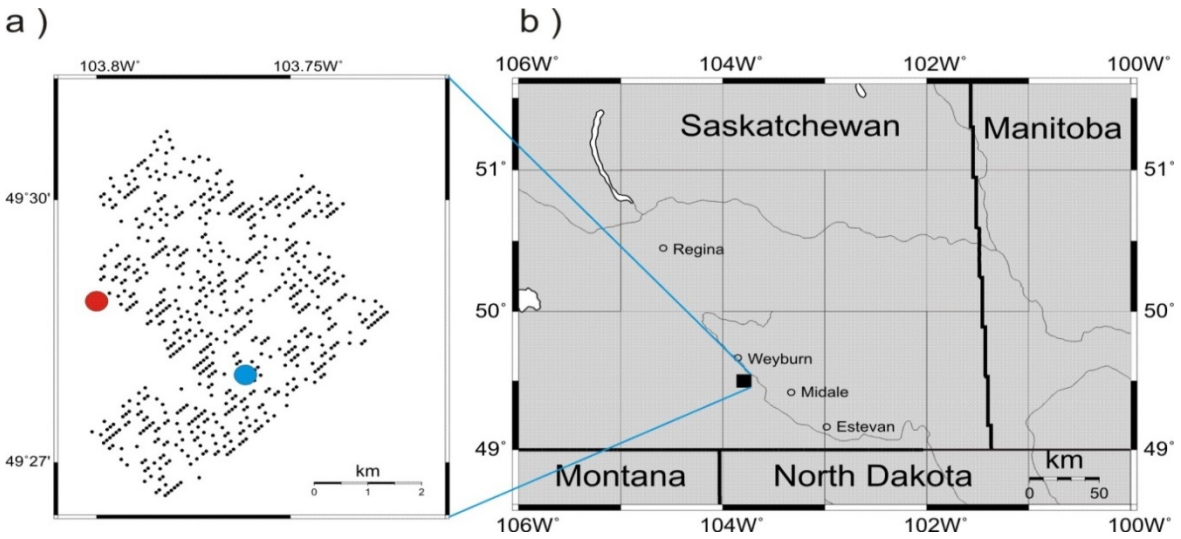

Figure 5.3. Weyburn seismic monitoring project area: a) 3C-3D survey layout and location of the wells used for VSP (blue) and for generating synthetics and AVO analysis (red); b) Location map in south-eastern Saskatchewan.

Table 5.1 Reservoir parameters used in modeling.

Parameters	**Baseline**	**Monitor**
Temperature	63^0C	56^0C ($52\sim58^0$C)
Oil API gravity	29 (25~34)	29 (25~34)
Gas gravity	1.22	Unchanged
CO_2 gravity	1.5249	Unchanged
Gas/Oil ratio (GOR)	30 L/L	Unchanged
Salinity	85,000 ppm NaCl	79,000 ppm NaCl
Water resistivity	0.149 ± 0.023 (ohm m)	0.104 ± 0.014 (ohm m)
Oil saturation in Marly zone	Average 53%	Average 30%
Oil saturation in Vuggy zone	Average 35%	Average 28%
Pore pressure	15 MPa	23 MPa near injector 8 MPa near producer
Confining pressure	32~33 MPa	Unchanged
Mineral bulk modulus (Brown, 2002)	83 GPa (Marly zone) 72 GPa (Vuggy zone)	Unchanged
Mineral shear bulk modulus (Brown, 2002)	48 GPa (Marly zone) 33.5 GPa (Vuggy zone)	Unchanged
Clay (shale) moduli	21 GPa (bulk) 7 GPa (shear)	Unchanged

5.4 Fluid substitution model

Fluid substitution modeling is a key tool in reservoir characterization. In this project, fluid substitution modeling was used to predict rock physic properties of the Weyburn reservoirs after CO_2 injection. Following Wang et al. (1998), Gassmann's equation was used to estimate the effects of CO_2 saturation on the elastic moduli within and near the reservoir. This equation relates the bulk modulus of fluid-saturated porous rock (K_{sat}) to the dry (K_{dry}) and matrix (K_{matr}) moduli as:

$$K_{sat} = K_{dry} + \frac{\left(1 - \frac{K_{dry}}{K_{matr}}\right)^2}{\frac{\phi}{K_f} + \frac{(1-\phi)}{K_{matr}} - \frac{K_{dry}}{K_{matr}^2}}, \tag{5.7}$$

where ϕ is the porosity, K_f is the bulk modulus of the reservoir fluid, and all parameters are taken at depth z. The difference between K_{matr} and K_{dry} is that K_{matr} represents the bulk modulus of the material of the rock matrix, whereas K_{dry} is the bulk modulus of a dry rock, which also contains pores and consequently $K_{dry} \leq K_{matr}$. Pore fluids generally consist of water, oil, gas, and CO_2, and the bulk modulus of their mixture (K_f) is a function of their relative saturations, temperature, salinity, pore pressure, etc. In this fluid substitution model, we assume that the volumes of fluids are simply added together, and the effects of dissolution of CO_2 in the oil-gas mixture are not considered. At the same time, the portion of gas dissolved in oil is accounted for by using a pressure-dependent gas-oil ratio equation.

The shear modulus $\mu_{sat} = \mu_{dry}$ is considered to be independent of fluid saturation. Assuming that K_{matr} is constant within the Marly and Vuggy zones, I inverted equation (5.7) to obtain the value of K_{dry} at the current reservoir pressure.

Further, pressure-dependence of the dry bulk and shear moduli of the Midale zones was approximated from the results of ultrasonic lab testing. Brown (2002) measured the differential-pressure related trends $K_{dry}(p)$ and $\mu_{dry}(p)$ under confining pressure 23 MPa and pore pressure 15 MPa. This confining pressure of 23 MPa was taken as the average of the vertical stress of 32–33 MPa and horizontal stress of 18–22 MPa. Brown (2002) also derived a polynomial formula describing the increase of K_{dry} with differential pressure, which we denote $K_B(p)$, and a similar dependence for μ_{dry}. Denoting the *in situ* differential pressure at baseline conditions by p_0, the pressure-corrected dry bulk modulus becomes:

$$K_{dry}(\mathrm{z}, p) = K_{\mathrm{dry}}(z) + K_{\mathrm{B}}(p) - K_{\mathrm{B}}(p_0), \tag{5.8}$$

and a similar equation for the shear modulus. Here, K_{dry} is estimated from equation (5.7), and p is the differential pressure. In our calculations, we took the vertical stress of 32.5 MPa as the confining pressure, which allowed relating the differential pressure in equation (5.8) to pore pressure in subsequent fluid-substitution estimates.

The quality of Gassmann's prediction for fluid substitution is highly dependent on the accuracy of fluid parameters and physical parameters of reservoir rocks. Several selections of the most appropriate models should be made in order to construct an adequate fluid-substitution model. These selections are briefly reviewed below.

5.4.1 Constitutive equation for CO_2

Previously, Brown (2002) calculated the bulk modulus and density of CO_2 by using the equation by Batzle and Wang (1992). However, recently, Xu (2006) modified these equations to provide more accurate estimates of the CO_2 properties (Figure 5.4). Note the significant

difference in the bulk moduli predicted by these methods, and also the broader minimum in V_P shifted to higher pore pressures in Xu's (2006) model.

5.4.2 Effective porosity in Gassmann's equation

Total rock porosity includes isolated pores and the volume occupied by clay-bound water. These volumes cannot be filled by the injected CO_2 and water. By contrast, effective porosity represents the interconnected pore volume into which fluid substitution can occur, and therefore it (and not the total porosity) should be used as parameter ϕ in equation (5.7). The effective porosity is lower than total porosity, its use leads to smaller changes in the elastic parameters. Therefore, time-lapse velocity, travel-time, and reflectivity variations estimated by using the effective porosity should be smaller than those derived from total porosity.

5.4.3 Shale corrections to matrix modulus of Marly dolomite zone

Although the porosity of Marly dolomite zone is high, its permeability is quite low,

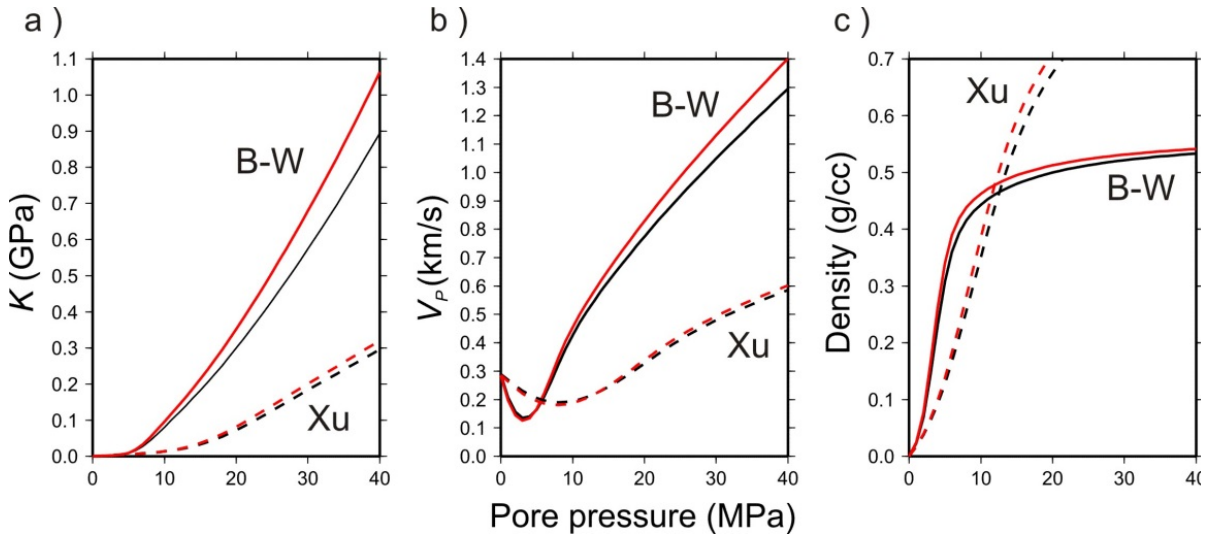

Figure 5.4. CO_2 properties calculated by using Xu's equations (dashed lines), and by using Batzle-Wang's equation (B-W; solid lines). Red lines are for temperature 56°C, black – for 63°C. Note that these curves are close to those predicted by program SUPERTRAPP (Don White, personal communication).

which is mainly caused by high shale content within its pores. Shale present within the pores (V_{sh} in Figure 5.5) effectively reduces the bulk modulus of the reservoir rock matrix (Figure 5.5). On the other hand, shale content is low within Vuggy zone, and it is ignored in our model.

Fluid-substituted logs were calculated by using pore pressure of 15 MPa and mixed fluids (40% CO_2, 48% brine and 12% oil). K_f of mixed fluids (green) is assumed constant, whereas K_f of *in situ* fluids (black) is variable.

Following Dvorkin et al. (2007), Morozov and Ma (2010) replaced the single-mineral K_m of dolostone within the Marly zone (equation 5.7) with the effective matrix bulk modulus calculated from a mixture of dolostone and shale by using shale parameters given in Table 5.1. Note that the use of shale corrections reduced the matrix bulk modulus K_m within Marly zone, which was assumed constant in previous studies (Brown, 2002) (Figure 5.5). Finally, in addition to the described elastic moduli and densities, other measured fluid and reservoir parameters (such as temperature, salinity, *etc.*; Table 5.1) were considered constant during the modeling described below.

The key part of the model is in using the Gassmann's equation to estimate the matrix (K_{matr}) and dry (K_{dry}) moduli of the reservoir and the surrounding host rocks. To achieve a stable and meaningful solution, we first assumed that K_{matr} was constant within each unit, and then applied corrections for volume fractions of clay in it. Further, the observed K was derived at each depth level from the seismic logs and density as $K = \rho\left(V_P{}^2 - \frac{4}{3}V_S{}^2\right)$, and K_{dry} was inverted from this value by using the Gassmann's equation (5.7). Several constraints were imposed to guarantee physically meaningful results (such as positive porosity, $K_{dry} < K_{matr}$, and other).

Further, because the values of the in situ K_{matr} are poorly known, we tried improving their estimates by using an optimization procedure. In each of the two units, K_{matr} was adjusted so that the dependence of compressibility K_{dry}^{-1} on the effective porosity was the closest to being linear (Figure 5.6). Finally, to adjust the log to any point within the study area, we stretched and shifted the obtained synthetic logs so that the reflections from the top of Marly and bottom of Vuggy corresponded to the markers observed in the stacked seismic sections.

From the edited and inverted logs (Figure 5.5), it now became possible to simulate realistic seismic AVA responses from Weyburn reservoir. Using the exact expression for reflection and mode conversion amplitude (Aki and Richards, 2002), oblique-incidence reflectivities derived for each ray parameter of incidence wave calculated. This resulted in "logs" of reflection amplitudes. Next, these "logs" were converted into the two-way reflection travel-time domain and convolved with the selected wavelet. Finally, three-term AVA analysis was performed on these synthetics, producing additional "logs" of *I*, *G*, and "AVA curvature" values. As expected, curvature values were insignificant within the offset (ray parameter) range of this study. Figure 5.7 shows such a wavelet-filtered AVA synthetic for the same (unstretched) well.

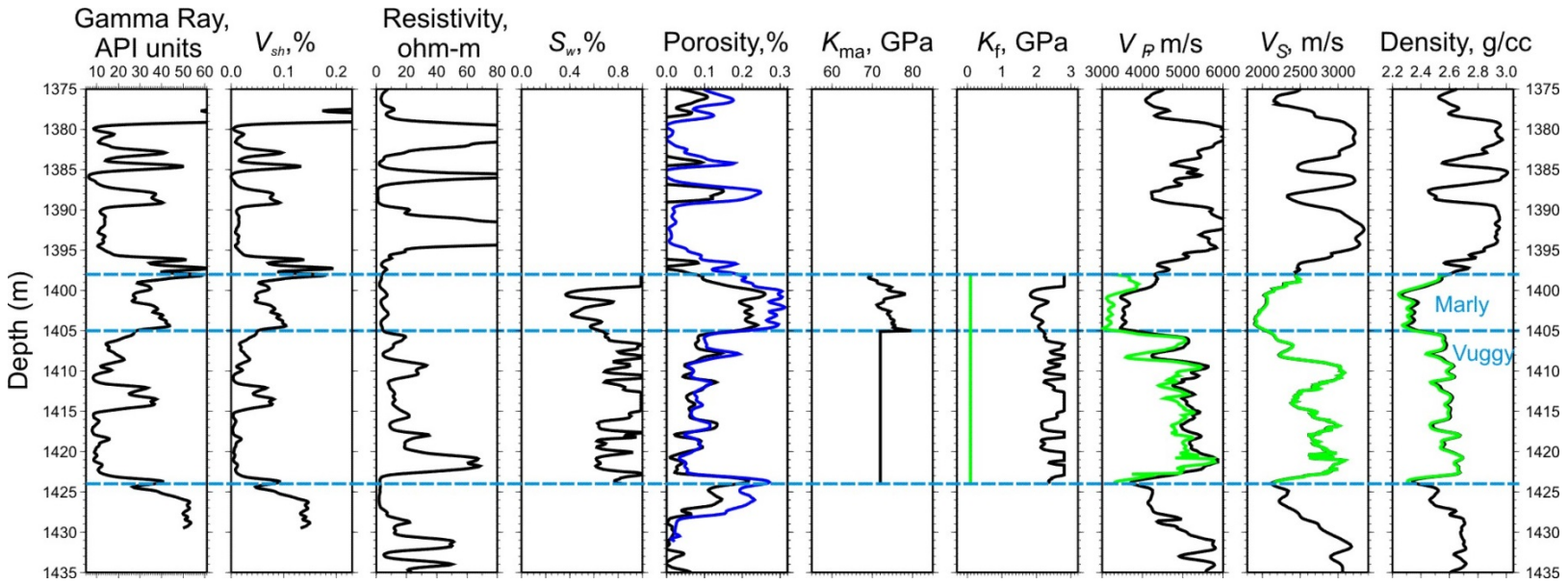

Figure 5.5. Fluid-substituted V_P, V_S and density logs (green) and original logs (black) combined with several other logs in well 102042300614. *V*sh is the shale content estimated from the gamma-ray log, and Sw is water saturation. The total and effective porosities are shown by blue and black lines, respectively. Fluid substitution is performed using extended Gassmann's equations, as described in section Modeling of pressure-saturation effects on AVA below.

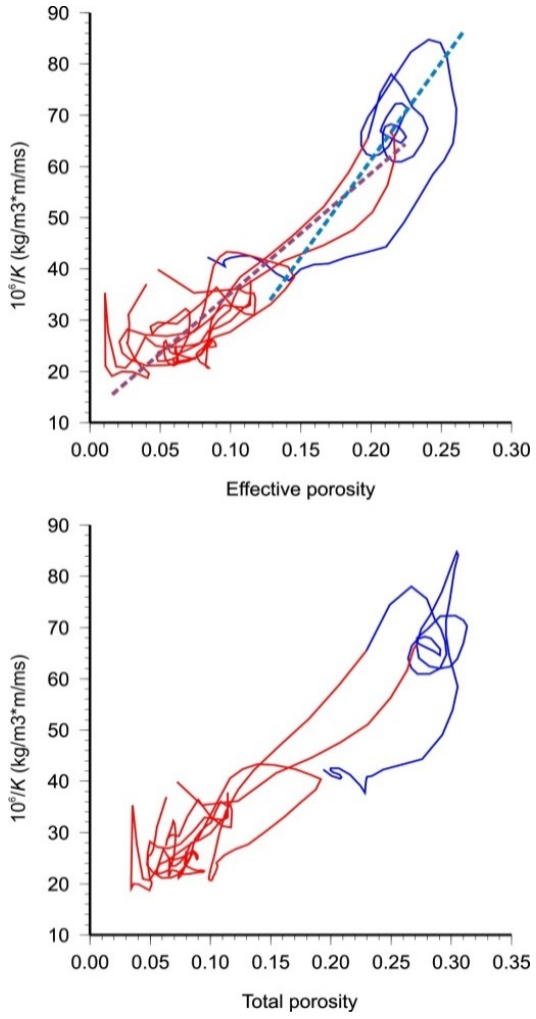

Figure 5.6. Cross-plots of $10^6/K_{dry}$ in optimal model versus the total and effective porosity for Marly (blue) and Vuggy (red) units. Dashed lines indicate the optimized trends of K_{dry}^{-1}(effective porosity).

5.5 AVA Attributes

In this Dissertation, the AVA approach is selected as the primary method for separation of CO_2 pressure and saturation effects. The principle of using AVA attributes for interpreting the seismic effects of pressure- and CO_2-saturation variations is similar to what illustrated in Figure 5.2. As shown below (section 5.5.6), pore-pressure variations make the (I,G) values to

move generally along a similar “wet-trend” line, whereas variations in the CO_2 saturation cause shifting across this trend line. Thus, the principal efforts in AVA data analysis is directed onto measuring the variations in the (I,G) attributes and identifying the regions in which the anomalies in I and G are correlated (as related to pressure variations) or anti-correlated (when

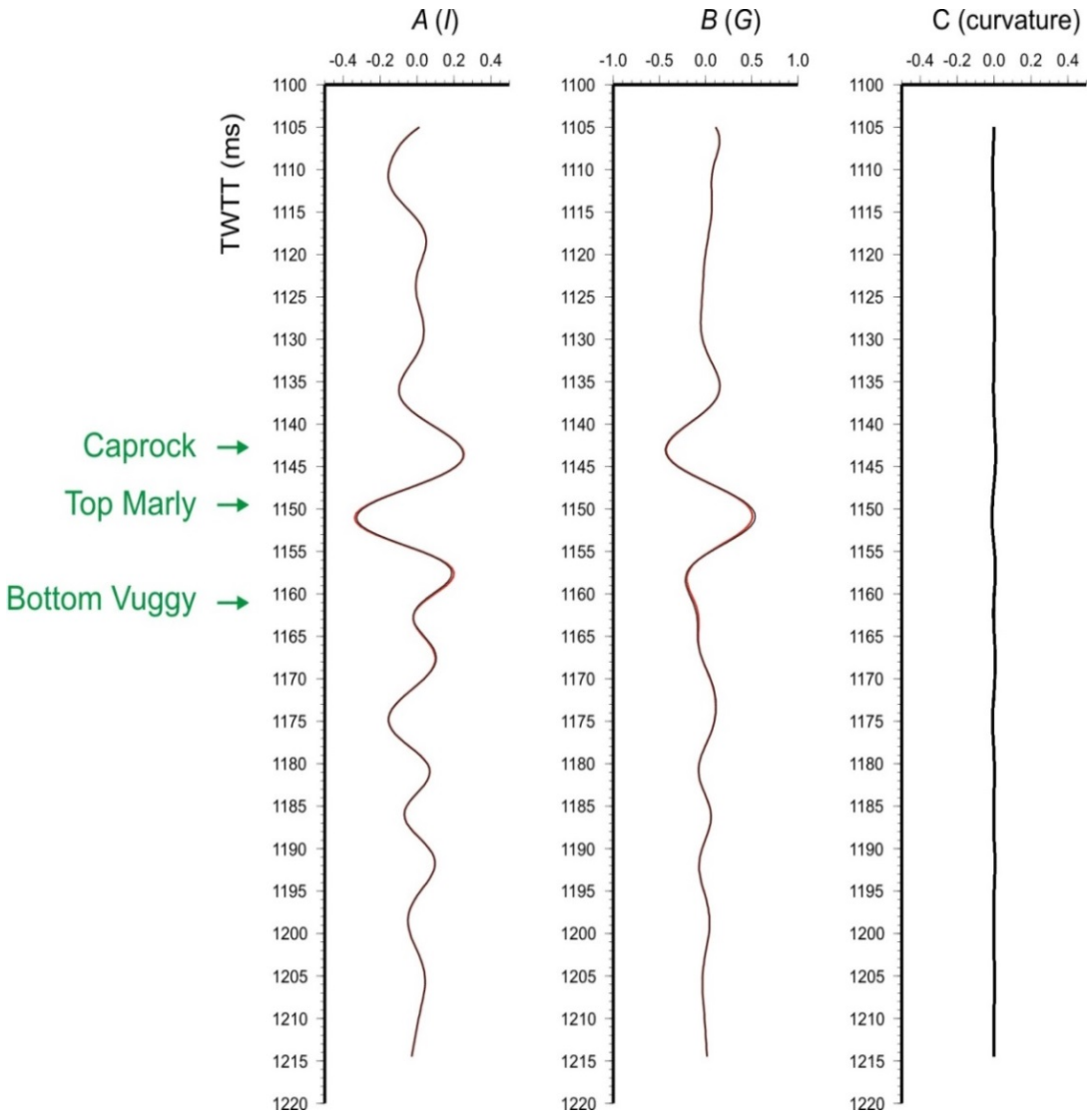

Figure 5.7: Three-term 40-Hz Ricker AVA synthetics derived from logs in Figure 5.5. A is the intercept (denoted I in this Dissertation), *B* is the gradient (*G*), and *C* is the third AVA term (curvature), plotted using comparable amplitude scales. Black curve corresponds to brine only, and red curve – to brine with 20% CO_2 within the reservoir. Note that the absolute values of *G* are about twice those of *I*, and that the curvature effect is small.

caused by variations in saturation). Generally, pressure variations most strongly affect the combination I - G, and CO_2-saturation variations control combination I + G. The second of these attributes is also approximately proportional to the S-wave reflection amplitude, $R_S(0)$, whereas the pressure indicator can be written as $I - G \approx 2\left[R_S(0) - R_P(0)\right]$. The principal expected seismic responses to variations or pore pressure and CO_2 saturation within the reservoir are summarized in the Table 5.2.

Unfortunately, as the modeling below shows, seismic attributes exhibit an acute sensitivity to small amounts of CO_2, and the slope of the above "trend" line varies with CO_2 saturation. Therefore, the effective discriminator attributes that we are seeking have a more general form of:

$$A_{pressure} = I + aG \text{, and } A_{saturation} = I - a^{-1}G \text{.} \tag{5.9}$$

where parameter a also depends on CO_2 saturation. Further, in practical measurements, it only appears possible to use a proxy value for parameter a, which is the empirical slope of the trend line observed in the plane of measured (I, G) attributes. These attributes are less instructive when expressed in terms of the normal-incidence reflectivities, $R_P(0)$ and $R_S(0)$ (Morozov and Ma, 2010; Baharvand Ahmadi et al., 2011).

5.6 AVA Modeling for Weyburn reservoir

Traditionally, AVA interpretation is based on two-layer or blocked-log models and small-contrast approximations. The most commonly used approximation for P-wave reflectivity was given by Shuey (1985) (equation (5.4)). Shuey's parameterization emphasizes the sensitivity of

Table 5.2: Summary of expected seismic responses of reflection from the top of Marly to pressure and CO_2 saturation

Attribute	Effect of pore pressure increase	CO_2 saturation increase
P-wave reflectivity ($R_P = I$; negative-polarity)	decrease	Decrease
AVA gradient, G (positive)	increase	Decrease
S-wave reflectivity (eq. (5.5))	decrease	no effect
$I + G$	no effect	Decrease
P-wave impedance	small decrease (due to density change)	Decrease
S-wave impedance	small decrease	no effect

the AVA gradient on the contrast in the Poisson's ratio across the boundary:

$$G = A_0 R_0 + \frac{\Delta\sigma}{\left(1-\sigma^2\right)},$$

Our fluid-substitution model incorporated computations derived from well-log measurements made at about 15-cm intervals throughout the entire zone of interest. This allowed detailed calculation of the reservoir response to the finite-bandwidth seismic wavelet. At the same time, while the exact expressions (4.7) used for modeling reflection responses, the traditional intercept (I) and gradient (G) attributes are extracted from these responses and utilized for interpreting the results.

The AVA intercept and gradient values were measured from ray-tracing synthetics over the 0–30° range of incidence angles. An exact ray-theoretical solution for reflection amplitudes

and a zero-phase Ricker wavelet were used to generate the synthetic seismograms. Depth-to-time conversion of well logs was performed at all individual depth log readings, which allowed bypassing typical problems related to log and seismic record resampling. In the following, AVA attributes and CO_2 discriminator are estimated and a simple CO_2-saturation – pore-pressure discriminator is proposed and tested.

5.7 Pore Pressure and Saturation

Pore pressure, also known as formation pressure, is the in-situ pressure of the fluids in the pores within the rock. The pore pressure equals the hydrostatic pressure when the pore fluids support the weight of only the overlying pore fluids. The lithostatic, or confining pressure results from the weight of the overlying sediments, including pore fluids (Carcione, 2003).

Knowledge and prediction of the pore pressure in the area is critical at different stages in the exploration and development process. In the exploration phase, prediction of pore pressure can facilitate evaluating the seal effectiveness and mapping hydrocarbon migration pathways. In the drilling phase, it can be vital for safe and economic drilling. The casing program also can be optimized and run safely using estimates of proper pore pressure and fracture pressure and well control problems, such as blowouts can be prevented (Dutta, 2002).

5.8 AVA effects of CO_2 Pressure and Saturation

In addition to conventional two-layer model, small contrast blocked-log model was also examined in this study. The first of these models (Table 5.3) represents an anhydrite/Marly interface, which is the upper boundary of the reservoir. Considering that the Marly zone is relatively thin (Figure 5.5) compared to the dominant wavelength, the second end-member model is constructed by removing the Marly zone and placing the anhydrite layer directly above the

Table 5.3. Parameters of two-layer models (Figure 5.8a)

Type of Rock	V_P (m/s)	V_S (m/s)	Density (g/cc)	Total porosity	Effective porosity
Anhydrite	5900.0	3250.0	2.90	0	0
Marly dolomite	3600.0	2000.0	2.31	0.29	0.20
Vuggy limestone	5100.0	2900.0	2.56	0.10	0.10

Vuggy zone (Table 5.3). AVA attributes of models with realistic depth variations of reflectivity are quite different from those of the conventional two-layered models (Figure 5.8). Interestingly, in the AVA cross-plots, the (*I*,*G*) points computed by using the realistic depth-dependent parameters are located between those of the anhydrite/Marly and anhydrite/Vuggy end-member models (Figure 5.8a). This effect occurs because of the half-length of the incident wavelet (~50 m at 40 Hz) exceeding the thickness of the reservoir, and particularly of its Marly zone. When the dominant frequency of the wavelet is increased, a separate reflection from the anhydrite/Marly contact becomes observed, and therefore the (*I*,*G*) values approach those of the anhydrite/Marly model. Conversely, when the dominant frequency of the wavelet is decreased, the reflectivity from Marly zone becomes relatively insignificant, and the (*I*,*G*) response approaches that of the anhydrite/Vuggy model (Figure 5.8a).

By using well-log based models, fluid saturations were simulated ranging from 100% water to 100% oil and to 100% CO_2. In the example presented here (Figure 5.9), the saturation of CO_2 (denoted S_{CO2}) in the mixture was varied from 0 to 100%, and the relative saturations of oil and water were maintained at the ratio of 1:4. This allowed examining the effect of CO_2, which is dominant compared to the relative composition of the liquid oil/water mixture. Pore pressures were varied from 7 to 23 MPa, which corresponded to the estimated variation of the pressure from the production to injection wells (Figure 5.8).

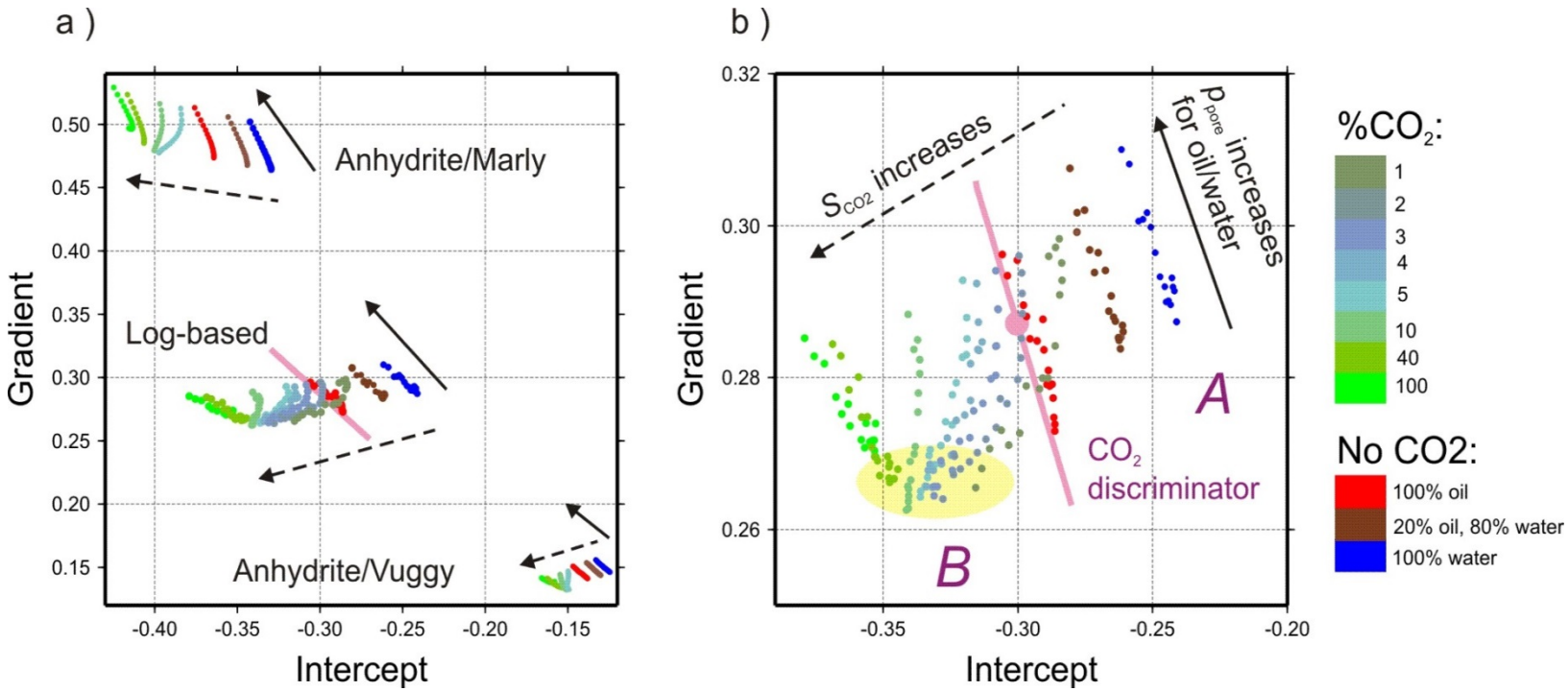

Figure 5.8. Modelled AVA cross-plots: a) from two-layered models and well-log based models; b) detail of the well-log model. 40-Hz Ricker wavelet was used. Solid and dashed arrows indicate the pore pressure increasing from 7 to 23 MPa, and CO_2 saturation increasing from 0 to 100%, respectively. Yellow ellipse indicates the area of (*I*,*G*) values converging at low pore pressure. Pink lines and large dot show the CO_2 discriminator (see text).

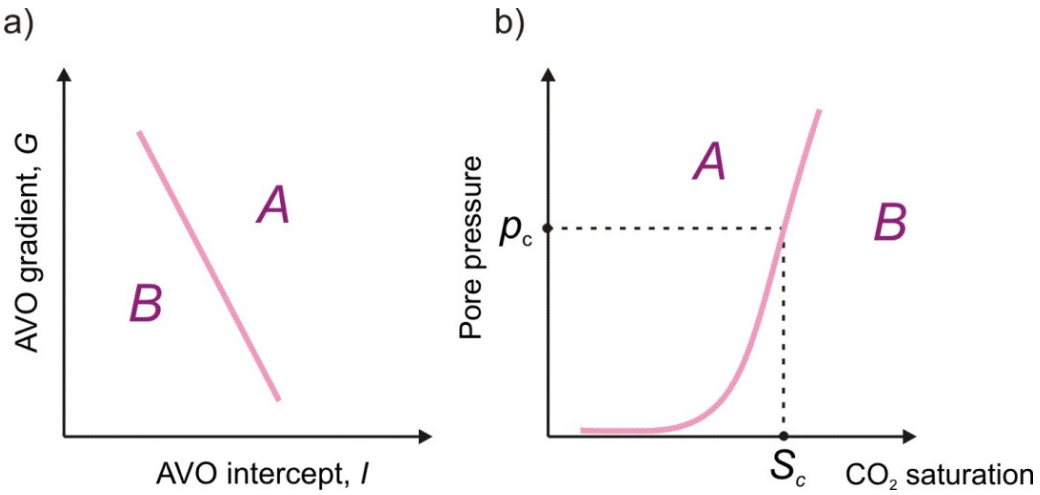

Figure 5.9. Principle of CO_2 discriminator: a) two zones in the (*I*,*G*) cross-plot (compare to Figure 5.8b); b) the same zones in the pressure-saturation domain.

When fluids contain even small amounts of CO_2, their bulk moduli are strongly affected by the pore pressure. For relatively low pore pressures (~7 MPa) and S_{CO2} changing from 0 to 1%, the (*I*,*G*) values of the reservoir rapidly move into the area indicated by the yellow ellipse in Figure 5.8b. Note that the amount of this shift is comparable to the total distance between the 100%-oil an 100%-water cases (Figure 5.8b). From this area, (*I*,*G*) values move with increasing pressure in a fan-like pattern, generally opposite to the general CO_2-saturation trend for $S_{CO2} \approx 1–5\%$ (*i.e.*, to the dashed arrow in Figure 5.8b) and in the direction of the oil/water pore-pressure trend when $S_{CO2} \approx 10–100\%$ (solid arrow). By contrast, changes in the oil/water mixture cause sub-parallel (*I*,*G*) trends that are consistently different from those caused by pore-pressure variations (brown and blue circles in Figure 5.8b).

Further, the above synthetics are used to investigate the possibility of discrimination between pressure and CO_2 saturation effects in seismic AVA data. As AVA cross-plots show, pore-pressure variations and CO_2 saturation effects cause contrasting shifts of reflections in the

intercept-gradient plane (Figure 5.8). Based on this difference, their separation should be feasible in principle.

Pink line in Figure 5.8b illustrates the approach to AVA classification with respect to the studied pressure-saturation variations proposed by Morozov and Ma (2010) and Baharvand Ahmadi et al. (2011). This "discriminator" line represents the lower bound of the CO_2-free distributions and subdivides the (*I*,*G*) plane into two zones denoted *A* and *B* (Figure 5.8b). In terms of the pressure-saturation parameters, these zones are separated by a pressure threshold whose shape can be described by specifying the cut-off saturation level S_c and pore pressure p_c (Figure 5.9). By checking the pore pressure values at which the (*I*,*G*) trends modeled for different S_{CO2} values cross the discriminator line (Figure 5.8b), we estimated $S_c \approx 2\%$ and $p_c \approx$ 18–20 MPa.

For each of the models (log-based or two-layer), such discriminator lines can be represented by their central points (I_0,G_0) (pink dot in Figure 5.8b) and slopes (d*G*/d*I*). If not seeking a precise discrimination of pore pressures (*i.e.*, allowing some vertical position uncertainty in Figure 5.9b), then a range of slopes can be selected for a fixed central point. This range was picked by eyeball-fitting different straight lines separating the "CO_2-free" and "CO_2-containing" distributions (black and blue lines in Figure 5.10a). This allowed estimating the uncertainty in (I_0, G_0, d*G*/d*I*) parameters. Further, both (I_0,G_0) and d*G*/d*I* depend on the dominant frequency of the wavelet. By measuring d*G*/d*I* from models with different frequencies of the incident Ricker wavelet, we estimated its dependence on the frequency (Figure 5.10a). Finally, by using the uncertainty bounds, a simplified empirical dependence was selected, giving the slope of the discriminator line (red line in Figure 5.10a). Note that for frequencies above 45 Hz, this slope is constant and approximately equal -1.4.

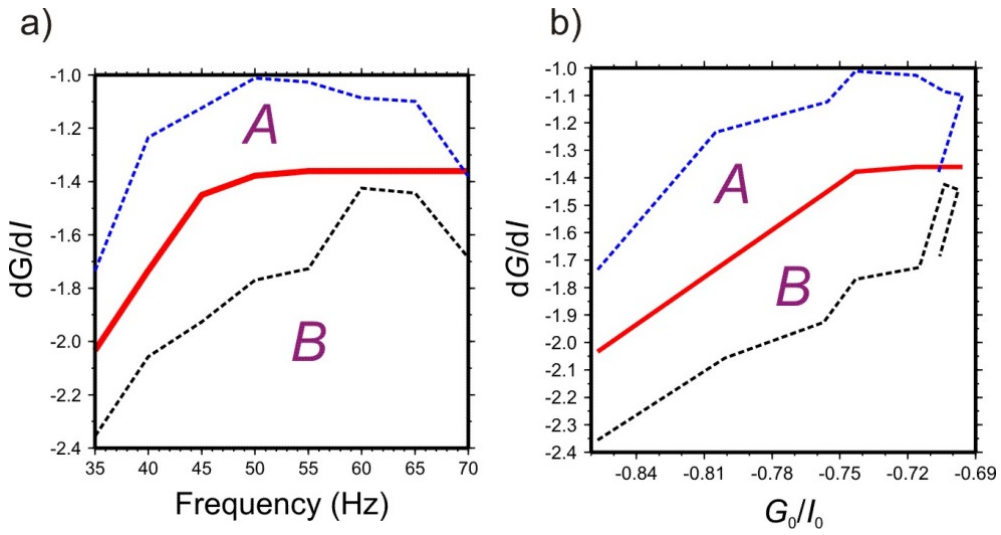

Figure 5.10. Dependence of the slope dG/dI of the discriminator line (Figure 5.8b) on: a) the wavelet frequency, and b) G_0/I_0 ratio. Blue and black dashed lines give two possible selections for such discriminators picked from the synthetics, and red line is the interpreted optimal discriminator. Note that the discrimination can be performed independently of the absolute amplitudes I_0 and G_0.

5.9 Implications for model observations

From Figure 5.8, the effects of pressure and saturation on AVA attributes are somewhat similar to the AVA classification in Figure 5.2. The pressure-related trend resembles the "mudrock line", i.e., the background variability of (I,G) parameters. Along this line a combination of AVA attributes (a-1G–I), with $a > 0$, increases in the direction of increasing pressure (Figure 5.8). Note that for $a = 1$, this combination is proportional to the S-wave reflectivity RS = (I–G)/2. In an orthogonal direction, another derived attribute, –(I+aG) increases in the direction of increasing CO_2 saturation. Such combinations of I and G will be used for mapping the variations of pressure and (low) CO_2 saturation below.

Interestingly, the slope dG/dI of the discriminator line can also be represented as a function of the ratio G_0/I_0 (Figure 5.10b). This relation is independent of both the frequency and

the amplitude of the incident wavelet. Therefore, it should be insensitive to the seismic amplitude scaling and could be directly applicable to reflection AVA data. In this type of AVA cross-plot, the cases with "some CO_2" should be located below the modeled red curve in Figure 5.10b.

Further in this Chapter, this model will be used for interpreting AVA effects in time-lapse 3-D VSP data for separation of CO_2 pressure and saturation effect. Further modeling and application to real seismic data in the future should provide additional insights into the utility and stability of this discriminator.

5.10 Preparation of time-lapse VSP data for AVA analysis

Time-lapse VSP data need to be carefully pre-conditioned for AVA analysis. The goal of this preconditioning is to attenuate the unwanted amplitude variations and noise that can distort the AVA behaviour. At the same time, we need to preserve the seismic amplitude variations related to variable angles of incidence, rock physics and reservoir properties. Chapter 2 summarized the processing steps applied to time-lapse VSP datasets. The purpose was to apply consistent and identical processing to the baseline and monitoring surveys and avoid any processing which might distort the AVA responses. One of the key processing steps consists in correcting for the geometrical spreading of VSP data. This step appears to be the most important for obtaining accurate AVA results. In this section, I consider two different models for geometrical spreading and try gaining a deeper insight into the effects of geometrical spreading.

5.10.1 Geometrical spreading correction

Geometrical spreading (GS) is the key factor determining the variation of both first arrivals and reflected seismic amplitudes. The GS is particularly strong in the VSP case, in which all receivers are located at progressively increasing distances from the source. As a result, the GS

has the leading effect on the AVA, and this effect needs to be corrected for before interpreting the dependencies of reflection amplitudes on incidence angles. When working with real data, the GS can also be highly variable (Chapter 3). It cannot be assumed from theoretical considerations and needs to be measured from the data.

In this Dissertation, I propose two empirical approaches to such GS measurement. Both of these approaches use the amplitudes of direct waves to create anisotropic models of amplitude decay within the subsurface. The first model is purely empirical, frequency-independent and assumes straight rays. This model optimizes a simple parametric form for the geometric spreading based on the angle of reflection and the total travel distance. In the second method, a layered model of the subsurface combining the GS, scattering, and inelastic dissipation is employed. This model was described in detail in Chapter 3.

5.10.2 Empirical Geometrical Spreading

To derive an empirical geometric spreading function for the study area, I used the amplitudes of the direct waves. After experimenting with several functional dependences on time and spatial coordinates, the following geometrical-spreading function was selected:

$$F\left(D,\varphi\right)=\frac{1}{D^{\nu}\left(1+\beta\sin^{2}\varphi\right)}. \tag{5.10}$$

where D is the travel distance measured along a straight line connecting the source and receiver, and φ is the ray take-off angle measured relative to the downward vertical direction. Generally, because of the rays bending upward in the layered structure with velocities increasing with depth, and also because of the effects of backscattering and attenuation, we expected the exponent ν to slightly exceed one. Similarly, bending rays should lead to the angle correction parameter being negative, $\beta < 0$. The specific form of term $\sin^2\varphi$ selected in the denominator of

expression 5.10 was relatively arbitrary and based on considerations of: 1) symmetry with respect to the vertical direction and to the free surface and 2) similarity to the angle dependence of reflection amplitude.

With the geometrical spreading (5.10) and a simple offset VSP geometry with straight rays, the amplitude of the first arrival (purple ray in Figure 5.11) recorded on the vertical component equals:

$$u = S\,\frac{1}{D^{\nu}\left(1+\beta\sin^2\varphi\right)}\cos\varphi = S\,\frac{z}{D^{\nu+1}\left(1+\beta\sin^2\varphi\right)}, \tag{5.11}$$

where S is the source amplitude, z is the receiver depth, and D is the source-receiver distance. By fitting this law to the first-arrival amplitude data for the range of angles φ = 0–45° in all shots, I estimated $\nu \approx 1.2$ and $\beta \approx -0.8$ (Figure 5.12). These values are further used for both the baseline and monitor datasets below.

Further, for a reflection from a near-horizontal reflector, the recorded vertical-component response to a reflected P-wave (green arrow and pink rays in Figure 5.11) is:

$$u = SFR\left(\varphi\right)\cos\varphi, \tag{5.12}$$

where $R(\varphi)$ is the reflection AVA response, and the geometrical spreading factor equals:

$$F = \frac{1}{\left(d_1+d_2\right)^{\nu}\left(1+\beta\sin^2\varphi\right)} = \left(\frac{x}{\sin\varphi}\right)^{-\nu}\frac{1}{1+\beta\sin^2\varphi}. \tag{5.13}$$

Here, I also generalize the traditional geometrical-spreading formula for spherical wavefronts $1/D$ to $1/D^{\nu}$, and use the values of $\nu \approx 1.2$ and $\beta \approx -0.8$ estimated from the measurements of first-arrival amplitudes above. Consequently, the total "geometrical" factor for reflections is independent of the reflection time and medium velocity:

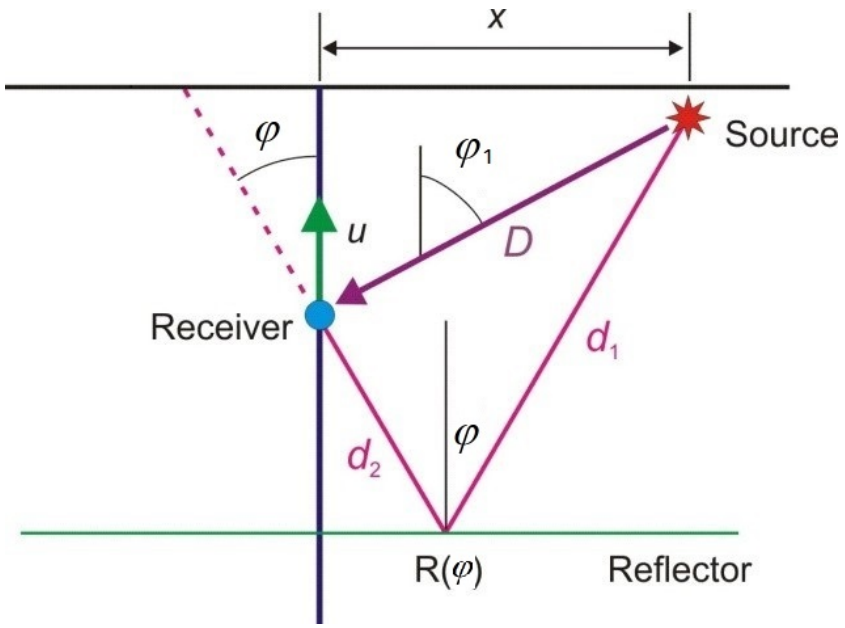

Figure 5.11. Modeled offset-VSP geometry. The VSP-to-CMP transform consists in adding to the VSP reflection time (pink ray) the time corresponding to the extension of this ray to the surface (dashed line). Labels also indicate the notation in equation 5.13. Purple ray corresponds to the first arrival, and D is the source-receiver distance.

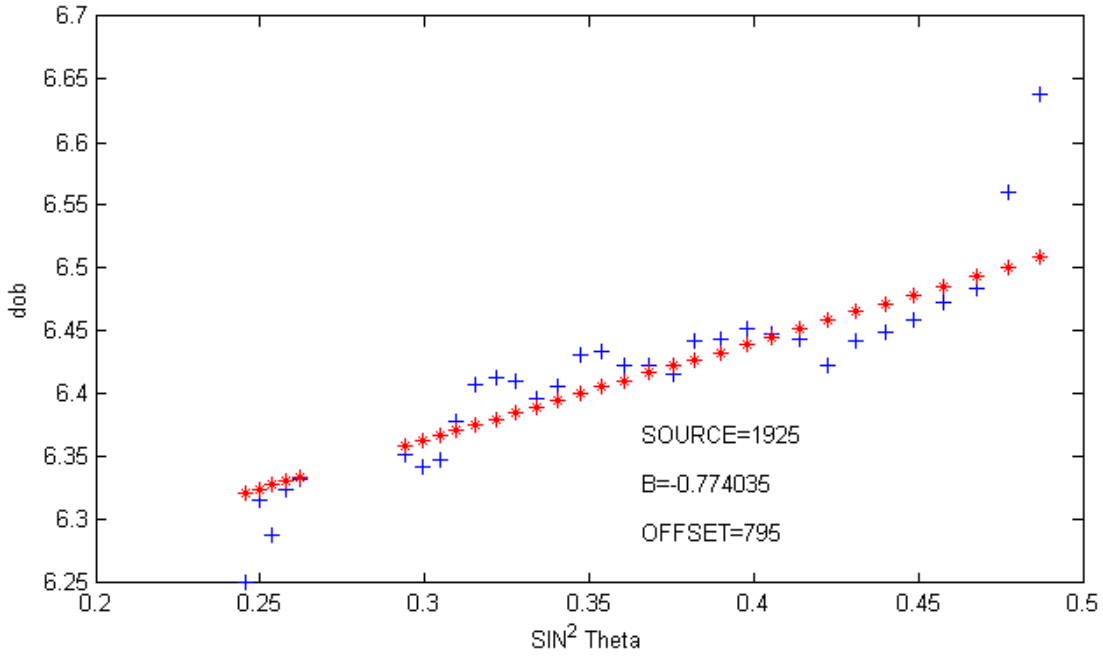

Figure 5.12: Example of first-arrival amplitudes (blue crosses) from one shot from dataset W1 and their fitting by eq. (5.11) (red).

$$F_{refl} = \cos\varphi \left(\frac{x}{\sin\varphi} \right)^{-\nu} \frac{1}{1+\beta \sin^2 \varphi}. \tag{5.14}$$

and the recorded pre-stack reflection amplitude can be modelled as:

$$u = SF_{refl} R(\varphi). \tag{5.15}$$

5.10.3 Combined model of Geometric Spreading, Scattering and Intrinsic Attenuation

The empirical GS method described in the preceding sections relies on a simple and frequency-independent straight-ray approximation. This method was used at the preliminary stages of VSP data analysis and the CDP-to CMP transform. In the AVA analysis, I used a more detailed GS model derived as part of the attenuation analysis in Chapter 3. This analysis resulted in a layered model of the subsurface combining the geometric spreading, scattering, and inelastic dissipation inverted from the first-arrival VSP amplitudes. In this Chapter, I assume that this model is also valid for reflected waves and extend the spreading model in Chapter 3 to downgoing and reflected rays in order to isolate the effects of the true reflected amplitude from the reservoir (5.11.1).

5.11 AVA analysis of time-lapse 3D VSP data:

In this Dissertation, I use the AVA as the primary effect from which the fluid-related variations near the reservoir can be detected in the VSP data. However, analysis of AVA effects is very challenging within the limited data coverage afforded by VSP acquisition, in which most subsurface locations are covered by only a single shot. At the same time, the spatial extent of VSP reflection-point coverage is also relatively limited. Therefore, I focused on measuring the AVA effects averaged over the entire area.

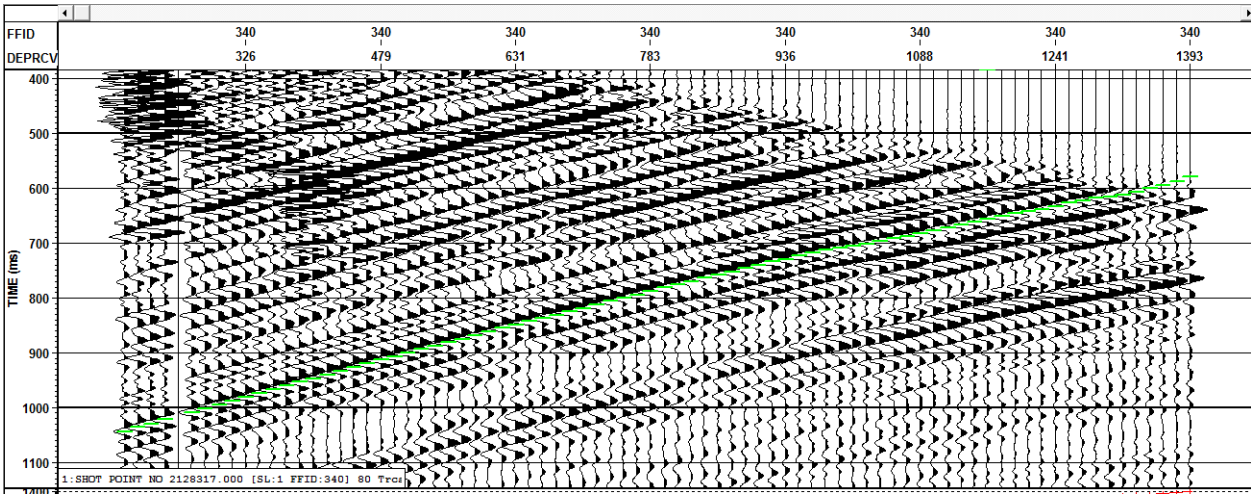

Figure 5.13. Picked travel-times of the top of Marly (green line) from an upgoing VSP shot (FFID 340) with 480 m offset from the VSP well.

The VSP-to-CDP transform intermixes the recorded amplitudes, and consequently they affect the AVA. Therefore, I performed an AVA analysis by using raw, vertical-component VSP records from the individual shots. In each of these shots, I predicted the expected travel-times of target reflections, and used them as a guidance for picking. The corresponding reflected arrivals were then carefully picked by using the modelled travel times (Figure 5.13). Along each of the picked reflection-moveout curves, I measured the peak-RMS (RMS between the zero crossings adjacent to the peak) amplitudes and tabulated them versus the incidence angles predicted by ray tracing for the corresponding depths and reflection times (Figure 5.13).

In addition to the reflected signal (5.15), random as well as coherent noise is present in the data. We can only account for the random part of the noise, by assuming that it is added to the signal incoherently, and consequently its energy is additive to the signal. It is convenient to denote the squared noise amplitude by $(Sn)^2$, where n is the noise-to-signal ratio. From the additive powers of the signal and noise, I obtain the following model for the recorded power u^2:

$$\frac{1}{S^2}u^2 = n^2 + \left[F_{refl}\left(I + G\sin^2\varphi\right)\right]^2, \tag{5.16}$$

where F_{refl} is the modelled geometrical spreading, intrinsic attenuation and scattering. The linear AVA expression (5.4) was also substituted for $R(\varphi)$. The factor $1/S^2$ in the left-hand side of this expression is specific to the entire shot, and it can be removed by normalizing the input values of u prior to the inversion. Thus, equation (5.16) gives an inverse problem for each shot, by solving which the values of n^2, I and G can be estimated.

The most important component of the above formula is F_{refl} which accounts for all geometric spreading, scattering and intrinsic attenuation for each ray travelling from the shot down to the reservoir and reflecting beck to each receiver level in the borehole. In order to accurately estimate F_{refl}, I use equation (3.3) describing the frequency-dependent attenuation coefficients accumulated along the rays for rays reflected from the reservoir (Figure 5.14).

5.11.1 AVA analysis model

I use the same six horizontal layers velocity model in Chapter 3 for performing ray tracing (Figure 3.2). In this model, rays were traced by using straight segments within each layer, and ray parameters were calculated by minimizing the errors between the observed and estimated travel times for reflections from Marly reservoir. Each layer is assigned a pair of anisotropic attenuation parameters γ and κ, after extended inversion provided earlier in details in Chapter 3. I performed the ray tracing for each shot reflected from Marly reservoir to each borehole receiver in order to calculate the reflected angle (ϕ) and the time spend in each layer ($t_i^{(j)}$) (Figure 5.14).

To obtain F_{refl}, I extended equation (3.11) to include the rays reflecting back from the Marly reservoir to each VSP receiver level:

$$F_{refl} = A_R(f)A_S(f)G_0(\Pi)\exp\left[-\chi^*(f,\Pi)\right], \tag{5.17}$$

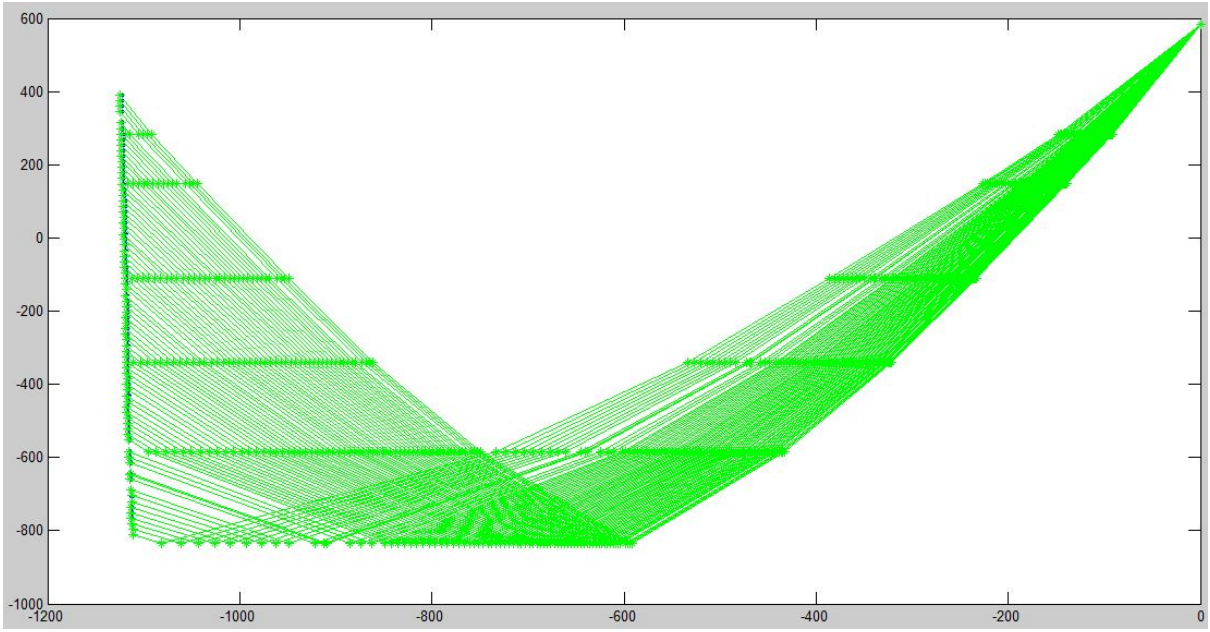

Figure 5.14. An example of ray tracing of a VSP shot at 1200 m offset from the VSP well.

where A_S and A_R are the source and receiver factors, $G_0(\Pi)$ is some "background" geometric spreading, the ray end time equals t, and the perturbation amount χ^* is accumulated along the ray:

$$\chi^*(f,\Pi) = \chi^* \equiv \int_{\text{Ray } j} \chi(f,t')dt', \tag{5.18}$$

where χ is the differential "intrinsic attenuation coefficient" (Morozov, 2010b). For a ray reflected from the layer m^{th} and reaching each level of VSP geophones (N_{layer}) χ^* can be written as:

$$\chi_j^* \equiv \sum_{i=1}^{m}\left[(\gamma_{1i} + f\,\kappa_{1i})t_i^{(j)} + (\gamma_{3i} + f\,\kappa_{3i})\bar{t}_i^{(j)}\right] + \sum_{i'=m}^{Nlayers}\left[(\gamma_{1i'} + f\,\kappa_{1i'})t_{i'}^{(j)} + (\gamma_{3i'} + f\,\kappa_{3i'})\bar{t}_{i'}^{(j)}\right] \tag{5.19}$$

where j is the number of the ray, $t_i^{(j)}$ is the travel time of the downgoing j^{th} ray in i^{th} layer, $\bar{t}_i^{(j)} = t_i^{(j)}\sin^2\varphi_i^{(j)}$ is the "horizontal" travel time, and $\varphi_i^{(j)}$ is the angle of the corresponding ray

segment relative to the vertical direction, and the summation is over all layers in the model. The same symbols marked with prime signs correspond to the upgoing (reflected) ray. The geophone response is factored as $A_{Rj}(f) = \Omega_j R_j A_G(f)$, where Ω_j is the directional factor (cosine of its orientation angle relative to the direction of wave propagation), $A_R(f)$ is the frequency response assumed to be the same for all geophones, and R_j is the scalar approximating the variation of geophone coupling within the VSP spread which obtained in Chapter 3. The receiver coupling obtained from equation (3.17) and source factor will be eliminated in AVA inversion process. Figure 5.15 and Figure 5.16 show examples of such solutions for reflections from the top of Marly in datasets W1 and W2. Such solutions were derived for every shot, and only solutions with consistent AVA responses (correlation coefficients exceeding 0.8 in Figure 5.15 and Figure 5.16) were used in further analysis.

5.11.2 Robust fitting method

For each VSP shot, the times of the reservoir reflection predicted in the layered velocity model. By superimposing these modeled times on the raw shot records, the actual reflection times from the reservoir are identified and picked. I use equation (5.16) for correcting the effects of spherical divergence, intrinsic attenuation and scattering. A modified “robust” fitting method (Walden,1991) similar to the method used for inverting the first-arrival travel times in Chapter 3, was employed for fitting the Shuey’s equation (equation (5.4)) to the corrected amplitudes. This method is superior to the least-squares method, because it is much less vulnerable to data outliers (Walden, 1991). The AVA inversion was performed in shot domain and the intercept, gradient and random noise factors we obtained by using equation (5.16).

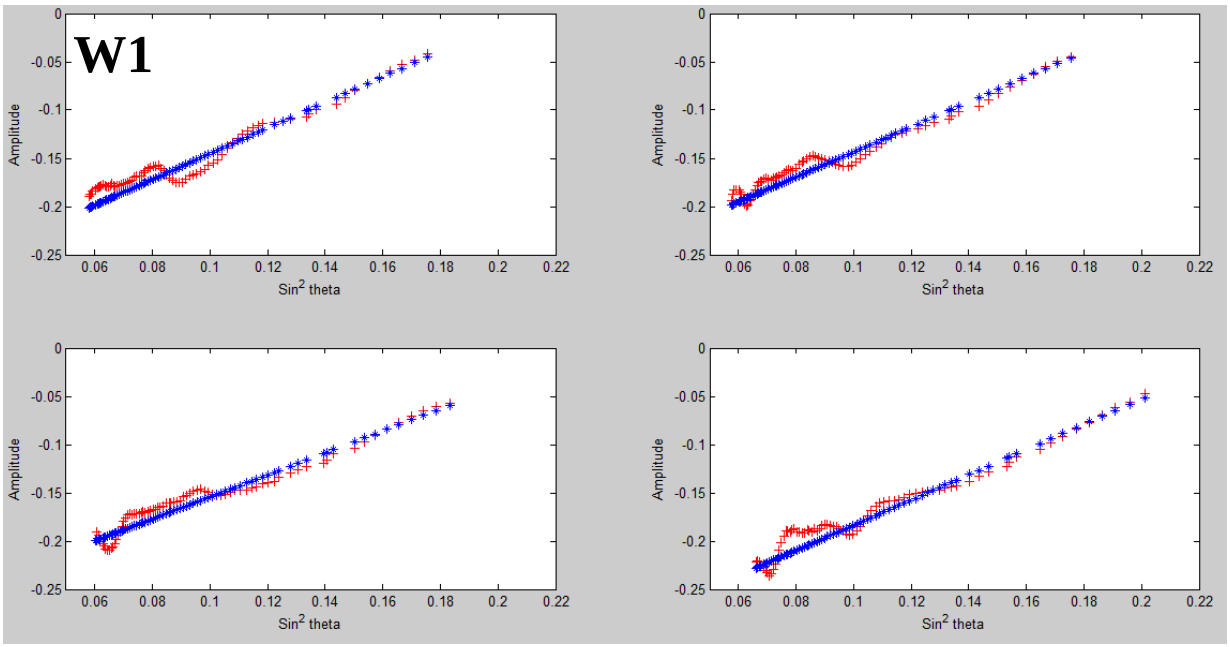

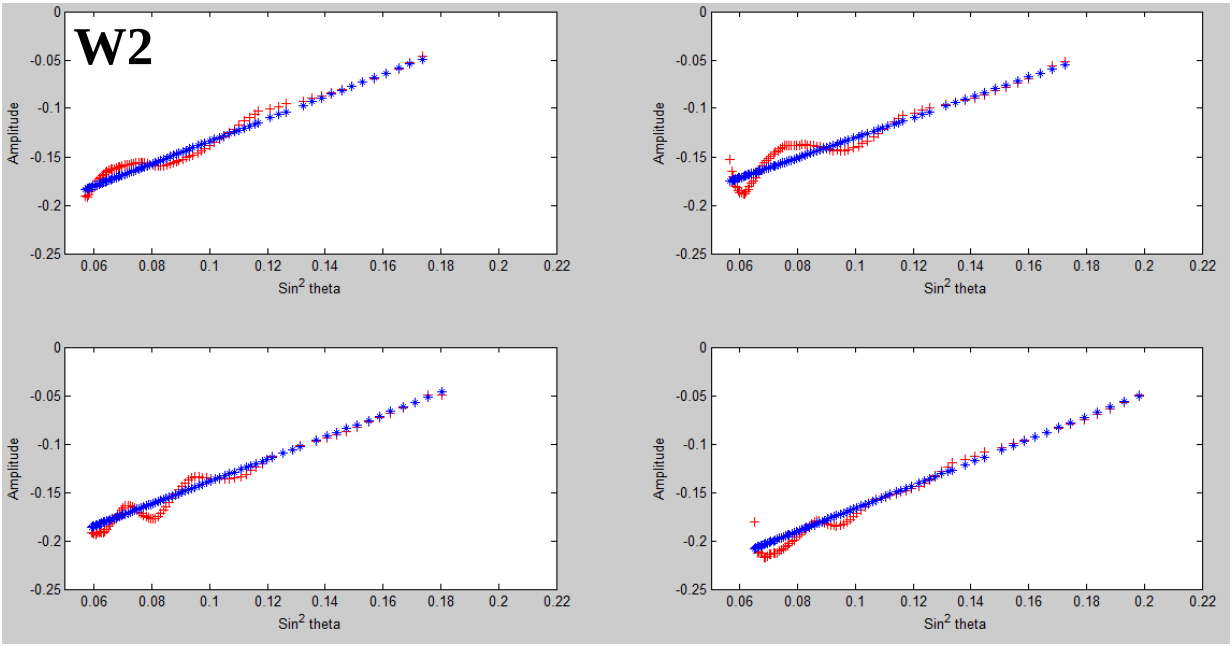

Figure 5.15: VSP AVA analysis measured on the reflector from Marly for four shots in baseline survey (W1) compared to monitoring survey (W2). Red dots show the picked amplitudes and blue dots are the amplitudes predicted by eq. (5.16).

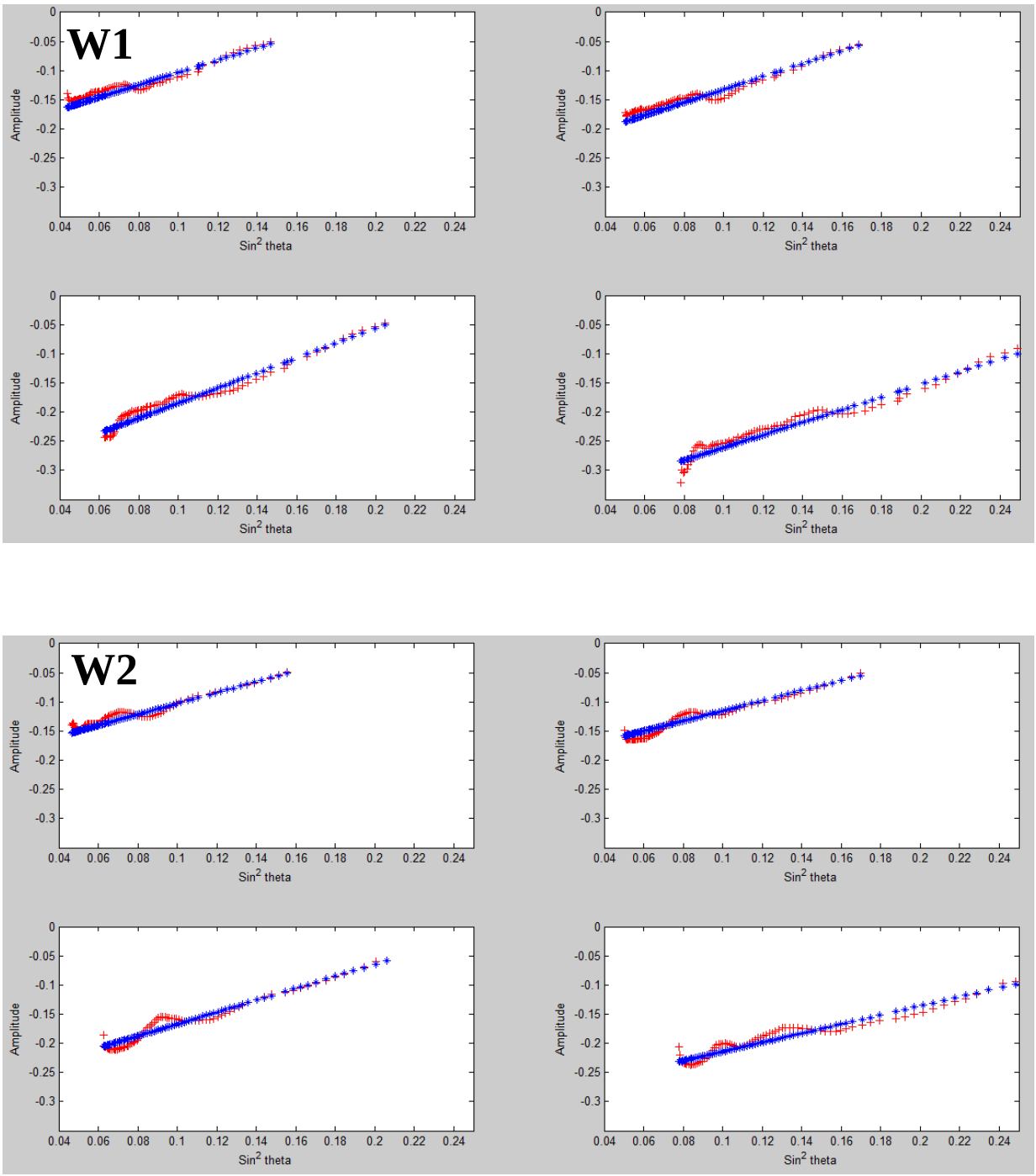

Figure 5.16: VSP AVA analysis measured on the reflector from Marly for four shots in baseline survey (W1) compared to monitoring survey (W2). Red dots show the picked amplitudes and blue dots are the amplitudes predicted by eq. (5.16).

5.12 AVA Results

Figure 5.15 and Figure 5.16 show examples of the amplitudes picked from Marly reservoir and corrected for geometrical spreading, scattering and intrinsic attenuation effects by using equation (5.16). These corrected amplitudes plotted versus angles up to 30° angles. The results show a linear dependence of the amplitudes on $\sin^2$(*incidence angle*). Therefore the two-term Shuey (equation (5.4)) should be suitable as the primary method for interpreting the results. The AVA attributes (intercept *I* and gradient *G*) can be assigned to reflection points located half-way between the surface positions of the shots and borehole receivers. Using the obtained intercepts and gradient, different attributes can be obtained which are important for estimating pressure and saturation changes of injected CO_2 in the reservoir. Table 5.2 summarizes some of these attributes and expected seismic response from the top of Marly to pressure and CO_2 saturation changes. In the following section, I propose several techniques for detecting CO_2 pressure and saturation effects from VSP AVA observations.

5.12.1 AVO cross-plots

Cross-plotting AVO/AVA attributes can provide valuable assessment of the AVA anomalies related to a background trend. My principal goal in this analysis is to measure the variations in the (*I*,*G*) attributes and identify the regions in which the anomalies of *I* and *G* are correlated (as related to pressure variations) or anti-correlated (when caused by variations in saturation; Section 5.4).

Plotting the AVA intercepts and gradients in the form of a cross-plot helps identifying the anomalous values that might be related to CO_2 flooding. In the AVA model (Figure 5.8), I showed that effects of CO_2 injection can be seen as separation of AVA response of monitoring survey from the baseline in AVA cross plot. Figure 5.17 shows an AVA cross plot for the

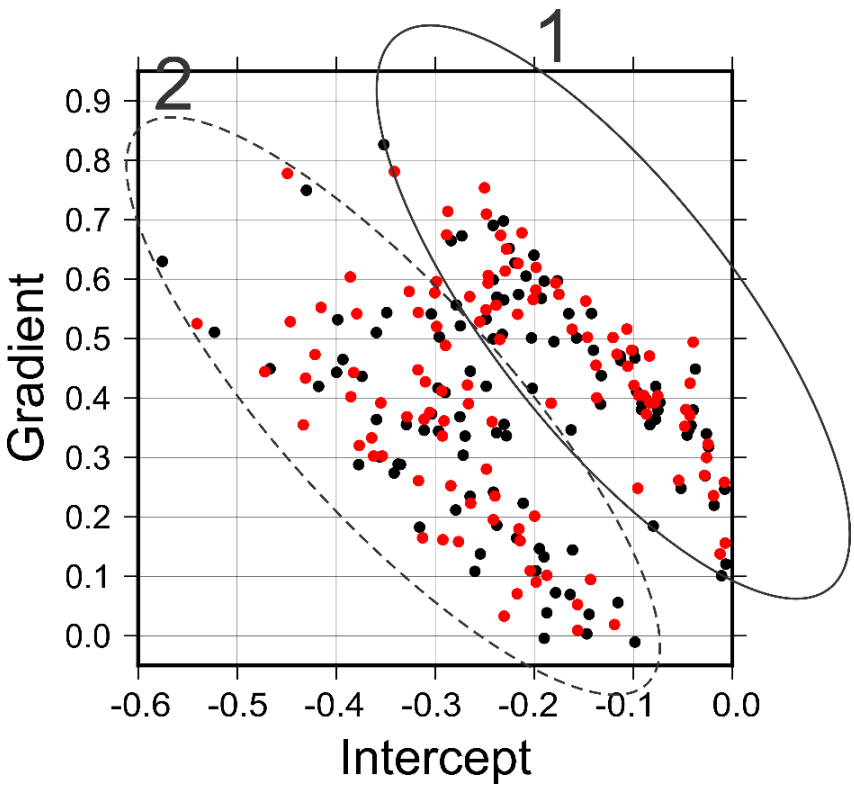

Figure 5.17: AVA Cross-plot of Weyburn VSP datasets at Marly reservoir level. Black dots represent the baseline VSP survey (1999) and red dots show the monitoring dataset (2001) containing CO_2. Two trends detected in the cross-plot are marked by ellipses labeled 1 and 2.

baseline and monitoring surveys. Two distinct trends in AVA response can be observed in this cross-plot, which are also correlated to the locations of AVA reflection sampling (Figure 5.17). The first trend (designated as “trend 1” hereafter; Figure 5.17) matches better with the area between two injection well patterns, while the second trend (“trend 2”) mostly correlates with the areas close to the injection well patterns (Figure 5.18). Furthermore, we subdivide the VSP area into four areas illustrated by letters A, B, C, and D in Figure 5.18. These areas are located in the southeast, southwest, northwest and centre area of the reflection coverage area, respectively (Figure 5.18).

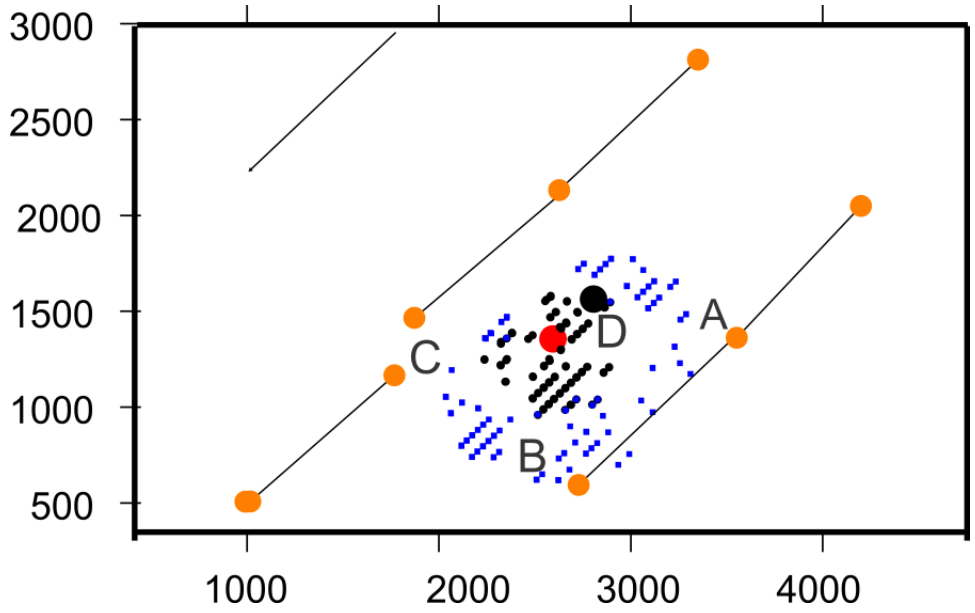

Figure 5.18: Areal extension of trend 1 (blue) and trend 2 (back) in the AVA cross-plot in Figure 5.17. For interpreting the pressure and saturation effects, the area of VSP reflections is subdivided to four zones labeled A, B, C and D.

5.12.2 AVO attributes

In this subsection, I discuss how the variations of (*I*,*G*) attributes observed in Figure 5.17 could be related to the variations of CO_2 pressure and saturation within the reservoir.

AVO intercept (*I*)

AVO Intercept (*I*) is one of the key attributes in AVA interpretation. The intercept gives a more accurate determination of $R_{P(0)}$ than the conventional P-wave stack, which represents an average of R_P over the recorded range of offsets. In Weyburn reservoir, a general decrease in the intercept values is expected as the result of CO_2 pore pressure and saturation increase (Table 5.2). This prediction agrees with what is observed from the intercept map at Marly reservoir level before and after CO_2 injection (Figure 5.19). Figure 5.19 shows a general decrease of intercept trend for the monitoring survey, with stronger differences between W2 and W1 occurring around the injection wells (trend 1) and negligible differences between two well

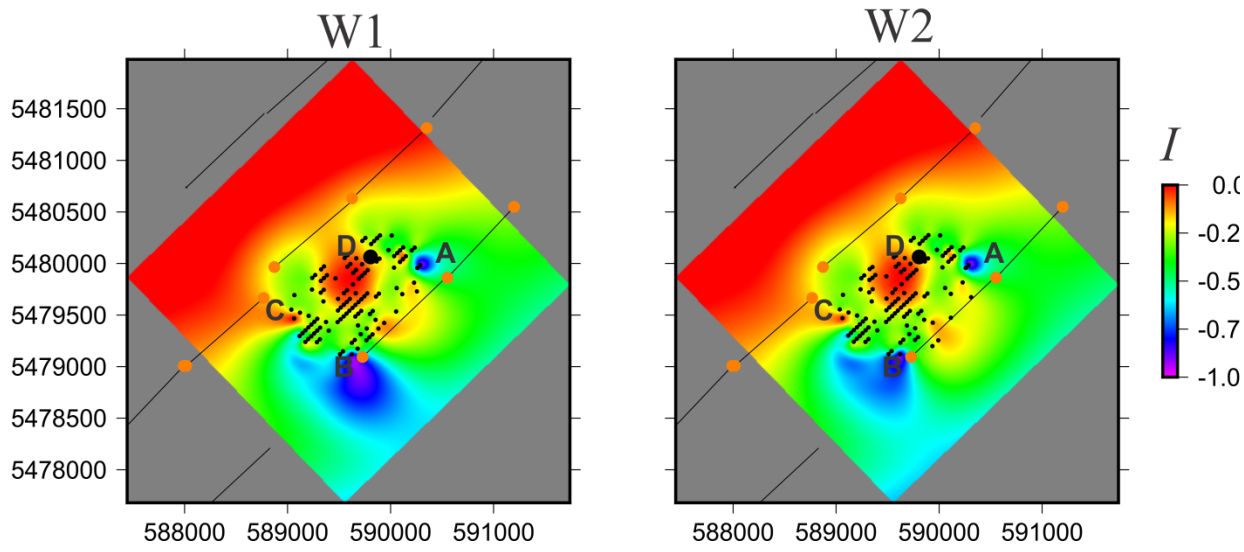

Figure 5.19: AVA intercept (*I*) at Marly reservor level for baseline (left) and monitoring (right) VSP data. Note that except for the central area, the values of *I* decreases after CO_2 injection.

patterns (trend 2). However, interpreting based on only one attribute (*I*) may not be very accurate, and we need to consider the attribute *G*.

AVO gradient (*G*)

Another useful AVA attribute which is also sensitive to the fluid content within the reservoir, is the gradient *G*. In Weyburn reservoir, gradient values are expected to increase in response to increasing pore pressure but to drop as the result of CO_2 saturation increase. My results for *G* (Figure 5.20) show both increasing and decreasing values at different locations within the trend 1 area (close to the injection wells). The AVA gradients decrease in the southeast corner of trend 1 area (A) but increase in the area close to C. The gradients also show a slight increase in area B, and no visible changes in the central area (D).

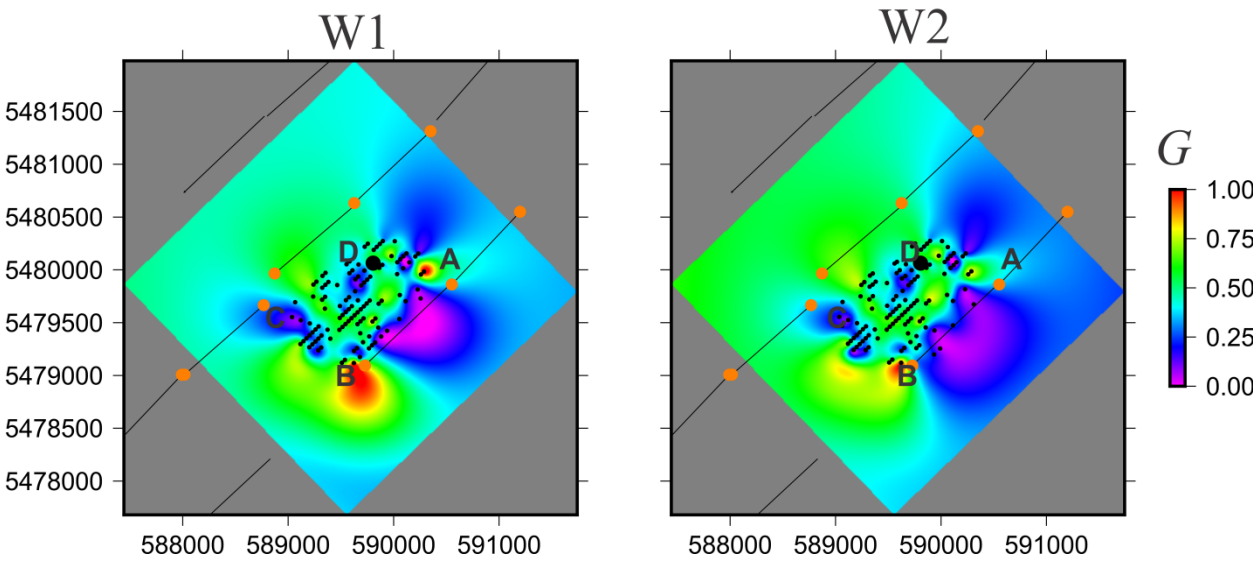

Figure 5.20: Gradient attribute (*G*) at Marly reservor level for baseline (left) and monitoring VSP survey (right). It can be noticed gradiant attriute changes after CO_2 injection in most areas around the well pattern.

S-wave reflectivity (*S*)

An increasing CO_2 saturation should not have any effect on the S-wave reflectivity, but increasing CO_2 pore pressure will decrease S-wave reflectivity (Section 5.5). Figure 5.21 shows the S-wave reflectivity estimated by equation (5.5) for the baseline and monitoring surveys. It appears that the S-wave reflectivity decreases in areas A and B in patterns parallel to the injection wells. This increase could be due to pore pressure increasing in these zones. However, no major changes are observed in other parts of the study area. This may suggest an increase in the CO_2 pore pressure close to the injection wells within the southern part of the coverage area.

***I+G* Attribute**

In contrast to the S-wave reflectivity, an increase in the CO_2 pore pressure should have no effect on the attribute (*I*+*G*), but increasing CO_2 saturation would decrease this attribute (Sections 5.4 and 5.5). Figure 5.22 shows the (*I*+*G*) attribute before and after CO_2 injection. Note

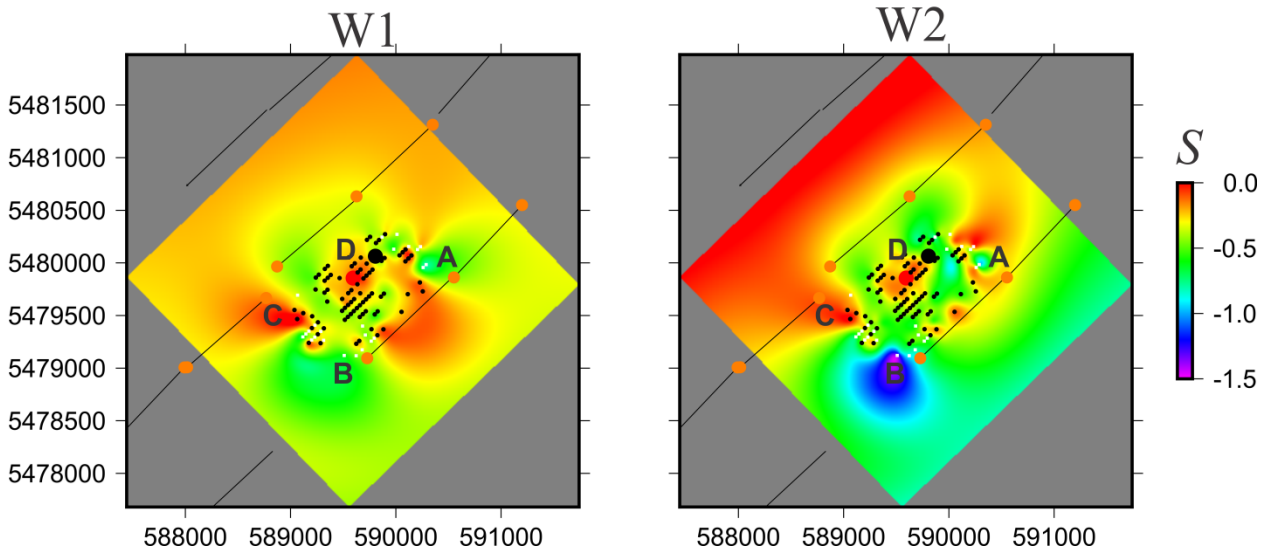

Figure 5.21: S-wave reflectivity attribute (*S*) at Marly reservor level for baseline (left) and monitoring VSP data (right). The decreasing S wave reflectivities between W1 and W2 may indicate increasing pore pressure.

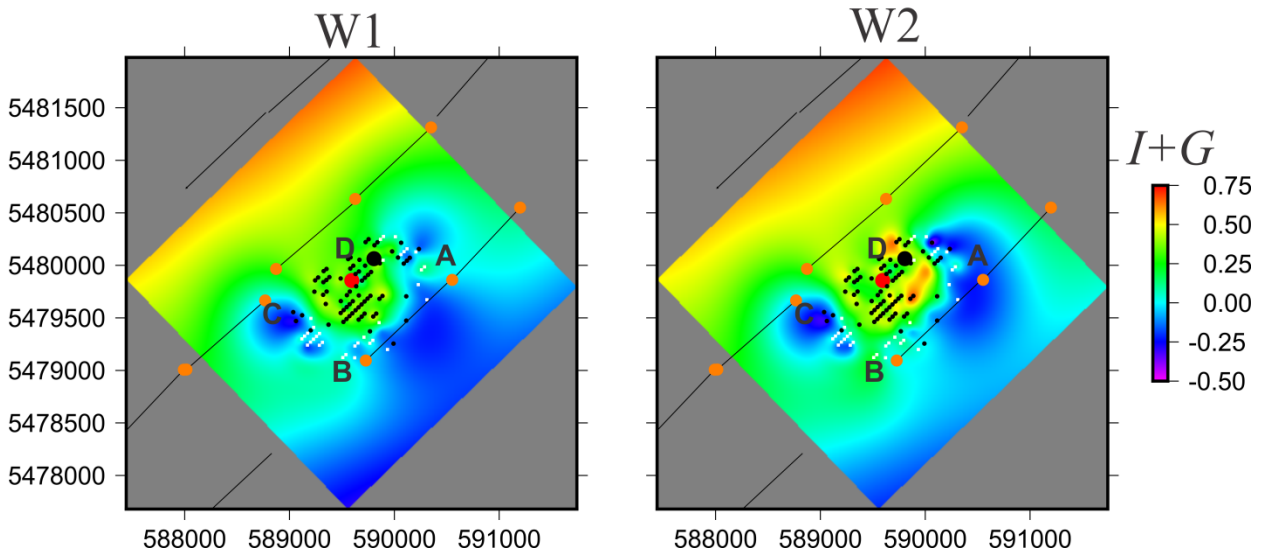

Figure 5.22: (*I*+*G*) attribute at Marly reservor level for baseline (left) and monitoring (right) VSP data. Note that area C and a part of area A show a decrease of the (*I*+*G*) attribute after CO_2 injection (W2). No significant changes can be observed in other areas. These variatuions suggest an increase in CO_2 saturation changes in the northwestern and eastern parts of of the survey.

that area C and a part of area A show a decrease of the (I+G) attribute after CO2 injection, while no major changes are observed in other areas. This observation may indicate an increasing in CO2 saturation within the northwestern and eastern parts of the survey.

5.13 Qualitative AVA interpretation in Weyburn VSP area

The qualitative interpretation is based on the general patters of the variations of the different AVA attributes from the baseline to monitoring surveys. Based on Table 5.2, the combination of changes in intercept, gradient, S wave reflectivity and (*I*+*G*) attributes suggest distinct areas affected by CO_2 pressure or saturation changes. Figure 5.23-Figure 5.26 show the changes in above attributes from baseline to monitoring surveys. In the following, I investigate the changes in AVA attributes in four different zones (A, B, C and D) in VSP area in order to draw a conclusion over changes in CO_2 pressure and saturation.

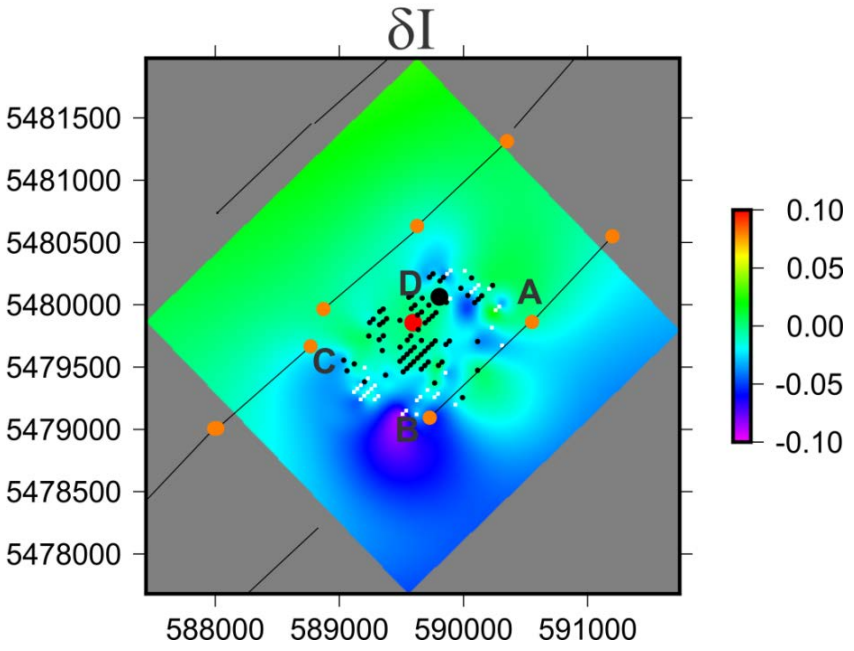

Figure 5.23: Differences in intercept attribute *I* from the baseline to monitoring survey (W2-W1). The attribute *I* decrease in most zones close to the injection well patterns.

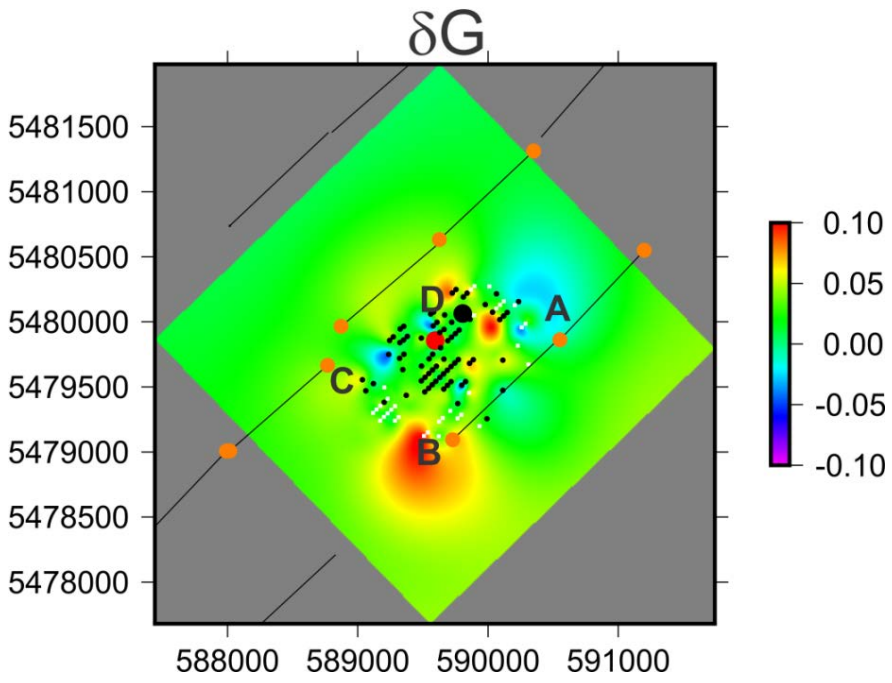

Figure 5.24: Differences in gradient attribute G from baseline to monitoring survey (W2-W1). This attribute is expected to increase with increasing pore pressure and decrease as a result of CO_2 saturation.

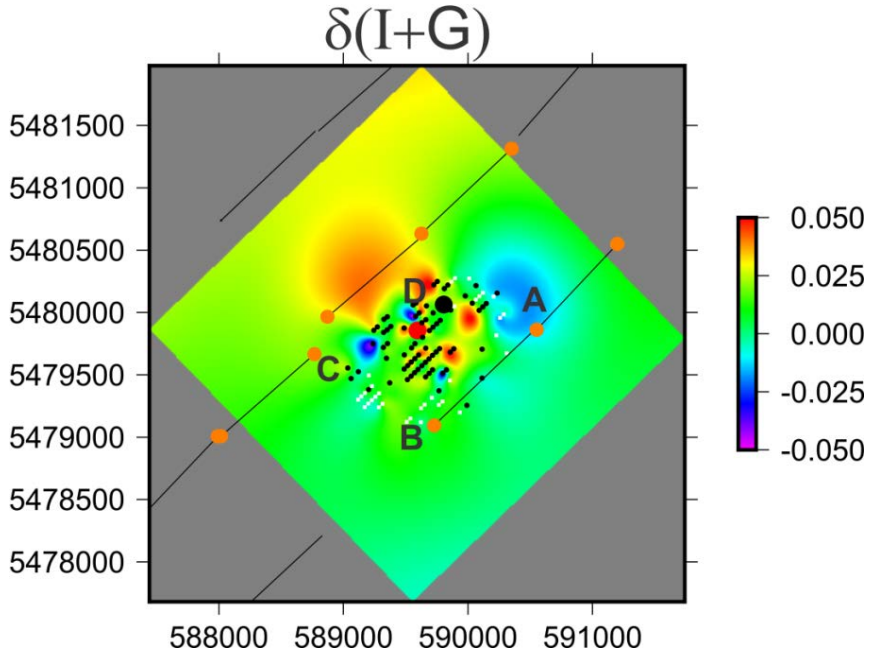

Figure 5.25: Differences in (*I*+*G*) attribute from baseline to monitoring survey (W2-W1). The (*I*+*G*) attribute decreases in areas A and C, which may suggest an increase in CO_2 saturation in these areas.

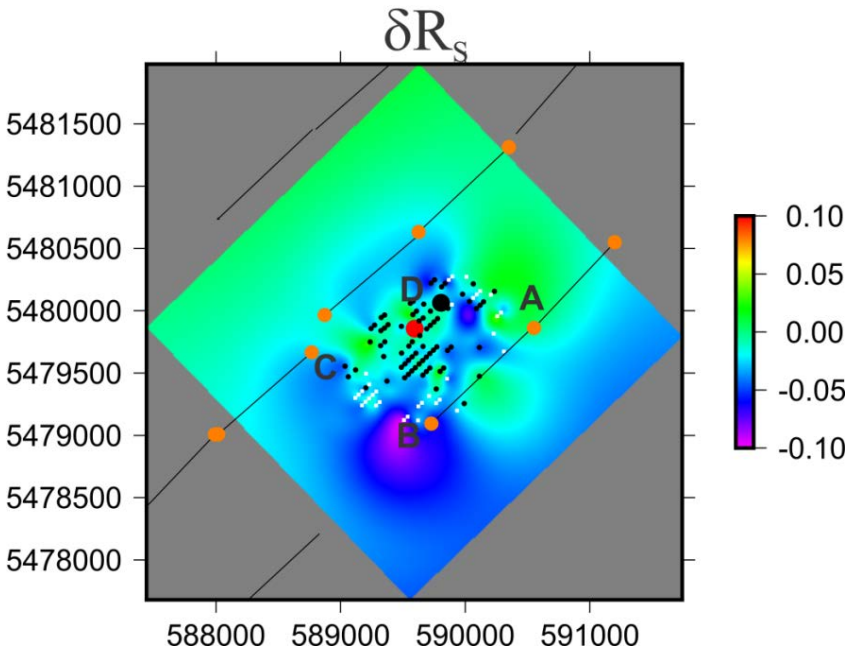

Figure 5.26: Differences in the S wave reflectivity from baseline to monitoring survey (W2-W1). The S wave reflectivity decreases in area B, close to the southwestern injection well pattern. This increase may be an indicator of pore pressure increasing in this area.

5.13.1 Area A: (Southeast)

The area A is located close to the eastern injection well pattern. The gradient (*G*) and (*I*+G) attributes decrease in this area (Figure 5.24 and Figure 5.25). However, S-wave reflectivity shows no considerable changes in this region (Figure 5.26). As shown in Table 5.2, all of this evidence may indicate that in this area, saturation effects are dominant over the pore pressure effects.

5.13.2 Area B (Southwest)

This area is close to the southwestern injection well and extends parallel to the southern well pattern to the east. The gradient increases in this area (Figure 5.24), while the intercept decreases (Figure 5.23). The (*I*+*G*) attribute does not change between the surveys W1 and W2

over this area (Figure 5.25), while the S wave reflectivity shows small decrease (Figure 5.26). All of these changes indicate pore pressure increasing effects as the result of CO_2 injection.

5.13.3 Area C (Northwest)

This area is close to the injection well located in the northwestern part of the study area. The gradient and (I+G) attribute decreases in this area (Figure 5.24 and Figure 5.25). However, S-wave reflectivity shows no considerable changes in this area (Figure 5.26). All of these observations suggest that the CO_2 saturation effects dominate the pore pressure effects in this area.

5.13.4 Area D (Centre Area)

In the central area, generally very small changes in intercept and gradient attributes are observed. Therefore, all resulting attributes (I+G, and S wave reflectivity) show almost no changes due to CO_2 injection. It seems that these areas are the least affected by CO_2 injection. However, some changes in neighbouring area can still be noticed. For example, the S-wave reflectivity decreases in this area in the vicinity of the injection well in the northeastern part of the survey.

5.14 Quantitative AVA Interpretation of Weyburn VSP

In this Section, I attempt further quantitative analysis of the anomalies described in Section 5.12. Figure 5.27 shows the directions of CO_2 pore pressure and saturation effects on a cross-plot display (ΔI, ΔG) in Marly reservoir based on the AVA model in Section 5.5 (Figure 5.8a). Based on this model, increasing pore pressure decreases AVA intercept and increases gradient. However, increasing CO_2 saturation decreases both intercept and gradient.

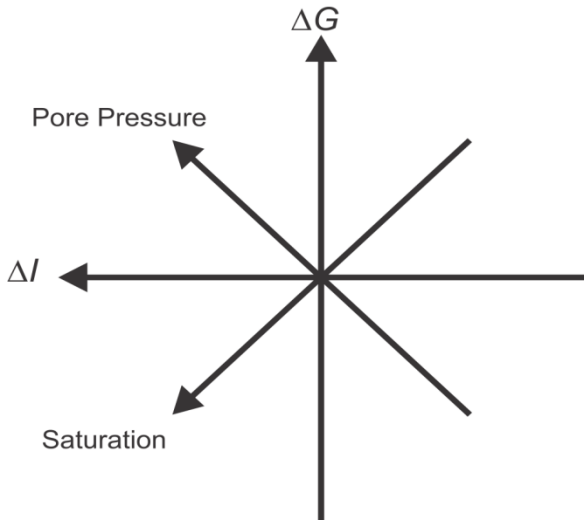

Figure 5.27: Schematic plot of the AVA intercept and gradient anomalies expected from CO_2 pore pressure and saturation variations.

Figure 5.28 shows a cross-plot display of intercept and gradient values for Marly reservoir for the baseline and monitoring surveys. Negative intercepts and positive gradients values in it agree with the model shown in Figure 5.8. The important question is how to estimate a CO_2 discriminator line (pink in Figure 5.8) for Weyburn dataset.

Figure 5.10a shows the dependence of the slope of CO_2 discriminator line (dG/dI) on the different frequencies of the modeled Ricker wavelet. The wavelet of VSP Weyburn data can be best approximated by a 40-Hz Ricker wavelet, and therefore, G/I ratio of the discriminator line can be estimated as ~1.74 (Figure 5.10a).

For this G/I ratio, Figure 5.10b gives a ratio of (G_{0C}/I_{0C}) equal to -0.8. Using these values, I draw several lines with different I_{0C} and G_{0C} (Figure 5.28). Based on the AVA cross-plots for the baseline and monitoring datasets, it seems that the thick pink line in Figure 5.28 can be a good choice for this discriminator. There are some uncertainties in determining the values of I_C,G_C, as shown by the dashed lines in Figure 5.28. Once a CO_2 discriminator line is determined,

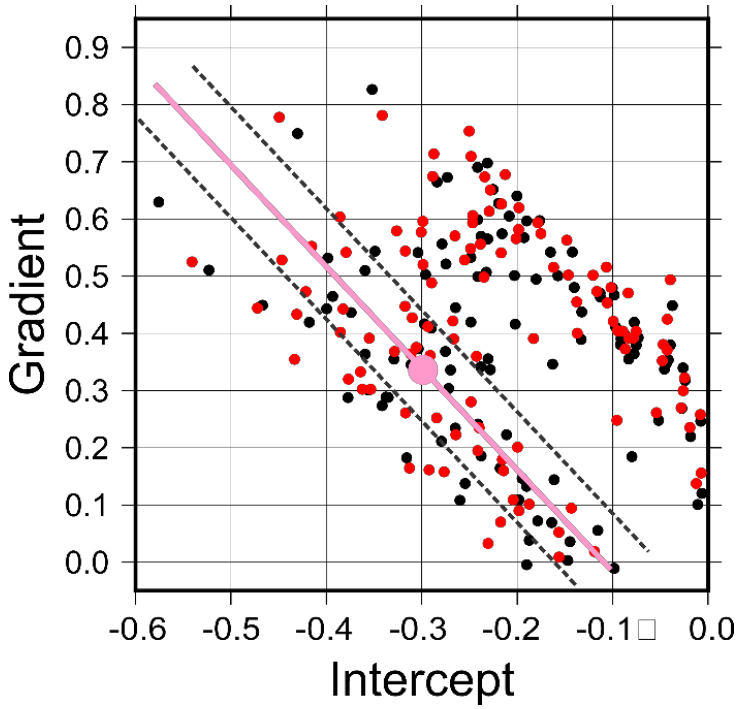

Figure 5.28: Cross-plot of the intercept and gradient for baseline (black dots) and monitoring (red dots). The possible CO_2 discriminator line is drawn as a pink line. Dashed lines show a rough estimate of the uncertainties of the discriminator line.

the next question to consider is how to separate the effects of CO_2 pore pressure and saturation quantitatively.

To construct an attribute differentiating between the pore-pressure and saturation effects, I define a new "CO_2 proxy" attribute, which illustrated as in Figure 5.29 (Baharvand Ahmadi et al., 2011).

Starting from the CO_2 discriminator, I construct a pair of deviations ("principal components") of (I,G) along and across its trend line:

$$\delta P_1 = G_0 - G_C, \text{ and } \delta P_2 = I - I_0, \tag{5.20}$$

where (I_C,G_C) is the centre of the distribution of all (I,G) values, and (I_0,G_0) is the projection of point (I,G) onto the trend line (Figure 5.29). Figure 5.30 shows AVA cross-plots of intercept and gradient for baseline and monitoring surveys with the empirical CO_2 discriminator trend and an

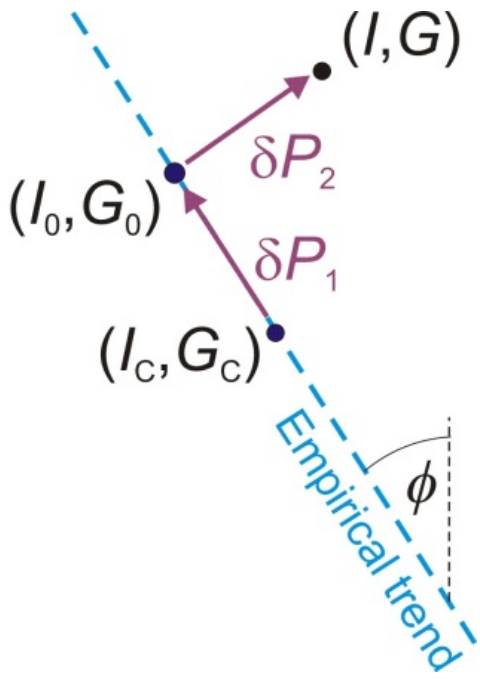

Figure 5.29. Construction of empirical proxy attributes emphasizing the deviations of AVA parameters along (δP_1) and across the trend line (δP_2). (I,G) is the measured AVA point, (I_0,G_0) is its projection onto the trend, and (I_C,G_C) is the centre of the distribution of all (I,G) points.

orthogonal direction used as a proxy CO_2-saturation attribute. Positive values (red colours in the plots below) of δP_1 and δP_2 correspond to the directions of increasing pressure and decreasing CO_2 saturation, respectively, as shown in Figure 5.31-Figure 5.32. The desired "CO_2 proxy" is therefore implemented by the new attribute ($-\delta P_2$). A differential attribute comparing the values of δP_1 and δP_2 in the monitor to baseline dataset is shown in Figure 5.33-Figure 5.34.

In these images, we are principally looking for negative values (purple), which would be related to increasing CO_2 saturation. Such areas are found along the southern CO_2 injector wells (Figure 5.34).

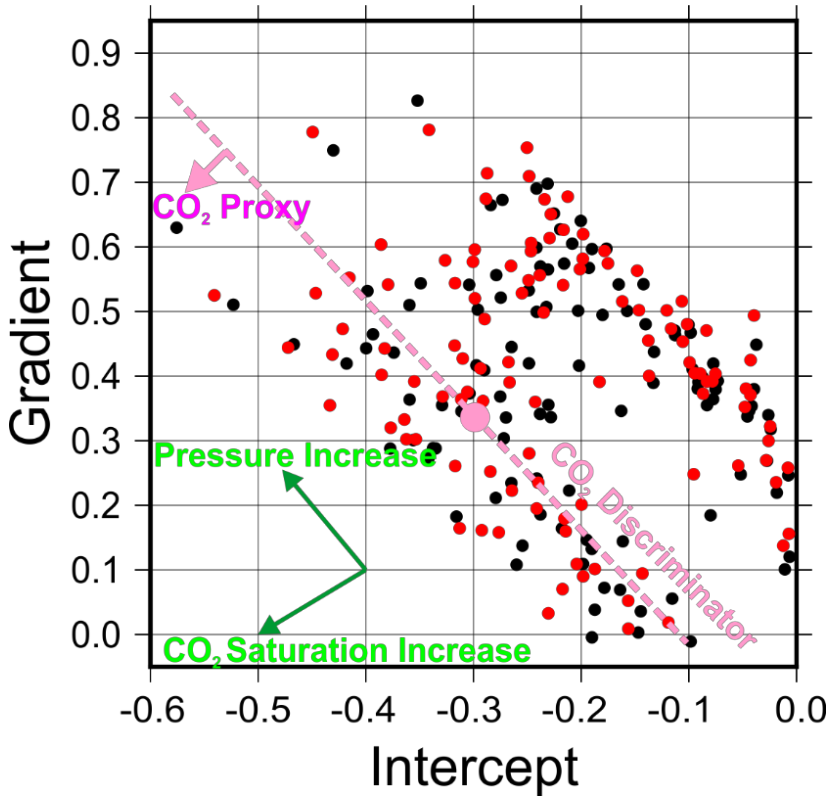

Figure 5.30: Cross-plots of AVA parameters *I* and *G* for Marly reflectors within the study area. Pink line indicate the empirical trend and an orthogonal direction used as a proxy CO_2-saturation attribute.

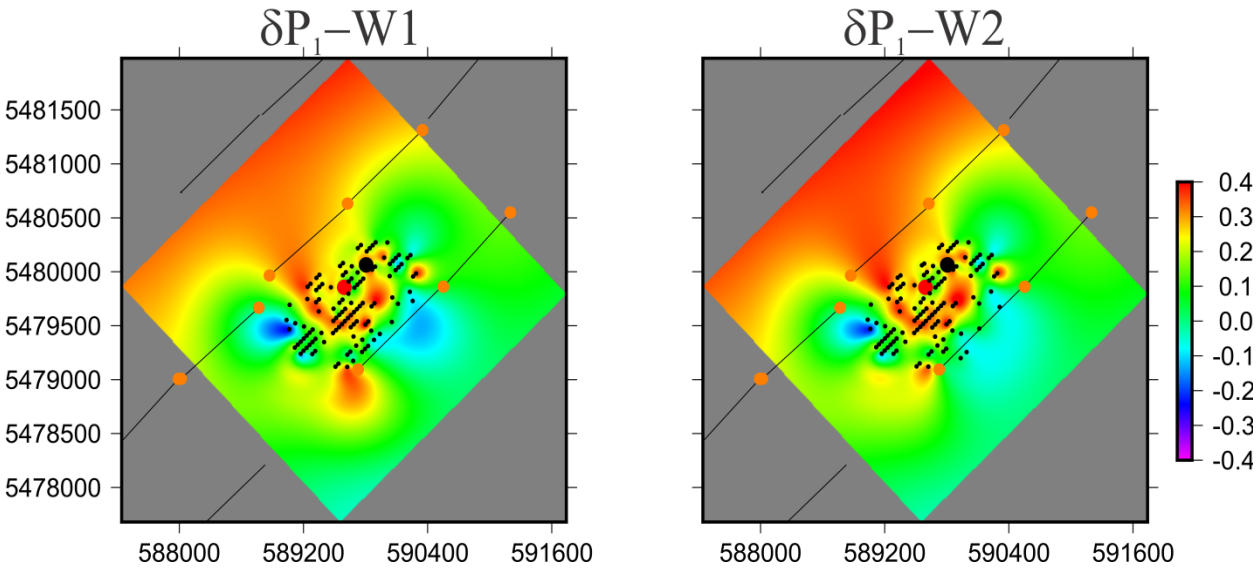

Figure 5.31: Attribute δP_1 for Marly reflection, for baseline (left) and monitoring survey (right).

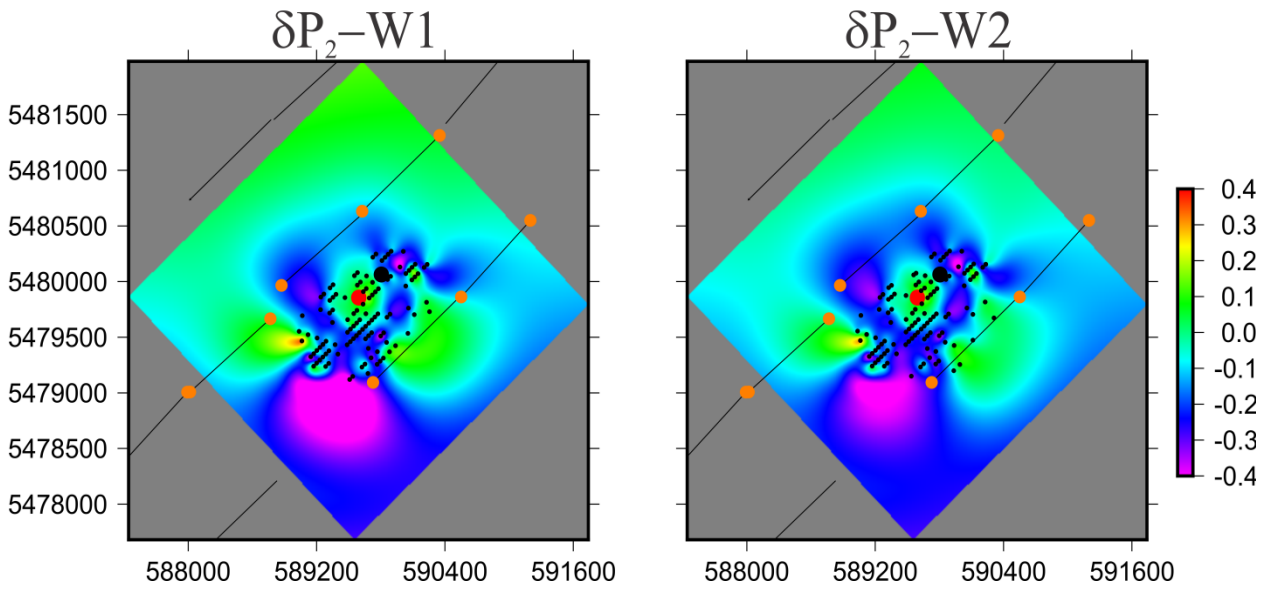

Figure 5.32 Attribute δP_2 for Marly reflection, for baseline (left) and monitoring survey (right).

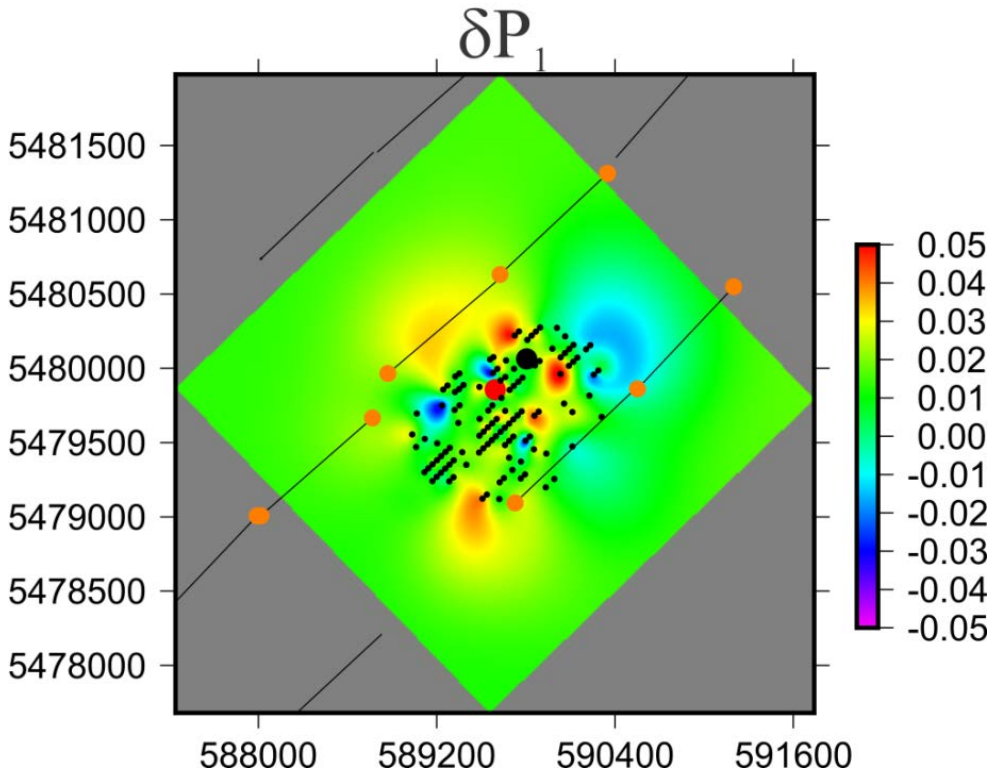

Figure 5.33: Differential attribute comparing the values of δP_1 (colour bar) for the monitor to baseline dataset. Positive values representing increasing CO_2 pressure.

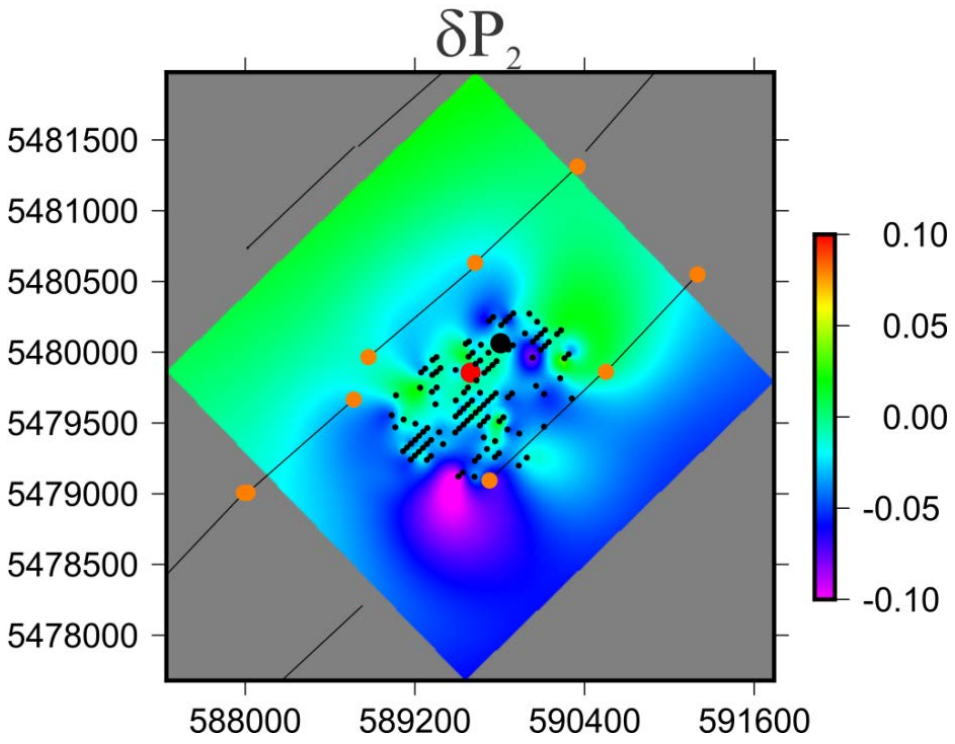

Figure 5.34: Differential attribute comparing the values of δP_2 in the monitor to baseline dataset. Negative values representing increasing CO_2 saturation in the injected area.

5.15 Separating CO_2 pressure and saturation effects

In subsection 5.13, I proposed a CO_2 discriminator line using a cross-plot of the measured AVA responses. The ultimate goal of this project is to quantify the CO_2 pressure and saturation in VSP area. To achieve this goal, I use a similar approach similar to Landrø (2001). Let us start from the same two-layer model as in the beginning of this Chapter (Table 5.3). This model represents an anhydrite/Marly interface, which is the upper boundary of the reservoir. I will consider two cases: 1) when the pressure is constant within Marly reservoir and the CO_2 saturation changes, and 2) when the CO_2 saturation is considered constant and pore pressure changes. I will also assume that the P and S wave velocities and density (V_{P1}, V_{S1} and ρ_1) within

the cap rock are unchanged after CO_2 injection. Within the reservoir, these parameters become V_{P2}', ρ_2' and V_{S2}' after CO_2 injection. Therefore, the change in P wave velocity as a result of CO_2 saturation in the reservoir is:

$$\Delta V_P{}^F = V_{P2}' - V_{P2}, \tag{5.21}$$

From Smith and Gidlow (1987) the reflection coefficient for the baseline survey can be estimated as:

$$R_0(\theta) = \frac{1}{2}\left(\frac{\Delta\rho}{\rho} + \frac{\Delta V_P}{V_P}\right) - \frac{2V_S{}^2}{V_P{}^2}\left(\frac{\Delta\rho}{\rho} + \frac{2\Delta V_S}{V_S}\right)\sin^2\theta + \frac{\Delta V_P}{2V_P}\tan^2\theta, \tag{5.22}$$

where V_P, V_S and ρ are the average parameters of P wave, S wave and density for layer 1 and layer 2. The reflection coefficient after CO_2 injection in layer 2 becomes:

$$R_1(\theta) = \frac{1}{2}\left(\frac{\Delta\rho'}{\rho'} + \frac{\Delta V_P'}{V_P'}\right) - \frac{2V_S'^2}{V_P'^2}\left(\frac{\Delta\rho'}{\rho'} + \frac{2\Delta V_S'}{V_S'}\right)\sin^2\theta + \frac{\Delta V_P'}{2V_P'}\tan^2\theta, \tag{5.23}$$

where

$$\Delta V_P' = V_{P2}' - V_{P1} = V_{P2} + \Delta V_P{}^F - V_{P1} = \Delta V_{P1} + \Delta V_P{}^F, \tag{5.24}$$

The above equation (5.24) can be similarly written for $\Delta\rho^F$. Assuming $\frac{\Delta V_P}{V_P} \ll 1$, and $\frac{\Delta V_P{}^F}{V_P} \ll 1$, and also ignoring higher-order terms in either $\frac{\Delta V_P}{V_P}$ or $\frac{\Delta V_P{}^F}{V_P}$, or combinations of them, equation (5.24) can be written as (Landrø, 2001):

$$R_1(\theta) = \frac{1}{2}\left(\frac{\Delta\rho}{\rho} + \frac{\Delta V_P}{V_P}\right) - \frac{2V_S{}^2}{V_P{}^2}\left(\frac{\Delta\rho}{\rho} + \frac{2\Delta V_S}{V_S}\right)\sin^2\theta + \frac{\Delta V_P}{2V_P}\tan^2\theta + \frac{1}{2}\left(\frac{\Delta\rho^F}{\rho} + \frac{\Delta V_P{}^F}{V_P}\right)$$

$$-\frac{2V_S{}^2}{V_P{}^2}\left(\frac{\Delta\rho^F}{\rho} + \frac{2\Delta V_S{}^F}{V_S}\right)\sin^2\theta + \frac{\Delta V_P{}^F}{2V_P}\tan^2\theta, \tag{5.25}$$

where the ratio of shear wave velocity to P-wave velocity is:

$$\frac{V_S'}{V_P'} = \frac{V_S\left(1+\frac{\Delta V_S{}^F}{2V_S}\right)}{V_P\left(1+\frac{\Delta V_P{}^F}{2V_P}\right)} \approx \frac{V_S}{V_P}, \tag{5.26}$$

where we also ignore all the second-order terms. If the term proportional to $\sin^2\theta$ in equation (5.2) does not change because of fluid substitution, the shear modulus can be assumed constant, which leads to the following equation for fluid substitution (Landrø, 2001):

$$\frac{\Delta\rho^F}{\rho} + \frac{2\Delta V_S{}^F}{V_S} = 0 \tag{5.27}$$

Therefore, for fluid substitution, the equation (5.22), becomes:

$$R_1(\theta) \approx R_0(\theta) + \frac{1}{2}\left(\frac{\Delta\rho^F}{\rho} + \frac{\Delta V_P{}^F}{V_P}\right) + \frac{\Delta V_P{}^F}{2V_P}\tan^2\theta, \tag{5.28}$$

and the change in P wave reflectivity in first-order is:

$$\Delta R^F(\theta) \approx \frac{1}{2}\left(\frac{\Delta\rho^F}{\rho} + \frac{\Delta V_P{}^F}{V_P}\right) + \frac{\Delta V_P{}^F}{2V_P}\tan^2\theta \tag{5.29}$$

In the second case, when pressure increases in the reservoir, the density increases. Figure 5.35 shows the changes in density as the result of pressure variations in Marly reservoir. This graph suggests that the pressure-related changes in the density are only about 2% over a 20-MPa pressure increase in the reservoir. This density variation is relatively small and can be ignored. Therefore, the corresponding equation for the pressure changes in the reservoir will be:

$$\Delta R^P(\theta) = \frac{1}{2}\frac{\Delta V_P{}^P}{V_P} - \frac{2V_S{}^2}{V_P{}^2}\frac{2\Delta V_S}{V_S}\sin^2\theta + \frac{\Delta V_P{}^P}{2V_P}\tan^2\theta, \tag{5.30}$$

Similarly, the reflectivity changes because of the pressure changes equal:

$$\Delta R^F(\theta) \approx \frac{1}{2}\left(\frac{\Delta\rho^F}{\rho} + \frac{\Delta V_P{}^F}{V_P}\right) - \frac{2V_S}{V_P{}^2}\frac{\Delta\rho^F}{\rho}\sin^2\theta + \frac{\Delta V_P{}^F}{2V_P}\tan^2\theta \tag{5.31}$$

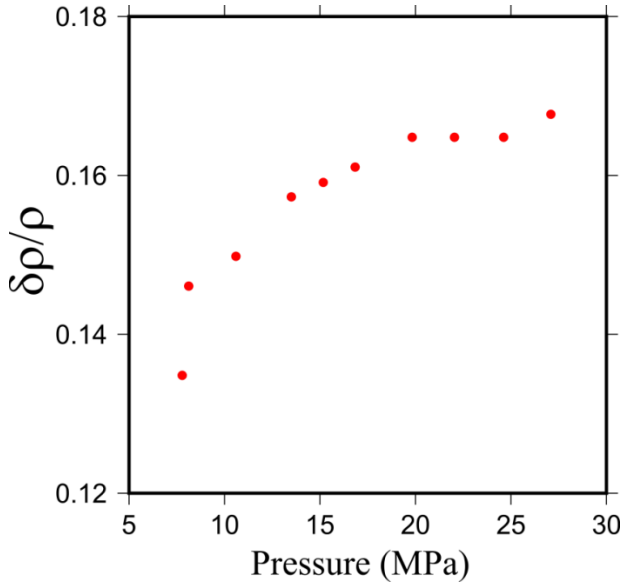

Figure 5.35: Relative changes in density as the result of pressure changes.

Once we obtain the relative variation of seismic parameters with respect to fluid-saturation and pore-pressure changes, we can determine the relationship between AVA attributes and CO_2 saturation and pore pressure. These parameters can be extracted from ultrasonic measurements on core samples. I use simplified relations between P-, S wave velocity and density parameters to CO_2 pore pressure and saturation changes based on the study by Brown (2002) on rock samples from Weyburn reservoir (Figure 5.36-Figure 5.38).

Based on these observations, I use a linear approximation with respect to the saturation changes and second-order approximation with respect to pressure:

$$\frac{\Delta V_P}{V_P} \approx A_P \Delta S + B_P \Delta P + C_P \Delta P^2, \tag{5.32}$$

$$\frac{\Delta V_S}{V_S} \approx A_S \Delta S + B_S \Delta P + C_S \Delta P^2, \tag{5.33}$$

$$\frac{\Delta \rho}{\rho} \approx A_\rho \Delta S, \tag{5.34}$$

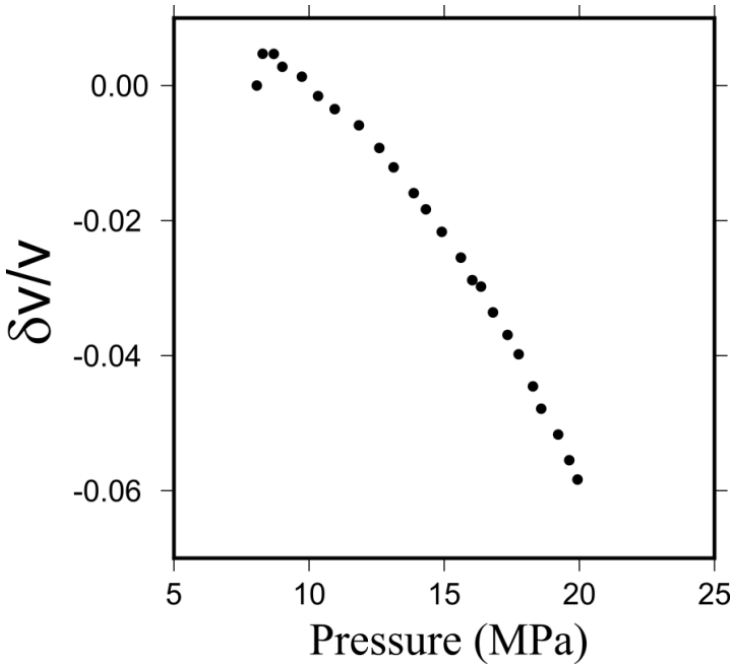

Figure 5.36: Relative changes of P wave velocity versus pressure changes (modified from Brown, 2002). It appears that the relationship between P-wave velocity and pressure can be described by a second-order relationship.

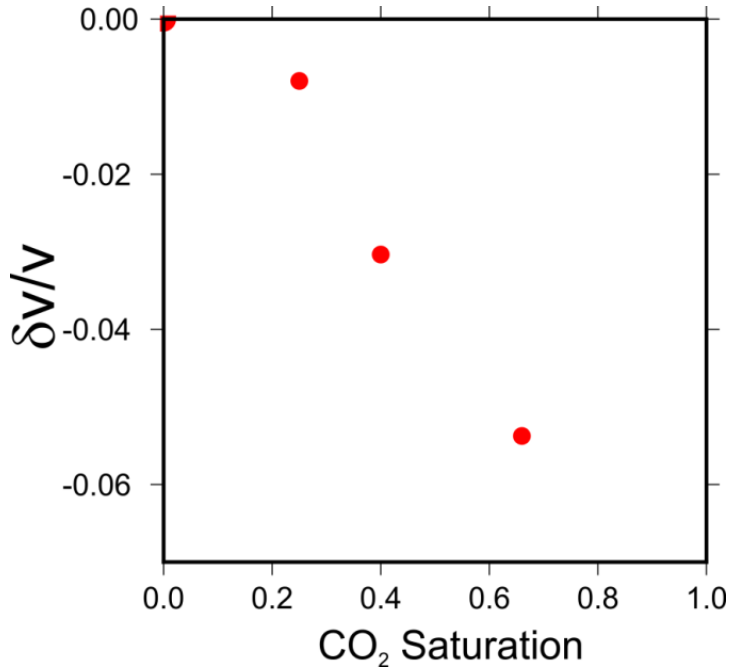

Figure 5.37: Relative variations of P-wave velocity as a function of CO_2 saturation (modified from Brown, 2002). I approximate this relation by a first-order expression.

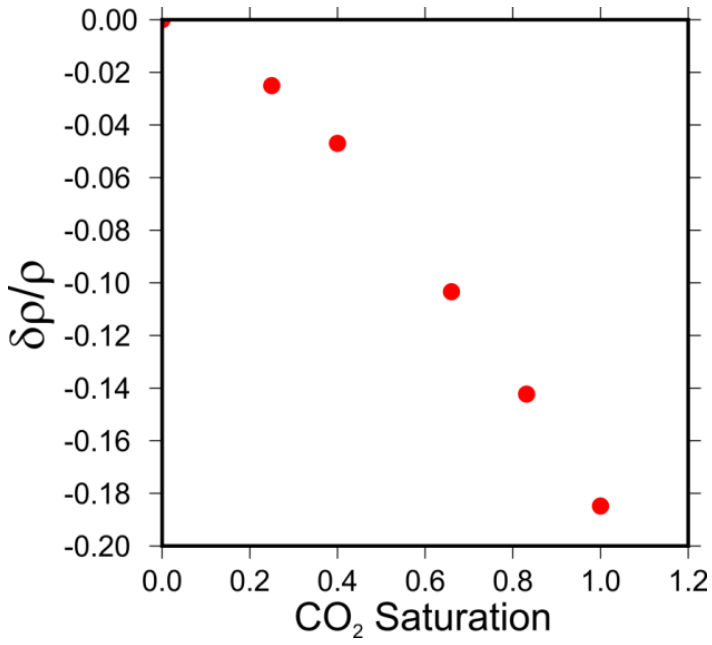

Figure 5.38: Relative changes of density versus CO_2 saturation (extracted and modified from Brown, 2002). It appears that the relationship between density and CO_2 saturation can be estimated by a near-linear dependence.

where ΔS and ΔP denote the changes in CO_2 saturation and net pressure, respectively, and A, B and C are empirical parameters for the sensitivities of the relative P wave, S wave and density variations to pressure and CO_2 saturation, as estimated from Figure 5.36 to Figure 5.38. Therefore, the combined effect of fluid and pressure changes on the angle-dependent reflectivity can be written as:

$$\Delta R \approx \frac{1}{2}(A_P \Delta S + A_S \Delta S + B_P \Delta P + C_P \Delta P^2) + \frac{1}{2}(A_P \Delta S + B_P \Delta P + C_P \Delta P^2)\tan^2\theta$$

$$-\frac{4V_S^2}{V_P^2}(B_S \Delta P + C_S \Delta P^2)\sin^2\theta \quad . \qquad (5.35)$$

Using the Shuey's equation (5.4) for the AVA analysis and assuming $\sin^2\theta \cong \tan^2\theta$ for below 30°, we can rewrite the above equation in terms of the variations of the AVA intercept and gradient:

$$\Delta I \approx \frac{1}{2}(A_P \Delta S + A_S \Delta S + B_P \Delta P + C_P \Delta P^2) \tag{5.36}$$

$$\Delta G \approx \frac{1}{2}(A_P \Delta S + B_P \Delta P + C_P \Delta P^2) - \frac{4V_S^2}{V_P^2}(B_S \Delta P + C_S \Delta P^2) \tag{5.37}$$

By solving the above equations, we have:

$$\Delta P = \frac{-b \pm \sqrt{b^2 - 4ac}}{2a} \tag{5.38}$$

where

$$a = C_{VP} - \frac{8V_S^2}{V_P^2} C_{VS} - \frac{C_{V_P} A_{V_P}}{A_{V_P} + A_\rho},$$

$$b = B_{V_P} - \frac{8V_S^2}{V_P^2} B_{V_S} - \frac{A_{V_P} B_{V_P}}{A_{V_P} + B_\rho},$$

$$c = \frac{2A_{V_P} \Delta I}{A_{V_P} + A_\rho} - 2\Delta G,$$

and the changes in CO_2 saturation become (Landrø ,2001):

$$\Delta S \approx \frac{1}{A_{V_P} + A_\rho}\left(2\Delta I - B_{V_P} \Delta P - C_{V_P} \Delta P^2\right). \tag{5.39}$$

The above equations can be solved by setting *Vp*/*Vs* = 2 and using the results for *I* and *G* from equation (5.16). Figure 5.39-and Figure 5.40 show the CO_2 pressure and saturation map for Weyburn VSP area from equation (5.3) and (5.3).

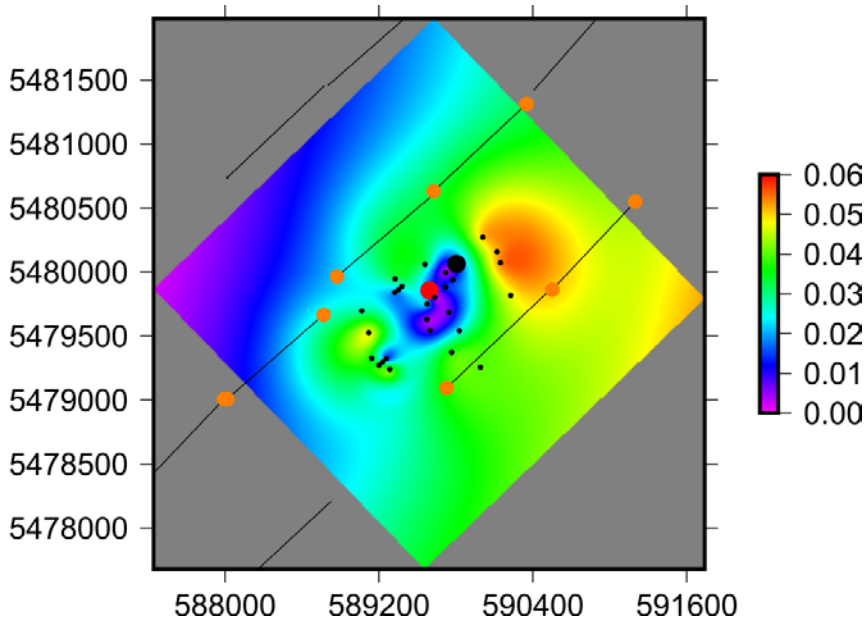

Figure 5.39: CO_2 saturation values estimated from equation (5.39). The maximum CO_2 saturation observed from these data is ~5%, which can be related to limitation of Weyburn seismic data for detecting CO_2 saturation for Weyburn area.

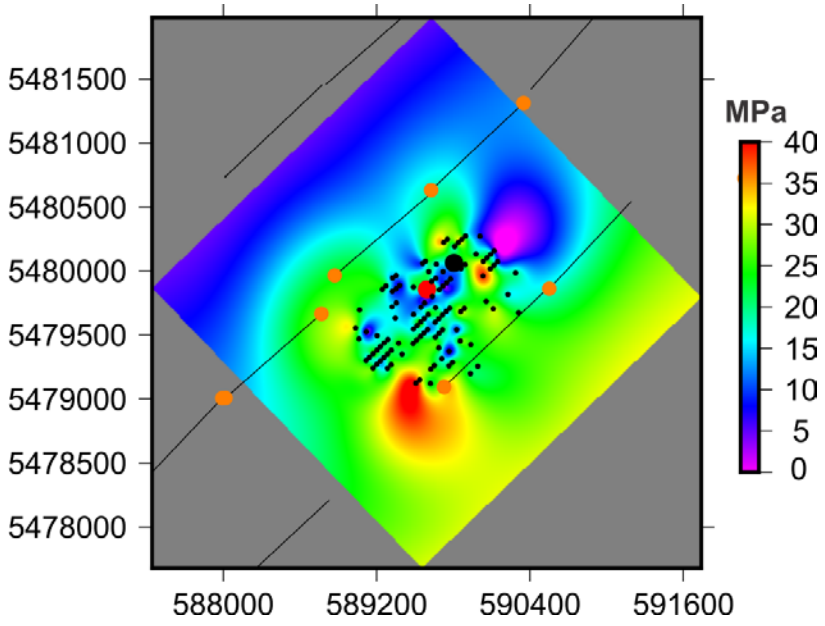

Figure 5.40: CO_2 pressure estimated from equation (5.38). The maximum CO_2 pressure estimated from VSP data is located close to the southern injection well. .CO_2 pressure variation is very small at the centre of the VSP area and is increases near injection wells.

5.16 Discussion

Several factors may affect the validity and accuracy of the above quantitative results. First, these results depend on the coefficients controlling the relations between density, P and S wave velocity with saturation and pressure. Additional rock-physics studies are likely required in order to test and substantiate these dependences, and to examine their variability within and around the reservoir. Significant assumptions were also made in equations (5.38) and (5.39), which may also affect the results. For example, I assumed that the CO_2 pressure affects the S wave velocity in a way similar to P wave. I also considered the empirical coefficients extracted for the well location as representative of the entire VSP area. The quality and consistency of these approximations still need to be studied.

Another interesting point for future studies relates to the above results on CO_2 saturation. As discussed by Morozov and Ma (2010), above this CO_2 saturation level, the AVA response "saturates" itself and does not allow further differentiation of the CO_2 saturation levels. Weyburn seismic data are capable of discriminating CO_2 saturations of up to 5%. My estimate of CO_2 saturation also reaches to maximum of ~5%, which appears to agree with this limitation for seismic data. Thus, in reality, the CO_2 saturation may actually be higher in areas where it is shown as near 5% in Figure 5.39.

Another important point relates to the sign of CO_2 saturation in equation (5.39). If pressure increase is large enough in (~15 MPa), the CO_2 saturation calculated from equation (5.39) becomes negative. This might be an indicator of reduced CO_2 saturation within the reservoir. Such negative values were dropped from Figure 5.39, which only shows the locations of increasing CO_2 saturation. For example, the area close to the southeast injection well shows an increase in pressure whereas the saturation changes only slightly in this area. However, in the

northern area, I observe an increase in CO_2 saturation with only a slight increase in pressure. The central area shows small changes in pressure and saturation, as it is expected and observed by other techniques (section 5.13).

Finally, the CO_2 pressure results indicate pressure increases occurring mostly along the southern injection wells, while saturation increases particularly in north-eastern area. It appears that the average pressure increase in the area is ~15-20 MPa and saturation changes by about 4% in the area. These values are comparable to typical reservoir simulation results.

CHAPTER 6: CONCLUSIONS AND RECOMMENDATIONS

This study set out to explore the potential of VSP data in reservoir studies and particularly in separation of effects of CO_2 pore pressure and saturation after injection into the reservoir. It establishes a robust and reliable link between physical properties of hydrocarbon reservoirs and seismic data. It also reduces the uncertainties of the AVA analysis through construction of a detailed anisotropic model combining the geometric spreading, scattering and intrinsic attenuation. Finally, it provides different techniques to separate effects of CO_2 pressure and saturation in the reservoir based on corrected amplitude.

In the following sections, I summarize the conclusions of the different aspects of this study and discuss the applications and limitations of the proposed methods. In the last section, I outline some directions and areas of future research arising from this Dissertation.

6.1 AVA-compliant VSP processing

Using VSP data for AVA analysis is still not a common practice in reservoir studies. VSP data mostly are used to tie seismic data to well data through constructing corridor stacks. There is still no standard flow for AVA-compliant processing of 3D VSP data. In this Dissertation, I processed VSP data in a way to preserve the amplitude to offset/angle relationships. Another challenge in processing of VSP data is transferring VSP data to surface midpoint locations (CMP) while maintaining the true amplitudes. Instead of using the VSP-to-CMP mapping, I recommend a processing flow based on calculation the VSP reflection angles from ray tracing.

6.2 Anisotropic (γ,κ) model for seismic attenuation

To resolve the rather complicated trade-off between the geometric spreading, "intrinsic Q," and scattering in VSP first-arrival waveforms, an integrated approach was developed, based on the scattering-theory approximation by Morozov (2008). For limited frequency bands, such dependences can be approximated as $\chi \approx \gamma + \kappa f$. This approach can be applied to many other studies (e.g., direct waves, reflection, or microseismic), and it has also been used in a variety of earthquake studies (Morozov, 2008, 2010a, 2010b). The approach offers two important advantages over conventional methods. First, it recognizes that the geometric spreading and scattering occur locally and can be measured concurrently with attenuation. Second, this model does not assume that the geometric spreading model can be modeled accurately and/or that scattering can be considered absent. The approach is also free from the uncertainties of material-Q models. The resulting values of both γ and κ measured from the Weyburn VSP survey were found to be anisotropic, *i.e*. dependent on the directions of wave propagation.

The inversion approach in this Dissertation focused on extracting complete and reliable empirical information about wave attenuation without considering any physical mechanisms. This approach can also be connected to conventional methods used for reservoir characterization by using seismic attenuation. The potential of this method is in complete characterization of the observable macroscopic attenuation parameters (spatially-variable, anisotropic γ and κ), which belong to the subsurface. These parameters should be further related to the four physical causes of wave-energy dissipation: 1) local variations of geometric spreading, 2) internal friction, 3) scattering (transmission losses and reflectivity), and 4) many types of internal dissipation of

mechanical energy into heat. Such mechanisms are usually described by the "intrinsic *Q*" of the material.

The fundamental criterion by which the γ- and κ- types of seismic wave attenuation are differentiated in this Dissertation consists in their frequency dependences. This criterion may provide important guidance for interpreting the petrophysical causes of seismic-wave attenuation. For example, the internal friction related to the presence of mobile pore fluids, moving dislocations, or grain-boundary sliding should lead to effects similar to solid and fluid viscosity (Biot, 1956; Landau and Lifshitz, 1986). For viscosity, the internal friction vanishes at zero frequencies, and consequently, viscosity should be entirely contained in κ. For such mechanisms, a frequency-dependent $\kappa \propto f$ is expected (*ibid*). Thermoelasticity is another key attenuation mechanism which might be included in κ or also in γ. Depending on the grain sizes and thermal properties of the material, its frequency dependence can range from about $\chi \propto \sqrt{f}$ to $\chi \propto f^2$ (i.e., $\kappa \propto f$; Landau and Lifshitz, 1986).

6.3 Separation of geometric spreading, scattering and intrinsic attenuation effects

By interpreting the resulting values of γ and κ, three key questions are addressed in this Dissertation: 1) how to characterize the contribution of spectral fluctuations in the "scattering attenuation", 2) how to characterize the "random" and "non-random" parts of scattering for a specific zone of interest, and 3) how to separate the effects of intrinsic attenuation, scattering on fine layering, and the variations of geometric spreading.

To answer these questions, a numerical model was formulated to study normal and oblique-incidence P and S wave propagation in a finely layered medium. Numerical modeling

allowed interpretation of the measured spreading effects and differentiation between random- and statistical-fluctuation effects inherent in scattering. “Fluctuation *Q*” was studied and shown to be significant in the observed seismic amplitudes. The results of statistical analysis are in good agreement with those obtained from the approach by O’Doherty and Anstey’s (1971) and from the localization theory. By contrast, this type of *Q* is omitted in the traditional empirical types of analysis and potentially included in “scattering *Q*” (Morozov and Baharvand Ahmadi, 2015).

Several limitations of the localization theory (such as large layer thicknesses, small-perturbation approximation, etc.) were overcome in this Dissertation by using the numerical propagator approach (section 4.3). Implementation of the method by using matrix time series is only slightly more complex than any other processing of well logs and production of waveform synthetics. This matrix approach can be used in many other applications, and it can be readily implemented in many programming packages, such as Matlab (as in this study), Octave, Mathematica, and it can also be compactly and efficiently coded in high-level computer languages such as C++.

6.4 AVA analysis and separation of CO_2 pressure and saturation effects

Separation of CO_2 pressure and saturation effects is the ultimate goal of this Dissertation. Three amplitude-based methods were proposed, all of which rely on the AVA measurements of VSP data: 1) time-lapse comparisons of AVA attributes, 2) AVA cross-plotting, and 3) quantitative estimation of the variations in CO_2 pressure and saturation.

From the first of the above methods, it was found that AVA attributes showed more sensitivity to pressure variations compared to saturation. Based on the changes in the AVA

intercept, gradient and shear wave reflectivity attributes, the area close to the southeastern well within the Weyburn VSP area (area B) showed the greatest changes in saturation.

The second method took advantage of the AVA intercept and gradient cross- plotting combined with an existing AVA model already calculated based on seismic and well-log data. By using a CO_2 discriminator line determined for the VSP and introducing two new AVA attributes (δP_1 and δP_2), I suggested a separation between the CO_2 pressure and saturation effects. These results are consistent with CO_2 pressure and saturation changes inferred from the AVA attributes.

Finally, by using the values of the AVA intercept and gradient quantitatively, I estimated the pressure and saturation variations within the area of injection. These results were obtained in units of pressure and saturation and are therefore easy to understand and should be comparable to other measurements performed during injection and geotechnical reservoir studies. The results from three techniques agree with each other and lead to similar conclusions. Based on a combination of these results, the area close to the southern well should have the highest pressure and the area between the northern and eastern wells show the maximum CO_2 saturation. However, the area in the center has the minimum effects of CO_2 saturation and pressure. The VSP dataset does not provide enough coverage for the North-western injection wells and make the interpretation in this area difficult.

6.5 Recommendations for further research

The (γ,κ) attenuation model used in this study is very general and can be used in numerous applications in exploration and global seismology (Morozov, 2008a, 2010a). A potentially very useful future application of it could be in forward and inverse modeling of

attenuation effects. The existing forward and inverse *Q*-filtering algorithms are based on the concept of the frequency-dependent *Q* of the medium (Wang, 2008). This concept uses the same relations (3.3) and (3.4) as our method, with the only difference being the restriction of the attenuation coefficient to the form of $\chi(f) = \pi f / Q(f)$. Therefore, if γ and κ are determined (as, for example, in Chapter 3), the conventional frequency-dependent *Q* of the medium becomes (see equation (3.5) and also Morozov, 2008a):

$$Q(f) = \frac{\pi f}{\gamma + \kappa f}. \tag{6.1}$$

Similarly to γ and κ, this $Q(f)$ would be anisotropic.

Thus, by using relation (6.1), the (γ,κ) attenuation models can be used in new types of forward and inverse *Q* filtering and other *Q*-related analysis. Note that in areas of wave focusing (i.e., where $\gamma < 0$) and sufficiently low κ, $Q(f)$ can be negative at low frequencies $f < f_c$, which may cause problems for the conventional model of attenuation (Rickett, 2006). Generally, the geometric spreading and frequency-independent scattering (as measured by γ) are not "*Q*-type" phenomena, and values of $Q(f) < 0$ are possible. Mathematical models and algorithms extending beyond the viscoelastic $Q(f)$ model and directly utilizing the geometric, scattering and other physical mechanisms of wave attenuation are therefore required.

The statistical models of scattering developed in this Dissertation are also very general and can be combined with many attenuation-based methods for reservoir characterization. The potential of this approach is in a more complete characterization of the macroscopic attenuation parameters (spatially variable, anisotropic γ and κ), which are associated with the subsurface structure. The fundamental criterion by which I differentiate between these effects consists in

their frequency dependences, which may provide an important guidance for precise interpretation of the petrophysical causes of attenuation. For example, the internal friction related to mobile dislocations or grain-boundary sliding should lead to effects similar to solid and fluid viscosity (Landau and Lifshitz, 1986) whereas mobile pore fluids and "mesoscopic" heterogeneities should lead to dissipation by means of Darcy flows and slow "fluid waves" (Biot, 1956).

Finally, several practical recommendations and specific observations arise from the application of the different methods of VSP data processing and interpretation in this study:

1) In designing seismic studies for CO_2 injection monitoring, it is important to emphasize the following factors:

    a) It is recommended that seismic data acquisition is conducted with an AVA analysis in mind. This means that the surveys should use identical (preferably permanently buried) receiver spreads with identical shot patterns and types. Very wide-aperture VSP surveys are likely not particularly useful.

    b) For precise calibration of seismic data, it is critical to use as close to raw dataset parameters (such as the source and receiver positions and types) as possible. This would ensure good repeatability of the data in the "pre-stack" domain.

    c) If feasible, multiple VSP recording (*i.e.*, recording the same shots in adjacent wells) could greatly improve the illumination of the subsurface and improve imaging.

    d) For datasets with high pre-stack repeatability of data acquisition, seismic processing should also employ time, amplitude, and wavelet calibration at the pre-stack stage.

e) VSP should be conducted as a calibration and aid to the surface 3-D recording. At the same time, methods for VSP processing and data analysis still need to be improved in order to confidently constrain the AVA effects observed from surface recording.

2) In surface-seismic and particularly VSP true-amplitude and AVA studies, the entire amplitude-decay should be modeled without subdividing it into a geometric spreading, "intrinsic *Q*," or scattering. This study may provide an important guidance for interpretation of the petrophysical causes of attenuation.

3) In terms of seismic attributes that can help distinguish the CO_2 saturation from pressure-related effects, combinations of the AVA intercept (*I*) and gradient (*G*) can be used. The monitoring procedure could be similar to the identification of Class III AVA anomalies:

a) An increase in pore pressure generally decreases *I* and increases *G*, i.e., it decreases ($aG–I$), with some $a > 0$. The same variation affects the S-wave reflectivity.

b) An increase in CO_2 saturation decreases both *I* and *G*, i.e., it should be sensitive to combinations like ($I+aG$).

4) This study shows the importance of well logs, core analysis, and lab measurements, which relate reservoir physical properties to the seismic parameters. In areas with better well coverage, the quantitative model for separating the CO_2 pore-pressure and saturation effects would be more reliable.

5) CO_2 produces the strongest effect on seismic properties when its saturation is low (below about 3%). This means that seismic monitoring should be conducted at the early stages of injection. Perhaps it would be advisable to conduct two "baseline" surveys prior to CO_2 injection, so that the variability outside of the CO_2 effects can be studied. This could be

particularly important if CO_2 injection is started after a history of water injection, as with the Weyburn reservoir.

LIST OF REFERENCES

Aki, K., 1980, Attenuation of shear-waves in the lithosphere for frequencies from 0.05 to 25 Hz: Physics of the Earth and Planetary Interiors, **21**, 50–60.

Aki, K., 1980b, Scattering and Attenuation of Shear Waves in the Lithosphere: Journal of Geophysical Research, **85**, 6496-6504.

Aki, K. and P. G. Richards, 2002, Quantitative Seismology: Second Edition: University Science Books, 139-144.

Avseth, P., T. Mukerji, and G. Mavko, 2005, Quantitative Seismic Interpretation: Applying Rock Physics Tools to Reduce Interpretation Risk: Cambridge University Press.

Baharvand Ahmadi, A., L. Gao, J. Ma and I. Morozov, 2011, CO_2 Saturation vs. Pressure Effects from time-lapse 3-D P-S surface and VSP seismic data: Final report as part of IEA GHG Weyburn-Midale CO_2 Monitoring and Storage Project, http://seisweb.usask.ca/Reports/Weyburn_USask_Report_Apr2011.pdf, last accessed October 22, 2016

Baharvand Ahmadi, A., and I. Morozov, 2011a, Time-lapse VSP data analysis from Weyburn CO_2 project: 2011 CSPG/CSEG/CWLS Convention, p. 1-4, http://cseg.ca/assets/files/resources/abstracts/2011/096-Time-Lapse_VSP_Data_Analysis_from_Weyburn_CO2_Project.pdf, last accessed Oct 22, 2016.

Baharvand Ahmadi, A., and I. Morozov, 2011b, Time-lapse variation with Angle (AVA) analysis in vertical seismic profiling of Weyburn reservoir, Saskatchewan, Canada: 2011 AGU Fall Meeting.

Baharvand Ahmadi, A., and I. Morozov, 2012, Anisotropic frequency-dependent spreading of seismic waves from VSP Data Analysis: 2012 CSPG/CSEG/CWLS Convention, p. 1-6, http://cseg.ca/assets/files/resources/abstracts/2012/120_GC2012_Anisotropic_Frequency-Dependent_Spreading_of_Seismic_Waves.pdf, last accessed Oct 22, 2016.

Baharvand Ahmadi, A., and I. Morozov, 2013a, Anisotropic frequency-dependent spreading of seismic waves from first-arrival vertical seismic profile data analysis: Geophysics, **78**, no. 6, C41–C52.

Baharvand Ahmadi, A., I. Morozov, 2013b, Separation of geometric spreading, scattering and intrinsic attenuation effects in VSP data: 2013 CSPG/CSEG/CWLS Convention, p. 1-5, http://cseg.ca/assets/files/resources/abstracts/2013/310_GC2013_Separation_of_GS_Scattering_Intrinsic_Attenuation_in_VSP_data.pdf, last accessed Oct 22, 2016.

Baharvand Ahmadi, A., and I. Morozov, 2014a, Separation of geometric spreading, scattering and intrinsic attenuation Effects in a VSP: 2014 CSPG/CSEG/CWLS Convention, p. 1, http://cseg.ca/assets/files/resources/abstracts/2014/286_GC2014_Separation_of_Geometric_Spreading_Scattering_Intrinsic_Attenuation_Effects_VSP.pdf

Baharvand Ahmadi., and I. Morozov, 2014b, Separation of geometric spreading, scattering and intrinsic attenuation effects in a VSP: Canadian Journal of Exploration Geophysics, **38**, no 1, P21-29.

Batzle, M. and Wang, Z., 1992, Seismic properties of pore fluids: Geophysics, 57, 1396-1408.

Behura, J., and I. Tsvankin, 2009, Estimation of interval anisotropic attenuation from reflection data: Geophysics, **74**, no. 6, A69–A74, doi: 10.1190/1.3191733.

Biot, M. A., 1956, Theory of propagation of elastic waves in a fluid-saturated porous solid, II: Higher-frequency range: Journal of the Acoustical Society of America, **28**, 168–178.

Blias, E., 2012, Accurate interval *Q*-factor estimation from VSP data: Geophysics, **77**, no. 3, WA149-WA156, doi: 10.1190/geo2011-0270.1.

Bortfield, R., 1961, Approximation to the reflection and transmission coefficients of plane longitudinal and transverse waves: Geophysical Prospecting, **9,** 485-502.

Brown, L.T., 2002, Integration of rock physics and reservoir simulation for the interpretation of time-lapse seismic data at Weyburn Field, Saskatchewan: M.Sc. Thesis, Reservoir Characterization Project, Colorado School of Mines.

Carcione, J. M., 1992, Anisotropic *Q* and velocity dispersion of finely layered media: Geophysical Prospecting, **40**, 761-783.

Carcione, J. M., H. B Helle, N.H. Pham, and T. Toverud, 2003, Pore pressure estimation in reservoir rocks from seismic reflection data: Geophysics, **68**, 1569-1579.

Castagna, J.P., M.L. Batzle, and R.L Eastwood, 1985, Relationships between compressional-wave and shear-wave velocities in clastic silicate rocks: Geophysics, **50**, 571-581.

Castagna, J.P., and M. M. Backus, 1993, AVO analysis-tutorial and review, in Castagna, J. and Backus, M.M., eds, Offset-dependent reflectivity-Theory and practice of AVO analysis: Society of Exploration Geophysics, 3-37

Castagna, J.P., and H.W Swan, 1997, Principles of AVO crossplotting: The Leading Edge, **16**, 337-342.

Castagna, J. P., H.W. Swan, and D. J. Foster, 1998, Framework for AVO gradient and intercept interpretation, Geophysics, Society of Exploration Geophysicists, **63**, 948–956

Červený, V., and I. Pšenčík, 2008, Quality factor *Q* in dissipative anisotropic media: Geophysics, **73**, no. 4, T63–T75, doi: 10.1190/1.2937173.

Chernov, L. A., 1960, Wave Propagation in a Random Medium: McGraw-Hill, New York, 35–57.

Churcher, P.L., and A.C. Edmonds, 1994, Reservoir characterization and geologic study of the Weyburn Unit, southeastern Saskatchewan: Prepared by P.L. Churcher, and A.C. Edmonds; T.J. Mullane, P.Tottrup, W.D. Barnhart, H. Usselman, J.R. Eade, J. Gilroy, J. Stewart. D. Bird, P. Way, D.W. Berndt, and C.B. Austin contributors.

Dainty, A.M., 1981, A scattering model to explain seismic *Q* observations in the lithosphere between I and 30 Hz: Geophysical Research Letters, **8**, 1126-1128.

Dankbaar, J.W.M. 1985, Separation of P and S waves. Geophysical Prospecting 33, 970-986.

Dankbaar, J.W.M. 1987, Vertical Seismic Profiling – Separation of P- and S- waves, Geophysical Prospecting, **35**, 803-814.

Der, Z.A., and Lees, A.C., 1985, Methodologies for estimating $t^*(f)$ from short-period body waves and regional variations of $t^*(f)$ in the United States: Geophysical Journal of Royal Astronomical Society: **82**, 125-140, doi: 10.1111/j.1365-246X.1985.tb05131.x.

Dutta, N. C., 2002, Geopressure prediction using seismic data: Current status and the road ahead, Geophysics, **67**, 2012–2041.

Dvorkin, J., G. Mavko, and B. Gurevich, 2007, Fluid substitution in shaley sediment using effective porosity: Geophysics, 72, O1-O8.Wang, Z., Cates, M. E., and Langan, R.T., 1998, Seismic monitoring of flood in a carbonate reservoir: A rock physics study, Geophysics, **63**, 1604–1617.

Frankel, A.D., and Wennerberg. L., 1987, Energy-flux model of seismic coda: Separation of scattering and intrinsic attenuation: Bulletin of the Seismological Society of America, **77**,

1223-1251.

Frankel, A., A. McGarr, J. Bicknell, J. Mori, L. Seeber, and E. Cranswick, 1990, Attenuation of high-frequency shear waves in the crust: measurements from New York State, South Africa, and southern California: Journal of Geophysical Research, **95**, 17441-17457, doi:10.1029/JB095iB11p17441.

Gao, L., and I. B. Morozov, 2010, AVO Analysis of 3-D/3-C Datasets from Weyburn CO_2 Storage and Monitoring Project: CSPG/CSEG/CWLS Convention, Calgary, AB, April 2010,http://www.geoconvention.com/uploads/2011abstracts/097-AVO_Analysis_of_3D_3C_Datasets.pdf

Gao, l., I. Morozov, 2011, AVO analysis of 3-D/3-C datasets form Weyburn CO_2 storage and monitoring project: CSPG/CSEG/CWLS Convention.

Gao, L., and I. B. Morozov, 2014, Receiver function analysis of time-lapse 3-C/3-D seismic reflection data: Canadian Journal of Exploration Geophysics, **39**(1), 30-36.

Hampson-Russell Assistant, website last accessed on 13/04/16 at http://www.cgg.com/en/What-We Do/GeoSoftware/Solutions/HampsonRussell.

Hardage, B. A., 1985, Vertical seismic profiling part A: principles: Second enlarged edition: Geophysical Press.

Harris, P. E., C. Kerner, and R. E. White, 1997, Multichannel estimation of frequency-dependent *Q* from VSP data: Geophysical Prospecting, **45**, 87–109.

Hinds, R.C., N.L. Anderson, and R.D. Kuzmiski, 1996, VSP interpretive Processing: Theory and Practice: Society of Exploration Geophysicists.

Hilterman, F., 1990, Is AVO the seismic signature of lithology? A case history of Ship Shoal-

south addition: The Leading Edge, **09** (06), 15-22.

Kinoshita, S., 1994, Frequency-dependent attenuation of shear waves in the crust of the southern Kanto area: Bulletin of the Seismological Society of America, **84**, 1387-1396.

Landau, L. D., and E. M. Lifshitz, 1986, Theory of elasticity, Course of theoretical physics: Elsevier, **7** (3rd English edition).

Landrø, M., 2001, Discrimination between pressure and fluid saturation changes from time-lapse seismic data: Geophysics, **66**, 3, 836-844.

Ma, J., I. Morozov, 2010, AVO modelling of pressure-saturation effects in Weyburn CO_2 sequestration: The Leading Edge, **29**,178-183.

Mangriotis, M.D., J.W. Rector III., E. Frederic Herkenhoff and J. C. Neu, 2013, Scattering versus intrinsic attenuation in the vadose zone: A VSP experiment: Geophysics, **78**, B49 B63.

Mayeda, K., Su, F. and Aki, K., 1991, Seismic albedo from the total seismic energy dependence on hypocentral distance in southern California: Physics of the Earth and Planetary Interiors, **67**, 104-114.

Miong, S.K., 2008, Borehole Geophysical Methods for Near-surface Characterization: M.Sc. thesis, University of Calgary.

Morozov, I. B., 2008a, Geometric attenuation, frequency dependence of *Q*, and the absorption band problem: Geophysical Journal International, **175**, 239–252.

Morozov, I. B., 2008b, Open-source software framework integrates data analysis: EOS, Trans. American Geophysical Union, **89**, 261-262.

Morozov, I., and L. Gao, 2009, Multi-Vintage, Pre-Stack Calibration of 3-C 3-D Time-Lapse

Seismic Data: CSPG/CSEG/WLS Convention, Calgary, May 2009.

Morozov, I. B., 2010a, On the causes of frequency-dependent apparent seismological *Q*: Pure and Applied Geophysics, **167**, 1131–1146.

Morozov, I. B., 2010b, Attenuation coefficients of Rayleigh and Lg waves: Journal of Seismology, **14**, 803–822.

Morozov, I. B., 2011, Mechanisms of geometric attenuation: Annals of Geophysics, **54**, 235–248.

Morozov, I., and A. Baharvand Ahmadi, 2015, Taxonomy of *Q*: Geophysics, **80**, no. 1, T41–T49.

Newman, P., 1973, Divergence effects in a layered earth: Geophysics, **38**, 481-488.

O'Doherty, R. F., and N. A. Anstey, 1971, Reflections on amplitudes: Geophysical Prospecting, **19**, 430–458.

Ostrander, W.J., 1982, Plane-wave reflection coefficients for gas sands at non-normal angles of incidence: 52nd Annual International Meeting of Society of Exploration Geophysics, Expanded Abstracts, 216-218.

Ostrander, W.J., 1984, Plane wave reflection coefficients for gas sands at non normal angles of incidence: Geophysics, **49**, 1637-1648.

Pendrigh, N. M., 2004, Core Analyses and Correlation to Seismic Attributes, Weyburn Midale Pool, Southeastern Saskatchewan: Part of Summary of Investigations volume 2004, **4,** 2004.

Petroleum Technology Research Centre, 2015, http://ptrc.ca/projects/weyburn-midale/faqs.

Poletto, F., and F. Miranda, 2004, Seismic while drilling, fundamentals of drill-bit seismic for

exploration: Handbook of Geophysical Exploration, **35**, 2004.

Reine, C., R. Clark, and M. van der Baan, 2012, Robust prestack *Q*-determination using surface seismic data: part 1-Method and synthetic examples: Geophysics, **77**, no. 1, R45-R56, doi: 10.1190/geo2011-0073.1.

Richards, P. G., and C. W. Frasier, 1976, Scattering of elastic wave from depth-dependent inhomogeneities: Geophysics, **41**, 441–458.

Richards, P.G., and W. Menke, 1983, The apparent attenuation of a scattering medium: Bulletin of the Seismological Society of America, **75**, 1005-1021.

Rickett, J., 2006, Integrated estimation of interval-attenuation profiles: Geophysics, **71**, no. 4, A19–A23, doi: 10.1190/1.2209722.

Rutherford, S. R., and R. H. Williams, 1989, Amplitude-versus-offset variations in gas sands: Geophysics, **54**, 680–688.

Sato, H., and M. Fehler, 1998, Seismic wave propagation and scattering in the heterogeneous earth: Springer-Verlag.

Shapiro, S. A., and H. Zien, 1993, The O'Doherty-Anstey formula and localization of seismic waves: Geophysics, **58**, 736–740.

Shapiro, S. A., H. Zien, and P. Hubral, 1994, A generalized O'Doherty-Anstey formula for waves in finely layered media: Geophysics, **59**, 1750–1762.

Shearer, P. M., 1999, Introduction to seismology: Cambridge University Press.

Shuey, R.T., 1985, A simplification of Zoeppritz equations, Geophysics, **50**, 609-614.

Smith, G. C., and P. M. Gidlow, 1987, Weighted stacking for rock property estimation and detection of gas: Geophysical Prospecting, **25**, 993–1014.

Stewart, R.R., and J.P DiSiena, 1989, The values of VSP in interpretation: The Leading Edge, **8**, 12, 16-23.

Stovas, A., and B. Ursin, 2007, Equivalent time-average and effective medium for periodic layers: Geophysical Prospecting, **55**, 871–882, doi: 10.1111/gpr.2007.55.issue-6.

Sun, L.F., B. Milkereit, and D.R. Schmitt, 2009, Measuring velocity dispersion and attenuation in the exploration seismic frequency band: Geophysics, **74**, no. 2, WA113-WA122, doi:10.1190/1.3068426.

Thomsen, L., 1986, Weak elastic anisotropy: Geophysics, **51**, 1954–1966, doi: 10.1190/1.1442051.

Tonn, R., 1991, The determination of the seismic quality factor *Q* from VSP data: a comparison of different computational methods: Geophysical Prospecting, **39**, 1–27, doi: 10.1111/j.1365-2478.1991.tb00298.x.

Tura, A., and D.E. Lumley, 1999, Estimating pressure and saturation changes from time- lapse AVO data: 61st Conference and Technical Exhibition, European Association Geoscience Engineering, Extended Abstracts, 1–38.

Ursin, B., 1990, Offset-dependent geometrical spreading in a layered medium: Geophysics, **55**, 492–496.

Van der Baan, M., 2002, Constant *Q* and a fractal, stratified Earth: Pure and Applied Geophysics, **159**, 1707-1718.

Verdon, J.P., Kendall, J-M., White, D.J., and Angus, D.A., 2010, Linking microseismic event observations with geomechanical models to minimise the risks of storing CO_2 in geological formations, Earth and Planetary Science Letters.

Verdon JP, White DJ, Kendall J-M, Angus DA, Fisher Q, Urbancic T, 2010b, Passive seismic monitoring of carbon dioxide storage at Weyburn: Leading Edge, 29(2) , 200–206.

VISTA Help and Tutorials, website last accessed on 13/04/16 at https://www.software.slb.com/products/vista.

Walden, A. T., 1991, Making AVO sections more robust: Geophysical Prospecting, **39**, 915–942.

Wang, Z.Z., H. Wang, and M.E. Cates, 1998, Elastic Properties of Solid Clays, Presented at the 1998 SEG Annual Meeting, New Orleans, 13-18 September. Paper No. 1998-1045.

Wang, Y., 2008, Seismic inverse *Q* filtering: Blackwell.

White, D. J., K. Hirsche, T. Davis, I. Hutcheon, R. Adair, G. Burrowes, S. Graham, R. Bencini, E. Majer, and S. C. Maxwell, 2004,Theme 2: Prediction, Monitoring and Verification of CO_2 movements, in M. Wilson and M. Monea, eds.: IEA GHG CO2 Weyburn-Midale Monitoring and Storage Project Summary Report 2000–2004.

White, D., 2008, Geophysical monitoring in the IEA GHG Weyburn-Midale CO2 monitoring and storage project: SEG Expanded Abstracts, **27**, 2846–2849.

White, D., 2009, Monitoring CO2 storage during EOR at the Weyburn-Midale Field: The Leading Edge, **28**, 838–842.

White, D., 2011, Geophysical monitoring of the Weyburn CO2 flood: Results during 10 years of injection for the Weyburn Geophysical Monitoring Team: 10th International Conference on Greenhouse Gas Control Technologies, Energy Procedia , **4**, 3628–3635.

Whittaker, S.G., 2005, Geological characterization of the Weyburn Field for geological storage of CO_2: Summary of Phase I results of the IEA GHG Weyburn CO_2 Monitoring and Storage Project; in Summary of Investigations 2005, Volume 1, Saskatchewan

Geological Survey, Sask. Industry Resources, Misc. Rep. 2005-4.1, CD-ROM, Paper A-1, 6p.

Wu, R. S., 1985, Multiple scattering and energy transfer of seismic waves— Separation of scattering effect from intrinsic attenuation — I. Theoretical modelling: Geophysical Journal of the Royal Astronomical Society, **82**, 57–80.

Wu, R. S., and K. Aki, 1988, Multiple scattering and energy transfer of seismic waves: Separation of scattering effect from intrinsic attenuation. II. Application of the theory to Hindh Kush region: Pure and Applied Geophysics, **128**, 49–80.

Wyatt, K.D., and S.B. Wyatt, 1981, Determining subsurface structure using vertical seismic profiling: 51st Annual International Meeting, Society of Exploration Geophysicists, Expanded Abstracts, 99–102.

Xu, H., 2006, Calculation of CO_2 acoustic properties using Batzle-Wang equations: Geophysics, **71**, F21–F23.

Yang, X., T. Lay, X-B. Xie, and M. S. Thorne, 2007, Geometric spreading of P_n and S_n in a spherical Earth model: Bulletin of the Seismological Society of America, **97**, 2053–2065.

Zeoppritz, K., 1919, On the reflection and penetration of seismic waves through unstable layers: Erdbebenwellen VIII B, Goettinger Nachr Edition, 66-84.

Zhu, Y., I. Tsvankin, and I. Vasconcelos, 2007, Effective attenuation anisotropy of thin layered media: Geophysics, **72**, no.5, D93–D106.

APPENDIX A

MATLAB CODES FOR MODELING WAVEFIELD FLUCTUATIONS

In the Appendices, I provide the most important part of Matlab source codes of the two key data analysis steps discussed in sections 4.3 and 5.11 .

The code in this Appendix A reads in and edits the well logs and blocks them into layers. It shuffles the values in each layer, and after balancing spectrum of refection coefficient finds the transmission response of that layer. The process repeated 100 times and the result compared to O'Doherty and Anstey (1971).

```
%%%%%%%%%%%%%%%%%%%%%%%%%%%%%%%%%%%%%%%%%%%%%%%%%%%%%%%%%%%%%%%%%%%%%%%%%%%%
%%%%%%%%%%%THIS CODE IS SUPPOSED TO READ THE WHOLE LOG, BREAK IT INTO SIX
%%%%%%%%%%%LAYERS, SHUFFLE THE VALUES OF LOG IN EACH LAYER, THEN TRY TO
BALANCE SPECTRUM of REFLECTION COEFFICIENT, THEN FIND THE
%%%%%%%%%%%TRANSMISSION RESPONSE OF THAT. IF WE DO IT LIKE 100 TIMES, IT
%%%%%%%%%%%SHOULD SMOOTH OUT THE TRANSMISSION CURVE.In the end we compare to
Doherty and Anstey Formula
%%%%%x=[2 4 6 5 1]    idx = randperm(length(x));  xperm = x(idx);
clc
clear
tic
close all
figure
set_current_layer=5;
% % % setting:frequency increment, layer no,number of relization, number of
angles,
for layer_no=5:5  %%%%%%So far it is only working for layers with same
frequency bands

    depth_interval=0.1;
    step_blocking=1;%%%%%%1 means 10cm
    load LOGS_INTERPOLATED.mat;
    IMPORT_LOG_TEMP=LOGS_INTERPOLATED;
    process_window=500;%%%%%%%%window size in length of samples for log
processing
    VELOCITY=[2185;2230;2330;2405;2970;3834];
    numer_of_realizations=100;
    frequencies=[150;150;130;130;110;100];
    boundaries=[1;1463;2823;5413;7693;10133;12383];%%%%%Boundaries of layer
corresponding to cell number
    frequency_band=frequencies(layer_no,1);
    frequecy_real=[0.5:4:frequency_band];
```

```
    %%%%%%%%%%%%%%%%%%%%%%%%%%%%%%%%%%%%%%%%%%%%%%%%%%%%%%%%%%%%%%%%%%%%%%%
    %%%%%%%%%%%%%%%%%%%%%%%%%%%%%%%%Processing of Log (log editing)
    %%%%%500 sample windows, getting mean and std. if the value minus mean is
    %%%%%bigger than 3.*std ==> it was replaced with local mean in that
window
    IMPORT_LOG_temp2=IMPORT_LOG_TEMP;
    IMPORT_LOG_temp2(:,3)=0;
    IMPORT_LOG_temp2(:,4)=0;
    IMPORT_LOG_temp2(:,5)=0;
    count=0;
    t=0;ss=0;

    for tts=3:5   %%%%VP RHO  VS
        for i=1:process_window:length(IMPORT_LOG_TEMP(:,1))
            if i+process_window<length(IMPORT_LOG_TEMP(:,1))
                for j=i:i+process_window
                    count=count+1;
                    DATA(count,1)=IMPORT_LOG_TEMP(j,tts);%%%%VP or VS or RHO
                end
                mean_local=mean(DATA(:,1));
                stad_local=std(DATA(:,1));
                ss=ss+1;
                for k=i:i+process_window
                    if abs(IMPORT_LOG_TEMP(k,tts)-mean_local)>3*stad_local
                        IMPORT_LOG_temp2(k,tts)=mean_local;
                        t=t+1;
                    end

                    if abs(IMPORT_LOG_TEMP(k,tts)-mean_local)<3*stad_local
                        IMPORT_LOG_temp2(k,tts)=IMPORT_LOG_TEMP(k,tts);
                    end

                    if
(k==10508)||(k==10509)||(k==10510)||(k==10711)||(k==10756)||(k==11527)||(k==1
1528)||(k==11529)||(k==11533)||(k==11534)||(k==11620)
                        IMPORT_LOG_temp2(k,tts)=mean_local;
                    end
                end
            end
            count=0;
        end

        for i=13002:length(IMPORT_LOG_TEMP(:,tts))
            count=count+1;
            DATA(count,1)=IMPORT_LOG_TEMP(i,tts);
        end

        mean_local=mean(DATA(:,1));
        stad_local=std(DATA(:,1));

        for k=13002:length(IMPORT_LOG_TEMP(:,1))
            if abs(IMPORT_LOG_TEMP(k,tts)-mean_local)>2.5.*stad_local
```

```
                IMPORT_LOG_temp2(k,tts)=mean_local;
            end

            if abs(IMPORT_LOG_TEMP(k,tts)-mean_local)<2.5.*stad_local
                IMPORT_LOG_temp2(k,tts)=IMPORT_LOG_TEMP(k,tts);
            end
        end
    end
    IMPORT_LOG_temp2(:,1)=IMPORT_LOG_TEMP(:,1);
    IMPORT_LOG_temp2(:,2)=IMPORT_LOG_TEMP(:,2);
    clear IMPORT_LOG;


%%%%%%%%%%%%%%%%%%%%%%%%%%%%%%%%%%%%%%%%%%%%%%%%%%%%%%%%%%%%%%%%%%%%%%%%%%%%%%%
    %%%%%%%%%%Blocking the log process
    %%%%%%%%%%
    count=0;
    t=0;ss=0;

    clear DATA;
    start_blocking=1;%%%%%%
    for tts=1:7   %%%%VP RHO  VS
        t=0;
        for i=start_blocking:step_blocking:length(IMPORT_LOG_temp2(:,1))-
step_blocking
            t=t+1;
            if t<length(IMPORT_LOG_temp2(:,1))-step_blocking-1
                for j=i:i+step_blocking-1
                    count=count+1;
                    DATA(count,1)=IMPORT_LOG_temp2(j,tts);%%%%VP or VS or RHO
                end
                mean_local=mean(DATA(:,1));


                IMPORT_LOG_temp3(t,tts)=mean_local;

                count=0;
            end
        end
    end

    for i=1:start_blocking+length(IMPORT_LOG_temp3(:,1))-1
        if i<start_blocking
            IMPORT_LOG_temp4(i,:)=IMPORT_LOG_temp2(i,:);
        end
        if i>=start_blocking
            IMPORT_LOG_temp4(i,:)=IMPORT_LOG_temp3(i-start_blocking+1,:);
        end
    end
```

```
%%%%%%%%%%%%%%%%%%%%%%%%%%%%%%%%%%%%%%%%%%%%%%%%%%%%%%%%%%%%%%%%%%%%%%%%%%
    %%%%%%%%%%%%%%%%%%%%%%%%%%%%%%%%%%%%%%%%%%%%%%%%%
    %%%%%%%%%%Start shuffling the log and make a new log

    for r=1:numer_of_realizations
%%%%%%%%%%%%%%%%%%%%%%%%%%%%%%%%%%%%%%%%%%%%Realization number

        frequency_band=frequencies(layer_no,1);
        RESULT_ONE_LAYER=zeros(length(frequecy_real(1,:)));%

        %%%%%%%%%%%%%%%%%%%%%%%%%%%%%%%%%%%%%%%%%%%%%%level selection
        counter=boundaries(layer_no,1);
        counter2=boundaries(layer_no+1,1);
        %%%%%%%%%%%%%%%%%%%%%%%%%%%%%%%%%%%%%%%%%%%%%%%%%%%%
        t=0;%%%%%%%%%%%%%%%t is level of cut
        for i=counter:counter2
            t=t+1;
            IMPORT_LOG_temp(t,:)=IMPORT_LOG_temp4(i,:);
        end

        for i=1:length(IMPORT_LOG_temp(:,1))-1

IMPORT_LOG_temp(i,7)=(IMPORT_LOG_temp(i+1,4).*IMPORT_LOG_temp(i+1,3)-
IMPORT_LOG_temp(i,4).*IMPORT_LOG_temp(i,3))./(IMPORT_LOG_temp(i+1,4).*IMPORT_
LOG_temp(i+1,3)+IMPORT_LOG_temp(i,4).*IMPORT_LOG_temp(i,3));
        end


        clear x
        clear idx
        clear xperm
        x= IMPORT_LOG_temp(:,1);
        idx = randperm(length(x));

        for kk=1:length(IMPORT_LOG_temp(:,1))
            IMPORT_LOG_temp5(kk,1)=IMPORT_LOG_temp(kk,1);
            IMPORT_LOG_temp5(kk,2)=IMPORT_LOG_temp(kk,2);
            IMPORT_LOG_temp5(kk,3)=IMPORT_LOG_temp(idx(1,kk),3);
            IMPORT_LOG_temp5(kk,4)=IMPORT_LOG_temp(idx(1,kk),4);
            IMPORT_LOG_temp5(kk,5)=IMPORT_LOG_temp(idx(1,kk),5);

        end

        %%%%%%%%%%%%%%%%%%%%%%%%%%%%%%%%%%%%%%%%%%%%%%%%%%%%

        IMPORT_LOG=IMPORT_LOG_temp5;
        t=length(IMPORT_LOG(:,1));%%%%%%%%%%%%%%%t is level of cut

        countt=0;
```

```
        %%%%%%%%%%%%%%%%%%%%%%%%%%%%%%%%%%%%%%%%%%%%%%%%%%Ray Number
Selection

        for i=1:-0.25:0
            countt=countt+1;
            ray_number(countt,1)=1.7815e-004-(i.*1.7815e-004);
        end

%%%%%%%%%%%%%%%%%%%%%%%%%%%%%%%%%%%%%%%%%%%%%%%%%%%%%%%%%%%%%%%%%%%%%%%%
        temp_random_series=IMPORT_LOG(:,1);%%%%Z;
        temp_random_series(:,2)=IMPORT_LOG(:,2);%%%%%TIME
        temp_random_series(:,3)=IMPORT_LOG(:,3);%%%VP
        temp_random_series(:,4)=IMPORT_LOG(:,4);%%%%RHO
        temp_random_series(:,5)=temp_random_series(:,3).*
temp_random_series(:,4);
        temp_random_series(:,6)=IMPORT_LOG(:,5);%%%%VS

        for i=1:length(temp_random_series(:,1))-1

temp_random_series(i,7)=(temp_random_series(i+1,4).*temp_random_series(i+1,3)
-
temp_random_series(i,4).*temp_random_series(i,3))./(temp_random_series(i+1,4)
.*temp_random_series(i+1,3)+temp_random_series(i,4).*temp_random_series(i,3))
;
        end

        for i=1:length(temp_random_series(:,1))-1

temp_random_series(i,8)=(temp_random_series(i+1,4).*temp_random_series(i+1,5)
-
temp_random_series(i,4).*temp_random_series(i,5))./(temp_random_series(i+1,4)
.*temp_random_series(i+1,5)+temp_random_series(i,4).*temp_random_series(i,5))
;
        end
        %%%%%%%%%%%%%%%%
        %%%%%%%%%%%TRY TO BALANCE SPECTRUM OF RANDOM RC AND REAL RC, THEN BY
ASSUMING FIXED DENSITY, CALCULATE VELOCITY.

        W1_random=fft(temp_random_series(:,7));%%%%%fft RC random log
        W2_real_log=fft(IMPORT_LOG_temp(:,7));%%%%%%FFT RC REAL LOG

        W1_spectrum_random=abs(W1_random);
        W2_spectrum_real_log=abs(W2_real_log);
        FILTER=W2_spectrum_real_log(:,1)./W1_spectrum_random(:,1);

        W1_random_shaped=W1_random.*FILTER;

        W1_random_RC_shaped_depth=ifft(W1_random_shaped);


LOG_SERIES=zeros(length(temp_random_series(:,1)),length(temp_random_series(1,
:)));
```

```
        LOG_SERIES(:,1)=temp_random_series(:,1);%%%%%Z
        LOG_SERIES(:,2)=temp_random_series(:,2);%%%%%TIME
        LOG_SERIES(:,4)=temp_random_series(:,4);%%%%%DENSITY
        LOG_SERIES(1,:)=temp_random_series(1,:);
        for i=2:length(temp_random_series(:,1))%%%%%%%%calculating V from RC
            LOG_SERIES(i,3)=((LOG_SERIES(i-1,3).*LOG_SERIES(i-
1,4)).*(W1_random_RC_shaped_depth(i-1,1)+1)./(LOG_SERIES(i,4).*(1-
W1_random_RC_shaped_depth(i-1,1)));
        end



        LOG_SERIES(:,5)=LOG_SERIES(:,3).* LOG_SERIES(:,4);

        %%%%%%%%%We have to estimate Vs from VP, SO WE USED A FIXED EQUATION
THAT WAS ALREADY BETWEEN VP AND VS FROM REAL LOG
        for kj=1:length(LOG_SERIES(:,6))
            LOG_SERIES(kj,6)=(LOG_SERIES(kj,3).*0.594)-260.54;%%%%VS
%%%%%%%%what about VS?!!!!
        end

        for i=1:length(LOG_SERIES(:,1))-1
            LOG_SERIES(i,7)=(LOG_SERIES(i+1,4).*LOG_SERIES(i+1,3)-
LOG_SERIES(i,4).*LOG_SERIES(i,3))./(LOG_SERIES(i+1,4).*LOG_SERIES(i+1,3)+LOG_
SERIES(i,4).*LOG_SERIES(i,3));
        end

        for i=1:length(LOG_SERIES(:,1))-1
            LOG_SERIES(i,8)=(LOG_SERIES(i+1,4).*LOG_SERIES(i+1,5)-
LOG_SERIES(i,4).*LOG_SERIES(i,5))./(LOG_SERIES(i+1,4).*LOG_SERIES(i+1,5)+LOG_
SERIES(i,4).*LOG_SERIES(i,5));
        end

        for i=1:length(LOG_SERIES(:,1))
            if LOG_SERIES(i,1)>counter2
                LOG_SERIES(i,3)=LOG_SERIES(counter,3);%%%%VP
                LOG_SERIES(i,4)=LOG_SERIES(counter,4);%%%%RHO
                LOG_SERIES(i,5)=LOG_SERIES(i,3).*
LOG_SERIES(i,4);%%%%%IMPEDANCE
                %%%%%%%%%%%for S wave
                for kj=1:length(LOG_SERIES(:,6))
                    LOG_SERIES(kj,6)=(LOG_SERIES(kj,3).*0.594)-260.54;%%%%VS
%%%%%%%%what about VS?!!!!
                end


            end
        end

        Z=LOG_SERIES(:,1);%%%%Depth
        VP=LOG_SERIES(:,3);
        VS=LOG_SERIES(:,6);
        RHO=LOG_SERIES(:,4);
```

```
        TN_1=eye(4);


        for ray_number_counteri=1:length(ray_number(:,1))
            P=ray_number(ray_number_counteri,1);
            transmit_p_angle(1,ray_number_counteri)=asin(P.*VP(1,1));
            reflected_p_angle(1,ray_number_counteri)=asin(P.*VP(1,1));

reflected_s_angle(1,ray_number_counteri)=asin(VS(1,1).*P);%%%%%%%%%%reflecte
d angle of s in layer 1
            transmit_s_angle(1,ray_number_counteri)=asin(VS(2,1).*P);%%%%%%%%
            for i=2:length(VP(:,1))

transmit_p_angle(i,ray_number_counteri)=asin(VP(i,1).*P);%%%%%%%%%%reflected
angle of p in layer i

transmit_s_angle(i,ray_number_counteri)=asin(VS(i,1).*P);%%%%%%%%transmited
angle of s in layer i

reflected_s_angle(i,ray_number_counteri)=transmit_s_angle(i,ray_number_counte
ri);

reflected_p_angle(i,ray_number_counteri)=transmit_p_angle(i,ray_number_counte
ri);
            end

            for kp=1:length(frequecy_real(1,:))
                frequency=frequecy_real(1,kp);
                clear i;
                TN_1=eye(4);
                TL_NUMBER(1,1)=1; TL_NUMBER(1,2)=1;  TL_NUMBER(1,3)=1;
TL_NUMBER(1,4)=1;TL_NUMBER(1,5)=1; TL_NUMBER(1,6)=1;  TL_NUMBER(1,7)=1;
TL_NUMBER(1,8)=1;TL_NUMBER(1,9)=1; TL_NUMBER(1,10)=1;  TL_NUMBER(1,11)=1;
TL_NUMBER(1,12)=1;TL_NUMBER(1,13)=1; TL_NUMBER(1,14)=1;  TL_NUMBER(1,15)=1;
TL_NUMBER(1,16)=1;

                for k=1:t-1  %%%%%%%%%%I only do that to level of cut
                    if t>=start_blocking
                        depth_interval=0.1.*step_blocking;
                    end

N_MATRIX(1,1)=sin(transmit_p_angle(k,ray_number_counteri));%%%%%%%%

N_MATRIX(1,2)=cos(transmit_s_angle(k,ray_number_counteri));%%%%%%%%

N_MATRIX(1,3)=sin(transmit_p_angle(k,ray_number_counteri));

N_MATRIX(1,4)=cos(transmit_s_angle(k,ray_number_counteri));

N_MATRIX(2,1)=cos(transmit_p_angle(k,ray_number_counteri));
                    N_MATRIX(2,2)=-
sin(transmit_s_angle(k,ray_number_counteri));
```

```
                    N_MATRIX(2,3)=-
cos(transmit_p_angle(k,ray_number_counteri));

N_MATRIX(2,4)=sin(transmit_s_angle(k,ray_number_counteri));

N_MATRIX(3,1)=2.*LOG_SERIES(k,4).*(LOG_SERIES(k,6).^2).*P.*cos(transmit_p_ang
le(k,ray_number_counteri));
                    N_MATRIX(3,2)=LOG_SERIES(k,4).*LOG_SERIES(k,6).*(1-
(2.*(LOG_SERIES(k,6).^2).*(P.^2)));
                    N_MATRIX(3,3)=-
2.*LOG_SERIES(k,4).*(LOG_SERIES(k,6).^2).*P.*cos(transmit_p_angle(k,ray_numbe
r_counteri));
                    N_MATRIX(3,4)=-LOG_SERIES(k,4).*LOG_SERIES(k,6).*(1-
(2.*(LOG_SERIES(k,6).^2).*(P.^2)));
                    N_MATRIX(4,1)=LOG_SERIES(k,4).*LOG_SERIES(k,3).*(1-
(2.*(LOG_SERIES(k,6).^2).*(P.^2)));
                    N_MATRIX(4,2)=-
2.*LOG_SERIES(k,4).*(LOG_SERIES(k,6).^2).*P.*cos(transmit_s_angle(k,ray_numbe
r_counteri));
                    N_MATRIX(4,3)=LOG_SERIES(k,4).*LOG_SERIES(k,3).*(1-
(2.*(LOG_SERIES(k,6).^2).*(P.^2)));
                    N_MATRIX(4,4)=-
2.*LOG_SERIES(k,4).*(LOG_SERIES(k,6).^2).*P.*cos(transmit_s_angle(k,ray_numbe
r_counteri));


M_MATRIX(1,1)=sin(transmit_p_angle(k+1,ray_number_counteri));%%%%%%%%

M_MATRIX(1,2)=cos(transmit_s_angle(k+1,ray_number_counteri));%%%%%%%%

M_MATRIX(1,3)=sin(transmit_p_angle(k+1,ray_number_counteri));

M_MATRIX(1,4)=cos(transmit_s_angle(k+1,ray_number_counteri));

M_MATRIX(2,1)=cos(transmit_p_angle(k+1,ray_number_counteri));
                    M_MATRIX(2,2)=-
sin(transmit_s_angle(k+1,ray_number_counteri));
                    M_MATRIX(2,3)=-
cos(transmit_p_angle(k+1,ray_number_counteri));

M_MATRIX(2,4)=sin(transmit_s_angle(k+1,ray_number_counteri));

M_MATRIX(3,1)=2.*LOG_SERIES(k+1,4).*(LOG_SERIES(k+1,6).^2).*P.*cos(transmit_p
_angle(k+1,ray_number_counteri));
                    M_MATRIX(3,2)=LOG_SERIES(k+1,4).*LOG_SERIES(k+1,6).*(1-
(2.*(LOG_SERIES(k+1,6).^2).*(P.^2)));
                    M_MATRIX(3,3)=-
2.*LOG_SERIES(k+1,4).*(LOG_SERIES(k+1,6).^2).*P.*cos(transmit_p_angle(k+1,ray
_number_counteri));
                    M_MATRIX(3,4)=-LOG_SERIES(k+1,4).*LOG_SERIES(k+1,6).*(1-
(2.*(LOG_SERIES(k+1,6).^2).*(P.^2)));
                    M_MATRIX(4,1)=LOG_SERIES(k+1,4).*LOG_SERIES(k+1,3).*(1-
(2.*(LOG_SERIES(k+1,6).^2).*(P.^2)));
```

```
                    M_MATRIX(4,2)=-
2.*LOG_SERIES(k+1,4).*(LOG_SERIES(k+1,6).^2).*P.*cos(transmit_s_angle(k+1,ray
_number_counteri));
                    M_MATRIX(4,3)=LOG_SERIES(k+1,4).*LOG_SERIES(k+1,3).*(1-
(2.*(LOG_SERIES(k+1,6).^2).*(P.^2)));
                    M_MATRIX(4,4)=-
2.*LOG_SERIES(k+1,4).*(LOG_SERIES(k+1,6).^2).*P.*cos(transmit_s_angle(k+1,ray
_number_counteri));


                    Ti_i_1=pinv(M_MATRIX)*N_MATRIX; %%%%inv(M)*N

                    Omega=2.*pi.*frequency;
                    Kx=Omega.*P; %%%%%Kx=w*P (Omega*P)and constant
%%%%%sqrt(Kx^2+Kz^2=K^2)=W/V

                    kzp=sqrt(((Omega.^2)./(LOG_SERIES(k,3).^2))-(Kx.^2));
                    kzs=sqrt(((Omega.^2)./(LOG_SERIES(k,6).^2))-(Kx.^2));



                    if isreal(kzp)==1
                        delta_phi_p=kzp.*depth_interval;
                    end

                    if isreal(kzs)==1
                        delta_phi_s=kzs.*depth_interval;
                    end

                    if k==1
                        delta_phi_p=0;
                        delta_phi_s=0;
                    end

                    TL_NUMBER(1,21)=LOG_SERIES(1,3).*
LOG_SERIES(1,4).*cos(transmit_p_angle(1,ray_number_counteri));%%%%%RHO*VP*COS
(i)=RHO*VP*(Kzp*VP/Omega)
                    TL_NUMBER(1,22)=LOG_SERIES(1,6).*
LOG_SERIES(1,4).*cos(transmit_s_angle(1,ray_number_counteri));%%%%%RHO*VS*Co
s(i)



                    TN_1=TN_1*Ti_i_1*[exp(1i.*delta_phi_p) 0 0 0;0
exp(1i.*delta_phi_s) 0 0; 0 0 exp(-1i.*delta_phi_p) 0; 0 0 0 exp(-
1i.*delta_phi_s)];


                    TL_NUMBER(k+1,1)=TN_1(1,1);%%%%G1
                    TL_NUMBER(k+1,2)=TN_1(1,2);%%%%G2
                    TL_NUMBER(k+1,3)=TN_1(1,3);%%%%G3
```

```
                    TL_NUMBER(k+1,4)=TN_1(1,4);%%%%G4
                    TL_NUMBER(k+1,5)=TN_1(2,1);%%%%G5
                    TL_NUMBER(k+1,6)=TN_1(2,2);%%%%G6
                    TL_NUMBER(k+1,7)=TN_1(2,3);%%%%G7
                    TL_NUMBER(k+1,8)=TN_1(2,4);%%%%G8
                    TL_NUMBER(k+1,9)=TN_1(3,1);%%%%G9
                    TL_NUMBER(k+1,10)=TN_1(3,2);%%%%G10
                    TL_NUMBER(k+1,11)=TN_1(3,3);%%%%G11
                    TL_NUMBER(k+1,12)=TN_1(3,4);%%%%G12
                    TL_NUMBER(k+1,13)=TN_1(4,1);%%%%G13
                    TL_NUMBER(k+1,14)=TN_1(4,2);%%%%G14
                    TL_NUMBER(k+1,15)=TN_1(4,3);%%%%G15
                    TL_NUMBER(k+1,16)=TN_1(4,4);%%%%G16
                    TL_NUMBER(k+1,21)=LOG_SERIES(k+1,3).*
LOG_SERIES(k+1,4).*cos(transmit_p_angle(k+1,ray_number_counteri));%%%%%RHO*VP
*COS(i)
                    TL_NUMBER(k+1,22)=LOG_SERIES(k+1,6).*
LOG_SERIES(k+1,4).*cos(transmit_s_angle(k+1,ray_number_counteri));%%%%%RHO*VP
*COS(i)


                    if k+1==t
                        TN_1_set=TN_1;
                    end

                end

                u_transmited_p_1=1;
                u_transmited_s_1=0;
                u_reflected_s_1=(((TN_1_set(3,3).*TN_1_set(4,1))-
(TN_1_set(4,3).*TN_1_set(3,1))).*u_transmited_p_1)./((TN_1_set(4,3).*TN_1_set
(3,4))-(TN_1_set(3,3).*TN_1_set(4,4)));
                u_reflected_p_1=-
(TN_1_set(4,1).*u_transmited_p_1+TN_1_set(4,4).*u_reflected_s_1)./TN_1_set(4,
3);

u_transmited_s_N=TN_1_set(2,1).*u_transmited_p_1+TN_1_set(2,3).*u_reflected_p
_1+TN_1_set(2,4).*u_reflected_s_1;

u_transmited_p_N=TN_1_set(1,1).*u_transmited_p_1+TN_1_set(1,3).*u_reflected_p
_1+TN_1_set(1,4).*u_reflected_s_1;

                TL_NUMBER(1,17)=u_transmited_p_1;%%%%%%P1+
                TL_NUMBER(1,18)=u_transmited_s_1;%%%%%%%S1+
                TL_NUMBER(1,19)=u_reflected_p_1;%%%%%%P1-
                TL_NUMBER(1,20)=u_reflected_s_1;%%%%%%S1-
                u_reflected_p_N=0;

                for kk=2:length(TL_NUMBER(:,1))
                    matrix_temp=[TL_NUMBER(kk,1) TL_NUMBER(kk,2)
TL_NUMBER(kk,3) TL_NUMBER(kk,4);TL_NUMBER(kk,5) TL_NUMBER(kk,6)
TL_NUMBER(kk,7) TL_NUMBER(kk,8); TL_NUMBER(kk,9) TL_NUMBER(kk,10)
```

```
TL_NUMBER(kk,11) TL_NUMBER(kk,12);TL_NUMBER(kk,13) TL_NUMBER(kk,14)
TL_NUMBER(kk,15) TL_NUMBER(kk,16)];

TL=matrix_temp*[u_transmited_p_1;u_transmited_s_1;u_reflected_p_1;u_reflected
_s_1];
                    TL_NUMBER(kk,17)=TL(1,1);%%%%%PN+
                    TL_NUMBER(kk,18)=TL(2,1);%%%%%SN+
                    TL_NUMBER(kk,19)=TL(3,1);%%%%%PN-
                    TL_NUMBER(kk,20)=TL(4,1);%%%%%%SN-
                end

                for k=1:length(TL_NUMBER(:,1))

TL_NUMBER(k,23)=0.5.*TL_NUMBER(k,21).*(abs(TL_NUMBER(k,17)).^2).*((Omega).^2)
;%%%%%%%%TRANSMITED FLUX ENERGY PN+

TL_NUMBER(k,24)=0.5.*TL_NUMBER(k,22).*(abs(TL_NUMBER(k,18)).^2).*((Omega).^2)
;%%%%%%%%TRANSMITED FLUX ENERGY SN+

TL_NUMBER(k,25)=0.5.*TL_NUMBER(k,21).*(abs(TL_NUMBER(k,19)).^2).*((Omega).^2)
;%%%%%%%%REFLECTED FLUX ENERGY PN-

TL_NUMBER(k,26)=0.5.*TL_NUMBER(k,22).*(abs(TL_NUMBER(k,20)).^2).*((Omega).^2)
;%%%%%%%%REFLECTED  FLUX ENERGY PS


                    TL_NUMBER(k,27)=TL_NUMBER(k,23)+TL_NUMBER(k,24)-
TL_NUMBER(k,25)-TL_NUMBER(k,26);%%%%%%%CONSERVATION

TL_NUMBER(k,28)=TL_NUMBER(k,27)./(0.5.*(TL_NUMBER(1,21)).*(abs(TL_NUMBER(1,17
)).^2).*((Omega).^2));%%%%%%Tranimted Energy PN+ + SN+

TL_NUMBER(k,29)=TL_NUMBER(k,24)./(0.5.*(TL_NUMBER(1,21)).*(abs(TL_NUMBER(1,17
)).^2).*((Omega).^2));%%%%%Transmited Energy SN+ Only

TL_NUMBER(k,30)=TL_NUMBER(k,23)./(0.5.*(TL_NUMBER(1,21)).*(abs(TL_NUMBER(1,17
)).^2).*((Omega).^2));
                end
                RESULT(kp,1)=frequency;%%%%%%%%

                RESULT(kp,2)=TL_NUMBER(k,28);

                if RESULT(kp,2)>1
                    RESULT(kp,2)=TL_NUMBER(1,28);%%%%%%%%%%We consider last
layer, but if energy biger than one---No way, we use first layer
                end

            end

            y=log(smooth(RESULT(:,1),RESULT(:,2),0.05));
            [Robust_model] = ROBUST(RESULT(:,1),y(:,1));
            %         figure
```

```
            plot(RESULT(:,1),log(smooth(RESULT(:,1),RESULT(:,2),0.05)))
            hold on
            %
plot(RESULT(:,1),Robust_model(1,1)+Robust_model(2,1).*RESULT(:,1),'k')
            %             ylim([-5 1])

            %%%%%%%%%
            kapa_s=-
2.*Robust_model(2,1)./(2.*((IMPORT_LOG_temp4(counter2,2).*0.001)-
(IMPORT_LOG_temp4(counter,2).*0.001)))%%%%%if slop in A=1 then in A^2 is
equal 2---if TWT==>divide by two, if OWT divide by 1
            gama_s=-
2.*Robust_model(1,1)./(2.*((IMPORT_LOG_temp4(counter2,2).*0.001)-
(IMPORT_LOG_temp4(counter,2).*0.001)))

            ray_number(ray_number_counteri,2)=gama_s;
            ray_number(ray_number_counteri,3)=kapa_s;

ray_number(ray_number_counteri,4)=Robust_model(1,1);%%%%%%%INTERCEPT
            ray_number(ray_number_counteri,5)=Robust_model(2,1);%%%%%%%SLOP

ray_number(ray_number_counteri,6)=asin(VELOCITY(layer_no,1).*P).*180./pi;%%%%
%%angle in each layer

RESULT_ONE_LAYER(:,ray_number_counteri)=RESULT(:,2);%%%%%%%Putting the result
of layer here

            if ray_number_counteri==1
                RESULT_ALL_REALIZATION(:,r)=RESULT(:,2);%%%%%%%%%%%NO SMOOTH

%%%%%%%%%%%%%%%%%%%%%%%%%%%%%%%%%%%%%%%%%%%%%%%%%%%%%%%%%%%%%%%%%%%%%%%%%%%%%
%%%%%%%%%%%%%%%

%%%%%%%%%%%%%%%%%%%%%%%%%%%%%%%%%%%%%%%%%%%%%%%%%%%%%%%%%%%%%%%%%%%%%%%%%%%%%
%%%%%%%%%%%%%%%
                %%%%%%%%%%%%%%%%%%%%%%%%%%%%Add Odoherty and Anstey estimate
                TIME_interval=0.5;
                REAL_LOG(:,1)=LOG_SERIES(:,1);
                REAL_LOG(:,2)=LOG_SERIES(:,2);
                REAL_LOG(:,3)=LOG_SERIES(:,3);
                REAL_LOG(:,4)=LOG_SERIES(:,4);
                REAL_LOG(:,5)=LOG_SERIES(:,3).*LOG_SERIES(:,4);
                [T_LOGS_INTERPOLATED] =
LOG_INTERPOLATION_TIME_CONST(REAL_LOG,TIME_interval);

                %%%%%RC AND Z define FOR TIME INTERPOLATED FUNCTION
                f_nyquist=1./(2.*TIME_interval.*0.001);
                sample_f=2.*f_nyquist./(length(T_LOGS_INTERPOLATED(:,1)));

                for i=1:length(T_LOGS_INTERPOLATED(:,5))-1

T_LOGS_INTERPOLATED(i,5)=((T_LOGS_INTERPOLATED(i+1,3).*T_LOGS_INTERPOLATED(i+
1,4))-
```

```
(T_LOGS_INTERPOLATED(i,3).*T_LOGS_INTERPOLATED(i,4))./((T_LOGS_INTERPOLATED(
i+1,3).*T_LOGS_INTERPOLATED(i+1,4))+(T_LOGS_INTERPOLATED(i,3).*T_LOGS_INTERPO
LATED(i,4)));
                    T_LOGS_INTERPOLATED(i+1,6)=i.*sample_f;
                end


T_LOGS_INTERPOLATED(length(T_LOGS_INTERPOLATED(:,5)),5)=T_LOGS_INTERPOLATED(l
ength(T_LOGS_INTERPOLATED(:,5))-1,5);
                T_LOGS_INTERPOLATED(:,7)=fft(T_LOGS_INTERPOLATED(:,5));


                for i=1:length(T_LOGS_INTERPOLATED(:,1))
                    if T_LOGS_INTERPOLATED(i,6)<=frequency_band
                        R_W(i,1)=T_LOGS_INTERPOLATED(i,6);%%%%%%FREQ
                        R_W(i,2)=abs(T_LOGS_INTERPOLATED(i,7)).^2;%%%%%%Power
Spectrum of RC
                    end
                end

                RESULT_ALL_ANSTEY(:,r)=R_W(:,2);

            end

            if ray_number_counteri==2
                RESULT_ALL_REALIZATION_2(:,r)=RESULT(:,2);
            end

            if ray_number_counteri==3
                RESULT_ALL_REALIZATION_3(:,r)=RESULT(:,2);
            end

            if ray_number_counteri==4
                RESULT_ALL_REALIZATION_4(:,r)=RESULT(:,2);
            end

            if ray_number_counteri==5
                RESULT_ALL_REALIZATION_5(:,r)=RESULT(:,2);
            end

            RESULT_ALL_idx(:,r)=LOG_SERIES(:,3);
        end
        for i=1:length(TL_NUMBER(:,1))
            TL_NUMBER(i,31)=TL_NUMBER(i,27)./TL_NUMBER(1,27);%%%%%%%ENERGY
CONSERVATION PERCENTAGE CHANGES
        end
        r
    end

    for i=1:length(RESULT_ALL_REALIZATION(:,1))
```

```
SMOOTH_AVERAGE_RESPONSE(i,layer_no)=mean(RESULT_ALL_REALIZATION(i,:));
    end

    for i=1:length(RESULT_ALL_REALIZATION(:,1))

SMOOTH_AVERAGE_RESPONSE_2(i,layer_no)=mean(RESULT_ALL_REALIZATION_2(i,:));
    end

    for i=1:length(RESULT_ALL_REALIZATION(:,1))

SMOOTH_AVERAGE_RESPONSE_3(i,layer_no)=mean(RESULT_ALL_REALIZATION_3(i,:));
    end

    for i=1:length(RESULT_ALL_REALIZATION(:,1))

SMOOTH_AVERAGE_RESPONSE_4(i,layer_no)=mean(RESULT_ALL_REALIZATION_4(i,:));
    end

    for i=1:length(RESULT_ALL_REALIZATION(:,1))

SMOOTH_AVERAGE_RESPONSE_5(i,layer_no)=mean(RESULT_ALL_REALIZATION_5(i,:));
    end

    for i=1:length(RESULT_ALL_ANSTEY(:,1))

SMOOTH_AVERAGE_ANSTEY(i,layer_no)=mean(RESULT_ALL_ANSTEY(i,:));%%%%%%%%%%%%%%
%ANSTEY
    end

    y=log(smooth(RESULT(:,1),SMOOTH_AVERAGE_RESPONSE(:,layer_no),0.05));

    [Robust_model_REALIZATION] = ROBUST(RESULT(:,1),y(:,1));
    kapa_s=-
2.*Robust_model_REALIZATION(2,1)./(2.*((IMPORT_LOG_temp4(counter2,2).*0.001)-
(IMPORT_LOG_temp4(counter,2).*0.001)))%%%%%if slop in A=1 then in A^2 is
equal 2---if TWT==>divide by two, if OWT divide by 1
    gama_s=-
2.*Robust_model_REALIZATION(1,1)./(2.*((IMPORT_LOG_temp4(counter2,2).*0.001)-
(IMPORT_LOG_temp4(counter,2).*0.001)))
    %     figure

plot(RESULT(:,1),log(smooth(RESULT(:,1),SMOOTH_AVERAGE_RESPONSE(:,layer_no),0
.05)),'k')
    hold on
    %
plot(RESULT(:,1),Robust_model_REALIZATION(1,1)+Robust_model_REALIZATION(2,1).
*RESULT(:,1),'k')
    RESULT_GAMA_KAPA(1,layer_no)=gama_s;
    RESULT_GAMA_KAPA(2,layer_no)=kapa_s;

end
```

```
toc

%%%%%%%Complimentary:

figure


plot(RESULT(:,1),log(SMOOTH_AVERAGE_RESPONSE(:,layer_no)),'r')
hold on
plot(RESULT(:,1),log(SMOOTH_AVERAGE_RESPONSE_2(:,layer_no)),'g')
hold on
plot(RESULT(:,1),log(SMOOTH_AVERAGE_RESPONSE_3(:,layer_no)),'y')
hold on
plot(RESULT(:,1),log(SMOOTH_AVERAGE_RESPONSE_4(:,layer_no)),'b')
hold on
plot(RESULT(:,1),log(SMOOTH_AVERAGE_RESPONSE_5(:,layer_no)),'k')
title('Layer 3: P wave RC Balance 100 realization response of layer 1Hz :r:0,
g=2 y=3 b=4 black=5')
xlabel('frequency (Hz)')

for i=1:length(RESULT_ALL_REALIZATION(:,1))

SMOOTH_AVERAGE_RESPONSE_ALL(i,layer_no)=(SMOOTH_AVERAGE_RESPONSE(i,layer_no)+
SMOOTH_AVERAGE_RESPONSE_2(i,layer_no)+SMOOTH_AVERAGE_RESPONSE_3(i,layer_no)+S
MOOTH_AVERAGE_RESPONSE_4(i,layer_no)+SMOOTH_AVERAGE_RESPONSE_5(i,layer_no))./
5;
end
hold on
if layer_no==1
    SMOOTH_AVERAGE_RESPONSE_temp=SMOOTH_AVERAGE_RESPONSE_ALL;
    RESULT_temp=RESULT(:,1);
    clear SMOOTH_AVERAGE_RESPONSE_ALL;
    clear RESULT;

    for i=1:length(SMOOTH_AVERAGE_RESPONSE_temp(:,1))
        if RESULT_temp(i,1)<130

SMOOTH_AVERAGE_RESPONSE_ALL(i,layer_no)=SMOOTH_AVERAGE_RESPONSE_temp(i,layer_
no);
            RESULT(i,1)=RESULT_temp(i,1);
        end
    end
end
if (layer_no==5)||(layer_no==6)
    for i=1:length(RESULT_ALL_REALIZATION(:,1))

SMOOTH_AVERAGE_RESPONSE_ALL(i,layer_no)=(SMOOTH_AVERAGE_RESPONSE(i,layer_no)+
SMOOTH_AVERAGE_RESPONSE_2(i,layer_no)+SMOOTH_AVERAGE_RESPONSE_3(i,layer_no)).
/3;
    end
end
```

```
[Robust_model_REALIZATION] =
ROBUST(RESULT(:,1),log(SMOOTH_AVERAGE_RESPONSE_ALL(:,layer_no)));
kapa_s=-
2.*Robust_model_REALIZATION(2,1)./(2.*((IMPORT_LOG_temp4(counter2,2).*0.001)-
(IMPORT_LOG_temp4(counter,2).*0.001)))%%%%%if slop in A=1 then in A^2 is
equal 2---if TWT==>divide by two, if OWT divide by 1
gama_s=-
2.*Robust_model_REALIZATION(1,1)./(2.*((IMPORT_LOG_temp4(counter2,2).*0.001)-
(IMPORT_LOG_temp4(counter,2).*0.001)))

plot(RESULT(:,1),Robust_model_REALIZATION(1,1)+RESULT(:,1).*Robust_model_REAL
IZATION(2,1),'k')
hold on

RESULT_GAMA_KAPA(1,layer_no)=gama_s;
RESULT_GAMA_KAPA(2,layer_no)=kapa_s;

%%%%%%%%%%%%%%%%%%%%%%%%%%%%%%%%%%%%%%%%%%%%%%%%%%%%%%%%%%%%%%%%%%%%%%%%%%%%
%%%%%%%%%%%%%%
%%%%%%%%%%%%%%%%%%%%%%%%%%%%%%%%%%%%%%%%%%%%%%%%%%%%%%%%%%%%%%%%%%%%%%%%%%%%
%%%%%%%%%%%%%%
%%%%%%%%%%%%%%%%%%%%%%%%%%%%%%%%%%%%Add Odoherty and Anstey estimate
TIME_interval=0.5;
REAL_LOG(:,1)=IMPORT_LOG_temp(:,1);
REAL_LOG(:,2)=IMPORT_LOG_temp(:,2);
REAL_LOG(:,3)=IMPORT_LOG_temp(:,3);
REAL_LOG(:,4)=IMPORT_LOG_temp(:,4);
REAL_LOG(:,5)=IMPORT_LOG_temp(:,3).*IMPORT_LOG_temp(:,4);
[T_LOGS_INTERPOLATED] = LOG_INTERPOLATION_TIME_CONST(REAL_LOG,TIME_interval);

%%%%%RC AND Z define FOR TIME INTERPOLATED FUNCTION
f_nyquist=1./(2.*TIME_interval.*0.001);
sample_f=2.*f_nyquist./(length(T_LOGS_INTERPOLATED(:,1)));

for i=1:length(T_LOGS_INTERPOLATED(:,5))-1

T_LOGS_INTERPOLATED(i,5)=((T_LOGS_INTERPOLATED(i+1,3).*T_LOGS_INTERPOLATED(i+
1,4))-
(T_LOGS_INTERPOLATED(i,3).*T_LOGS_INTERPOLATED(i,4))./((T_LOGS_INTERPOLATED(
i+1,3).*T_LOGS_INTERPOLATED(i+1,4))+(T_LOGS_INTERPOLATED(i,3).*T_LOGS_INTERPO
LATED(i,4)));
    T_LOGS_INTERPOLATED(i+1,6)=i.*sample_f;

end

T_LOGS_INTERPOLATED(length(T_LOGS_INTERPOLATED(:,5)),5)=T_LOGS_INTERPOLATED(l
ength(T_LOGS_INTERPOLATED(:,5))-1,5);
T_LOGS_INTERPOLATED(:,7)=fft(T_LOGS_INTERPOLATED(:,5));


%%%%%%%%%%
for i=1:length(T_LOGS_INTERPOLATED(:,1))
```

```
    if T_LOGS_INTERPOLATED(i,6)<=frequency_band
        R_W(i,1)=T_LOGS_INTERPOLATED(i,6);%%%%%%FREQ
        R_W(i,2)=abs(T_LOGS_INTERPOLATED(i,7)).^2;%%%%%%Power Spectrum of RC

    end
end

T=((IMPORT_LOG_temp4(counter2,2).*0.001)-
(IMPORT_LOG_temp4(counter,2).*0.001));

T_w(:,1)=R_W(:,1);%%%%%%%%FREQ
T_w(:,2)=exp(-R_W(:,2).*T);

plot(T_w(:,1),smooth(T_w(:,1),2.*log(T_w(:,2)),0.05),'r-.')%%%%%%energy
multiplies by 2

%%%%%%%%%%%%%%%%%%%%%%%%%%%%%%%%%%%%%%%%%%%%%%%%%%%%%%%%%%%%%%%%%%%%%%%%%%%%%%%%
%%%%%%%%%%%
%%%%%%%%%%%%%%%%%%%%%%%%%%%%%%%%%%%%%%%%%%%%%%%%%%%%%%%%%%%%%%%%%%%%%%%%%%%%%%%%
%%%%%%%%%
%%%%%%%CROSS PLOT RESULT GAMA AND KAPA
for i=1:numer_of_realizations
    if i<=numer_of_realizations
        [Robust_model_REALIZATION] =
ROBUST(RESULT(:,1),log(RESULT_ALL_REALIZATION(:,i)));
        kapa_s=-
2.*Robust_model_REALIZATION(2,1)./(2.*((IMPORT_LOG_temp4(counter2,2).*0.001)-
(IMPORT_LOG_temp4(counter,2).*0.001)))%%%%%if slop in A=1 then in A^2 is
equal 2---if TWT==>divide by two, if OWT divide by 1
        gama_s=-
2.*Robust_model_REALIZATION(1,1)./(2.*((IMPORT_LOG_temp4(counter2,2).*0.001)-
(IMPORT_LOG_temp4(counter,2).*0.001)))
        RESULT_GAMA_KAPA_FINAL(i,1)=gama_s;
        RESULT_GAMA_KAPA_FINAL(i,2)=kapa_s;
    end

    if (i>100)&&(i<=200)
        [Robust_model_REALIZATION] =
ROBUST(RESULT(:,1),log(RESULT_ALL_REALIZATION_2(:,i-100)));
        kapa_s=-
2.*Robust_model_REALIZATION(2,1)./(2.*((IMPORT_LOG_temp4(counter2,2).*0.001)-
(IMPORT_LOG_temp4(counter,2).*0.001)))%%%%%if slop in A=1 then in A^2 is
equal 2---if TWT==>divide by two, if OWT divide by 1
        gama_s=-
2.*Robust_model_REALIZATION(1,1)./(2.*((IMPORT_LOG_temp4(counter2,2).*0.001)-
(IMPORT_LOG_temp4(counter,2).*0.001)))
        RESULT_GAMA_KAPA_FINAL(i,1)=gama_s;
        RESULT_GAMA_KAPA_FINAL(i,2)=kapa_s;
    end

    if (i>200)&&(i<=300)
```

```
        [Robust_model_REALIZATION] =
ROBUST(RESULT(:,1),log(RESULT_ALL_REALIZATION_3(:,i-200)));
        kapa_s=-
2.*Robust_model_REALIZATION(2,1)./(2.*((IMPORT_LOG_temp4(counter2,2).*0.001)-
(IMPORT_LOG_temp4(counter,2).*0.001)))%%%%%if slop in A=1 then in A^2 is
equal 2---if TWT==>divide by two, if OWT divide by 1
        gama_s=-
2.*Robust_model_REALIZATION(1,1)./(2.*((IMPORT_LOG_temp4(counter2,2).*0.001)-
(IMPORT_LOG_temp4(counter,2).*0.001)))
        RESULT_GAMA_KAPA_FINAL(i,1)=gama_s;
        RESULT_GAMA_KAPA_FINAL(i,2)=kapa_s;
    end

    if (i>300)&&(i<=400)
        [Robust_model_REALIZATION] =
ROBUST(RESULT(:,1),log(RESULT_ALL_REALIZATION_4(:,i-300)));
        kapa_s=-
2.*Robust_model_REALIZATION(2,1)./(2.*((IMPORT_LOG_temp4(counter2,2).*0.001)-
(IMPORT_LOG_temp4(counter,2).*0.001)))%%%%%if slop in A=1 then in A^2 is
equal 2---if TWT==>divide by two, if OWT divide by 1
        gama_s=-
2.*Robust_model_REALIZATION(1,1)./(2.*((IMPORT_LOG_temp4(counter2,2).*0.001)-
(IMPORT_LOG_temp4(counter,2).*0.001)))
        RESULT_GAMA_KAPA_FINAL(i,1)=gama_s;
        RESULT_GAMA_KAPA_FINAL(i,2)=kapa_s;
    end

    if (i>400)&&(i<=500)
        [Robust_model_REALIZATION] =
ROBUST(RESULT(:,1),log(RESULT_ALL_REALIZATION_5(:,i-400)));
        kapa_s=-
2.*Robust_model_REALIZATION(2,1)./(2.*((IMPORT_LOG_temp4(counter2,2).*0.001)-
(IMPORT_LOG_temp4(counter,2).*0.001)))%%%%%if slop in A=1 then in A^2 is
equal 2---if TWT==>divide by two, if OWT divide by 1
        gama_s=-
2.*Robust_model_REALIZATION(1,1)./(2.*((IMPORT_LOG_temp4(counter2,2).*0.001)-
(IMPORT_LOG_temp4(counter,2).*0.001)))
        RESULT_GAMA_KAPA_FINAL(i,1)=gama_s;
        RESULT_GAMA_KAPA_FINAL(i,2)=kapa_s;
    end
end
figure
plot(RESULT_GAMA_KAPA_FINAL(:,1),RESULT_GAMA_KAPA_FINAL(:,2),'b*')
title('Layer 3 gama kapa result')
xlabel(' gama s')
ylabel('ylebel')
T=((IMPORT_LOG_temp4(counter2,2).*0.001)-
(IMPORT_LOG_temp4(counter,2).*0.001));
T_w(:,1)=R_W(:,1);%%%%%%%%FREQ
T_w(:,2)=exp(-SMOOTH_AVERAGE_ANSTEY(:,layer_no).*T);

plot(T_w(:,1),smooth(T_w(:,1),2.*log(T_w(:,2)),0.05),'r-.')%%%%%%energy
multiplies by 2
```

APPENDIX B

MATLAB CODES FOR AVA ANALYSIS

The following code perform AVA analysis on baseline and monitoring VSP surveys after correcting geometrical spreading, intrinsic attenuation and scattering (5.11).

```
%%%%%This MATLAB code intended to perform AVA analysis of baseline VSP
%%%%%survey. I correct the effect of geometrical spreading, intrinsic
%%%%%attenuation and scattering.
clc
clear
load RUN_P_REAL_REAL.mat;  %%%%%
load W1_SHOT_COORDINATE.dat;%%%%%
load W1_VSP_MARLY_TG_AFT_ALIGNMENT_14JULY.dat;
load W1_shift_step1_14JULY.dat;

close all


%%%%%Setup

span2=0.10;
ANGLE_SWITCH=2; %%%%1 for angle and 2 for sin^2theta display
YMIN=-0.55;%%%
YMAX=0;%%%%
XMIN=0;%%%%
XMAX=80;%%%%


W_TIME_GATE=W1_VSP_MARLY_TG_AFT_ALIGNMENT_14JULY;
W_TIME_SHIFT=W1_shift_step1_14JULY;

for i=1:length(W_TIME_GATE(:,1))
    for j=1:length(W_TIME_SHIFT(:,1))
        if
(W_TIME_GATE(i,1)==W_TIME_SHIFT(j,1))&&(W_TIME_GATE(i,2)==W_TIME_SHIFT(j,2))
            W_TIME_GATE(i,4)=W_TIME_GATE(i,3)+(W_TIME_SHIFT(j,3));
        end
    end
end

for i=1:length(W_TIME_GATE(:,1))
    if W_TIME_GATE(i,4)==0
        W_TIME_GATE(i,4)=W_TIME_GATE(i,3);
    end
end
```

```
N_selected_shots=[1:1:119]';%%%%Sequence of shots to read
span=0.10;
NO_PANEL=4;%Number of OF PANEL TO DISPLAY AVA RESULTS

%%%%%ATTENUATION MODEL
GAMA1=[-2;-0.35;1.23;-0.24;3.92;2.76];
KAPA1=[0.12;0.135;0.0473;0.0163;0.0255;0.1437];
GAMA3=[0;-13;-16;-13;-34;-35];
KAPA3=[0;0.05;0.2;0.25;0.5;0.004];

R_DISTANCE=zeros(1,length(SEGP(:,1)));
SIN_SQUARE_INCIDENCE_MATRIX=zeros(6,length(SEGP(:,1)));%%%SIN^theta INCIDENCE
SIN_SQUARE_REFLECTION_MATRIX=zeros(6,length(SEGP(:,1)));%SIN^theta REFLECTION
COS_THETA_DIRECTIVITY=zeros(1,length(SEGP(:,1)));%%%%%%%%%%%%%%%DIRECTIVITY
R_Distance=zeros(1,length(SEGP(:,1)));
GAMA_INCIDENCE=0;
KAPA_INCIDENCE=0;
GAMA3_INCIDENCE=0;
KAPA3_INCIDENCE=0;
GAMA_REFLECTION=0;
KAPA_REFLECTION=0;
GAMA3_REFLECTION=0;
KAPA3_REFLECTION=0;
frequency=40;
METHOD_NUM=1;%%%%%%%%%%%%%%%%%%%%%%%%%%%%%1 For random noise consideration
PLOT_NUM=2;

%%%%%%%%%%%%%%%%%%%%%%%%%%%%%%%%%%%%%%%%%%%%%%%
for i=1:length(SEGP(:,1))
    for j=1:6
        if THICKNESS_MATRIX_REFLECTION(j,i)~=0
            SIN_SQUARE_REFLECTION_MATRIX(j,i)=1-
((THICKNESS_MATRIX_REFLECTION(j,i)./LENGTH_MATRIX_REFLECTION(j,i)).^2);
%%%%%%SIN^2 theta REFLECTION
        end
    end
end
%%%%%%%%%%%%%%%%%%%%%%%%%%%%%%%%%%%%

for i=1:length(SEGP(:,1))
    SIN_SQUARE_INCIDENCE_MATRIX(:,i)=1-
((LAYERS(:,4)./LENGTH_MATRIX_INCIDENCE(:,i)).^2); %%%%%%SIN^2 theta INCIDENCE

R_Distance(1,i)=sum(LENGTH_MATRIX_INCIDENCE(:,i))+sum(LENGTH_MATRIX_REFLECTIO
N(:,i));%%%%%%TOTAL_DISTANCE

TT_RESERV_CALC_TOTAL(1,i)=sum(TIME_MATRIX_INCIDENCE(:,i))+sum(TIME_MATRIX_REF
LECTION(:,i));%%%%

    %%%%%%%%%%%%%%%%%%%%%%%%%%%%%%%%%%%%%%%%%%%%%%%
    %%%%MODEL GEOMETRICAL SPREADING, SCATTERING AND INTRINSIC ATTENUATION
```

```
    for layer=1:6

GAMA_INCIDENCE=GAMA_INCIDENCE+(GAMA1(layer,1).*TIME_MATRIX_INCIDENCE(layer,i)
.*0.001);

KAPA_INCIDENCE=KAPA_INCIDENCE+(KAPA1(layer,1).*TIME_MATRIX_INCIDENCE(layer,i)
.*0.001);

GAMA3_INCIDENCE=GAMA3_INCIDENCE+(GAMA3(layer,1).*TIME_MATRIX_INCIDENCE(layer,
i).*0.001.*SIN_SQUARE_INCIDENCE_MATRIX(layer,i));

KAPA3_INCIDENCE=KAPA3_INCIDENCE+(KAPA3(layer,1).*TIME_MATRIX_INCIDENCE(layer,
i).*0.001.*SIN_SQUARE_INCIDENCE_MATRIX(layer,i));
    end

    for layer=6:-1:SEGP(i,15)

GAMA_REFLECTION=GAMA_REFLECTION+(GAMA1(layer,1).*TIME_MATRIX_REFLECTION(layer
,i).*0.001);
        KAPA_REFLECTION=
KAPA_REFLECTION+(KAPA1(layer,1).*TIME_MATRIX_REFLECTION(layer,i).*0.001);

GAMA3_REFLECTION=GAMA3_REFLECTION+(GAMA3(layer,1).*TIME_MATRIX_REFLECTION(lay
er,i).*0.001.* SIN_SQUARE_REFLECTION_MATRIX(layer,i));

KAPA3_REFLECTION=KAPA3_REFLECTION+(KAPA3(layer,1).*TIME_MATRIX_REFLECTION(lay
er,i).*0.001.* SIN_SQUARE_REFLECTION_MATRIX(layer,i));
    end

    ATTAUATION_TOTAL(1,i)=exp(-
((GAMA_INCIDENCE+frequency.*KAPA_INCIDENCE)+(GAMA3_INCIDENCE+frequency.*KAPA3
_INCIDENCE)+(GAMA_REFLECTION+KAPA_REFLECTION.*frequency)+(GAMA3_REFLECTION+KA
PA3_REFLECTION.*frequency)));%%%%%%%%ALL ATTENUATION
    GAMA_INCIDENCE=0;
    KAPA_INCIDENCE=0;
    GAMA3_INCIDENCE=0;
    KAPA3_INCIDENCE=0;
    GAMA_REFLECTION=0;
    KAPA_REFLECTION=0;
    GAMA3_REFLECTION=0;
    KAPA3_REFLECTION=0;
    INCIDENCE_SIN_SQUARE_RESERVOIR(1,i)=SIN_SQUARE_INCIDENCE_MATRIX(6,i);
    COS_THETA_DIRECTIVITY(1,i)=sqrt(1-
(SIN_SQUARE_REFLECTION_MATRIX(SEGP(i,15),i)));
end


for i=1:length(SEGP(:,1))
    X_TOTAL(i,1)=INCIDENCE_SIN_SQUARE_RESERVOIR(1,i);%%%%%%%%%SIN^2 THETA
INCIDENCE RESERVOIR
    Y_TOTAL(i,1)=-SEGP(i,2); %%%%%%%AMPLITUDE PICKED
    REC_DEPTH_TOTAL(i,1)=SEGP(i,14);%%%%%%%%%%DEPTH RECEIVER
    FFID_TOTAL(i,1)=SEGP(i,7);
```

```
    FFID(i,1)=SEGP(i,7);
    SOURCE_TOTAL(i,1)=SEGP(i,4);
    SOURCE(i,1)=SEGP(i,4);
    OFFSET_TOTAL(i,1)=SEGP(i,5);
    R_TOTAL(i,1)=R_Distance(1,i);%%%%%%%%DISTANCE
    TIME_RESER_PICKED(i,1)=SEGP(i,8);%%%%%%%%%%%%TIME OF PICKED RESERVOIR
    ATTENUATION(i,1)=ATTAUATION_TOTAL(1,i);%%%%%%%%%%ATTENUATION SUM OF
GT+F*KAPA*T +GAMA3*T+F*KAPA3*T
    COS_THETA_DIRECTIVITY_TOTAL(i,1)=COS_THETA_DIRECTIVITY(1,i);
end
s=0;

SOURCE_SORTED=sort(SOURCE);
N = histc(SOURCE,SOURCE_SORTED);%Counting number of traces per FFID
SOURCE_SORTED(N==0) = [];
N(N==0) = [];%Counting number of traces per FFID
kk_count=1;  count_g=1;
count=1; legendtext ='';

for ii=1:length(N(:,1))
    X=zeros(N(ii,1),1);%%%%%SIN SQUARE INCIDENCE TO RESERVOIR
    Y=zeros(N(ii,1),1);%%%%%raw AMP
    REC_DEPTH=zeros(N(ii,1),1);
    OFFSET=zeros(N(ii,1),1);
    SOURCE=zeros(N(ii,1),1);
    yy2=zeros(N(ii,1),1);
    yyp1=zeros(N(ii,1),1);
    yEst=zeros(N(ii,1),1);
    yEst_ROBUST=zeros(N(ii,1),1);
    ANGLE_RECIEVED_RES=zeros(N(ii,1),1);
    ANGLE_RECIEVED_REC=zeros(N(ii,1),1);
    R=zeros(N(ii,1),1);
    TIME=zeros(N(ii,1),1);
    ATTEN=zeros(N(ii,1),1);%%%%%%
    TT_ERROR=zeros(N(ii,1),1);

    for j=1:N(ii,1)
        X(j,1)=X_TOTAL(j+s,1);%X=Sin^2theta
        Y(j,1)=Y_TOTAL(j+s,1);%%%%%% AMP
        REC_DEPTH(j,1)=REC_DEPTH_TOTAL(j+s,1);
        OFFSET(j,1)=OFFSET_TOTAL(j+s,1);
        FFID(j,1)=FFID_TOTAL(j+s,1);
        SOURCE(j,1)=SOURCE_TOTAL(j+s,1);
        ANGLE_RECIEVED_RES(j,1)=asin(sqrt(X_TOTAL(j+s,1)));%%%%RAD

ANGLE_RECIEVED_REC(j,1)=acos(COS_THETA_DIRECTIVITY_TOTAL(j+s,1));%%%%RAD
        R(j,1)=R_TOTAL(j+s,1);%%%%%%R
        TIME(j,1)=TIME_RESER_PICKED(j+s,1);%TIME
        ATTEN(j,1)=ATTAUATION_TOTAL(1,j+s);%%%%ATTENUATION SUM OF GT+F*KAPA*T
+GAMA3*T+F*KAPA3*T
    end
```

```
    yy2 = smooth(REC_DEPTH,Y,span,'moving');%

    %%%%%-------------------------------------------------------------------
--

    h2=floor(count/4);
    if mod(count,4)==0
        h2=h2-1;
        pa=count-(h2*4);
    elseif h2==0

        pa=count;
    elseif  h2>=1
        pa=count-(h2*4);
    end

    %%%%%%%%%%%%%

    %%%%% PERFORMING AVA


[n_squared,index_A,index_B,scaling_factor,TOTAL_DECAY]=AVO_MIN_ERROR_NOISE_AT
TENUATION1(X,yy2,OFFSET,SOURCE,R,ATTEN,ANGLE_RECIEVED_REC);


    alpha (1,ii)=index_A;%Intercept
    alpha (2,ii)=index_B;%Gradiient
    alpha (3,ii)=n_squared;%Noise
    alpha (5,ii)=SOURCE(1,1);
    alpha (6,ii)=max(OFFSET(:,1));
    for ff=1:length(W1_Source_FFID(:,1))
        if SOURCE(1,1)== W1_Source_FFID(ff,2)
            ffid=W1_Source_FFID(ff,3);
            for sst=1:length(W1_SHOT_COORDINATE(:,3))
                if ffid==W1_SHOT_COORDINATE(sst,2)
                    alpha (7,ii)=W1_SHOT_COORDINATE(sst,3);%%%%X COORDINATE
                    alpha (8,ii)=W1_SHOT_COORDINATE(sst,4);%%%%Y COORDINATE
                end
            end
        end
    end

    yEst=zeros(length(yyp1(:,1)),1);

    h1=floor(count/NO_PANEL);

    if mod(count,NO_PANEL)==0
        h1=h1-1;
        p=count-(h1*NO_PANEL);
    elseif h1==0
```

```
        p=count;
    elseif  h1>=1
        p=count-(h1*NO_PANEL);
    end

    for pp=1:length(yy2(:,1))
        yEst(pp,1) = n_squared +
(1./R(pp,1)).*cos(ANGLE_RECIEVED_REC(pp,1)).*ATTEN(pp,1).*((index_A+(index_B.
*X(pp,1))));
    end

    r = corr2(yy2,yEst);%%%%%%%CORRELAION COEFF

    alpha (4,ii)=r;

    count_g=count_g+1;

    %---------------------------
    %%%PLOTTING THE RESULTS
    figure(h1+3)

    subplot(2,2,p)

    plot(asin(sqrt(X)).*180./3.1415,((yy2.*scaling_factor)./TOTAL_DECAY)-
n_squared,'r+',asin(sqrt(X)).*180./3.1415,index_A+index_B.*X,'b*')

    ylabel('Amplitude')
    xlabel('Sin^2 theta')
    tex4=text(max(X)-((max(X)-min(X))/2),((max(yy2).*(scaling_factor)-
((max(yy2).*(scaling_factor)-
min(yy2).*(scaling_factor))/5)).*0.3)./median(TOTAL_DECAY),[sprintf('SOURCE=%
2i',SOURCE(1,1))]);
    tex=text(max(X)-((max(X)-min(X))/2),((max(yy2).*(scaling_factor)-
((max(yy2).*(scaling_factor)-
min(yy2).*(scaling_factor))/5)).*0.2)./median(TOTAL_DECAY),[sprintf('I=%2f',i
ndex_A)]);
    tex1=text(max(X)-((max(X)-min(X))/2),(((max(yy2).*(scaling_factor)-
((max(yy2).*(scaling_factor)-
min(yy2).*(scaling_factor))/5)).*0.1))./median(TOTAL_DECAY),[sprintf('G=%2f',
index_B)]);
    tex2=text(max(X)-((max(X)-min(X))/2),(((max(yy2).*(scaling_factor)-
((max(yy2).*(scaling_factor)-
min(yy2).*(scaling_factor))/5)).*0.05))./median(TOTAL_DECAY),[sprintf('r=%2f'
,r)]);
    s=s+ N(ii,1);
    count=count+1;
    %%%%Output AVA Results

    X_total(:,ii)=X(:,1);
    yy2_total(:,ii)=yy2(:,1);
    scaling_factor_total(1,ii)=scaling_factor;
    TOTAL_DECAY_total(:,ii)=TOTAL_DECAY(:,1);
```

```
yy2_tatal_scaled(:,ii)=(scaling_factor.*yy2_total(:,ii))./(TOTAL_DECAY_total(
:,ii));%%%%%
    n_squared_total(1,ii)=n_squared(1,1);
    index_A_total(1,ii)=index_A(1,1);%Intercept
    index_B_total(1,ii)=index_B(1,1);%Gradient
    source_total(1,ii)=SOURCE(1,1);
    R_total(:,ii)=R(:,1);
    ATTEN_total(:,ii)=ATTEN(:,1);
    ANGLE_RECIEVED_REC_total(:,ii)=ANGLE_RECIEVED_REC(:,1);
    OFFSET_total(:,ii)=OFFSET(:,1);
    TT_ERROR_total(:,ii)=TT_ERROR(:,1);
end
```